



Universitat Autònoma de Barcelona

ADVERTIMENT. L'accés als continguts d'aquesta tesi doctoral i la seva utilització ha de respectar els drets de la persona autora. Pot ser utilitzada per a consulta o estudi personal, així com en activitats o materials d'investigació i docència en els termes establerts a l'art. 32 del Text Refós de la Llei de Propietat Intel·lectual (RDL 1/1996). Per altres utilitzacions es requereix l'autorització prèvia i expressa de la persona autora. En qualsevol cas, en la utilització dels seus continguts caldrà indicar de forma clara el nom i cognoms de la persona autora i el títol de la tesi doctoral. No s'autoritza la seva reproducció o altres formes d'explotació efectuades amb finalitats de lucre ni la seva comunicació pública des d'un lloc aliè al servei TDX. Tampoc s'autoritza la presentació del seu contingut en una finestra o marc aliè a TDX (framing). Aquesta reserva de drets afecta tant als continguts de la tesi com als seus resums i índexs.

ADVERTENCIA. El acceso a los contenidos de esta tesis doctoral y su utilización debe respetar los derechos de la persona autora. Puede ser utilizada para consulta o estudio personal, así como en actividades o materiales de investigación y docencia en los términos establecidos en el art. 32 del Texto Refundido de la Ley de Propiedad Intelectual (RDL 1/1996). Para otros usos se requiere la autorización previa y expresa de la persona autora. En cualquier caso, en la utilización de sus contenidos se deberá indicar de forma clara el nombre y apellidos de la persona autora y el título de la tesis doctoral. No se autoriza su reproducción u otras formas de explotación efectuadas con fines lucrativos ni su comunicación pública desde un sitio ajeno al servicio TDR. Tampoco se autoriza la presentación de su contenido en una ventana o marco ajeno a TDR (framing). Esta reserva de derechos afecta tanto al contenido de la tesis como a sus resúmenes e índices.

WARNING. The access to the contents of this doctoral thesis and its use must respect the rights of the author. It can be used for reference or private study, as well as research and learning activities or materials in the terms established by the 32nd article of the Spanish Consolidated Copyright Act (RDL 1/1996). Express and previous authorization of the author is required for any other uses. In any case, when using its content, full name of the author and title of the thesis must be clearly indicated. Reproduction or other forms of for profit use or public communication from outside TDX service is not allowed. Presentation of its content in a window or frame external to TDX (framing) is not authorized either. These rights affect both the content of the thesis and its abstracts and indexes.



Metal nanoparticle carbon nanocomposites to produce electrochemical devices for environmental water monitoring

WENCHAO DUAN

DOCTORAL THESIS

Doctoral Studies in Material Science

Supervised by Dr. César Fernández-Sánchez and Dr. Martí Gich Garcia

Tutor: Dr. Martí Gich Garcia

El **Dr. César Fernández Sánchez** (Investigador Científic del CSIC), el **Dr. Martí Gich Garcia** (Científic Titular del CSIC)

CERTIFIQUEN:

Que en Wenchao Duan, amb un Màster en Química Inorgànica per la Universitat de Shandong, Xina ha dut a terme aquesta tesi doctoral sota la seva direcció i que porta per títol "**Metal nanoparticle carbon nanocomposites to produce electrochemical devices for environmental water monitoring**", la qual queda recollida en aquesta memòria per optar al grau de Doctor en Ciència de Materials.

.

I perquè així consti, signen el present certificat

Dr. César Fernández Sánchez

Dr. Martí Gich Garcia

Wenchao Duan

Bellaterra, 14 de juliol de 2022

Acknowledgments

Dedicated to the nobles I have met in the past 30 years

Here, I most want to express my gratitude to **my parents**. They are so brave, strong, and visionary. We all know that education is a long-term investment process, and you don't know what the future returns will be. But they were not afraid of hardship and forged ahead. When they were living in extreme poverty and the future was gloomy, they still made a desperate attempt to keep my brother, sister and me going to school. They were unmoved by the cynicism of some people around them.

At the same time, my father and mother did not forget to teach me by word and deed. First of all, they dared to let me go, let me try and let me make my own decisions. My father always appeared in time to make up for me when I made mistakes. They did not spoil their children, so I began to accept the tempering of society when I was a child. They told me from childhood that the only one who can save you is yourself, you are your own savior, and you must be self-reliant. I am very fortunate to have such wise parents.

Secondly, I would like to thank my motherland and the China Scholarship Council, who sponsored me and gave me this precious opportunity to study abroad, gain knowledge and experience different cultures. These four years of study abroad will definitely have an important impact on my life.

I would also like to thank my two mentors, **Dr. Martí Gich** and **Dr. César Fernández-Sánchez**. I still remember when I first arrived in Barcelona and Martí picked me up at the airport. After hearing that I had never seen the sea, he made a special trip and took me to see the beach and sea. Then he showed me the research institute and my apartment. This meticulous care immediately made me, a foreigner, feel warm, as if I had found a home. From the time I entered the laboratory, César taught me to do experiments step by step. My English listening was not good, so he repeated every detail of the experiment over and over again. He even wrote up the experimental steps and details and emailed them to me, helping me until I fully understood them.

In the first year and the second year of my Ph.D., I was full of imaginative ideas, many unrealistic. My mentors didn't dismiss my thoughts, but were tolerant, allowed me to explore, and agreed to buy some reagents so I could do a few attempts. Even if a lot of experiments failed or proved useless, they always put the protection of my interests first.

When I was approaching graduation, they worked overtime to help me revise my papers and thesis. When submitting the papers to the targeted journal, they respected my wishes. They readily assisted in my job search demands. They would ask me about my plans for the future and make suggestions according to my plans, including recommending optional post-doctoral positions. How did I meet such good mentors during the four years!

Next, I would like to thank my two cousins, Wenming Xin and Wenbin Xin, for their guidance and help. I would like to thank the Xingda Foundation for their financial support during my university years, enabling me to successfully complete my university studies. Thanks to my master's supervisor, Professor Haibing Xia, who led me to a preliminary understanding of scientific research. Thank you, sister Tingting Miao and brother-in-law Shiming Liu for your care and help. Special thanks to Dorothy Bohn for helping me. She is like a mother, who help me improve my spoken English with kindness and patience.

Thanks to Anna Roig, Javier del Campo, Murat Gunes and Miquel Torras for guidance and help with my experiments. Thanks to the laboratory members of the two research groups for their help and care, and also thanks to the technicians, Neus, Sergi, Marta, Albert, Julio Fraile, Roberta Ceravola, Amable Bernabé, XRD service, the people from the Clean Room at CNM, specially Roser Mas and also give thanks to Josefina, Mercè and Toni that helped me get the samples from the wastewater treatment plant and to Amelia Arrojo from CETEMAS for the wood samples.

Then, I would like to thank my brother and sister for their meticulous care for my parents during the 4 years I have been abroad so that I could study with peace of mind in my thirties.

From the moment I set foot in Barcelona to now holding my graduation thesis, time passed quickly like a white pony's shadow across a crevice. There was joy, hesitation, and fatigue. The taste of it can only be experienced if you experience it yourself. Graduation with a doctoral degree is not the end of the study, but a new beginning. I hope that I can still get your guidance, help and teaching in my new journey.

Foreword and Scope of the Thesis

Water is a precious resource that is essential for all forms of life on Earth. With the development of industry, agriculture, and an increasing human population concentrating in the megalopolis, large amounts of wastewater are produced and discharged. While approximately 80% of wastewater worldwide remains uncollected and untreated, the increasing awareness that water is a finite, vulnerable resource calls for increased monitoring and treatment of a large number of pollutants. In wastewater, a particularly relevant pollution impact comes from organic matter, halogenated compounds and heavy metals, which namely contribute to water deleterious effects on human beings and the environment. As a result, various regulations are set for these pollutants in water. The intensive monitoring of water quality enforced by new wastewater management directives calls for the development of fast and low-cost analytical platforms that enabled timely and robust detection of a variety of chemical pollutants. Electrochemical sensors are poised to become alternative technologies for the sensitive analysis of environmentally relevant chemicals due to the merits of low-cost, rapid detection, simplicity, portability, low power requirements, safety of operation and potential in-situ and semi-continuous analysis.

In this context, this thesis focuses on developing low-cost and easy-to-use miniaturized electrochemical sensors for the analysis of the organic matter, halogenated compounds and heavy metals in waters. For this purpose, several functional materials are tailored synthesized and processed to fabricate thick-film and thin-film sensors by screen-printing and lithography available industrial processes.

Three electrode composite materials are prepared that comprise a porous carbon matrix and metal or metal oxide nanoparticles. Several sol-gel chemical synthesis approaches are studied to produce a carbon copper-based nanoparticle nanocomposite material. With the aim of contributing to the circular economy and looking at a more sustainable alternative for producing these materials, a silver nanoparticle-doped porous carbon matrix is prepared using bread waste impregnated with a silver nanoparticle precursor. Also, porous carbon composites are prepared from wood by-products and further modified with bismuth nanoparticles.

The developed materials are electrochemically evaluated using paste electrodes before producing large batches of commercial-like screen-printed single-use electrodes that are applied to the detection of the already mentioned target analytes.

Thin-film carbon electrodes are also produced on Si/SiO₂ substrates by a combined sol-gel material synthesis and photolithography/dry etching process at the wafer level. Conventional three-electrode electrochemical cells of planar configuration are produced and developed as sensor devices for detecting organic load by electrodepositing copper nanoparticles (Cu NPs) on the working electrode under controlled potentiostatic conditions. In addition, a simple fluidic device is fabricated that includes a flow cell to integrate the thin-film carbon electrodes and carry out the Cu NPs electrodeposition and organic load detection in an automatic fashion.

This thesis is divided into 7 Chapters. **Chapter 1** is a general introduction that describes the state-of-the-art in water pollution, the motivation of the work as well as the standard and alternative analytical approaches for water pollutant detection. It emphasizes the high demand for rapid and reliable analytical platforms that could be massively applied in-field. This chapter also summarizes the development of metal nanoparticle-modified porous carbon electrode materials and the two main fabrication approaches of screen-printing and photolithography/etching processes for the fabrication of thick-film and thin-film electrochemical devices. It finishes by discussing the interest in applying such devices to monitoring chemical oxygen demand (COD), organohalides and heavy metals in waters.

Chapter 2 summarizes the aims and objectives of the thesis.

Chapter 3 describes the preparation and characterization of three types of copper-based nanoparticle-modified porous carbon materials, a bread waste-derived silver nanoparticle carbon composite material, and carbon materials derived from three types of wood by-products.

Chapter 4 focuses on evaluating the electrochemical performance of the materials produced in Chapter 3. For this carbon paste electrodes were fabricated and applied to the analysis of COD, halogenated compounds and standard redox species.

Chapter 5 reports the fabrication and characterization of the screen-printed electrodes with the materials prepared in Chapter 3 and evaluated in Chapter 4. The electrochemical performance of the produced screen-printed electrodes was thoroughly assessed by detecting COD, halogenated compounds and heavy metals. In addition, a new design of

screen-printed electrodes with a modified paper disk component is presented to enable sample-to-result measurements with a miniaturized electrochemical platform for on-site analysis.

Chapter 6 describes the preparation of robust carbon thin films at the wafer level by a sol-gel process and the fabrication of electrodes by a combined photolithographic and dry etching process. The produced sensors are integrated into a simple fluidic device and customized for the rapid chronoamperometric monitoring of COD by modifying their surface with Cu NPs.

Chapter 7 shows the general conclusions of the thesis and some perspectives for future work.

Table of Contents

Acknowledgments

Foreword and scope of the thesis

Index

Chapter 1 Introduction - background and motivation of the thesis.....	1
Summary.....	1
1.1 State-of-the-art in water pollution.....	2
1.2 Standard analytical approaches for water pollutant detection.....	6
1.3 Alternative analytical platforms for water pollutant detection.....	10
1.4 Metal nanoparticle-modified porous carbon electrode materials.....	12
1.5 Developing thick- and thin-film carbon-derived electrodes.....	16
1.6 Electrochemical sensor applications for COD, organohalides and heavy metals in water.....	21
References.....	25
 Chapter 2 Aims and Objectives.....	 39
 Chapter 3 Synthesis of porous carbon nanocomposites modified with metal nanoparticles.....	 41
Summary.....	41
3.1 Introduction.....	42
3.2 Synthesis of composites of porous carbon and Copper-based nanoparticles.....	43
3.2.1 Physical mixing method for the preparation of composites of porous C and Cu ₂ O nanoparticles.....	44

3.2.2 One-pot synthesis of composites of porous carbon and Cu nanoparticles.....	46
3.2.3 Structural and morphological characterization.....	46
3.3 Synthesis of silver nanoparticle-modified porous carbon nanocomposites.....	56
3.3.1 Impregnation approach to preparing Ag-doped carbon nanocomposites.....	56
3.2.2 Structural and morphological characterization.....	57
3.4 Synthesis of wood-derived porous carbon nanocomposites.....	61
3.5 Conclusions.....	69
References.....	70

Chapter 4 Electroanalytical evaluation of metal nanoparticle-modified porous carbon nanocomposites for monitoring water pollutants.....74

Summary.....	74
4.1 Introduction.....	75
4.1.1 Evaluating the performance of the nanomaterials with Carbon Paste Electrodes...	75
4.2 Electrochemical performance of Copper-based nanoparticle-modified carbon nanocomposites: analysis of chemical oxygen demand.....	76
4.2.1 Evaluation of the electrode response for COD analysis.....	77
4.2.2 Analysis of the wastewater samples.....	82
4.3 Electrochemical performance of Silver nanoparticle-modified carbon nanocomposites: analysis of Halides and Organohalides.....	85
4.3.1 Halide detection.....	85
4.3.2 Analysis of organohalide molecules in water.....	95
4.4 Electrochemical performance of wood-derived carbon material: analysis of redox species.....	104
4.4.1 Electrochemical assessment of the wood-derived carbon paste electrodes.....	104

4.5 Conclusions.....	110
References.....	112

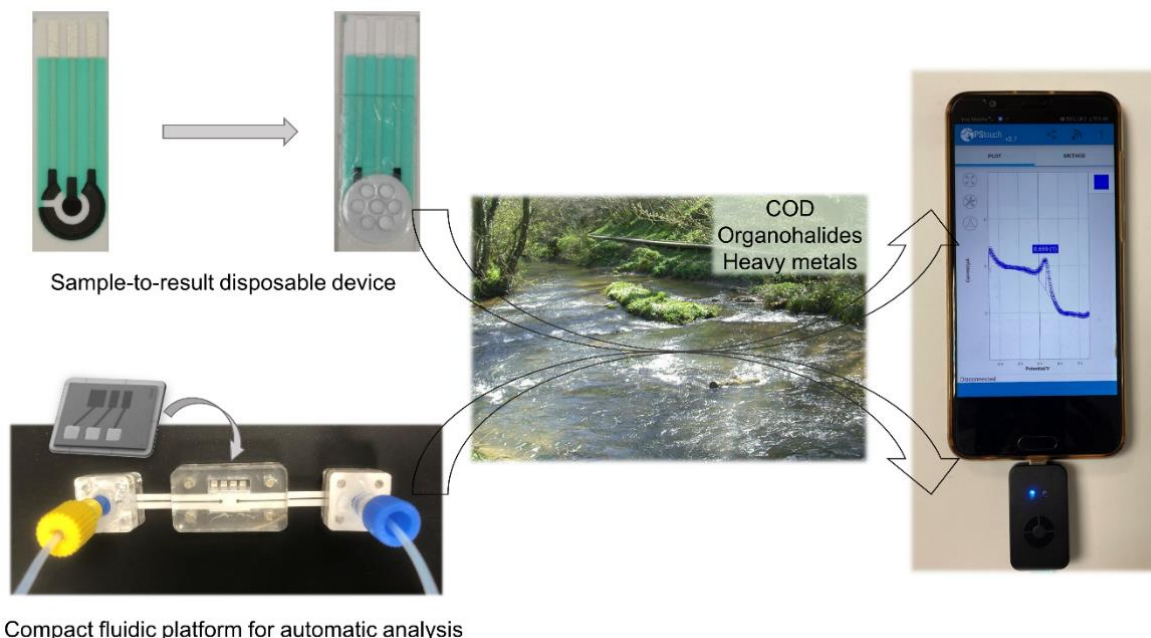
Chapter 5 Preparation and characterization of metal nanoparticle-modified carbon nanocomposite screen-printed electrodes.....119

Summary.....	119
5.1 Introduction.....	120
5.2 Fabrication and electrochemical characterization of Cu/C screen-printed electrodes.....	121
5.2.1 Preparation of Cu/C ink and screen-printing fabrication of Cu/C composite electrodes.....	121
5.2.2 Electrochemical assessment of SPE_Cu/C: analysis of COD.....	123
5.2.3 Integration of a paper disk with the SPE_Cu/C sensor for one-step COD measurements.....	126
5.2.4 Analysis of water samples in the laboratory.....	130
5.2.5 In-field analysis of COD in an urban wastewater treatment plant.....	133
5.3 Fabrication and electrochemical characterization of screen-printed Ag/C electrodes.....	136
5.3.1 Preparation of Ag/C ink and screen-printing fabrication of Ag/C electrodes.....	136
5.3.2 Electrochemical assessment of SPE_Ag/C: Analysis of Chloride.....	141
5.3.3 Application of the SPE_Ag/C to the analysis of sucralose and trichloroacetic acid.....	146
5.4 Fabrication and electrochemical characterization of wood-derived screen-printed carbon electrodes.....	154
5.4.1 Electrochemical performance of Bi or Sb modified SPE_C _c devices: Analysis of heavy metals.....	157
5.5 Conclusions.....	165

References.....	166
Chapter 6 Fabrication and characterization of metal nanoparticle-modified carbon/silica thin-film electrochemical devices.....	171
Summary.....	171
6.1 Introduction.....	172
6.2 Fabrication and characterization of Cu NP-modified carbon/silica thin film electrode device.....	173
6.2.1 Preparation of C/SiO ₂ films.....	173
6.2.2 Optimization of the conductivity of the carbon/silica thin films.....	177
6.2.3 Fabrication of carbon/silica thin-film electrodes at the wafer level by a photolithographic and etching process.....	180
6.2.4 Electrochemical characterization of the carbon/silica thin film electrodes.....	183
6.2.5 Electrodeposition of Cu NPs on the surface of carbon/silica electrodes.....	185
6.2.6 Evaluation of the sensor performance for COD analysis.....	190
6.2.7 Implementation of the Cu NP-modified C/SiO ₂ sensor in a modular fluidic system.....	196
6.2.8 Analysis of urban wastewater samples.....	201
6.3 Conclusions.....	202
References.....	205
Chapter 7 Conclusions and further work.....	208
7.1 General conclusions.....	208
7.2 Ongoing and further work.....	209
Conferences and Publications of this Ph.D. Thesis.....	212
The Author.....	215

Chapter 1

Introduction – background and motivation of the thesis



Graphic summary of the Ph.D. thesis

Summary

This chapter presents a state-of-the-art about water pollution focusing on classical and innovative analytical platforms for the detection of water pollutants. It highlights the urgent need for rapid and reliable approaches that could be massively applied on-site at the point of need. It also includes a brief description of the development of metal nanoparticle-modified porous carbon electrode materials and the two main fabrication strategies used for material implementation into thick-film and thin-film electrochemical devices. These are screen-printing and photolithography/etching microfabrication processes, respectively. The chapter also describes the interest in applying such devices to monitoring chemical oxygen demand (COD), organohalides, and heavy metal pollutants in waters.

1.1 State-of-the-art in water pollution

Water is the core of life. It is fundamental for species survival, making it the most precious natural resource on the Earth planet. Access to clean and pure water for everybody is of high concern worldwide. Since the first Industrial Revolution, civilization has faced the harmful effects of industrial growth, urbanization, and rapid population expansion on water resources. Many hazardous chemical substances and untreated sewage end up in water sources, resulting in severe damage to the ecosystems and human health.¹

Around 90% of untreated sewage is released into water bodies in developing countries and 2.0 million tons of sewage and other effluents were discharged into the world's water bodies per day.² According to the World Health Organization (WHO), drinking water in many countries does not meet the WHO standards, and 80% of diseases are considered to be waterborne.³ As a direct or indirect result, around 3.2 million children die from drinking polluted water each year in developing countries.⁴ Figure 1.1 shows a global map of population-based estimates of the number of deaths due to water pollution in different countries.⁵ The highest number of deaths occurs in sub-Saharan Africa and some southeast Asian countries. Water pollution caused by anthropogenic activities not only disturbs ecosystems but also poses a huge threat to the integrity of the systems and the health of humankind.^{6,7}

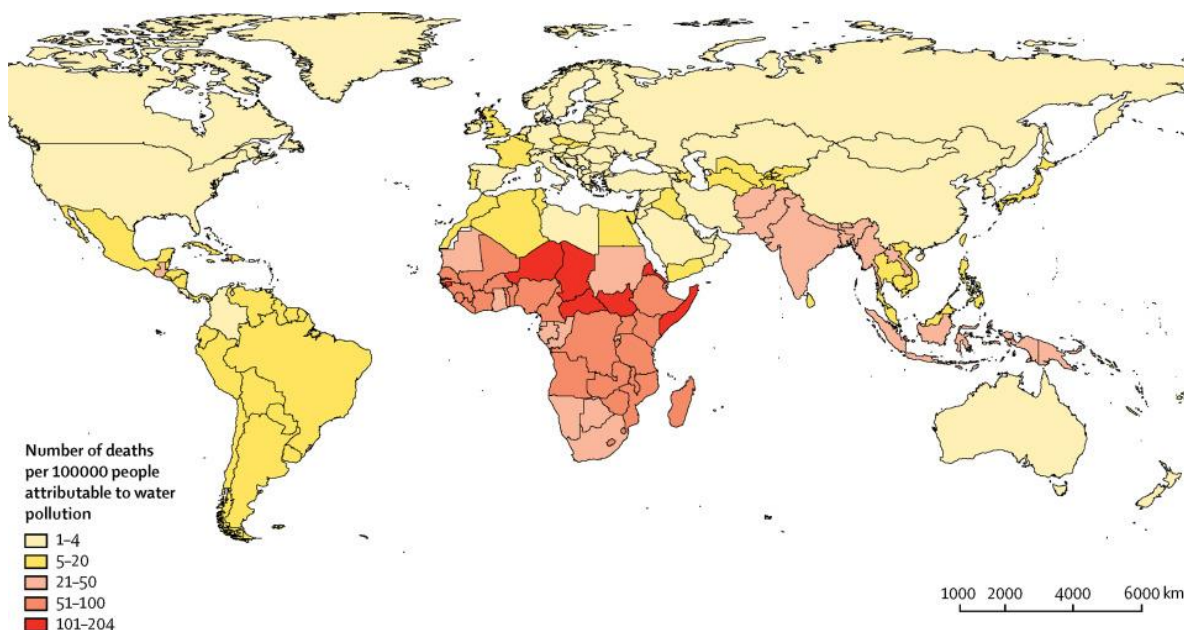


Figure 1.1. Number of deaths per 100 000 people due to water pollution in 2015.⁵

Figure 1.2. shows a schematic of the main sources of water pollution. Also, Table 1.1. includes information about the different pollutants produced in those sources. Industrial waste pollution can occur whenever toxic byproducts of the production chains are not safely processed and disposed of in the environment. This happens in different industrial sectors including electronics,⁸ food and beverage processing,⁹ petrochemicals¹⁰ and rubber production processes.¹¹ As a result, heavy metals, plastics, organohalides and other hazardous materials are released into the environment, disrupting habitats, causing harm to human beings and overburdening our waste management infrastructures.^{12–14} Agriculture pollutants mainly come from the excessive use of pesticides, herbicides and fertilizers.¹⁵ Pesticides and herbicides enter and bioaccumulate in the food chain, causing deleterious effects on aquatic organisms and further on humans. Excessed quantities of fertilizers and organic matter in waters produce eutrophication processes. Contamination events in drinking water produced by microorganisms such as bacteria and protozoa (cholera) could occur by uncontrolled livestock waste disposal.¹⁶ Domestic pollutants, including food waste and detergents, also contribute to an increase in organic matter and reduce oxygen supply to waterborne organisms, eventually giving rise to eutrophication.¹⁶

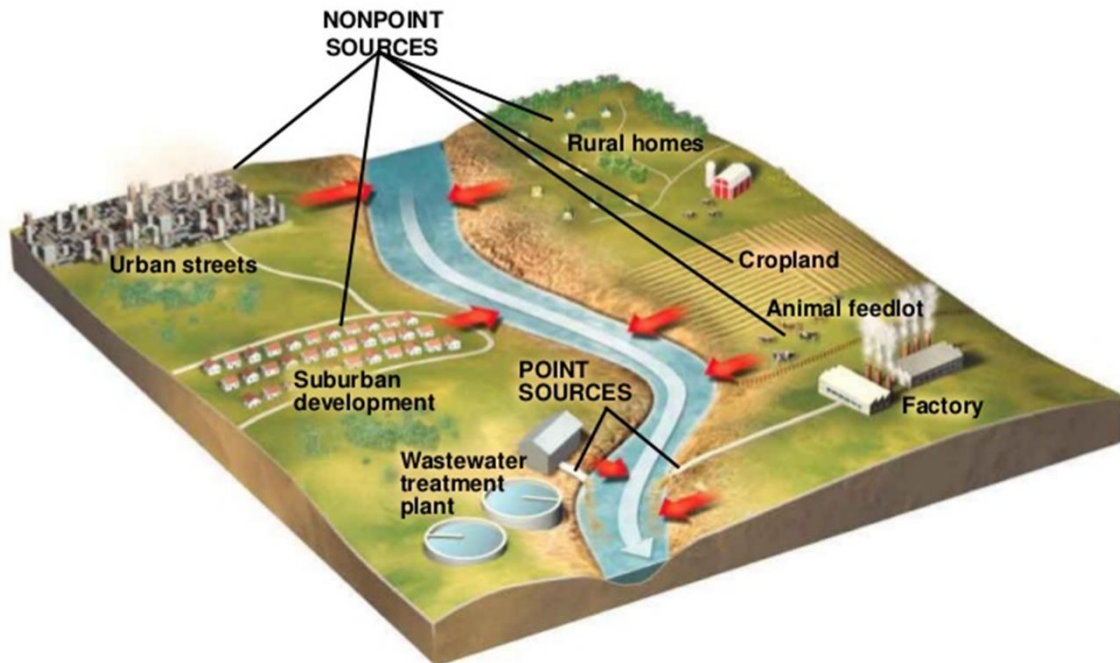


Figure 1.2. Sources of water pollution.¹⁷

Table 1.1 Sources of water contamination and the possible effects.

Sources	Components/pollutants	Possible effects
Industry	Heavy metals	Highly toxic accumulation through the food chain in the organism. ¹⁸
	Plastics	The plastics accumulated in the water bodies affect the living creatures and cause indirect harm to the seafood and further on human health. ^{14,19}
	Organohalides	Cause reproductive and neurotoxic health effects in humans and immunotoxic and carcinogenic effects in wildlife and humans. ²⁰
Agriculture	Excessive fertilizer	Results into eutrophication of water bodies. ²¹
	Pesticides, herbicides	Affect humans in many ways, such as disruption in the function of sex hormones and reproduction performance. ²²
Livestock	Microorganisms such as bacteria and protozoa	Perhaps causing waterborne diseases, namely cholera. ¹⁶
Domestic sewage	Food waste and detergents	Reducing oxygen supply to waterborne organisms and giving rise to eutrophication. ¹⁶

From what has been mentioned above, the number of biological and chemical species that can be found in waters increases steadily, and the list of those considered harmful is also continuously growing. The European Union (EU) and other governmental agencies have issued reports and directives defining lists of substances that should be prioritized for testing in water and setting limits on the maximum allowable concentrations that drinking water must have.²³ For example, the last EU directive on water policy (2013/39/EU) lists priority substances that should be monitored because they pose a serious threat to human health and the aquatic environment.²⁴ The list includes 45 pollutants grouped into five major categories: hydrocarbons, halogenated hydrocarbons, alkyl phenols, pesticides, and heavy metals.²³

Some of the pollutants in the list are biodegradable organic matter. The decomposition of pollutants will consume the oxygen dissolved in the water body that may eventually generate an anoxic state in the water ecosystem, resulting in the death of many aquatic organisms. In addition, the list also contains certain synthetic organic pollutants that are impossible to degrade by biological activities, including halogenated hydrocarbons, alkyl phenols and pesticides. They can persist in the water environment for a long time, being potentially mutagenic, carcinogenic or producing microbial resistances.^{25–27} Furthermore, many heavy metals are considered harmful pollutants. Heavy metals include both metals and metalloids with a high atomic weight and a density at least five times greater than water.²⁸ Lead (Pb), cadmium (Cd), mercury (Hg), arsenic (As), nickel (Ni), and chromium (Cr) are regarded as the major heavy metal pollutants for the aquatic environment.^{12,18,29} Overexposure to these metals produces harmful effects on human health. Heavy metal ions are highly soluble in water and show a strong affinity for the nucleophilic sites of certain biomacromolecules such as proteins and oligonucleotides.³⁰ Thus, different body organs can be affected by acute or chronic toxic effects due to heavy metal ion intake, which produces nervous system disorders, immune system dysfunction, kidney dysfunction, congenital disabilities, and skin lesions. Cumulative and synergistic adverse effects can also occur if exposed to two or more heavy metals simultaneously.^{31–33}

With the continuous growth of the consumer society, emerging water pollutants have steadily appeared, such as artificial sweeteners, disinfection byproducts (DBP), microplastics, nanomaterials, etc.^{16,34–37} Among them, artificial sweeteners, including sucralose, acesulfame, and cyclamate, are widely used as low-calorie sugar substitutes in

various food and beverages.^{35,38} Sweeteners are difficult to metabolize by the human body so they are excreted and can accumulate in surface waters.^{39,40} Unlike other environmental pollutants, DBPs are generated in situ during water potabilization or swimming pool treatments or by reactions of disinfectants (chlorine, chloramines, ozone, chlorine dioxide, UV)³⁴, but its presence could have unexpected synergistic consequences.¹⁶ One representative example of this family of chemicals is trichloroacetic acid (TCA). TCA is a byproduct of water chlorination that is considered of high environmental concern due to its widespread use in agriculture.⁴¹ TCA can be produced by photooxidation of chlorinated solvents (especially for trichloroethane and tetrachloroethene) present in the atmosphere and also in water disinfection processes carried out in industrial laundry and swimming pools.⁴² Also, TCA has been applied as a preemergence herbicide, and a peeling agent for sun-damaged skin, wrinkles and tattoos.⁴² Because of its potential mutagenic and carcinogenic effects,⁴³ WHO has set a maximum allowable concentration of 0.6 μM of TCA in drinking water.⁴⁴

We are certain that water pollution is one of the main issues of the global water crisis, together with the overuse of water resources and more and more frequent water drought episodes. Quality-controlled water monitoring is necessary to optimize water consumption and make the most of our water resources and reutilization processes. Thus, there is an urgent need to develop reliable and robust analytical platforms to monitor the chemical composition of water to preserve the required quality of this precious asset and prevent the spread of diseases while maintaining healthy ecosystems.

1.2 Standard analytical approaches for water pollutant detection

Considering the variety of water pollutants mentioned in the previous section, developing analytical approaches for robust water monitoring appears to be an arduous task. Priority lists of contaminants set up by the different authorities define the substances that should be strictly controlled²⁴, together with other parameters that contribute to the physico-chemical properties of water, such as pH and conductivity. For these, standard methods have already been identified that are mostly based on well-established classical analytical techniques carried out using bench-top equipment in laboratories designed for that purpose (Table 1.2).⁴⁵ This makes the analyses long and cumbersome because one must deal with the sample collection, stabilization, transport, and storage. As a result, current analyses are not

carried out with the frequency required to monitor a water body or they have not been yet established.

In this Thesis, we have put the focus on the following target analytes: chemical oxygen demand, organohalide pollutants, artificial sweeteners and heavy metals.

Chemical oxygen demand (COD) is one of the established parameters to estimate water contamination by organic matter.⁴⁶ The COD value of water samples reflects the amount of oxygen that should be consumed for decomposing (oxidizing) dissolved and suspended organic compounds.⁴⁷ Indeed, it has been defined as the mass concentration of oxygen consumed for fully oxidizing the organic matter of a liquid sample. The potassium dichromate titration method is the standard analytical technique to measure COD (Figure 1.3). With this method, one defines the COD as the concentration of O_2 equivalent to the concentration of dichromate anion ($Cr_2O_7^-$) required to fully oxidize the organic matter of a water sample, taking into account that 1 mol of $Cr_2O_7^-$ oxidizes the amount of organic matter equivalent to 1.5 mol of O_2 .^{46,48}

Table 1.2. Standard methods to monitor certain pollutants and parameters of water.⁴⁵

	Parameter	Equipment
1	Chemical oxygen demand	Titration
2	Organic compounds in drinking water	Liquids-solid extraction and capillary column gas chromatography/mass spectrometry
3	Metals and trace elements in water and wastes	Inductively coupled plasma-atomic emission spectrometry
4	Trace elements in water and wastes	Inductively coupled plasma-mass spectrometry
5	Organochlorine pesticides	Gas chromatography-halogen-sensitive detector
6	Conductance	Conductivity meter
7	pH	pH meter

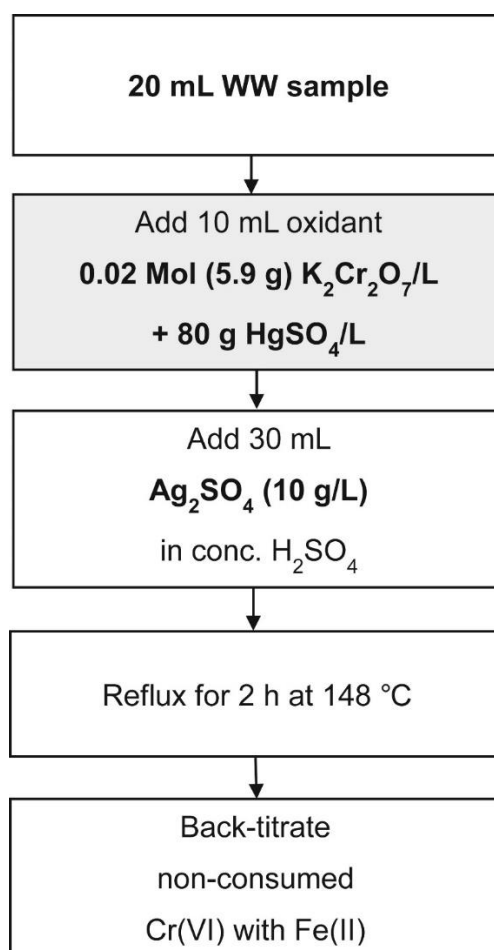


Figure 1.3. Flow chart of standard COD method according to DIN 38409-H41 (1980).⁴⁹ WW means wastewater.

COD has been widely used for evaluating water quality, especially for assessing the treatment efficiency of urban and industrial wastewaters. In the EU, the discharge of treated water effluents from wastewater treatment plants (WWTPs) must have organic matter concentrations below the legal COD limit of 125 mg L⁻¹ O₂, or, alternatively, display a reduction relative to the values of the water influents of at least 75%.⁵⁰ The titration method for COD determination has been in use for about 150 years and it has been widely adopted in many countries for its accuracy, reliability, and reproducibility.⁴⁶ However, despite not requiring any bulky and costly instrumentation, it presents several important limitations related to its low sensitivity, and, above all, the use of large amounts of chemicals that are highly toxic (e.g. HgSO₄), expensive (e.g. Ag₂SO₄), and hazardous (concentrated H₂SO₄).⁴⁷ Moreover, it is a technique implemented in specialized laboratories that can hardly be adapted to high throughput screening schemes because it is a long process that requires

several hours to be completed as the sample has to be collected, stabilized and transported before analysis. Moreover, it involves a long reflux processing step (2-4 h).⁵¹

With the continuous development of technology, instrumental analysis has dominated modern analytical chemistry and users are continuously pushing the instrument performances, trying to improve or discover new methodologies/strategies or seeking new applications.³⁵ Spectroscopy, mass spectrometry, separation (chromatography. Figure 1.4), thermal analysis and microscopy are the most widely used instrumental methods.⁵² Most of them have been implemented for the detection of water pollutants and accepted as standard methods in different framework directives.^{44,53–55}



Figure1.4. A gas chromatograph with a headspace sampler.⁵⁶

Instrumental analysis equipment shows the versatility required to be adapted to the analysis of various water pollutants including those selected in this Thesis, that is **organohalide pollutants, artificial sweeteners and heavy metals**. Instrumental analytical methods show the merits of accuracy and sensitivity that enable the detection of very small quantities of substances and provide reliable results.³⁵ However, these make use of highly costly and bulky bench-top equipment, tedious sample pretreatment processes in most cases, and a skilled professional's operation, making them difficult to deploy for in-field frequent analyses.³⁴

During the 21st century, we are more and more aware of climatic change and the emergency calls carried out to try to preserve our ecosystems. The identification of more and more

hazardous chemicals in waters poses a huge challenge to the different countries and organizations in the preservation of the quality of water. Compact, fast, easy to use, economic, portable, and potentially deployable analysis tools will certainly aid in the rapid detection of such pollutants to effectively tackle their harmful effects. Indeed, the different directives clearly state this urgent necessity and lately, the research community is making huge efforts to assess a vast array of analysis techniques for on-site environmental monitoring.^{57,58} Several representative examples illustrating the scope, versatility and potential application in this scenario are described in the following section.

1.3 Alternative analytical platforms for water pollutant detection

The current demand for water pollutant monitoring tools includes analytical tools showing high sensitivity, and low cost, that can be implemented to monitor multiple analytes, on-site and produce data for timely warning or identification of any potential hazard.⁵⁹ Thus, a variety of emerging alternative approaches are being developed, including electrochemical devices together with colorimetric and fluorescence-based detection platforms.⁶⁰

Electrochemical devices include cost-effective, easy-to-use, low-power solutions for carrying out the rapid, sensitive, selective analysis of a wide range of analytes.^{52,58,61,62} They can be seen as one of the most blooming analytical techniques to effectively monitor water pollutants. Electroanalytical methods take advantage of the redox properties of many different chemical species, linking current, potential or charge to their concentration.⁶³ Most methods are based on the analysis of phenomena taking place at the interface generated when an electrode is immersed in a solution.^{64,65} In this context, there are mainly two types of electrochemical techniques, that is (Chrono)amperometry (Voltammetry) and Potentiometry (Figure 1.5):

- (a) Amperometric or voltammetric techniques are based on the measurement of the change in the oxidation state of electroactive species due to the application of a direct-current potential or potential scan. Such change produces a Faradaic current, which is proportional to the analyte concentration.⁵²
- (b) The potentiometric method involves estimating the potential (E) of an electrochemical cell at zero current. Here, the potential is proportional to the logarithm of the analyte concentration.⁶⁶

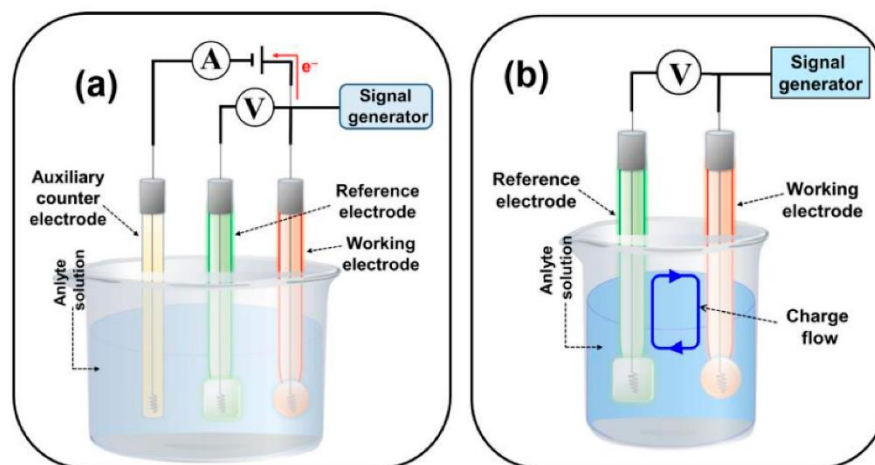


Figure 1.5. Schematic diagram of an electrochemical cell setup for (a) chronoamperometric/voltammetric and (b) potentiometric applications.⁶⁷

The three-electrode electrochemical cell arrangement shown in Figure 1.5 (a), comprises a working electrode (WE), a reference electrode used to measure the potential at the working electrode/solution interface, and a counter electrode to inject current in the electrical circuit to keep constant the potential at the working electrode. The electrochemical cell is connected to an electrochemical working station and potentiostatic or galvanostatic measurements can be performed to measure the concentration of target analytes.

There is an electron transfer between the working electrode and the solution redox species during the electrochemical reaction process. When a potential scan is applied to the cell and the electron transfer kinetics are faster than the mass transport from the bulk of the solution to the electrode solution interface, a reversible electrochemical response is produced. By contrast, if electron transfer is slow and other side processes such as adsorption of electroactive species govern the electrochemical process, irreversible electrochemical responses are recorded. Intermediate rates of electron transfer define a quasi-reversible electrochemical regime that in practice mostly governs the electrochemical detection of many electroactive species.⁶⁸

Electroanalytical approaches provide a high sensitivity toward the detection of many electroactive species. The Randles–Ševčík equation described the Faradaic current measured for a reversible electrochemical process, controlled by diffusion of the redox species:^{52,69}

$$I_{p,f}^{rev} = \pm 0.446nFA_{real}C\sqrt{\frac{nFDv}{RT}}.$$

This equation directly correlates the concentration of the electroactive analyte (C) to the recorded current (I), with (n) being the number of transferred electrons during the electrochemical reaction, (F) the Faraday constant, (A_{real}) the electroactive area of the electrode, (v) the potential scan rate, (D) the diffusion coefficient of the chemical species under study, (R) the universal gas constant and (T) the temperature.

Under standard working conditions ($T = 273.15$ K and $P = 100$ kPa), this equation can be simplified:

$$I_{p,f}^{rev} = \pm 2.69 * 10^5 n^{3/2} A_{real} C \sqrt{Dv}.^{52,65}$$

In the particular case where the electroactive species undergoing a redox process have been identified, the electrons being transferred, the scan rate and the diffusion coefficient are known, and the electrode active area previously measured, the recorded faradaic current is directly proportional to the analyte concentration in solution.⁵²

1.4 Metal nanoparticle-modified porous carbon electrode materials

The latest developments in manufacturing and computing capabilities have allowed the production of miniaturized electrochemical devices (Figure 1.6), making it possible to develop compact analytical tools to analyze water pollutants.^{52,70,71} This is highly beneficial for carrying out analysis at the location of interest, especially when samples should be rapidly measured to detect contamination outbreaks due to unexpected phenomena. Such processes require immediate analysis to improve the spatial-temporal resolution of monitoring. For this, electrochemical sensor platforms are becoming promising analytical tools for decentralized (in-field) analysis.

Many different conductive materials have been applied to the development of electrochemical devices. More and more functional materials with superior electrochemical and electrocatalytic properties are being designed and synthesized to provide electrochemical devices with particular and exceptional features for specific applications. This Thesis focuses on nanocomposite materials showing a particular configuration.



Figure 1.6. Portable electrochemical readers that can be employed in electrochemical biosensing. A) Commercially available pocket-sized potentiostats: i) PocketStat (from IVIUM Technologies®); ii) DropStat (from DropSens®), and iii) EmStat (from PalmSens®). B) Smartphone-based potentiostats. C) Conventional glucometer adapted for other electrochemical biosensing applications.⁷²

As outlined in the previous section, most electrochemical techniques are based on the reactions that occur at the working electrode solution interface. Therefore, the electrode physicochemical properties, mainly its surface chemistry and conductivity features are pivotal for achieving adequate electrochemical reaction kinetics and excellent analytical performance in terms of sensitivity, selectivity, the limit of detection, accuracy and reproducibility.^{16,73,74} Among the different materials that have been assessed for electroanalytical purposes, carbon stands out due to its low cost, relative inertness, wide potential window, the versatility of carbon allotropes and rich surface chemistry features.⁷⁵ The abundance of carbon compared to other popular electrode materials such as gold and platinum is another important added value that makes it arguably the most fashionable electrode substrate for analytical applications.

Different synthesis methods have been developed to prepare carbon materials.⁷⁶ The application of sol-gel / pyrolysis synthesis strategies using resorcinol-formaldehyde precursors has gradually been welcomed by researchers.⁷⁷ Porous carbon matrices using this well-established synthetic approach have been thoroughly developed by our group to

pioneer the fabrication of miniaturized porous carbon-based electrochemical devices using screen-printing or lithographic technologies.^{78,79}

Figure 1.7 illustrates the sol-gel process. Resorcinol and formaldehyde precursors are first mixed in a solvent. Over time, the precursors hydrolyze, polymerize, and produce colloidal particles that, under certain conditions, clump and eventually cross-link, forming a non-flowable network. The sol-gel approach shows very interesting features.⁸⁰ First, these composite materials are generated from a liquid that can be processed as films over different substrates or produced in bulk shaped by the container. Second, the sol-gel chemistry enables the mixing of different precursors at the molecular level while incorporating other additives into the gel matrix to provide a final material with some added functionalities. Third, the porosity of the produced material can be tailored, by controlling the initial sol-gel synthesis conditions and applying post-treatment methods to the wet gel.⁷⁷ All this makes the sol-gel synthesis approaches to produce carbon materials a highly interesting option for manufacturing carbon electrodes and applying them for chemical sensor purposes.

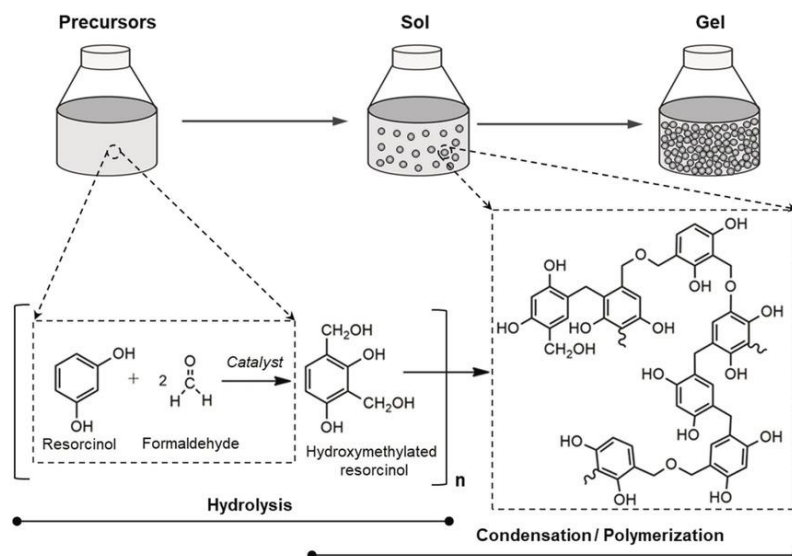


Figure 1.7. Resorcinol-formaldehyde sol-gel process.⁷⁷

On the other hand, with the increasing awareness of environmental protection and the clear vision of achieving more sustainable chemical synthesis strategies, there has been a strong trend toward developing the so-called "Green Science" strategy aiming at converting waste into valuable carbon materials.^{81,82} An interesting example of sustainability is the recent trend of converting biowaste or biomass into activated carbon. Biowaste and biomass comprise

crops, animal or plant-based materials, food residues, garbage, alcohol fuels, and landfill gas, considered the more eco-friendly carbon precursors by researchers worldwide.⁸³ The global annual biomass production contains around 1.05×10^{17} g of carbon, which has drawn the research community's attention over recent years.⁸⁴ In addition, for many years, agricultural waste and forest byproducts were directly discarded into the environment or incinerated, causing serious environmental problems.⁸⁵ This issue has been forecasted worldwide and the smart move to mitigate it is to recycle the biomass and biowaste. Therefore, utilizing biomass residues to manufacture carbon-based materials for electrochemical applications is an environmentally friendly and promising approach.

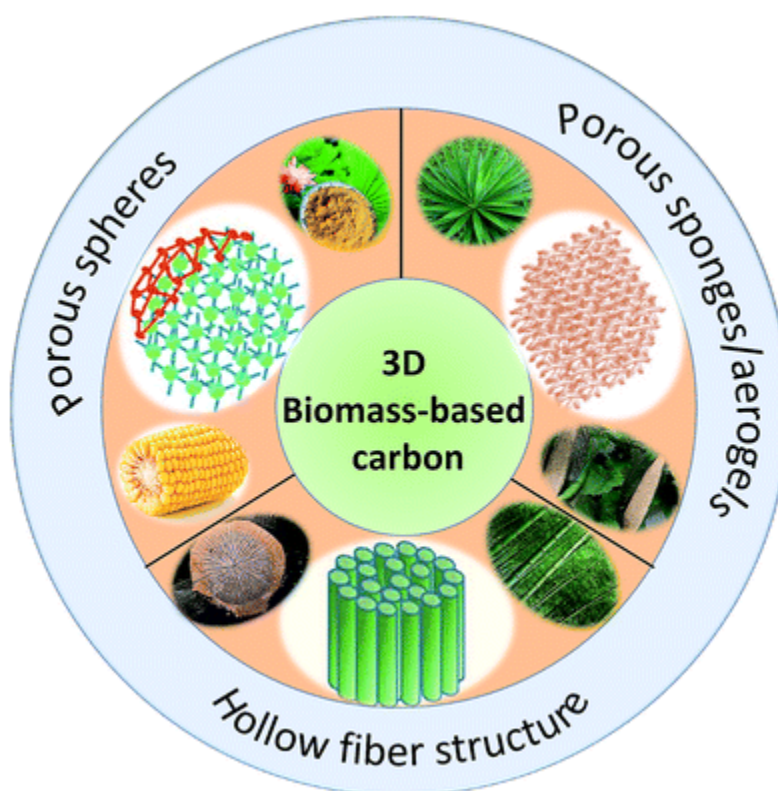


Figure 1.8. 3D carbon-based nanostructures from different forms of carbon and their combination with pseudo-active materials.⁸⁶

Biomass-derived carbon materials are highly favored because of their unique structure, high sustainability, widespread availability, renewable energy and economic compatibility (Figure 1.8).^{86,87} Biomass, benefiting from complex designs of nature, exhibits unique properties, including regular surface morphology, high porosity, excellent electrical conductivity, surface chemical functionalities and chemical stability.⁸⁴ The resulting biomass-derived carbon

materials can be applied for a wide variety of potential applications, such as carbon dioxide (CO₂) capture,⁸⁸ hydrogen storage,⁸⁹ water treatment,⁹⁰ catalysis,⁹¹ adsorption separation (bioremediation),⁹² and electrochemical sensing.⁸¹

In recent years, the electrochemical performance and electrocatalytic activity of existing carbon materials can be significantly improved by the incorporation of metal nanoparticles; this has opened up the door for applications in electrocatalysis.^{84,93} The catalytic properties of the nanoparticles can reduce the overpotential required for a reaction to become kinetically viable.⁷⁷ Metal nanoparticles of different compositions and structures can catalyze different reactions. These, combined with carbon-based materials, can be applied to develop electrocatalytic sensors for environmental water monitoring. Some good examples are those based on Cu NPs applied to analyze COD in water,^{51,94,95} Ag NPs used to detect halogenated compounds,^{96–98} or Bi NPs utilized to detect heavy metals.^{73,99,100}

The electrodes' structural properties also take advantage of the synergistic combination of nanoparticles and biowaste-derived carbon materials. For instance, a large surface-area-to-volume ratio improves the signal-to-noise ratio and the resulting device sensitivity.^{101,102} It also positively affects the device fabrication costs, making it an excellent option for the mass production of electrochemical sensor devices.

1.5 Developing thick- and thin-film carbon-derived electrodes

A thick film is a material layer that ranges in thickness from 1 µm to 100 µm, while a thin film can be a thousand times thinner, as shown in Figure 1.9. Both of them can be used to construct functional devices. The characteristics of a film and its application area are primarily determined by the used material composites and the fabrication technology.¹⁰³

The main manufacturing technique for the thick film is screen printing (stenciling) which, in addition to being used in manufacturing electronic devices, can also be used for various graphic reproduction targets. **Screen-printing technology** became one of the key manufacturing/miniaturization techniques of electronic devices during the 1950s.¹⁰⁴ It has been used over the past decades to produce compact electrochemical cells on planar substrates, mainly ceramic and polymeric, aiming at developing low-cost electrochemical

devices that could be single-use and deployed for in-field / point-of-care applications.¹⁰⁵ One excellent example is the glucose sensor manufactured at a very large scale and used worldwide by diabetes patients.^{106,107} Different carbon- and metal-based inks have been produced to define the thick-film (few tens of microns thick) electrodes.

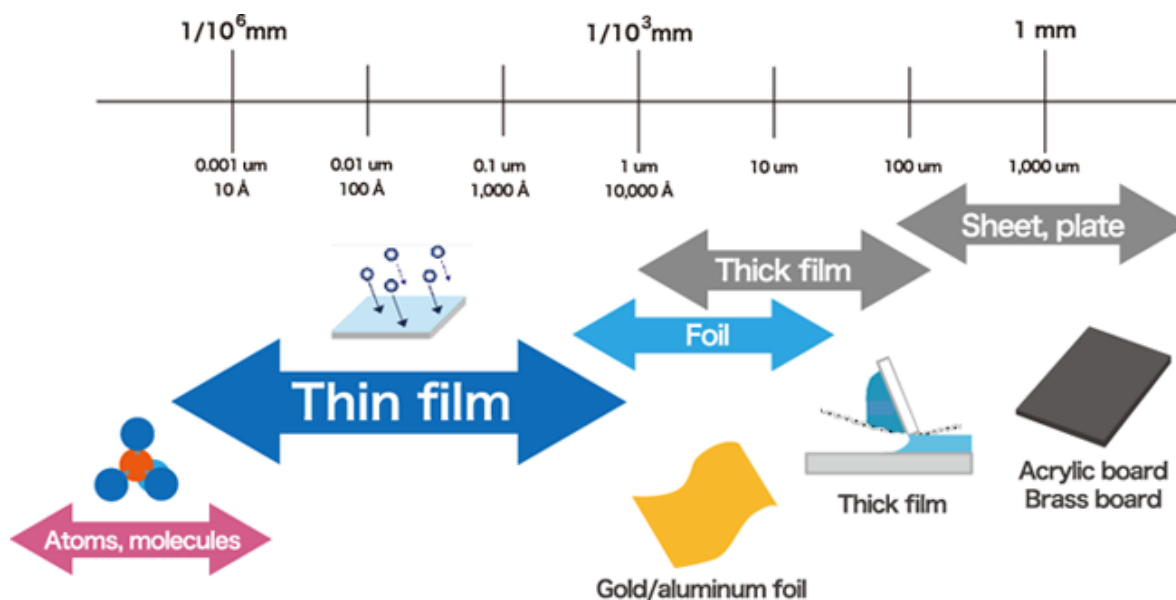


Figure 1.9. Classification of films.¹⁰³

Figure 1.10 shows the schematic representation of the fabrication process of screen-printed electrodes (SPEs).¹⁰⁸ First, the substrate and stencil are aligned on the screen printer (Figure 1.10B). Then, the printing ink is injected into the stencil close to the printed pattern (Figure 1.10C). The stencil design is then printed on the underlying substrate by forcing the ink to go through the stencil with a squeegee (Figure 1.10D, 1.10E and 1.10F). Similarly, other components can be printed sequentially on the same substrate.¹⁰⁵

Since SPEs are commonly single-used^{109,110}, drawbacks related to electrode fouling due to adsorption of the chemical species present in the measuring solution or produced during the electrochemical process, tedious pretreatment steps and repeated calibration processes required using conventional electrodes such as glassy carbon and solid metal electrodes, are circumvented.⁵² The screen-printing technique provides versatility in electrode design, material compatibility and modifications, and offers a cost-effective large-scale production of highly reproducible sensors.^{111, 112} As a result, SPE miniaturized electrochemical sensors have stood out as powerful alternative platforms in modern analytical chemistry, applied in

a plethora of fields such as forensics, environment, food, or cancer biomarker analysis.⁵² The SPEs can help bridge the transition gap from traditional lab-based techniques to miniaturized, quicker and cheaper tests for health and environmental monitoring.

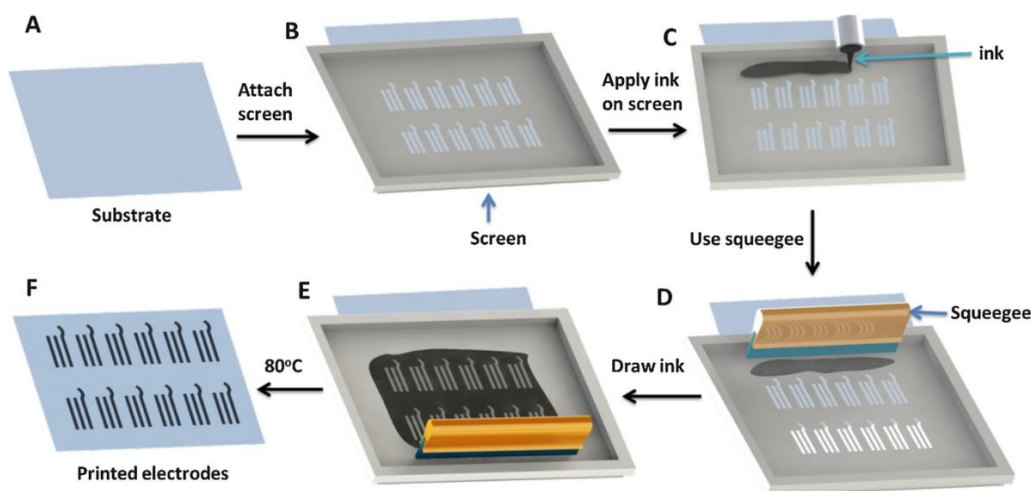


Figure 1.10. Schematic representation of the fabrication process of screen-printed electrodes.¹⁰⁸

However, every coin has two sides. The ink of the SPE always contains binders and other additives, which will hinder its electron transfer ability and hence its redox performance.¹⁰⁵ Furthermore, the SPEs are developed to meet the demand for single-use miniaturized electrochemical probes to enable on-site detection, but will not be suitable for automatic in-field monitoring for repeated measurements carried out over extended time periods.¹⁰⁵

Thin-film carbon electrodes are produced from pure carbon compositions and this is reflected in their improved electrochemical performance compared with SPE mentioned above.¹¹³ Up to now, various techniques have been used to develop thin carbon films on technically relevant substrates, which chiefly involve gas phase deposition or liquid phase deposition, followed by pyrolysis steps.¹¹⁴ Gas-phase deposition techniques comprise physical and chemical vapor deposition. Still, these film production methods require complex equipment and critical deposition conditions, such as vacuum or an inert atmosphere, gas flow adjustments, and relatively high pyrolysis temperatures, which are demanding and expensive.^{115,116} Liquid-phase deposition consists of coating a substrate with a polymer precursor that is further pyrolyzed to produce a carbon film. This technique preserves the merits of low cost, simplicity, and versatility of available polymer precursors and superior

electrochemical performance.^{117,118} However, most of the reported thin-film electrodes prepared by the liquid phase deposition face a challenge which is the poor adhesion between the produced carbon film and the substrate. This issue is manifested by film delamination when soaked in solvents required for film processing and electrochemical device operation.^{117,119} This drawback can shorten electrode self-life and limit its potential applications.¹¹⁷

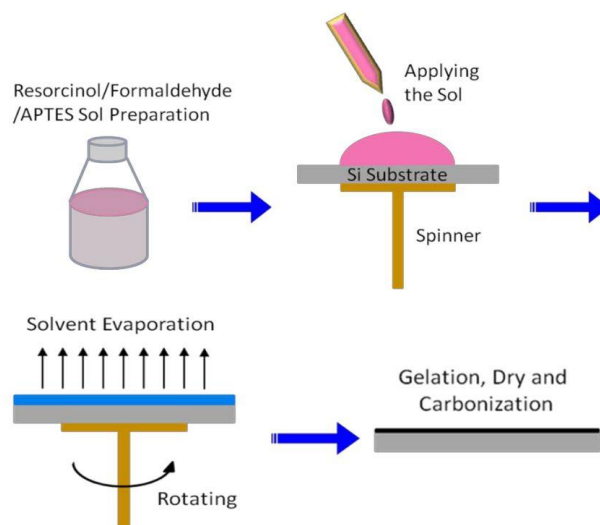


Figure 1.11. Preparation of thin film with the one-pot sol-gel process.¹¹³

In this context, our group has worked on the facile preparation of robust silica-carbon thin films on oxidized silicon substrates, solving the challenge mentioned above.¹¹³ The preparation process consists in obtaining hybrid organic-inorganic gel films by a sol-gel approach followed by film pyrolysis in a reducing atmosphere. This process involves three main steps: (1) sol preparation, (2) spin-coating and formation of an organic thin film and, (3) pyrolysis in a tubular furnace in a reducing atmosphere (Figure 1.11). The adherence between the carbon film and the substrate was improved by incorporating a silica precursor, aminopropyltriethoxysilane (APTES), in a resorcinol/formaldehyde sol-gel formulation used to prepare the films. The addition of APTES results in the formation of siloxane chemical bonds (-Si-O-Si-) and the formation of a silica network firmly anchored on the oxidized silicon substrate and intertwined with the organic resorcinol/formaldehyde gel. After pyrolysis, this silica network provides good adhesion of the resulting carbon film to the substrate.

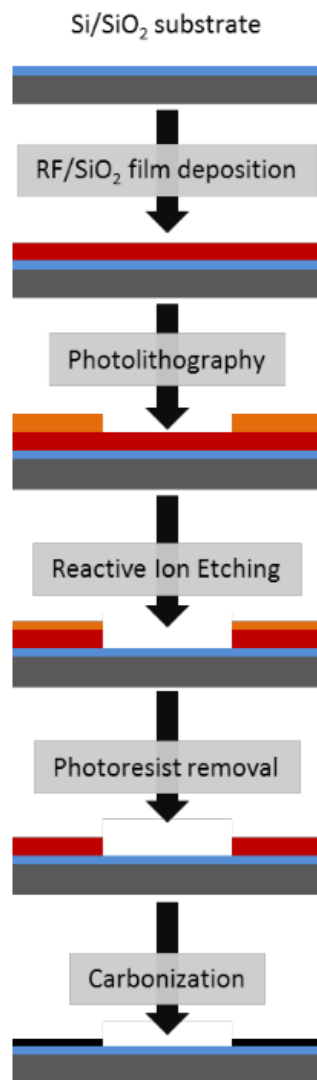


Figure 1.12. Schematic representation of the fabrication of C/SiO₂ thin films by microfabrication route.¹¹⁴

Furthermore, our group also investigated three microfabrication routes to prepare miniaturized thin-film electrodes from these carbon-silica films.¹¹⁴ Among them, a schematic diagram of the most effective microfabrication approach is shown in Figure 1.12. In short, an organic film was first spin-coated on the Si/SiO₂ substrate. Then the photolithography and etching processes were performed to get the organic/silica strips. Next, the miniaturized thin-film electrodes were obtained after the pyrolysis process.

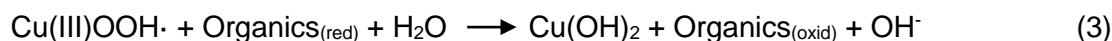
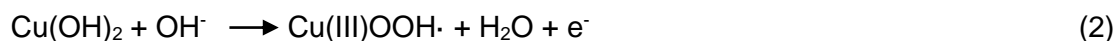
The electrochemical characterization of the miniaturized thin-film carbon electrodes revealed they are highly promising for engineering an electroanalytical platform. In addition,

the miniaturized thin-film carbon electrodes could be functionalized with gold and bismuth nanoparticles to be applied to the electrochemical analysis of heavy metals.¹¹⁴ However, there is still room for improvement. The main challenge is achieving conductivity values high enough to allow an excellent electrochemical performance of the resulting devices and the control over the functional chemical groups produced on their surface during the fabrication process. Furthermore, the wafer-scale chip fabrication requires mass-producing them at a low cost and with high reproducibility yields, something which had not been fully demonstrated in our previous works.

1.6 Electrochemical sensor applications for COD, organohalides and heavy metals in water

Sensors incorporating copper-based nanomaterials are highly suitable for COD monitoring. This is because the intermediate products generated during the electrocatalytic oxidation of copper (CuO, Cu(OH)₂) provide reaction sites for hydroxyl radicals that enable the oxidation of organics at low potentials.^{120,121} When working with copper-based nanomaterials, the oxidation overpotential is further decreased and larger oxidation currents are observed as a result of their large surface area and higher electrocatalytic activity.^{122–125} The corresponding chemical reactions (Equation I) and the schematic of the mechanism of the electro-oxidation of organic matter at the copper nanoparticles-modified electrode (Figure 1.13) are shown below.

Equation I



Moreover, copper-based nanomaterials present low ecotoxicity and human toxicity (non-carcinogenic)¹²⁶. These nanomaterials have a low environmental footprint compared to other heavy metals and appear as a low-risk, environmentally friendly material option. Recent reports illustrate the promising combination of carbon materials and copper nanoparticles (Cu NPs) for achieving unique glucose and COD analysis performances.^{122,127,128} However, the production of the sensor platforms used in those works required several steps, including the modification of commercial graphite electrodes by drop-casting or by an

electrodeposition process^{122,127–129}, making them unattractive for industrial production. Finding new cost-effective approaches to prepare composites of carbon and copper-based nanoparticles would be highly attractive for developing electrochemical sensors of COD.

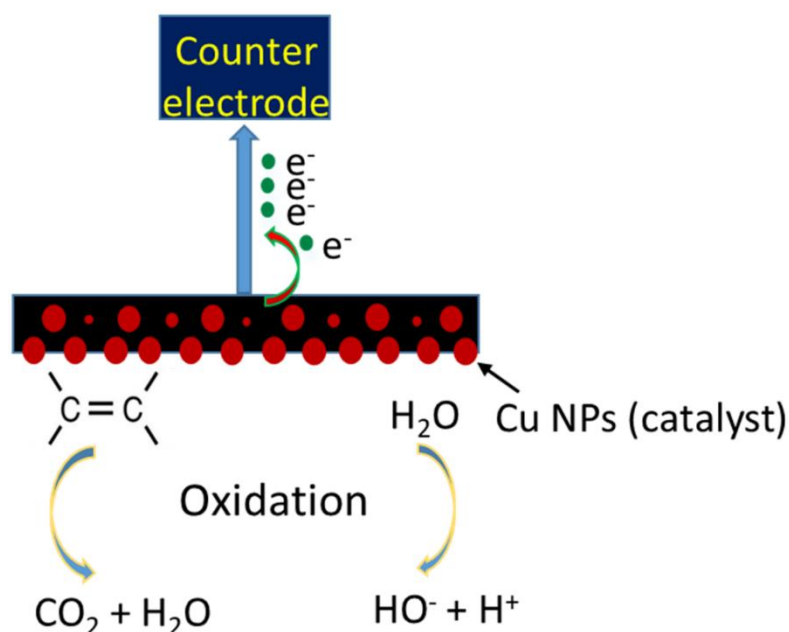


Figure 1.13. Schematic of the mechanism of the electro-oxidation of organic matter at the copper nanoparticles-modified electrode.

The catalytic properties of silver have long been known^{130,131}. Among them, Ag NPs have been shown to be electrocatalytically active towards the cleavage of halide bonds¹³². In this context, Ag NPs modified carbon materials combined with electrochemical analytical techniques have been used for the remediation / removal¹³³ and analysis^{96,134} of hazardous chlorinated compounds. Similarly, an electrochemical sensor device based on a composite of carbon modified with Ag NPs would be a good candidate for detecting halogenated compounds.

The most likely mechanism underpinning the electrochemical analysis of halogenated compounds with AgNP/C electrodes includes a dehalogenation process previous to the electrochemical detection.^{97,98,133} The mechanism of dehalogenation on silver has been widely investigated in previous papers.^{135–137} It proceeds via the adsorption of the halogenated compound “RCI” on the surface of the electrode, resulting in an “attenuated

radical” intermediate of the kind $R\cdots Cl\cdots Ag$ (Figure 1.14a).¹³⁵ The strong interaction of RCl with Ag NPs improves the kinetics of the dehalogenation reaction because the C-Cl bond is significantly weakened due to the new interactions, $Cl\cdots Ag$ and $R\cdots Ag$. In addition, the interaction of RCl with Ag NPs reduces the activation energy of the dissociative electron transfer (DET) process (Figure 1.14b), and facilitates the transfer of electrons (Figure 1.14a).^{133,137} The possible cleavage mechanism of the C-Cl bond can be visualized in Equation II below.¹³³

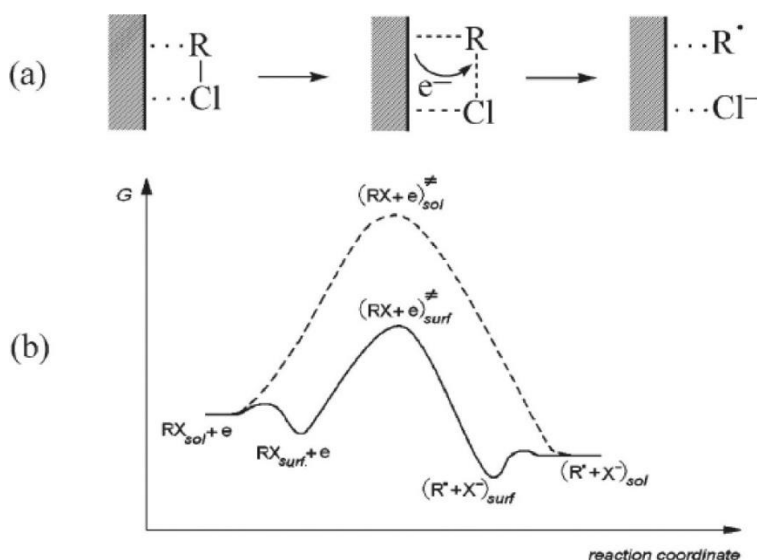


Figure 1.14. (a) Schematic diagram of the concerted dissociative DET at Ag; (b) reaction coordinate diagram: outer-sphere DET (dashed curve) and Ag catalyzed DET (solid curve).¹³³

Equation II



After the dehalogenation process, the free ion X^- is released and it can adsorb onto the surface of Ag NPs. Then the free ion X^- can react with the Ag NPs on the surface of the electrode to form a silver halide precipitate through the following reaction $Ag + X^- \rightarrow AgX + e^-$ ($X = Cl^-$, Br^- and I^-).^{138,139} Thus, in an electrochemical process, this reaction can generate an oxidation current that can be applied to analyze the concentration of halide anions and in turn halogenated compounds.

Bismuth-modified carbon electrodes have been of widespread use for detecting heavy metal ions.⁷³ Bismuth is a relatively environmentally benign element with low toxicity. The bismuth-modified carbon electrodes exhibit a low background current in the presence of dissolved oxygen, a large cathodic electrochemical window, wide linear dynamic range, well-defined stripping responses, excellent resolution of neighboring peaks, and high sensitivity.⁷⁵ Such excellent properties make bismuth-modified carbon electrodes highly attractive for on-site environmental analysis of heavy metal ions.⁷⁵ The Bi species is typically generated by electrodepositing or co-depositing Bi with the analyte ions onto a carbon support electrode.⁷³ The Bi modified electrodes are always combined with the Anodic Stripping Voltammetry (ASV) technique to analyze heavy metals.²⁸ ASV is an effective electrochemical analysis method involving a two-step process (Figure 1.15 and Equation III).²⁸ The first one is the electrodeposition of the heavy metal analyte, Equation III (1), through a cathodic reduction of a labile or free metal ion to its zero-valence metallic state on the Bi surface. The second process is the anodic oxidation or dissolution, called the stripping step, which will bring the analyte metal ions back into the solution (Figure 1.15 and Equation III (2)).²⁸ Experimentally, the analysis of oxidative stripping peaks in the recorded current-potential plots is applied to determine the concentration of metal ions in the solution. The amplified stripping signal resulting from bismuth-based electrodes reflects the ability of bismuth to form “fused” multicomponent alloys with targeted heavy metals.¹⁴⁰

Equation III

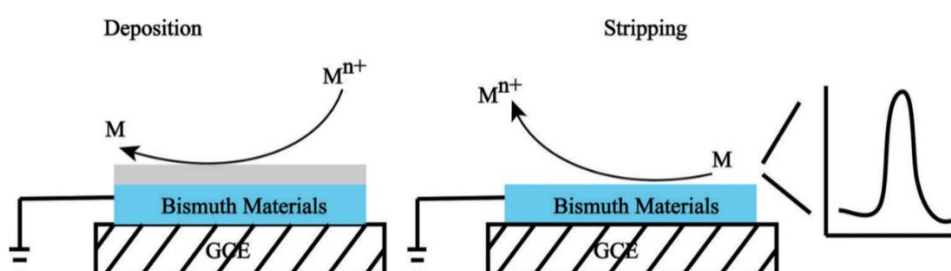
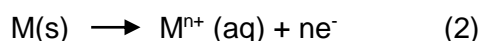
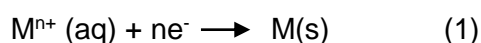


Figure 1.15. A schematic diagram of measurement of heavy metal ions using anodic stripping voltammetry.¹⁴⁰

References

1. Liyanage CP, Yamada K. Impact of population growth on the water quality of natural water bodies. *Sustainability*. 2017 Aug 9;9(8):1405.
2. World Water Assessment Programme (United Nations). *Water for People, Water for Life: A Joint Report by the Twenty-three UN Agencies Concerned with Freshwater*. UNESCO Pub.; 2003.
3. Naeem K, Syed TH, Abdus S, Nargis J, Kyong SK. Physicochemical investigation of the drinking water sources from Mardan, Khyber Pakhtunkhwa, Pakistan. *International journal of physical sciences*. 2013 Sep 9;8(33):1661-71.
4. Abbaspour S. Water quality in developing countries, south Asia, South Africa, water quality management and activities that cause water pollution. *IPCBE*. 2011;15(94):e102.
5. Landrigan PJ, Fuller R, Acosta NJ, Adeyi O, Arnold R, Baldé AB, Bertollini R, Bose-O'Reilly S, Boufford JI, Breysse PN, Chiles T. The Lancet Commission on pollution and health. *The lancet*. 2018 Feb 3;391(10119):462-512.
6. Rathi BS, Kumar PS, Vo DV. Critical review on hazardous pollutants in water environment: Occurrence, monitoring, fate, removal technologies and risk assessment. *Science of The Total Environment*. 2021 Nov 25;797:149134.
7. Arman NZ, Salmiati S, Aris A, Salim MR, Nazifa TH, Muhamad MS, Marpongahtun M. A review on emerging pollutants in the water environment: existences, health effects and treatment processes. *Water*. 2021 Nov 17;13(22):3258.
8. Belova L, Vialkova E, Glushchenko E, Burdeev V, Parfenov Y. Treatment of electroplating wastewaters. *InE3S Web of Conferences 2020 (Vol. 203, p. 03009)*. EDP Sciences.
9. Ahmad T, Aadil RM, Ahmed H, ur Rahman U, Soares BC, Souza SL, Pimentel TC, Scudino H, Guimarães JT, Esmerino EA, Freitas MQ. Treatment and utilization of dairy industrial waste: A review. *Trends in Food Science & Technology*. 2019 Jun 1;88:361-72.
10. Borup MB, Middlebrooks EJ. *Pollution control in the petrochemicals industry*. CRC

Press; 2018 Jan 18.

11. Arachchige U, Sithari GM, Tgahr T, Tharakie GM, Tharuka KV. Environmental pollution by tire manufacturing industry. *Int. J. Sci. Technol. Res.* 2018;8:80-1.
12. Muharrem IN, Ince OK. An overview of adsorption technique for heavy metal removal from water/wastewater: a critical review. *International Journal of Pure and Applied Sciences.* 2017;3(2):10-9.
13. Richardson SD, Plewa MJ. To regulate or not to regulate? What to do with more toxic disinfection by-products?. *Journal of Environmental Chemical Engineering.* 2020 Aug 1;8(4):103939.
14. Seltenrich N. New link in the food chain? Marine plastic pollution and seafood safety.
15. Boxall AB. New and emerging water pollutants arising from agriculture.
16. Ojha A. Materials in electrochemical detection of water pollutants. In *Sensors in Water Pollutants Monitoring: Role of Material 2020* (pp. 161-185). Springer, Singapore.
17. Arefin MA, Mallik A. Sources and causes of water pollution in Bangladesh: A technical overview. *Bibechana.* 2018;15:97-112.
18. Jain R, Thakur A, Kaur P, Kim KH, Devi P. Advances in imaging-assisted sensing techniques for heavy metals in water: Trends, challenges, and opportunities. *TrAC Trends in Analytical Chemistry.* 2020 Feb 1;123:115758.
19. Rochman CM. Microplastics research—from sink to source. *Science.* 2018 Apr 6;360(6384):28-9.
20. Kodavanti PR, Loganathan BG. Organohalogen pollutants and human health. *The international encyclopedia of public health.* Eds. SR Quah, WC Cockerham. 2017 Jan 1;5:359-66.
21. Rahman KA, Zhang D. Effects of fertilizer broadcasting on the excessive use of inorganic fertilizers and environmental sustainability. *Sustainability.* 2018 Mar 9;10(3):759.
22. Sankhla MS, Kumari M, Sharma K, Kushwah RS, Kumar R. Water contamination through pesticide & their toxic effect on human health. *International Journal for Research in Applied Science and Engineering Technology.* 2018 Feb 1;6(1):967-70.
23. Díaz-González M, Gutiérrez-Capitán M, Niu P, Baldi A, Jiménez-Jorquera C,

Fernández-Sánchez C. Electrochemical devices for the detection of priority pollutants listed in the EU water framework directive. *TrAC Trends in Analytical Chemistry*. 2016 Mar 1;77:186-202.

24. Kern K. New standards for the chemical quality of water in Europe under the new Directive 2013/39/EU. *Journal for European Environmental & Planning Law*. 2014 Jan 1;11(1):31-48.
25. Pereira LC, de Souza AO, Bernardes MF, Pazin M, Tasso MJ, Pereira PH, Dorta DJ. A perspective on the potential risks of emerging contaminants to human and environmental health. *Environmental Science and Pollution Research*. 2015 Sep;22(18):13800-23.
26. Richardson SD, Ternes TA. Water analysis: emerging contaminants and current issues. *Analytical chemistry*. 2011 Jun 15;83(12):4614-48.
27. Amy G, Bull R, Craun GF, Pegram RA, Siddiqui M, World Health Organization. Disinfectants and disinfectant by-products. World Health Organization; 2000.
28. Borrill AJ, Reily NE, Macpherson JV. Addressing the practicalities of anodic stripping voltammetry for heavy metal detection: a tutorial review. *Analyst*. 2019;144(23):6834-49.
29. Niu P, Fernández-Sánchez C, Gich M, Ayora C, Roig A. Electroanalytical assessment of heavy metals in waters with bismuth nanoparticle-porous carbon paste electrodes. *Electrochimica Acta*. 2015 May 20;165:155-61.
30. Vardhan KH, Kumar PS, Panda RC. A review on heavy metal pollution, toxicity and remedial measures: Current trends and future perspectives. *Journal of Molecular Liquids*. 2019 Sep 15;290:111197.
31. Gazwi HS, Yassien EE, Hassan HM. Mitigation of lead neurotoxicity by the ethanolic extract of *Laurus* leaf in rats. *Ecotoxicology and environmental safety*. 2020 Apr 1;192:110297.
32. Balali-Mood M, Naseri K, Tahergorabi Z, Khazdair MR, Sadeghi M. Toxic mechanisms of five heavy metals: mercury, lead, chromium, cadmium, and arsenic. *Frontiers in pharmacology*. 2021 Apr 13;12:643972.
33. Cobbina SJ, Chen Y, Zhou Z, Wu X, Zhao T, Zhang Z, Feng W, Wang W, Li Q, Wu X, Yang L. Toxicity assessment due to sub-chronic exposure to individual and

mixtures of four toxic heavy metals. *Journal of hazardous materials*. 2015 Aug 30;294:109-20.

34. Richardson SD, Ternes TA. Water analysis: emerging contaminants and current issues. *Analytical Chemistry*. 2021 Nov 28;94(1):382-416.
35. Richardson SD, Kimura SY. Water analysis: emerging contaminants and current issues. *Analytical Chemistry*. 2019 Dec 11;92(1):473-505.
36. Kumar M, Borah P, Devi P. Priority and emerging pollutants in water. In *Inorganic Pollutants in Water 2020 Jan 1* (pp. 33-49). Elsevier.
37. Ghangrekar MM, Chatterjee P. Water pollutants classification and its effects on environment. In *Carbon nanotubes for clean water 2018* (pp. 11-26). Springer, Cham.
38. Wang QP, Simpson SJ, Herzog H, Neely GG. Chronic sucralose or l-glucose ingestion does not suppress food intake. *Cell Metabolism*. 2017 Aug 1;26(2):279-80.
39. Oppenheimer J, Eaton A, Badruzzaman M, Haghani AW, Jacangelo JG. Occurrence and suitability of sucralose as an indicator compound of wastewater loading to surface waters in urbanized regions. *Water research*. 2011 Jul 1;45(13):4019-27.
40. Sharma VK, Oturan M, Kim H. Oxidation of artificial sweetener sucralose by advanced oxidation processes: a review. *Environmental Science and Pollution Research*. 2014 Jul;21(14):8525-33.
41. Liu B, Hu X, Deng Y, Yang S, Sun C. Selective determination of trichloroacetic acid using silver nanoparticle coated multi-walled carbon nanotubes. *Electrochemistry communications*. 2010 Oct 1;12(10):1395-7.
42. Kurd M, Salimi A, Hallaj R. Highly sensitive amperometric sensor for micromolar detection of trichloroacetic acid based on multiwalled carbon nanotubes and Fe (II)–phtalocyanine modified glassy carbon electrode. *Materials Science and Engineering: C*. 2013 Apr 1;33(3):1720-6.
43. Wright JM, Schwartz J, Dockery DW. The effect of disinfection by-products and mutagenic activity on birth weight and gestational duration. *Environmental health perspectives*. 2004 Jun;112(8):920-5.
44. World Health Organization. Guidelines for drinking-water quality: second addendum. Vol. 1, Recommendations. World Health Organization; 2008.

45. Approved CWA Chemical Test Methods | US EPA. <https://www.epa.gov/cwa-methods/approved-cwa-chemical-test-methods#number>.
46. Geerdink RB, van den Hurk RS, Epema OJ. Chemical oxygen demand: Historical perspectives and future challenges. *Analytica Chimica Acta*. 2017 Apr 8;961:1-1.
47. Huang X, Zhu Y, Yang W, Jiang A, Jin X, Zhang Y, Yan L, Zhang G, Liu Z. A self-supported CuO/Cu nanowire electrode as highly efficient sensor for COD measurement. *Molecules*. 2019 Aug 28;24(17):3132.
48. International Organization for Standardization. Water Quality: Determination of the Chemical Oxygen Demand. International Organization for Standardization; 1989.
49. Kolb M, Bahadir M, Teichgräber B. Determination of chemical oxygen demand (COD) using an alternative wet chemical method free of mercury and dichromate. *Water research*. 2017 Oct 1;122:645-54.
50. Directive EU. Council Directive of 21. May 1991 concerning urban waste water treatment (91/271/EEC). *J. Eur. Commun.* 1991;34:40.
51. Li J, Luo G, He L, Xu J, Lyu J. Analytical approaches for determining chemical oxygen demand in water bodies: a review. *Critical reviews in analytical chemistry*. 2018 Jan 2;48(1):47-65.
52. Ferrari AG, Rowley-Neale SJ, Banks CE. Screen-printed electrodes: Transitioning the laboratory in-to-the field. *Talanta Open*. 2021 Aug 1;3:100032.
53. Su J, Ji D, Lin M, Chen Y, Sun Y, Huo S, Zhu J, Xi B. Developing surface water quality standards in China. *Resources, Conservation and Recycling*. 2017 Feb 1;117:294-303.
54. Acrylamide OC. National Primary Drinking Water Regulations. *Kidney*. 2009;2(4-D):0-7.
55. Directive EU. Directive 2013/39/EU of the European Parliament and of the Council of 12 August 2013 amending Directives 2000/60/EC and 2008/105/EC as regards priority substances in the field of water policy. *Off J Eur Union L*. 2013 Aug;226:1-7.
56. Azma A, Zhang Y. Application and development of instrumental analysis in water quality analysis. In *The 5th National and 3rd International Conference of Environmental Sciences, Agriculture and Natural Resource*, 1â (Vol. 19).

57. Hairom NH, Soon CF, Mohamed RM, Morsin M, Zainal N, Nayan N, Zulkifli CZ, Harun NH. A review of nanotechnological applications to detect and control surface water pollution. *Environmental Technology & Innovation*. 2021 Nov 1;24:102032.
58. Pena-Pereira F, Bendicho C, Pavlović DM, Martín-Esteban A, Díaz-Álvarez M, Pan Y, Cooper J, Yang Z, Safarik I, Pospiskova K, Segundo MA. Miniaturized analytical methods for determination of environmental contaminants of emerging concern—a review. *Analytica Chimica Acta*. 2021 May 8;1158:238108.
59. Sicard C, Glen C, Aubie B, Wallace D, Jahanshahi-Anbuhi S, Pennings K, Daigger GT, Pelton R, Brennan JD, Filipe CD. Tools for water quality monitoring and mapping using paper-based sensors and cell phones. *Water research*. 2015 Mar 1;70:360-9.
60. Peyravi M, Jahanshahi M, Tourani H. Analytical methods of water pollutants detection. *InInorganic Pollutants in Water 2020 Jan 1* (pp. 97-113). Elsevier.
61. Potes-Lesoinne HA, Ramirez-Alvarez F, Perez-Gonzalez VH, Martinez-Chapa SO, Gallo-Villanueva RC. Nanomaterials for electrochemical detection of pollutants in water: A review. *Electrophoresis*. 2022 Jan;43(1-2):249-62.
62. Torrinha Á, Morais S. Electrochemical (bio) sensors based on carbon cloth and carbon paper: An overview. *TrAC Trends in Analytical Chemistry*. 2021 Sep 1;142:116324.
63. Guth U, Vonau W, Zosel J. Recent developments in electrochemical sensor application and technology—a review. *Measurement Science and Technology*. 2009 Jan 27;20(4):042002..
64. Bard AJ, Faulkner LR, White HS. *Electrochemical methods: fundamentals and applications*. John Wiley & Sons; 2022 May 3.
65. Compton RG, Banks CE. *Understanding voltammetry*. World Scientific; 2018 Jul 4.
66. Zhou L, Liu D, Liu L, He L, Cao X, Wang J, Wang ZL. Recent advances in self-powered electrochemical systems. *Research*. 2021 Mar 12;2021.
67. Curulli A. Electrochemical biosensors in food safety: challenges and perspectives. *Molecules*. 2021 May 15;26(10):2940.
68. Brett C, Oliveira Brett AM. *Electrochemistry: principles, methods, and applications*. 1993.

69. García-Miranda Ferrari A, Foster CW, Kelly PJ, Brownson DA, Banks CE. Determination of the electrochemical area of screen-printed electrochemical sensing platforms. *Biosensors*. 2018 Jun 8;8(2):53.
70. Ainla A, Mousavi MP, Tsaloglou MN, Redston J, Bell JG, Fernández-Abedul MT, Whitesides GM. Open-source potentiostat for wireless electrochemical detection with smartphones. *Analytical chemistry*. 2018 Apr 16;90(10):6240-6.
71. Dryden MD, Wheeler AR. DStat: A versatile, open-source potentiostat for electroanalysis and integration. *PloS one*. 2015 Oct 28;10(10):e0140349.
72. da Silva ET, Souto DE, Barragan JT, de F. Giarola J, de Moraes AC, Kubota LT. Electrochemical biosensors in point-of-care devices: recent advances and future trends. *ChemElectroChem*. 2017 Apr;4(4):778-94.
73. Mohamad Nor N, Ramli NH, Poobalan H, Qi Tan K, Abdul Razak K. Recent Advancement in Disposable Electrode Modified with Nanomaterials for Electrochemical Heavy Metal Sensors. *Critical reviews in analytical chemistry*. 2021 Jul 5:1-36.
74. Wu S, Li K, Zhang Z, Chen L. Synthesis of imprinted chitosan/AuNPs/graphene-coated MWCNTs/Nafion film for detection of lead ions. *New Journal of Chemistry*. 2020;44(33):14129-35.
75. Zhang W, Zhu S, Luque R, Han S, Hu L, Xu G. Recent development of carbon electrode materials and their bioanalytical and environmental applications. *Chemical Society Reviews*. 2016;45(3):715-52.
76. Liang C, Li Z, Dai S. Mesoporous carbon materials: synthesis and modification. *Angewandte Chemie International Edition*. 2008 May 5;47(20):3696-717.
77. Niu P, Gich M, Roig A, Fernández-Sánchez C. Metal Nanoparticle Carbon Gel Composites in Environmental Water Sensing Applications. *The Chemical Record*. 2018 Jul;18(7-8):749-58.
78. Niu P, Fernández-Sánchez C, Gich M, Navarro-Hernández C, Fanjul-Bolado P, Roig A. Screen-printed electrodes made of a bismuth nanoparticle porous carbon nanocomposite applied to the determination of heavy metal ions. *Microchimica Acta*. 2016 Feb;183(2):617-23.
79. Niu P, Asturias-Arribas L, Jordà X, Goñi AR, Roig A, Gich M, Fernández-Sánchez C.

Carbon–Silica Composites to Produce Highly Robust Thin-Film Electrochemical Microdevices. *Advanced Materials Technologies*. 2017 Dec;2(12):1700163.

80. Niu P. Carbon Xerogel nanocomposite materials for electrochemical devices: application to heavy metal detection. *Universitat Autònoma de Barcelona*; 2015 Sep 18.
81. Bhat VS, Supriya S, Hegde G. Biomass derived carbon materials for electrochemical sensors. *Journal of the Electrochemical Society*. 2019 Dec 19;167(3):037526.
82. Tabac S, Eisenberg D. Pyrolyze this paper: can biomass become a source for precise carbon electrodes?. *Current Opinion in Electrochemistry*. 2021 Feb 1;25:100638.
83. Abdullah SH, Hanapi NH, Azid A, Umar R, Juahir H, Khatoon H, Endut A. A review of biomass-derived heterogeneous catalyst for a sustainable biodiesel production. *Renewable and Sustainable Energy Reviews*. 2017 Apr 1;70:1040-51.
84. Benny L, John A, Varghese A, Hegde G, George L. Waste elimination to porous carbonaceous materials for the application of electrochemical sensors: Recent developments. *Journal of Cleaner Production*. 2021 Mar 25;290:125759.
85. Cui J, Xi Y, Chen S, Li D, She X, Sun J, Han W, Yang D, Guo S. Prolifera-Green-Tide as Sustainable Source for Carbonaceous Aerogels with Hierarchical Pore to Achieve Multiple Energy Storage. *Advanced Functional Materials*. 2016 Dec;26(46):8487-95.
86. Bi Z, Kong Q, Cao Y, Sun G, Su F, Wei X, Li X, Ahmad A, Xie L, Chen CM. Biomass-derived porous carbon materials with different dimensions for supercapacitor electrodes: a review. *Journal of materials chemistry a*. 2019;7(27):16028-45.
87. Tang X, Liu D, Wang YJ, Cui L, Ignaszak A, Yu Y, Zhang J. Research advances in biomass-derived nanostructured carbons and their composite materials for electrochemical energy technologies. *Progress in Materials Science*. 2021 May 1;118:100770.
88. Sriram G, Supriya S, Kurkuri M, Hegde G. Efficient CO₂ adsorption using mesoporous carbons from biowastes. *Materials Research Express*. 2019 Dec 23;7(1):015605.
89. Blankenship LS, Mokaya R. Cigarette butt-derived carbons have ultra-high surface area and unprecedented hydrogen storage capacity. *Energy & Environmental*

Science. 2017;10(12):2552-62.

90. Liao X, Chen C, Wang Z, Wan R, Chang CH, Zhang X, Xie S. Changes of biomass and bacterial communities in biological activated carbon filters for drinking water treatment. *Process Biochemistry*. 2013 Feb 1;48(2):312-6.
91. Mathew AT, Bhat VS, Supriya S, Maiyalagan T, Varghese A, Hegde G. TEMPO mediated electrocatalytic oxidation of pyridyl carbinol using palladium nanoparticles dispersed on biomass derived porous nanoparticles. *Electrochimica Acta*. 2020 Sep 10;354:136624.
92. Li YQ, Samad YA, Polychronopoulou K, Alhassan SM, Liao K. Carbon aerogel from winter melon for highly efficient and recyclable oils and organic solvents absorption. *ACS Sustainable Chemistry & Engineering*. 2014 Jun 2;2(6):1492-7.
93. Pang H, Sun P, Gong H, Zhang N, Cao J, Zhang R, Luo M, Li Y, Sun G, Li Y, Deng J. Wood-Derived Bimetallic and Heteroatomic Hierarchically Porous Carbon Aerogel for Rechargeable Flow Zn–Air Batteries. *ACS Applied Materials & Interfaces*. 2021 Aug 15;13(33):39458-69.
94. Gutiérrez-Capitán M, Baldi A, Gómez R, García V, Jiménez-Jorquera C, Fernández-Sánchez C. Electrochemical nanocomposite-derived sensor for the analysis of chemical oxygen demand in urban wastewaters. *Analytical chemistry*. 2015 Feb 17;87(4):2152-60.
95. Badr IH, Hassan HH, Hamed E, Abdel-Aziz AM. Sensitive and Green Method for Determination of Chemical Oxygen Demand Using a Nano - copper Based Electrochemical Sensor. *Electroanalysis*. 2017 Oct;29(10):2401-9.
96. Bashami RM, Soomro MT, Khan AN, Aazam ES, Ismail IM, El-Shahawi MS. A highly conductive thin film composite based on silver nanoparticles and malic acid for selective electrochemical sensing of trichloroacetic acid. *Analytica Chimica Acta*. 2018 Dec 7;1036:33-48.
97. Chiu MH, Cheng WL, Muthuraman G, Hsu CT, Chung HH, Zen JM. A disposable screen-printed silver strip sensor for single drop analysis of halide in biological samples. *Biosensors and Bioelectronics*. 2009 Jun 15;24(10):3008-13.
98. Bujes-Garrido J, Izquierdo-Bote D, Heras A, Colina A, Arcos-Martínez MJ. Determination of halides using Ag nanoparticles-modified disposable electrodes. A

- first approach to a wearable sensor for quantification of chloride ions. *Analytica chimica acta*. 2018 Jul 5;1012:42-8.
99. Sivakumar R, Lee NY. Recent progress in smartphone-based techniques for food safety and the detection of heavy metal ions in environmental water. *Chemosphere*. 2021 Jul 1;275:130096.
 100. Liu X, Yao Y, Ying Y, Ping J. Recent advances in nanomaterial-enabled screen-printed electrochemical sensors for heavy metal detection. *TrAC Trends in Analytical Chemistry*. 2019 Jun 1;115:187-202.
 101. Zhang X, Jiang M, Niu N, Chen Z, Li S, Liu S, Li J. Natural-product-derived carbon dots: from natural products to functional materials. *ChemSusChem*. 2018 Jan 10;11(1):11-24.
 102. Zhong L, Jiang C, Zheng M, Peng X, Liu T, Xi S, Chi X, Zhang Q, Gu L, Zhang S, Shi G. Wood Carbon Based Single-Atom Catalyst for Rechargeable Zn–Air Batteries. *ACS Energy Letters*. 2021 Sep 21;6(10):3624-33.
 103. Kunene TJ, Tartibu LK, Ukoba K, Jen TC. Review of atomic layer deposition process, application and modeling tools. *Materials Today: Proceedings*. 2022 Feb 24.
 104. Li M, Li YT, Li DW, Long YT. Recent developments and applications of screen-printed electrodes in environmental assays—A review. *Analytica chimica acta*. 2012 Jul 13;734:31-44.
 105. Suresh RR, Lakshmanakumar M, Arockia Jayalatha JB, Rajan KS, Sethuraman S, Krishnan UM, Rayappan JB. Fabrication of screen-printed electrodes: opportunities and challenges. *Journal of Materials Science*. 2021 May;56(15):8951-9006.
 106. Newman JD, Turner AP. Home blood glucose biosensors: a commercial perspective. *Biosensors and bioelectronics*. 2005 Jun 15;20(12):2435-53.
 107. Hu J. The evolution of commercialized glucose sensors in China. *Biosensors and Bioelectronics*. 2009 Jan 1;24(5):1083-9.
 108. VinuMohan AM. Screen-Printed Electrochemical Sensors for Environmental Contaminants. In *Nanosensor Technologies for Environmental Monitoring 2020* (pp. 85-108). Springer, Cham.
 109. Barek J. How to improve the performance of electrochemical sensors via minimization

of electrode passivation. *Chemosensors*. 2021 Jan 6;9(1):12.

110. Geto A, Noori JS, Mortensen J, Svendsen WE, Dimaki M. Electrochemical determination of bentazone using simple screen-printed carbon electrodes. *Environment international*. 2019 Aug 1;129:400-7.
111. Barros Azeredo NF, Ferreira Santos MS, Sempionatto JR, Wang J, Angnes L. Screen-printed technologies combined with flow analysis techniques: moving from benchtop to everywhere. *Analytical Chemistry*. 2021 Dec 1;94(1):250-68.
112. Foster CW, Kadara RO, Banks CE. Fundamentals of screen-printing electrochemical architectures. In *Screen-printing electrochemical architectures 2016* (pp. 13-23). Springer, Cham.
113. Niu P, Asturias-Arribas L, Gich M, Fernández-Sánchez C, Roig A. Electrochemically active thin carbon films with enhanced adhesion to silicon substrates. *ACS Applied Materials & Interfaces*. 2016 Nov 16;8(45):31092-9.
114. Niu P, Asturias-Arribas L, Jordà X, Goñi AR, Roig A, Gich M, Fernández-Sánchez C. Carbon–Silica Composites to Produce Highly Robust Thin-Film Electrochemical Microdevices. *Advanced Materials Technologies*. 2017 Dec;2(12):1700163.
115. Romero P, Postigo PA, Baquedano E, Martínez J, Boscá A, de Villoria RG. Controlled synthesis of nanocrystalline glass-like carbon thin films with tuneable electrical and optical properties. *Chemical Engineering Journal*. 2016 Sep 1;299:8-14.
116. Keeley GP, McEvoy N, Nolan H, Holzinger M, Cosnier S, Duesberg GS. Electroanalytical sensing properties of pristine and functionalized multilayer graphene. *Chemistry of Materials*. 2014 Mar 11;26(5):1807-12.
117. Jung CH, Kim WJ, Jung CH, Hwang IT, Khim D, Kim DY, Lee JS, Ku BC, Choi JH. A simple PAN-based fabrication method for microstructured carbon electrodes for organic field-effect transistors. *Carbon*. 2015 Jun 1;87:257-68.
118. Wei L, Nitta N, Yushin G. Lithographically patterned thin activated carbon films as a new technology platform for on-chip devices. *Acs Nano*. 2013 Aug 27;7(8):6498-506.
119. Kim J, Song X, Kinoshita K, Madou M, White R. Electrochemical studies of carbon films from pyrolyzed photoresist. *Journal of the Electrochemical Society*. 1998 Jul 1;145(7):2314.

120. Felix S, Kollu P, Raghupathy BP, Jeong SK, Grace AN. Electrocatalytic oxidation of carbohydrates and dopamine in alkaline and neutral medium using CuO nanoplatelets. *Journal of Electroanalytical Chemistry*. 2015 Feb 15;739:1-9.
121. Marioli JM, Kuwana T. Electrochemical characterization of carbohydrate oxidation at copper electrodes. *Electrochimica Acta*. 1992 Jun 1;37(7):1187-97.
122. Diksy Y, Rahmawati I, Jiwanti PK, Ivandini TA. Nano-Cu modified Cu and nano-Cu modified graphite electrodes for chemical oxygen demand sensors. *Analytical Sciences*. 2020:20P069.
123. Cao P, Zhao K, Quan X, Chen S, Yu H. Efficient and stable heterogeneous electro-Fenton system using iron oxides embedded in Cu, N co-doped hollow porous carbon as functional electrocatalyst. *Separation and Purification Technology*. 2020 May 1;238:116424.
124. Li X, Min X, Hu X, Jiang Z, Li C, Yang W, Zhao F. In-situ synthesis of highly dispersed Cu-Cu_xO nanoparticles on porous carbon for the enhanced persulfate activation for phenol degradation. *Separation and Purification Technology*. 2021 Dec 1;276:119260.
125. Chen W, Fu X, Chan WP, Veksha A, Lisak G. Carbon nanosheet-carbon nanocage encapsulated Cu composite from chemical vapor deposition of real-world plastic waste for tailored CO₂ conversion to various products. *Applied Materials Today*. 2021 Dec 1;25:101207.
126. Ahamed A, Ge L, Zhao K, Veksha A, Bobacka J, Lisak G. Environmental footprint of voltammetric sensors based on screen-printed electrodes: an assessment towards “green” sensor manufacturing. *Chemosphere*. 2021 Sep 1;278:130462.
127. Espro C, Marini S, Giusi D, Ampelli C, Neri G. Non-enzymatic screen printed sensor based on Cu₂O nanocubes for glucose determination in bio-fermentation processes. *Journal of Electroanalytical Chemistry*. 2020 Sep 15;873:114354.
128. Beitollahi H, Garkani Nejad F, Tajik S, Jahani S, Biparva P. Voltammetric determination of amitriptyline based on graphite screen printed electrode modified with a Copper Oxide nanoparticles. *International Journal of Nano Dimension*. 2017 Jul 1;8(3):197-205.
129. Badr IH, Hassan HH, Hamed E, Abdel-Aziz AM. Sensitive and Green Method for Determination of Chemical Oxygen Demand Using a Nano - copper Based

Electrochemical Sensor. *Electroanalysis*. 2017 Oct;29(10):2401-9.

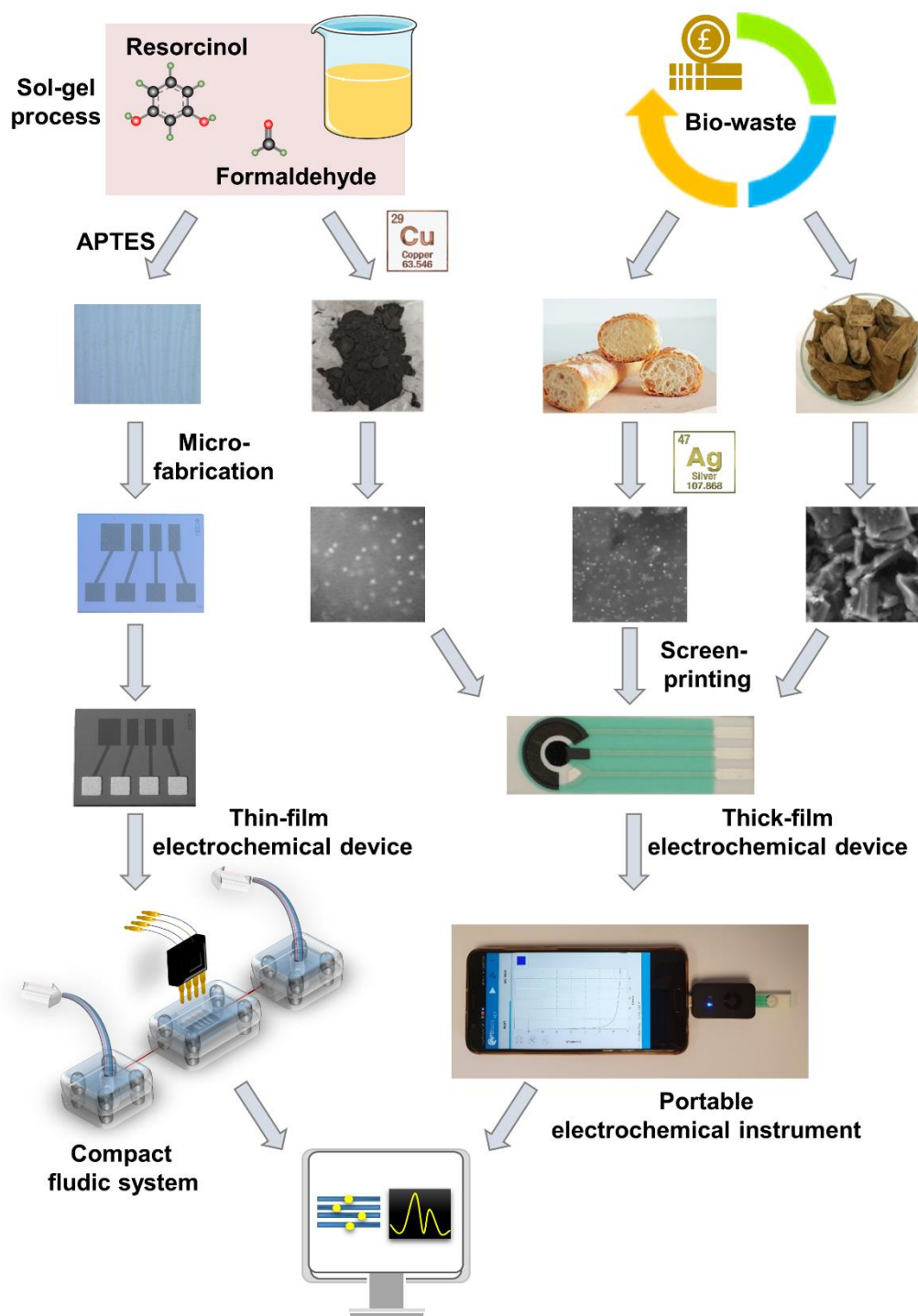
130. Dong XY, Gao ZW, Yang KF, Zhang WQ, Xu LW. Nanosilver as a new generation of silver catalysts in organic transformations for efficient synthesis of fine chemicals. *Catalysis Science & Technology*. 2015;5(5):2554-74.
131. Xu R, Wang D, Zhang J, Li Y. Shape - dependent catalytic activity of silver nanoparticles for the oxidation of styrene. *Chemistry—An Asian Journal*. 2006 Dec 18;1(6):888-93.
132. Rondinini S, Mussini PR, Muttini P, Sello G. Silver as a powerful electrocatalyst for organic halide reduction: the critical role of molecular structure. *Electrochimica acta*. 2001 Jul 30;46(20-21):3245-58.
133. Lou YY, Fontmorin JM, Amrane A, Fourcade F, Geneste F. Metallic nanoparticles for electrocatalytic reduction of halogenated organic compounds: A review. *Electrochimica Acta*. 2021 May 1;377:138039.
134. Qian D, Li W, Chen F, Huang Y, Bao N, Gu H, Yu C. Voltammetric sensor for trichloroacetic acid using a glassy carbon electrode modified with Au@ Ag nanorods and hemoglobin. *Microchimica Acta*. 2017 Jul;184(7):1977-85.
135. Foresti ML, Innocenti M, Forni F, Guidelli R. Electrosorption valency and partial charge transfer in halide and sulfide adsorption on Ag (111). *Langmuir*. 1998 Nov 24;14(24):7008-16.
136. Yin H, Cao X, Lei C, Chen W, Huang B. Insights into electroreductive dehalogenation mechanisms of chlorinated environmental pollutants. *ChemElectroChem*. 2020 Apr 17;7(8):1825-37.
137. Isse AA, Mussini PR, Gennaro A. New insights into electrocatalysis and dissociative electron transfer mechanisms: the case of aromatic bromides. *The Journal of Physical Chemistry C*. 2009 Aug 20;113(33):14983-92.
138. Arai K, Kusu F, Noguchi N, Takamura K, Osawa H. Selective determination of chloride and bromide ions in serum by cyclic voltammetry. *Analytical biochemistry*. 1996 Aug 15;240(1):109-13.
139. Chiu MH, Cheng WL, Muthuraman G, Hsu CT, Chung HH, Zen JM. A disposable screen-printed silver strip sensor for single drop analysis of halide in biological samples. *Biosensors and Bioelectronics*. 2009 Jun 15;24(10):3008-13.

140. Song Y, Chen J. Multifunctional Bismuth-Based Materials for Heavy Metal Detection and Antibiosis. In Bismuth-Advanced Applications and Defects Characterization 2018 Jun 20. IntechOpen.

Chapter 2

Aims and Objectives

Thesis outline



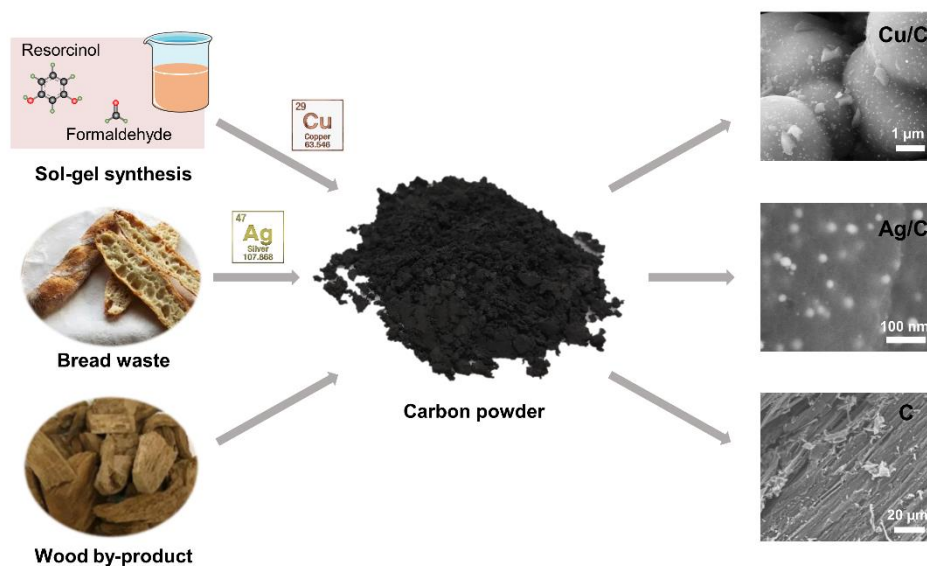
The main objective of this thesis was the development of novel sustainable electrochemical sensors for the sensitive analysis of water pollutants. In particular, we focused on the measurement of Chemical Oxygen Demand (COD), and the quantitative detection of organohalides and heavy metals. To this aim, metal nanoparticle-modified porous carbon nanocomposites were synthesized and further processed to manufacture miniaturized thick-film and thin-film electrochemical devices by screen printing and microfabrication techniques. A full assessment of the analytical performance of the different devices was carried out.

To achieve these goals, the following specific objectives were defined. They are also outlined in the Scheme shown above.

1. Synthesizing porous carbon nanocomposites functionalized with functional metal and metal oxide nanoparticles (Cu, Cu₂O, and Ag).
2. Assessing the electrochemical performance of the synthesized nanocomposites for analyzing the water pollutants mentioned above.
3. Setting up a screen-printing fabrication process using the developed nanocomposite materials to produce single-use thick-film electrochemical devices that could be combined with a compact instrumentation device for in-field analytical measurements.
4. Designing and developing metal nanoparticle-modified carbon/silica thin-film electrochemical devices to be integrated into compact fluidic platforms that could potentially be deployed for in-field water monitoring.

Chapter 3

Synthesis of porous carbon nanocomposites modified with metal nanoparticles



Summary

This chapter is divided into three parts. The first part shows the preparation of composites comprising a porous carbon matrix with Cu or Cu₂O nanoparticles based on the sol-gel chemical synthesis. The second part reports the synthesis of a porous carbon matrix containing Ag nanoparticles by the impregnation method using bread waste as the starting material. The third part describes the preparation of porous carbon materials using wood byproducts as the starting material. The structure and morphology of the resulting materials were characterized by Particle Size analysis, Nitrogen Adsorption-Desorption isotherm studies, Scanning Electron Microscopy (SEM) and X-ray diffraction (XRD).

3.1 Introduction

Carbon allotropes such as amorphous carbon, graphite, carbon nanotubes and graphene are excellent electrode material candidates thanks to their high electrical conductivity, wide potential windows, chemical and electrochemical stability, and a variety of possible surface chemistries, which make them versatile for further functionalization.¹⁻⁴ The latter is a particularly relevant advantage considering that many target analytes cannot be detected with a bare carbon electrode. The high overpotentials required to detect them produce hydrogen or oxygen due to water hydrolysis. This limitation can be overcome by functionalizing carbon-based electrodes with appropriate catalysts that can lower the target analyte detection potential. One excellent approach is the use of metal nanoparticle carbon nanocomposites to produce electrochemical platforms for a variety of sensing applications.

Some content described in Chapter 1 is very briefly introduced below, to put the work of this chapter into perspective. Carbon materials can be modified with functional copper nanoparticles to produce a composite that can oxidize organic compounds at low oxidation potentials. This is because the intermediate products generated during the electrocatalytic oxidation of copper (Cu_2O , CuO , $\text{Cu}(\text{OH})_2$) provide reaction sites for hydroxyl radicals that enable the oxidation of organics at low potentials.^{5,6} When working with copper-based nanomaterials, the oxidation overpotential is further decreased and large oxidation currents are observed as a result of their large surface area and higher electrocatalytic activity.⁷⁻¹⁰ Thus, carbon/Cu nanoparticle composites can be exploited to make electrodes for the electrochemical monitoring of the Chemical Oxygen Demand (COD) in waters.

Ag nanoparticles (Ag NPs) combined with carbon materials is another example of introducing a specific catalyst to increase the functionality of carbon materials, making the resulting nanocomposite appealing for the removal¹¹ and analysis^{12,13} of hazardous chlorinated compounds. This is because the integration of Ag NPs in carbon structures can reduce organic halides at small negative potentials, well above those inducing the hydrogen evolution reaction. Then, the halide anions released into the solution can be measured the oxidation of Ag NPs to form Ag halides gives rise to an anodic current at low anodic potentials.¹⁴⁻¹⁶

A convenient method to prepare the functional nanoparticle-doped carbon material is the resorcinol/formaldehyde sol-gel process.¹⁷ The sol-gel chemistry enables the mixing of different metal precursors at the molecular level while incorporating other additives into the

gel matrix, providing the final material with some additional functionalities. An important advantage of this one-step liquid processing is that it is scalable and compatible with the industrial production of the material.

Another interesting approach to preparing heteroatom-doped functional carbon nanomaterials is the direct carbonization of biomass and biowaste.¹⁸ Bioresources contain a high percentage of carbohydrates that can be easily converted into a carbon material. Upscaling the bio-waste into a high-added-value material is a simple and sustainable method that has been progressively gaining attention in the context of the so-called circular bio-economy.

3.2 Synthesis of composites of porous carbon and Copper-based nanoparticles

Composites of porous carbon and Cu-based nanoparticles have been prepared following three sol-gel based methods that are schematically summarized in Figure 3.1. A detailed description and characterization are given in sections 3.2.1 and 3.2.2.

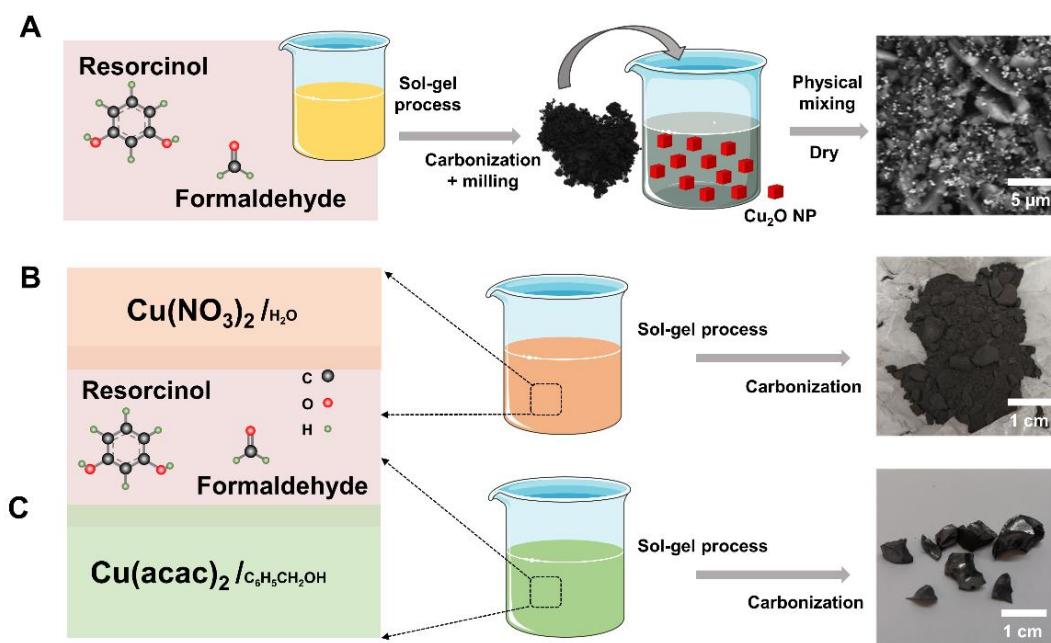


Figure 3.1. Schematic representation of the preparation process of three materials: (A) Cu₂O/C, (B) Cu/C₁, (C) Cu/C₂.

3.2.1 Physical mixing method for the preparation of composites of porous C and Cu₂O nanoparticles

Cu₂O NPs with a polyvinylpyrrolidone (PVP, average molecular weight: 3500 g/mol, ACROS Organics) surface coating were synthesized using a microwave-assisted thermal decomposition protocol in a Microwave Advanced Flexible Synthesis Platform (flexiWAVE) from Milestone, at 2.45 GHz frequency and 750 W power.¹⁹ In short, 1.36 g PVP (0.39 mmol) was dissolved in 40 mL benzyl alcohol by continuous sonication. Then, 110 mg of Cu(acac)₂ (0.42 mmol) were dissolved in the previous solution that turned bluish with a 10.50 mM Cu(acac)₂ concentration. This preparation was repeated three times, and a total of 4 tubes were placed together in the MW reactor. Then the Microwave tubes, under continuous stirring, were first heated at 60°C for 5 min to ensure that the precursor is completely dissolved, and then heated to 200°C and kept at this temperature for 10 min. The final solution was dark-brown, and no precipitation was observed, indicating that the as-produced NPs were dispersed in the solution. To precipitate the NPs and remove PVP excess, 35 ml acetone was added to 10 ml of solution (16 test tubes) and centrifuged at 9000 rpm for 15 min, repeating the process twice. Then, the sediment from each tube was collected for further use. The TEM analysis confirmed that the collected sediment consisted of Cu₂O NPs of 150-250 nm in size (Figure 3.2 A and electron diffraction pattern in Figure 3.2 B).

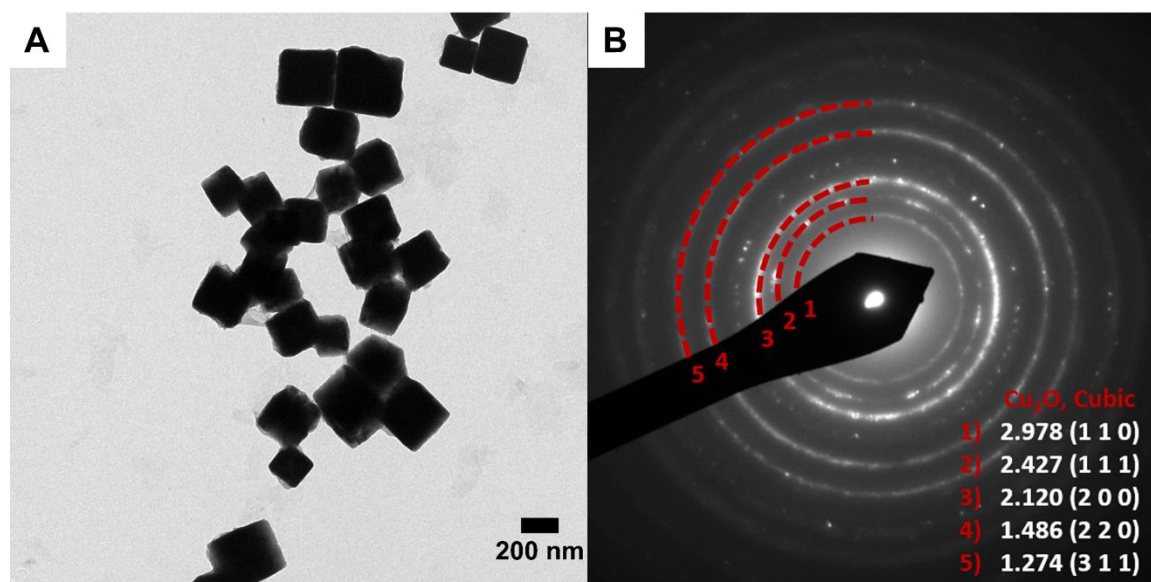


Figure 3.2. TEM images of Cu₂O NPs (A), and corresponding electron diffraction pattern indexed according to the cubic Cu₂O (B).

The porous carbon material was prepared in bulk following the protocol described in our previous work, with slight variations.¹⁷ This included the following steps. First, 6 g resorcinol and 57 mg of Na_2CO_3 were dissolved in 13 mL Milli-Q water (18 M Ω cm, Millipore). Then 8.2 mL of formaldehyde solution were quickly added to the mixture under stirring conditions. The resulting solution was sealed in a glass vial and placed in a stove at 60 °C for 24 h. A wet gel was thus generated which was then dried in a fume hood at room temperature for 2 days to produce a xerogel material. Finally, the xerogel was carbonized at 1050 °C in an Ar atmosphere for 2 h. The pyrolyzed C material was ball milled in a Retsch Mixer Mill MM 400 (30 min/15 Hz) using a zirconia jar (10 mL) and 2 zirconia balls (12 mm in diameter) to obtain a powder with an average particle size of 5 μm (Figure 3.3 A and Figure 3.1 A). Thereafter, 0.5 g of C powder and 35 mg of Cu_2O NPs were added to 2 mL of Milli-Q water and thoroughly stirred to get a uniform dense suspension. This was dried in the oven at 60 °C for two days and a mixture of C powder and Cu_2O NPs was obtained (Figure 3.1 A). The resulting material was labeled $\text{Cu}_2\text{O}/\text{C}$.

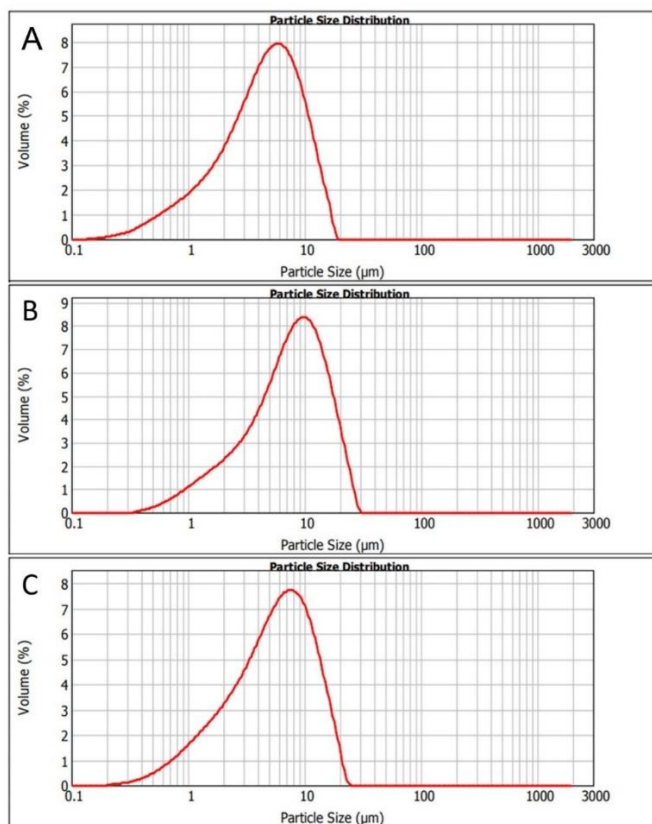


Figure 3.3. Graph of the particle size distribution of pure C powder (A), Cu/C_1 powder (B), and Cu/C_2 powder (C).

3.2.2 One-pot synthesis of composites of porous carbon and Cu nanoparticles

Two carbon xerogel-based materials containing Cu NPs were prepared by two distinctive one-pot sol-gel synthesis approaches. The first one closely follows the synthesis of the porous carbon material described in section 3.2.1. Here, 6 g of resorcinol was firstly dissolved in 8 mL of Milli-Q water and then 8.2 mL of formaldehyde was added. The solution was stirred for 1h, and then 5 mL of a water solution containing 0.12 g/mL Cu (II) nitrate hydrated ($\text{Cu}(\text{NO}_3)_2 \cdot x\text{H}_2\text{O}$) was added (Figure 3.1 B). The remaining steps were the same as the ones in the synthesis of the porous C, described above. This carbon xerogel with Cu NPs was labeled as Cu/C_1.

The second approach was as follows: 300 mg copper (II) acetylacetonate ($\text{Cu}(\text{acac})_2$) and 1.5 g resorcinol were dissolved in 3.25 mL benzyl alcohol solution and stirred for 8 min. Then, 2.05 mL of formaldehyde was added to the solution (Figure 3.1 C). The remaining steps were the same as those of pure carbon materials. The obtained carbon xerogel was labeled Cu/C_2.

Both materials were ball milled for further processing under the same conditions described in section 3.2.1. The resulting powders contained particles of the Cu/C_1 and Cu/C_2 nanocomposites with an average diameter of 8.5 μm (Figure 3.3 B) and 6.5 μm (Figure 3.3 C), respectively.

3.2.3 Structural and morphological characterization

The three obtained materials were thoroughly characterized by Mastersizer 2000 (Malvern Instruments), FEI Quanta 200F scanning electron microscope (SEM) with energy-dispersive X-ray microanalysis (EDX), X-ray diffraction (XRD), and nitrogen adsorption-desorption isotherms.

Figure 3.4 A shows the nitrogen adsorption and desorption isotherm of the pure C, evidencing its porosity. According to the BET model, the surface area of pure C was calculated to be 49 m^2g^{-1} (Table 3.1). The adsorption at low nitrogen relative pressures ($P/P_0=0.0-0.1$) indicates the presence of a significant volume of micropores ($< 2\text{nm}$).²⁰ The slope of the isotherms at intermediate relative pressures ($0.3 < P/P_0 < 0.8$) and the increase in the adsorbed volume at high relative pressures ($0.9 < P/P_0 < 1.0$) reveals, the existence of mesopores (2-50 nm) and macropores (50-7500 nm), respectively.²⁰ The total pore volume

calculation was $0.054 \text{ cm}^3\text{g}^{-1}$ based on the nitrogen adsorbed at P/P_0 of ca. 0.995 (Table 3.1). The BJH pore size distribution curve acquired from the adsorption isotherm confirmed the presence of pores mostly in the micropore and mesopore regions with a small fraction of macropores. The lack of overlap and irreversibility of the adsorption and desorption isotherm at low pressures could indicate the interaction of nitrogen with the material surface or an elastic deformation of the material with increasing pressures.²¹ The similarity of the absorption-desorption isotherms of $\text{Cu}_2\text{O}/\text{C}$, Cu/C_1 and Cu/C_2 composites, shown in Figure 3.4 A-C and Table 3.1, indicates that the three materials exhibit a very similar porosity.

Table 3.1. Textural properties of pure C, Cu/C_1 , and Cu/C_2 composites.

sample	pure C	Cu/C_1	Cu/C_2
surface area (m^2g^{-1})	49	33	44
total pore volume (cm^3g^{-1})	0.054	0.031	0.046

Figure 3.5 A shows the SEM image of cubic nanoparticles as obtained by microwave synthesis. According to the TEM characterization described in section 3.2.1, the cubes are made of Cu_2O (Figure 3.2 A and Figure 3.2 B). Figure 3.5 B shows the SEM image of the $\text{Cu}_2\text{O}/\text{C}$ composite. It can be noticed that the nanocubes tend to accumulate between larger pieces of the carbon xerogel. The SEM images of Cu/C_1 and Cu/C_2 composites taken before the milling are presented in Figures 3.5 C and 3.5 E respectively. Cu/C_2 shows a bulky structure while the carbon matrix in the Cu/C_1 composite is formed by fused microbead particles that coalesced during the sol-gel process and resulted from the low solution pH caused by the use of copper nitrate.²² The low magnification images of samples Cu/C_1 (Figure 3.5 C) and Cu/C_2 (Figure 3.5 E) show that the globular structure of the former results in a larger surface area of macropores. This different microstructure is responsible for the contrasting appearance of the as-prepared composites, with Cu/C_1 composite being a soft powder-like material and Cu/C_2 a hard monolith (Figure 3.1 B and 3.1 C). The higher magnification SEM backscattered electron images of Cu/C_1 and Cu/C_2 in Figures 3.5 D and 3.5 F reveal the presence of small bright particles on the surface of larger dark particles. The bright contrast of the small particles can be attributed to the presence of Cu while the darker matrix in which those are embedded corresponds to the porous carbon xerogel. The particles prepared by one-step synthesis appear to be spherical and uniformly distributed in the carbon matrix.

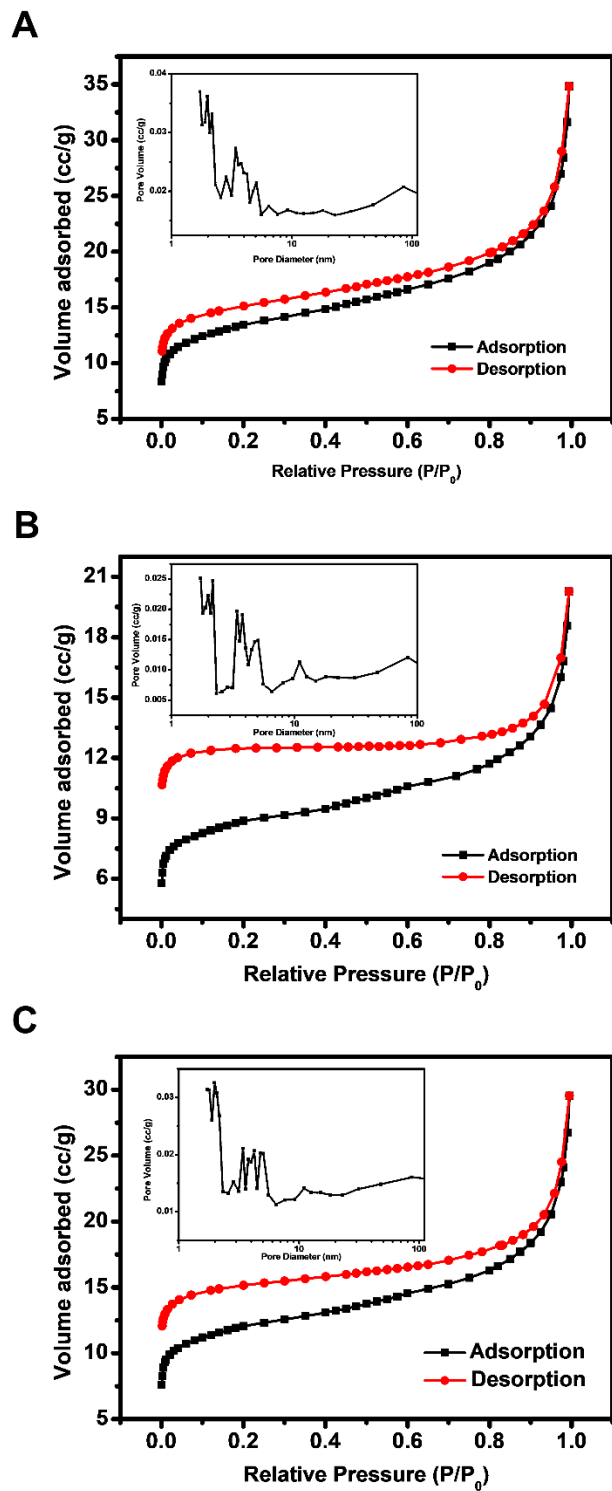


Figure 3.4. N_2 adsorption and desorption isotherm of the (A) pure C, (B) Cu/C₁ and (C) Cu/C₂ composites. Inset shows the pore size distributions determined using the BJH method.

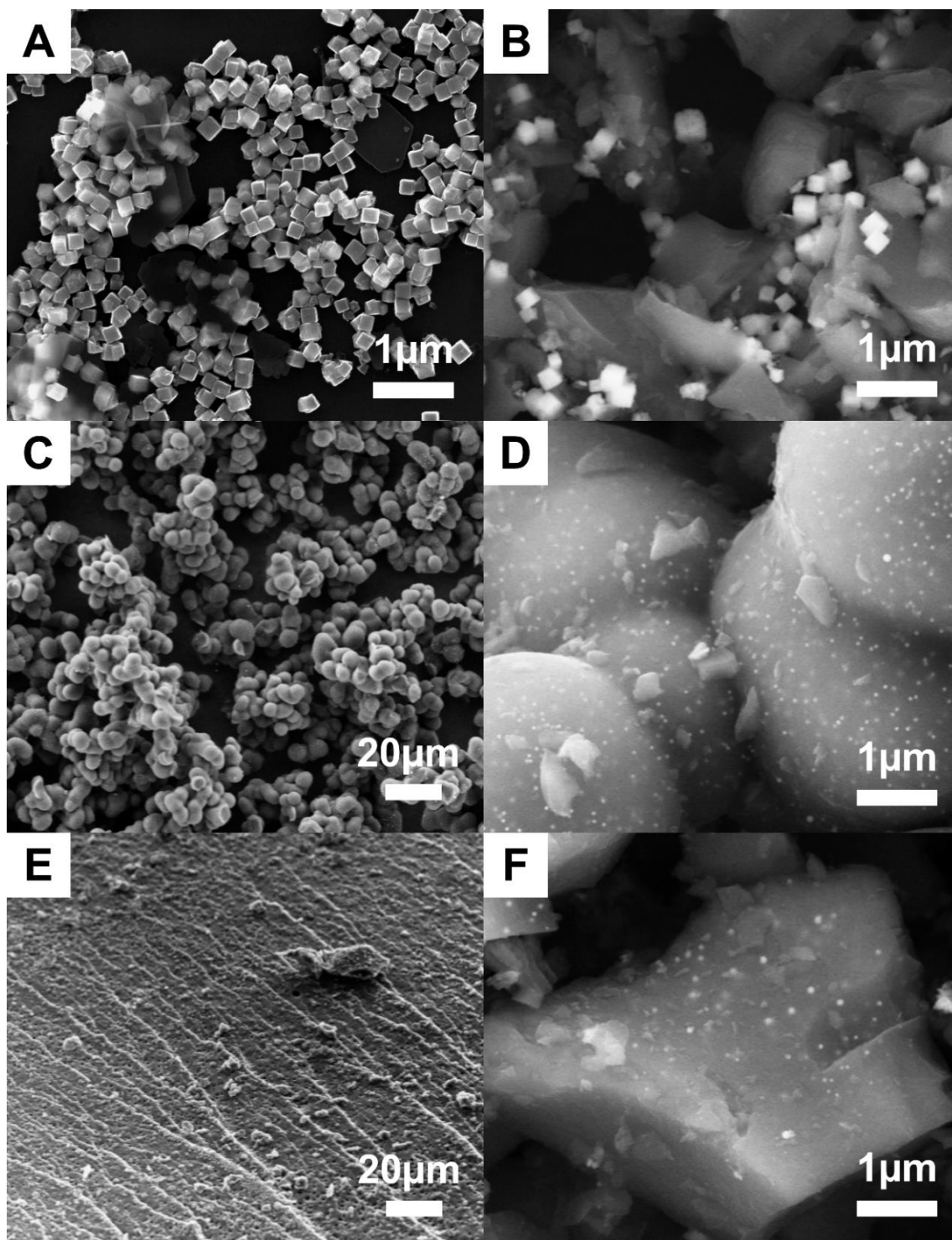


Figure 3.5. Secondary electron SEM images of Cu₂O NPs (A), Cu₂O/C (B), Cu/C₁ (C and D) and Cu/C₂ (E and F). Figures C and E are before milling, Figures D and F are after milling.

Particle size distributions were obtained from a detailed study of different SEM images (Figure 3.6). In the case of the Cu₂O/C composite, Cu₂O cubes present a relatively broad distribution of sizes centered around 200 nm (Figure 3.6 A and 3.6 B). The particles located inside the microbead-like structure of Cu/C_1 material show sizes in the range of about 50-60 nm (Figure 3.6 C and 3.6 D). By contrast, the particles found outside the microbead-like structure show a larger size (about 130 nm), which can be related to the absence of spatial constraints during the material synthesis. The Cu/C_2 material shows particle sizes ranging from 60 to 80 nm (Figure 3.6 E and 3.6 F). EDX analysis revealed that the mass ratio of Cu to C is very similar for the different nanocomposite materials, giving the following mass percentages of Cu: 6 wt. % for Cu₂O/C, 7.9 wt. % for Cu/C_1 and 7.1 wt. % for Cu/C_2 (Figure 3.7, 3.8, 3.9 and Table 3.2).

Table 3.2 The major chemical element ratios in the three produced materials.

Sample	Element	wt. %	at. %
Cu ₂ O/C composite	C	94	98.8
	Cu	6	1.2
Cu/C_1 composite	C	92.1	98.5
	Cu	7.9	1.5
Cu/C_2 composite	C	92.9	98.58
	Cu	7.1	1.42

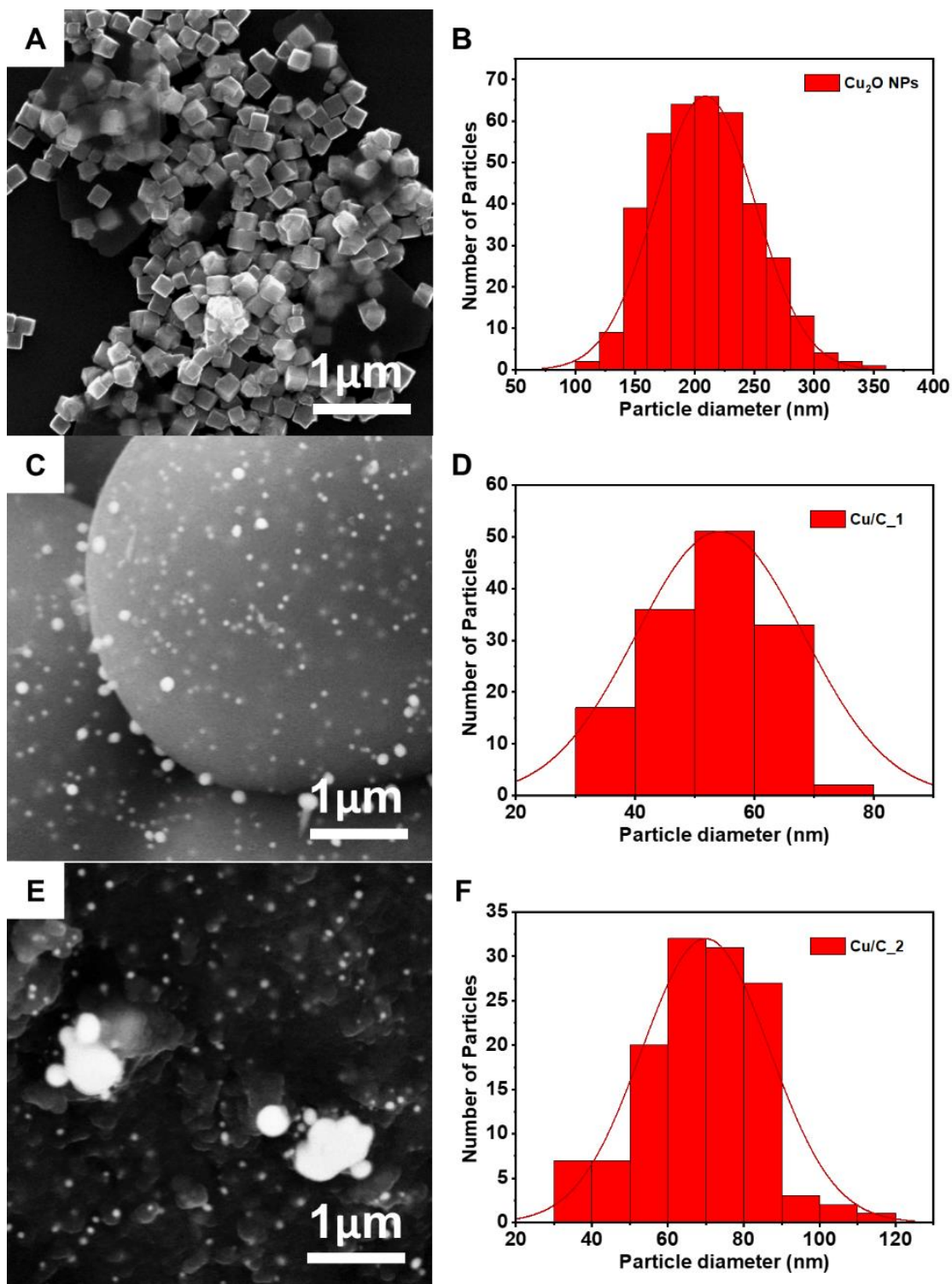


Figure 3.6. SEM images of Cu_2O NPs (A) and composites of Cu/C_1 (C) and Cu/C_2 (E) showing Cu particles. From the detailed analysis of more than 10 images, particle size distribution histograms (B), (D) and (F) were obtained.

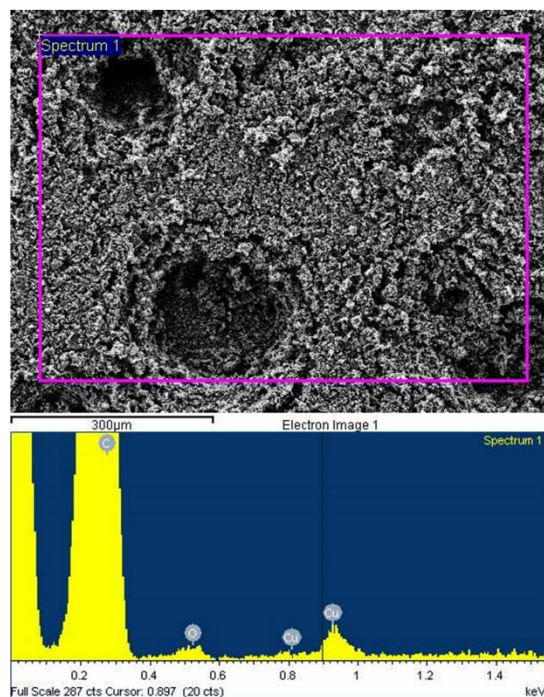


Figure 3.7. Energy dispersive spectroscopy (EDS) spectra of $\text{Cu}_2\text{O}/\text{C}$ composite. The EDS analysis revealed copper (Cu) and carbon (C) as the major chemical elements in the material.

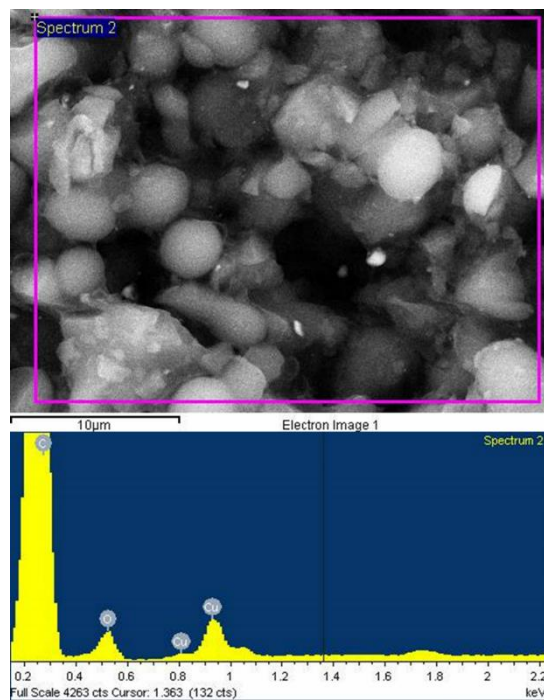


Figure 3.8. Energy dispersive spectroscopy (EDS) spectra of Cu/C_1 composite. The EDS analysis revealed copper (Cu) and carbon (C) as the major chemical elements in the material.

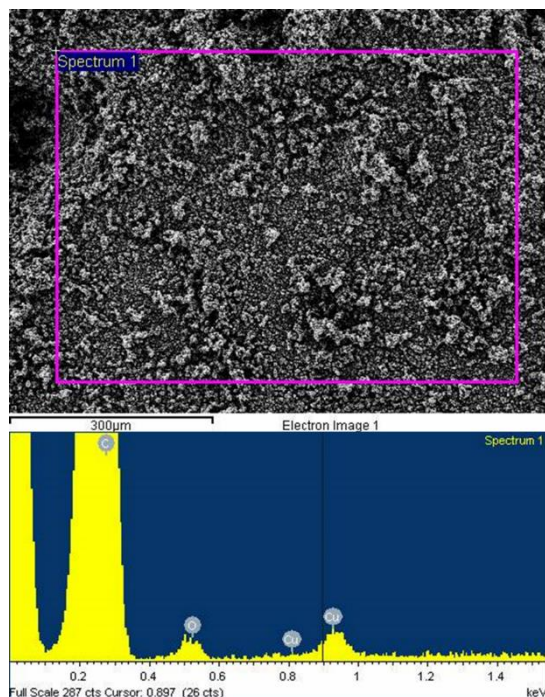


Figure 3.9. Energy dispersive spectroscopy (EDS) spectra of Cu/C₂ composite. The EDS analysis revealed copper (Cu) and carbon (C) as the major chemical elements in the material.

The nanocomposite materials were also studied by XRD (Figure 3.10). The broad bump located at around 23.5° in pure C, Cu₂O/C, Cu/C₁ and Cu/C₂ nanocomposites is associated with a pure amorphous carbon structure. In the pattern corresponding to Cu₂O/C, the four peaks at 29.4° , 36.3° , 42° and 61.2° can be ascribed to the reflections associated with the (110), (111), (200) and (220) planes of the Cu₂O crystalline structure, respectively. In contrast, the diffraction peaks observed for the Cu/C nanocomposites are characteristic of face-centered cubic (fcc) crystalline Cu, corresponding to the planes (111), (200) and (220), at 2θ values of ca. 43.2° , 50.4° and 74.1° . Thus, XRD patterns confirm that the pre-synthesized nanoparticles prepared by the microwave-assisted technique consist of cuprous oxide, in agreement with the electron diffraction pattern (Figure 3.2 B) while in the case of Cu/C₁ and Cu/C₂ nanocomposites, metallic copper nanoparticles are present.

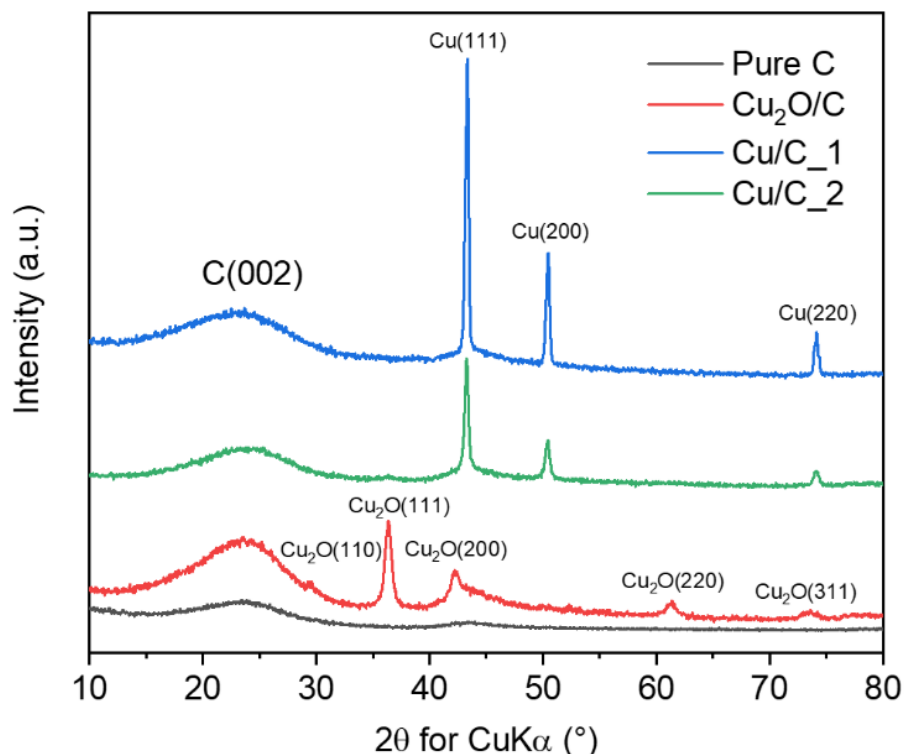


Figure 3.10. X-ray diffraction patterns of pure C, Cu₂O/C, Cu/C₁ and Cu/C₂ nanocomposites.

The diffractograms were analyzed by Rietveld refinement (Figure 3.11) by considering the presence of the following phases: the face-centered cubic structure of Cu (space group *Fm-3m*) for Cu/C₁ and Cu/C₂ and the cubic Cu₂O (space group *Pn-3m*) for Cu₂O/C and Cu/C₂, in the latter as a minor phase. The contribution of amorphous carbon was treated as a background. The analysis revealed a crystalline size of Cu₂O in Cu₂O/C of about 60 nm, much smaller than the 200 nm average size of the Cu₂O cubes of this sample, which indicates that the cubes are polycrystalline. On the other hand, the crystal size of Cu as obtained from the refinements of Cu/C₁ and Cu/C₂ is around 40 nm, in fairly good agreement with the sizes of Cu nanoparticles observed by SEM, which can thus be mostly considered as single crystals.

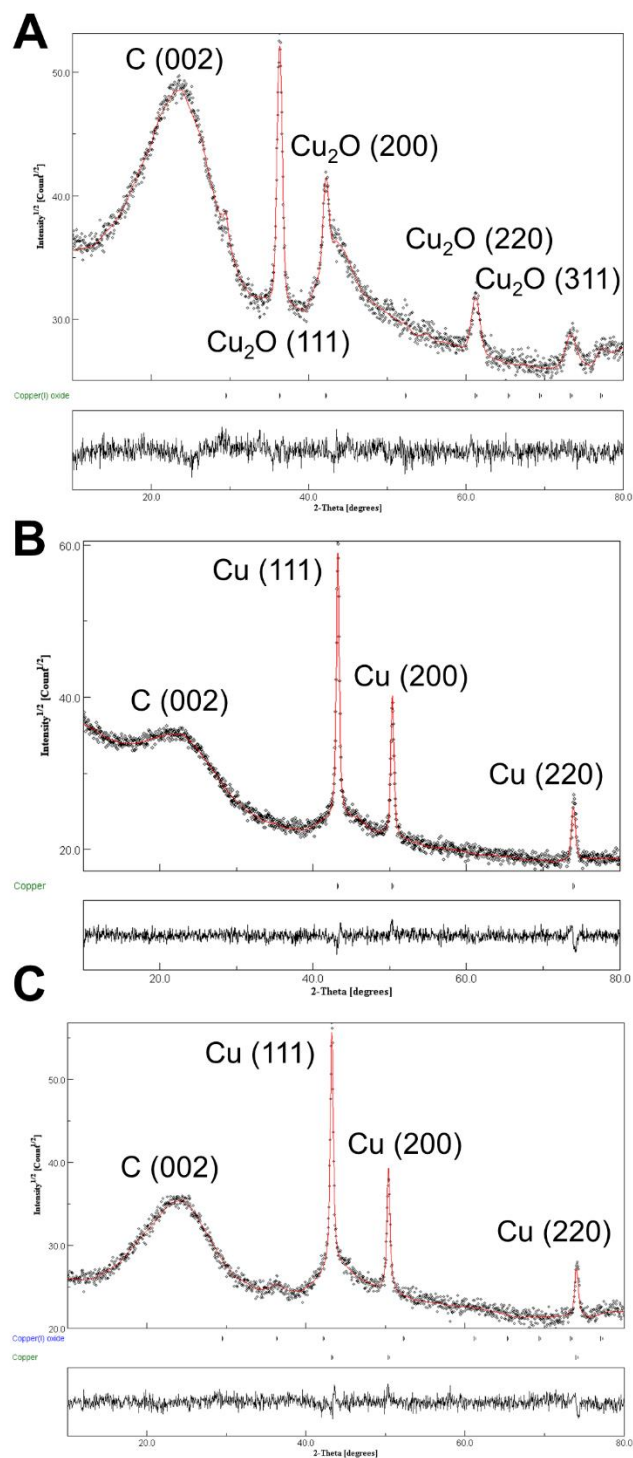


Figure 3.11. X-ray diffraction patterns of three composites. (A) $\text{Cu}_2\text{O}/\text{C}$, (B) Cu/C_1 and (C) Cu/C_2 . The red lines correspond to the profiles obtained by Rietveld refinement.

3.3 Synthesis of silver nanoparticle-modified porous carbon nanocomposites

A very simple synthetic approach that makes use of bread biowaste material to obtain a composite of porous carbon and silver nanoparticles is described in detail in this section.

3.3.1 Impregnation approach to preparing Ag-doped carbon nanocomposites

Salt-free bread was bought from a local supermarket, with a salt content of 0.05 g/100 g (see the bread compositional information in Table 3.3). The bread was placed in a cool and dry place for 2 weeks before using it for composite synthesis.

Table 3.3. Bread composition provided by a local supermarket.

net amount	210 g
nutritional information	average values per 100 g
energy value	1361 kJ/321 kcal
fats	1 g
saturated	0.30 g
monounsaturated	0.12 g
polyunsaturated	0.58 g
carbohydrates	68 g
sugars	0.68 g
dietary fiber	2.7 g
protein	8.6 g
salt	0.05 g

The preparation of Ag/C nanocomposites comprised the impregnation of the bread in deionized water containing silver nitrate, at a mass ratio of silver nitrate:water:bread of 1:59:15. After impregnation for 5 min, the mixture was fully stirred to obtain a slurry-like structure. Thereafter, a 1 cm thick layer of the mixture was poured onto a glass dish (Petri dish perhaps?), which was placed in a stove at 60 °C for 2 days to induce evaporation of water. The resulting dry material was pyrolyzed at 1050°C in an Ar atmosphere for 2 h. The Ag/C nanocomposite material that was formed was then ball milled in a Retsch Mixer Mill MM 400 for 10 min at 15 Hz, using a 10-ml zirconia jar and two 12-mm diameter zirconia

balls to obtain a powder with an average particle size of 12 μm (Figure 3.12). A pure C material was also prepared for comparison purposes following the same procedure described above but without carrying out the impregnation step in the silver nitrate solution.

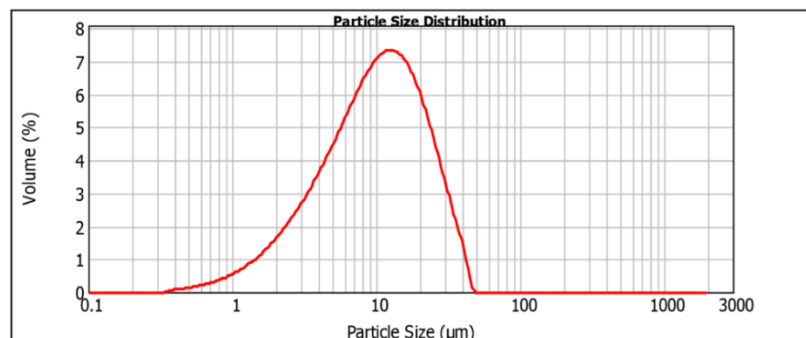


Figure 3.12. Graph of the particle size distribution of the Ag/C powder after ball milling.

3.3.2 Structural and morphological characterization

SEM images of the Ag/C nanocomposite recorded at different magnifications, shown in Figure 3.13 A, reveal the presence of uniformly distributed small bright spherical particles on the surface of a dark matrix or embedded in it. The bright contrast of the spherical particles indicates the presence of Ag metal while the darker matrix can be attributed to carbon. Particle size distributions obtained from the SEM images indicate that the sizes of these small bright particles were in the range of 25 to 40 nm (Figure 3.13 B). The EDX analysis revealed a mass ratio of Ag to C of around 1:3 (Figure 3.14 and Table 3.4).

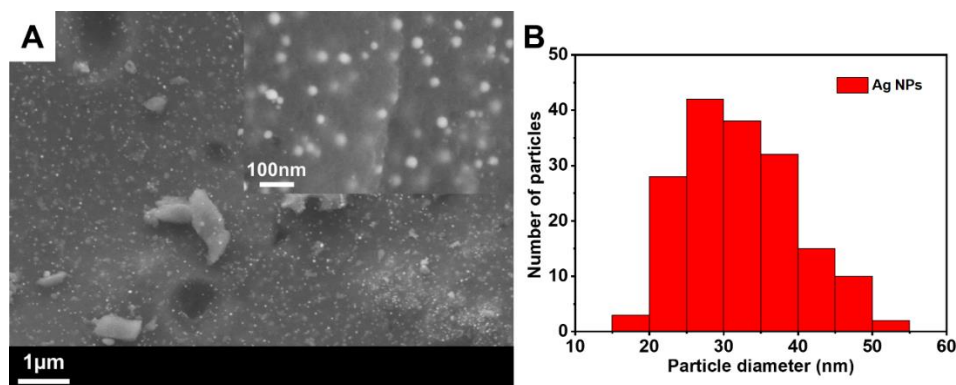


Figure 3.13. (A) Secondary electron SEM images of Ag/C nanocomposite. The inset shows a higher magnification image of the same sample. (B) the particle size distribution histogram of Ag NPs in the Ag/C composite material.

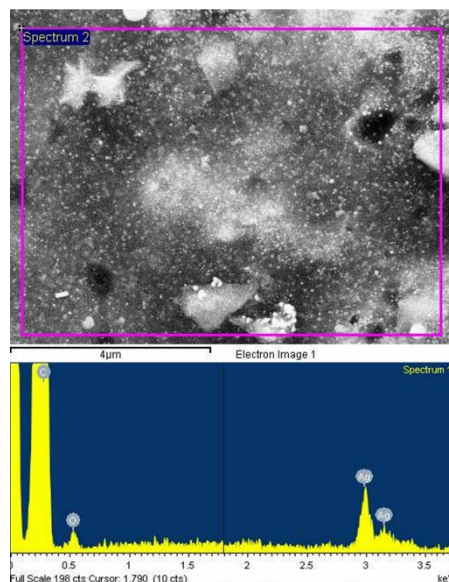


Figure 3.14. Energy dispersive X-ray (EDX) spectra of Ag/C composite. The EDX analysis revealed silver (Ag) and carbon (C) as the major chemical elements in the material.

Table 3.4 The major chemical element ratios in the Ag/C composite material.

Element	wt. %	at. %
C	68.57	88.63
Ag	23.15	3.33
O	8.29	8.04

Nitrogen adsorption and desorption isotherms of the Ag/C composite material (Figure 3.15 A) indicated the presence of micropores (<2 nm), mesopores (2-50 nm) and macropores (50-7500 nm), according to the BET model, the slope and the shape of the adsorption curve.^{20,23} The surface area of Ag/C nanocomposite was calculated to be $11.58 \pm 0.03 \text{ m}^2 \cdot \text{g}^{-1}$ (Table 3.5), with a total pore volume of $0.015 \pm 0.002 \text{ cm}^3 \cdot \text{g}^{-1}$ according to the nitrogen adsorption at a relative pressure P/P_0 of ca. 0.995. The BJH pore size distribution curve obtained from the adsorption isotherm confirmed the existence of pores mostly in the micropore and mesopore scale with a small proportion of macropores. From the characterization of the porosity of pure C made from bread waste, a surface area of $8.55 \pm 0.03 \text{ m}^2 \cdot \text{g}^{-1}$ and a total pore volume of $0.012 \pm 0.001 \text{ cm}^3 \cdot \text{g}^{-1}$ were obtained (Figure 3.15 B and Table 3.5). The incorporation of silver particles slightly increases the porosity of the

composite, which has a positive effect on the targeted application of the material as the electrochemical working electrode.

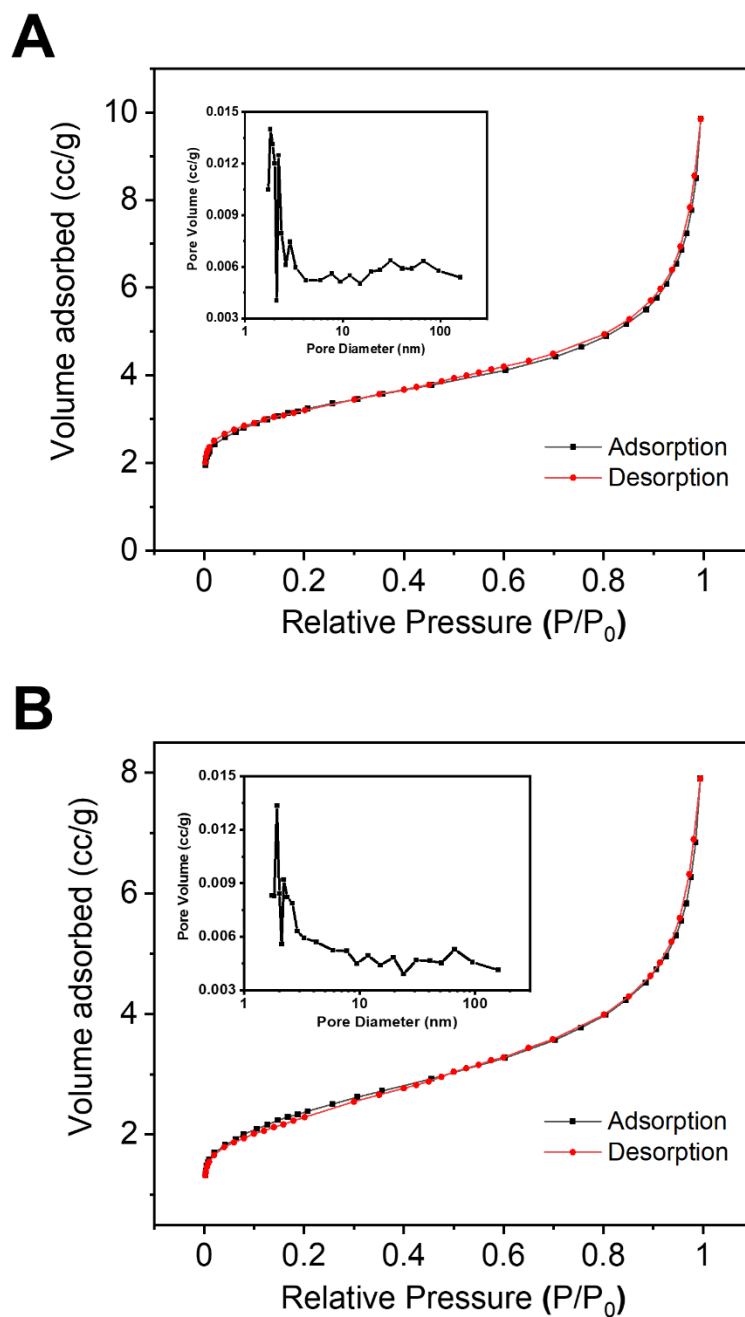


Figure 3.15. N_2 adsorption and desorption isotherms of the, (A) Ag/C and (B) pure C composites. Inset shows the pore size distribution determined using the BJH method.

Table 3.5. Textural properties of pure C and Ag/C composite made from bread.

Sample	Ag/C composite	pure C
surface area (m^2g^{-1})	11.58 ± 0.03	8.55 ± 0.03
total pore volume (cm^3g^{-1})	0.015 ± 0.002	0.012 ± 0.001

The Ag/C nanocomposite and the pure C material were also studied by XRD (Figure 3.16). For both materials, the diffractograms present a broad bump at around $2\theta = 23.6^\circ$, which corresponds to the scattering induced by the amorphous carbon. In the pattern of Ag/C composite, the four peaks located at 38.1° , 44.4° , 64.6° , and 77.4° can be respectively assigned to the (111), (200), (220), and (311) planes of the face-centered cubic Ag crystalline structure. This confirms that the nanoparticles obtained during the pyrolysis consist of crystalline metallic silver.

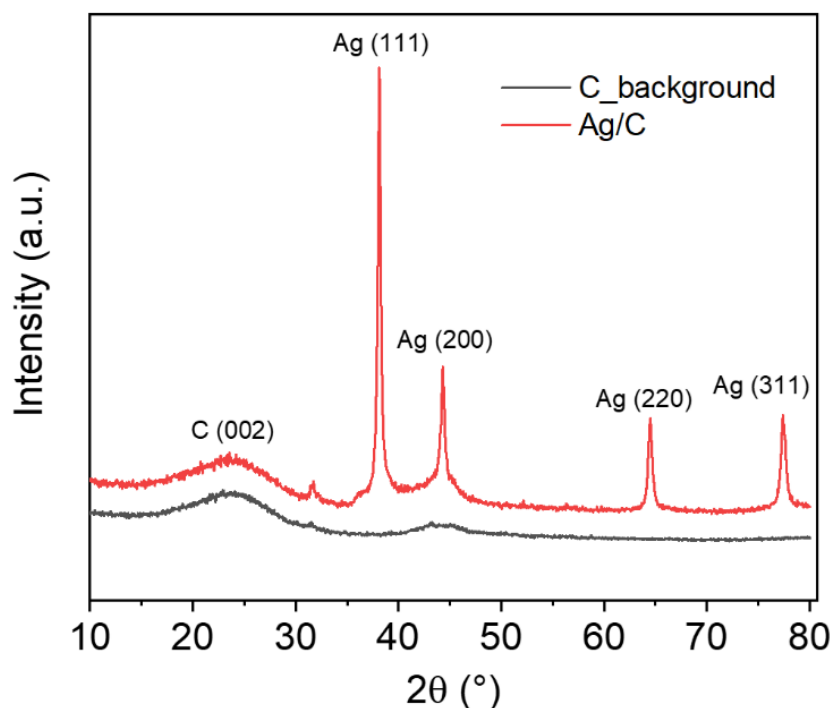


Figure 3.16. X-ray diffraction patterns of the pure C and Ag/C composite.

3.4 Synthesis of wood-derived porous carbon nanocomposites

Following the same principle of exploiting biowaste to prepare carbon nanocomposites, in this section, we describe the upscaling of wood by-products into carbon materials.

Figure 3.17 shows the optical images of the 3 types of wood by-product materials collected from the wood engineering process and provided by Dr. Amelia Arrojo from Centro Tecnológico y Forestal de la Madera (CETEMAS, Asturias). The 3 types of wood by-product materials are sourced from *Pinus Pinaster* (Maritime Pine, Figure 3.17A), *Castanea sativa* (Chestnut, Figure 3.17B), and *Quercus robur* (Oak tree, Figure 3.17C), which preserve different structural textures and compositions.²⁴ The structure and composite information of the three materials and the corresponding pyrolytic carbon materials were first studied and compared.

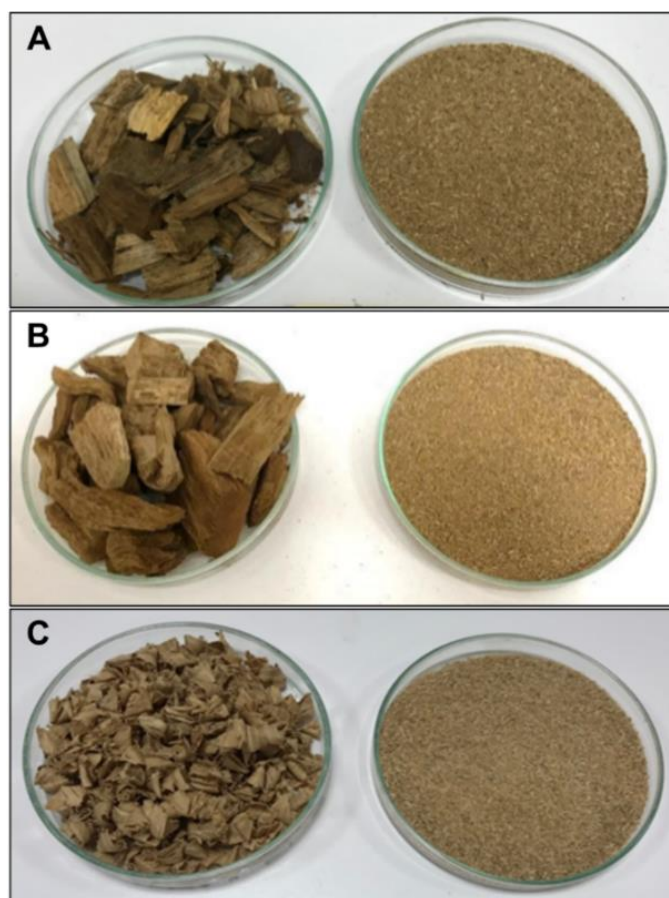


Figure 3.17. Optical images of the 3 types of wood by-product materials. (A) Pine, (B) Chestnut, (C) Oak. The sawdust (right side) size is around 1 mm and the evaporation dishes have a diameter of 14 cm.

The wood by-product materials were processed as sawdust with a size of around 1 mm (Figure 3.17, right side). Then the sawdusts were carbonized at 1050°C for 2 h at the Ar condition. Afterward, the pyrolyzed material was ball-milled in a Retsch Mixer Mill MM 400 using a zirconia jar (10 mL) and 2 zirconia balls (12 mm in diameter) to obtain a powder with an average particle size of around 10 μm (Figure 3.18 and 3.19).



Figure 3.18 Optical image of the carbon powder derived from wood material.

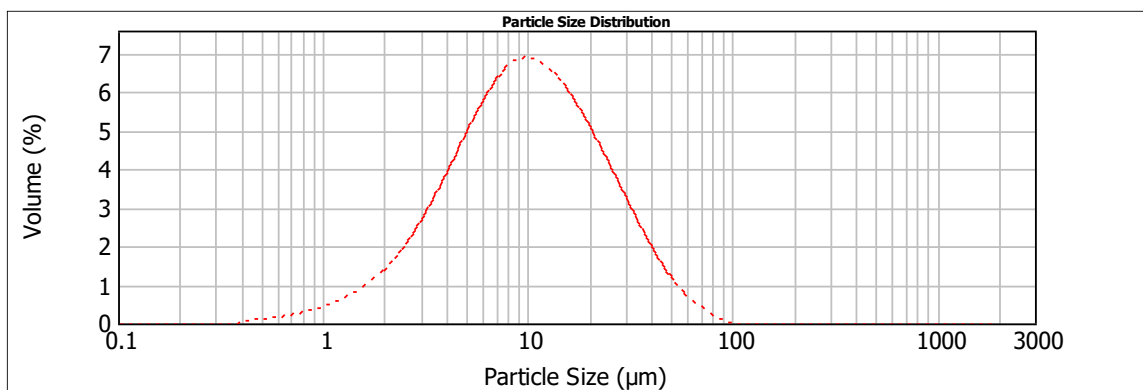


Figure 3.19. Particle size distribution of the wood-derived C powder after ball-milling.

Figure 3.20 shows SEM images of the 3 resulting carbon materials, which are respectively labeled as C_p (carbon derived from the Pine tree), C_c (carbon derived from the Chestnut tree), and C_o (carbon derived from the Oak tree). The three carbon materials show different textures that are reminiscent of their initial assembled fibrous structure, displaying surfaces with plenty of crackings and wrinkles.

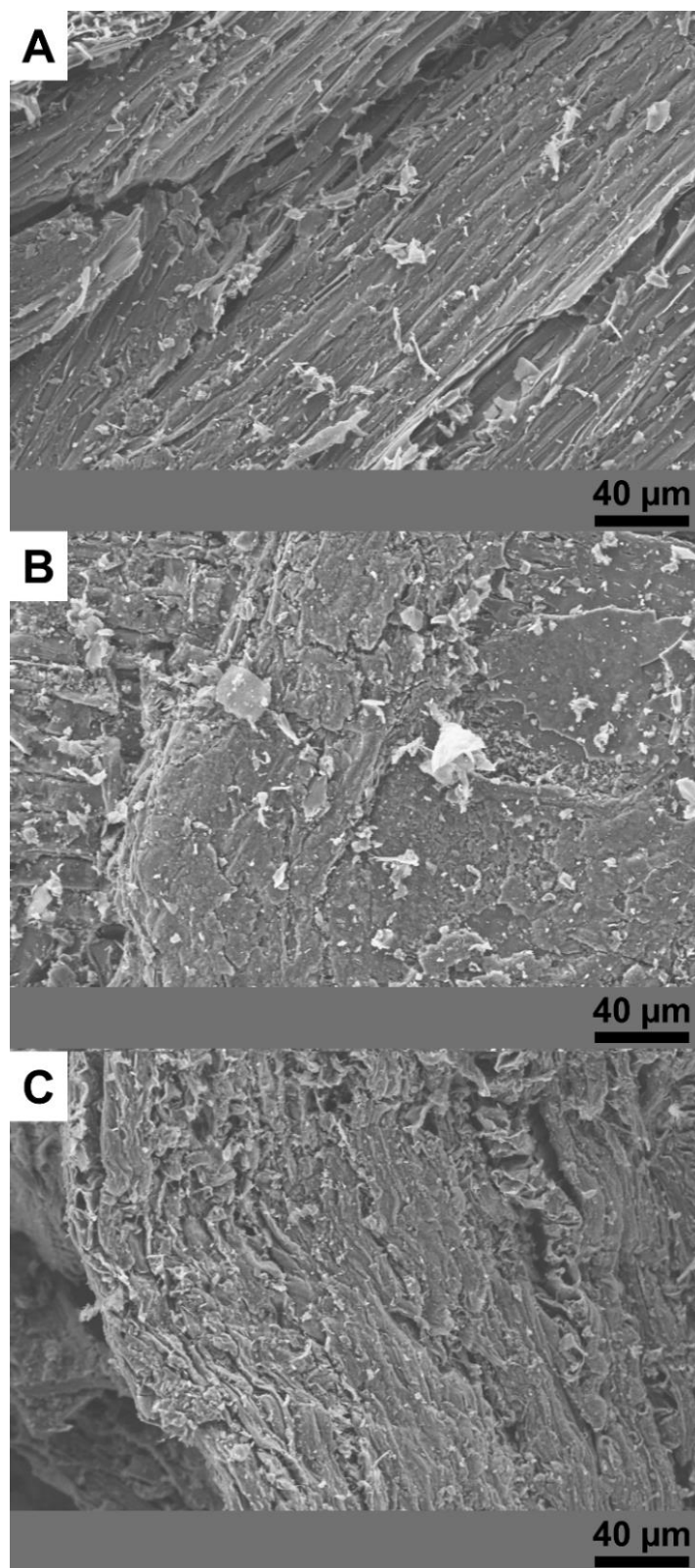


Figure 3.20. SEM images of the 3 types of carbon materials derived from wood by-product materials. (A) C_p , (B) C_c and (C) C_o .

Wood is mostly composed of lignocellulose, comprising hemicellulose, cellulose and lignin.²⁵ The relative mass content of these biopolymers can be quantitatively analyzed by the thermogravimetric (TG) method thanks to their distinct characteristic thermal decomposition temperatures.^{26,27} We performed the TG analysis (Figure 3.21, black curves) obtaining the corresponding thermogravimetric (DTG) curves (Figure 3.21, red curves). These are quite similar for the 3 samples. An initial mass loss of less than 5 % associated with the loss of moisture is observed between around 25°C and 120°C. Between 170°C and 375°C, the curves display a significant (~60 %) and steep loss of mass. Then, above this temperature, the mass continues to decrease steadily but at a decreased rate up to about 800°C where it tends to level off. From the DTG signals, one can clearly distinguish two fast decomposition processes occurring in the 170°C-375°C range which together with the more sluggish mass loss observed at higher temperatures can account for the thermal decomposition of the three biopolymers contained in wood. Indeed, these results are in accordance with the previously published literature, which concluded that the woody biopolymer with the lowest thermal stability is hemicellulose, followed by the thermal decomposition of cellulose and finally by the one of the lignin at higher temperatures.²⁶⁻²⁹

In order to assess the woody biomass composition, the DTG curves were deconvoluted with three Gaussian peaks correspondingly associated with the three lignocellulosic components (Figures 3.22A, 3.22C and 3.22E).^{26,27} The different fractions of lignocellulosic components in each sample were obtained from areas of each Gaussian contribution and normalized to the total area of lignocellulosic decompositions in the DTG curves. The obtained results, summarized in Table 3.6, indicate that Chestnut wood presents the lowest hemicellulose content, with 33% lignocellulose, while this value increases to about 51% for the Oak wood.

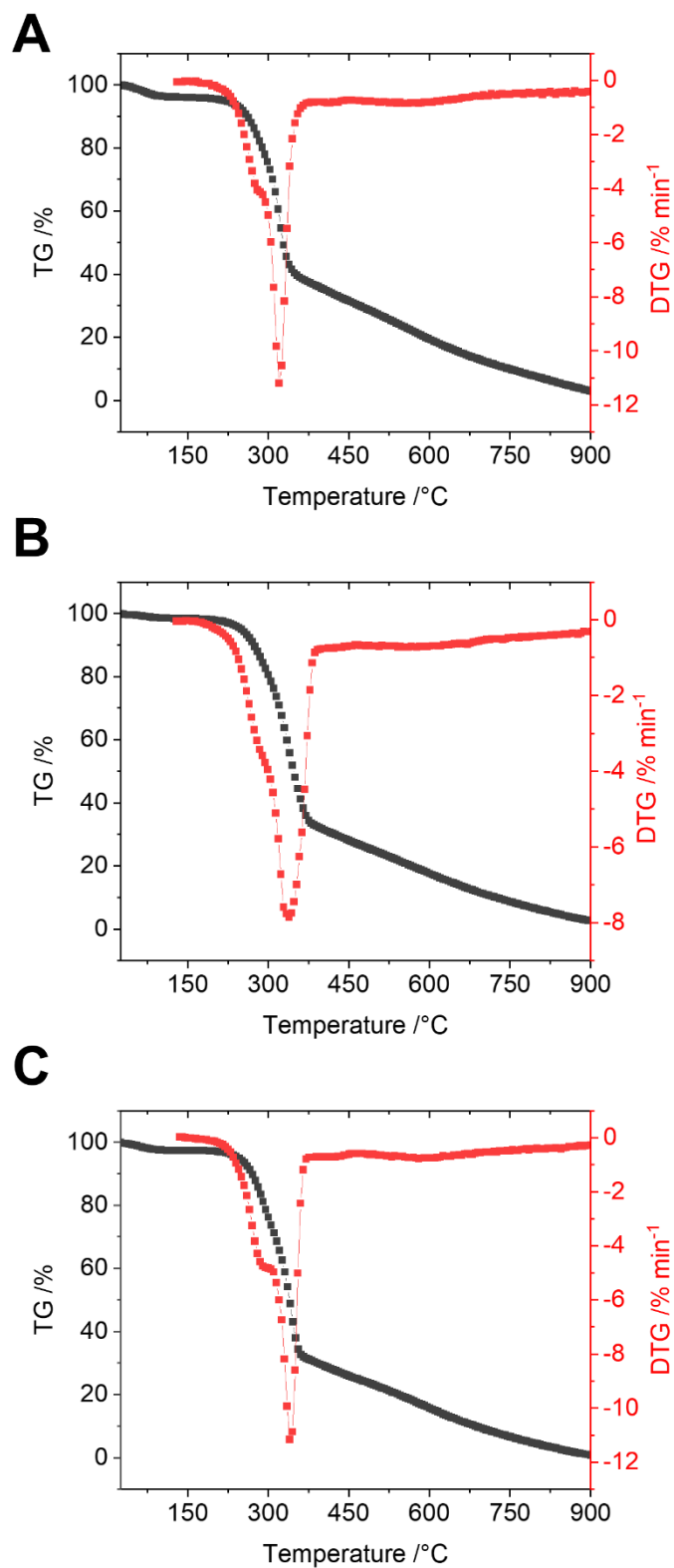


Figure 3.21. TG curves (black) and DTG curves (red) of the three wood by-product materials.

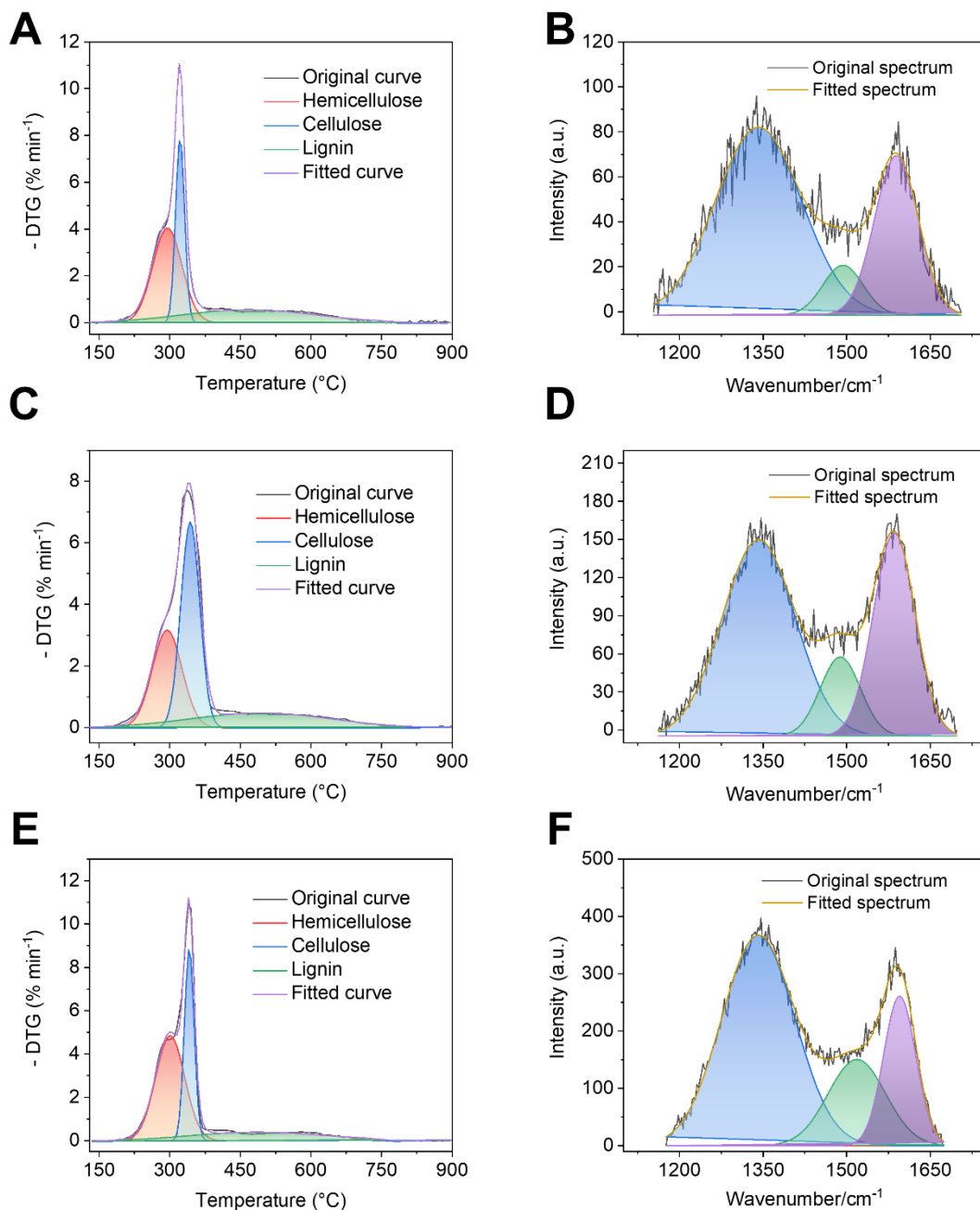


Figure 3.22. Deconvoluted DTG profile (A, C, E) of the three wood by-product materials and the Raman spectrum (B, D, F) of the corresponding derived carbon materials. Pinus Pinaster (A), C_p (B), Chestnut (C), C_c (D), Oak (E), and C_o (F).

Figure 3.22B, 3.22D and 3.22F show Raman spectroscopy measurements of the three carbon materials obtained from wood. All spectra present two broad bands centered at around 1585 cm⁻¹ and 1340 cm⁻¹. The first band (G band) corresponds to the E_{2g} mode of graphite and is associated with the sp² coordinated carbon while the second (D band) is

known to progressively arise when the graphite crystallinity decreases and has been related to the appearance of sp^3 carbon.³⁰ To satisfactorily fit the spectra, three Gaussian LorenCross functions were needed, with one additional band at around 1500 cm^{-1} (Figure 3.22B, 3.22D and 3.22F). From the deconvolution, we evaluated the ratios of the G and D bands integrated peak intensities (I_G/I_D), known to present a positive correlation with the electronic conductivity.³¹ The I_G/I_D ratios of the C_c , C_p and C_o carbons respectively obtained from Chestnut, Pine and Oak decrease in the following order $C_c > C_p > C_o$ (Table 3.6)

Table 3.6. Comparison of the characterization results from TG analyses, Raman spectrum analyses, BET analyses and electrochemical measurements.

		C_p	C_c	C_o
TG analysis	Percentage of hemicellulose in the wood by-product material	45%	33%	51%
	Percentage of cellulose + lignin in the wood by-product material	55%	67%	49%
Raman spectrum analysis	I_G/I_D	0.43	0.59	0.31
BET analysis	Surface area (m^2g^{-1})	31.0 ± 0.2	32.8 ± 0.1	18.9 ± 0.1
	Total pore volume ($\cdot 10^{-3}\text{ cm}^3\text{g}^{-1}$)	31 ± 1	41 ± 1	22 ± 1

Figure 3.23 shows the nitrogen adsorption and desorption isotherms and pore size distributions of three produced carbon materials. A gradual increase in adsorption occurs up to $P/P_0 \sim 1$, which indicates the porosity of the produced material.²⁰ Based on the BET model and the nitrogen adsorbed at P/P_0 of ca. 0.995, the surface areas and the total pore volume of the three composites are shown in Table 3.6. The BJH pore size distribution curves (Figure 3.23) obtained from the adsorption isotherm confirmed the existence of micropores ($< 2\text{nm}$), mesopores ($2\text{-}50\text{ nm}$) and macropores ($50\text{-}7500\text{ nm}$). In addition, we find the surface area and total pore volume of three carbon materials have this order: $C_c > C_p > C_o$, which could be ascribed to the unique structure and complex designs of nature of the trees.^{32,33} The absence of overlap and irreversibility of the adsorption and desorption

isotherms at low pressure may indicate nitrogen interaction with the material surface or elastic deformation of the material with increasing pressure.^{21,23}

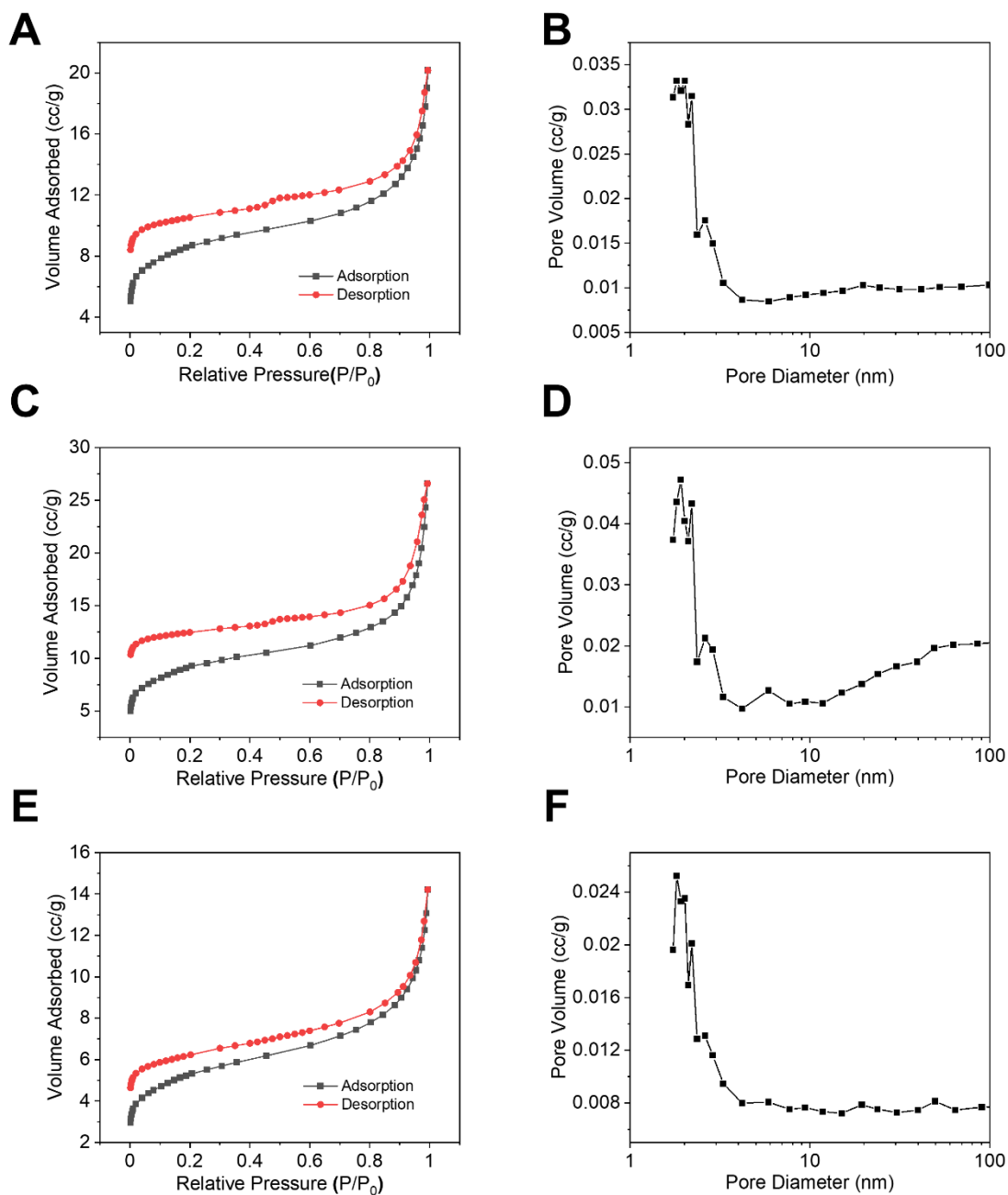


Figure 3.23. N_2 adsorption and desorption isotherms (A, C and E) and pore size distributions (B, D and F) of C_p (A and B), C_c (C and D) and C_o (E and F) materials.

3.5 Conclusions

Three composites comprising a porous carbon matrix with Cu or Cu₂O nanoparticles were successfully synthesized by combined sol-gel and pyrolysis processes. A thorough characterization of the materials evidenced different structures and morphology. A Ag/C nanocomposite was synthesized via high-temperature pyrolysis of a silver-containing dried bread paste, prepared by impregnating bread waste with a silver precursor solution. The generated functional Ag NPs were uniformly distributed in the carbon matrix. Three different porous carbon materials derived from wood by-products were also produced by a pyrolysis process. They show different textures, with plenty of cracks and wrinkles. The lignocellulosic composition of the three wood materials shows a correlation with the structural properties of the resulting carbon materials.

The electrochemical performance of these materials for the monitoring of water pollutants is presented in the following chapters using carbon paste and screen-printed electrode configurations.

References

1. Ferrari AG, Elbardisy HM, Silva V, Belal TS, Talaat W, Daabees HG, Banks CE, Brownson DA. The influence of lateral flake size in graphene/graphite paste electrodes: an electroanalytical investigation. *Analytical Methods*. 2020;12(16):2133-42.
2. McCreery RL. Advanced carbon electrode materials for molecular electrochemistry. *Chemical reviews*. 2008 Jul 9;108(7):2646-87.
3. Oztekin Y, Tok M, Bilici E, Mikoliunaite L, Yazicigil Z, Ramanaviciene A, Ramanavicius A. Copper nanoparticle modified carbon electrode for determination of dopamine. *Electrochimica Acta*. 2012 Aug 1;76:201-7.
4. Emir G, Dilgin Y, Ramanaviciene A, Ramanavicius A. Amperometric nonenzymatic glucose biosensor based on graphite rod electrode modified by Ni-nanoparticle/polypyrrole composite. *Microchemical Journal*. 2021 Feb 1;161:105751.
5. Felix S, Kollu P, Raghupathy BP, Jeong SK, Grace AN. Electrocatalytic oxidation of carbohydrates and dopamine in alkaline and neutral medium using CuO nanoplatelets. *Journal of Electroanalytical Chemistry*. 2015 Feb 15;739:1-9.
6. Marioli JM, Kuwana T. Electrochemical characterization of carbohydrate oxidation at copper electrodes. *Electrochimica Acta*. 1992 Jun 1;37(7):1187-97.
7. Diksy Y, Rahmawati I, Jiwanti PK, Ivandini TA. Nano-Cu modified Cu and nano-Cu modified graphite electrodes for chemical oxygen demand sensors. *Analytical Sciences*. 2020:20P069.
8. Cao P, Zhao K, Quan X, Chen S, Yu H. Efficient and stable heterogeneous electro-Fenton system using iron oxides embedded in Cu, N co-doped hollow porous carbon as functional electrocatalyst. *Separation and Purification Technology*. 2020 May 1;238:116424.
9. Li X, Min X, Hu X, Jiang Z, Li C, Yang W, Zhao F. In-situ synthesis of highly dispersed Cu-Cu₂O nanoparticles on porous carbon for the enhanced persulfate activation for phenol degradation. *Separation and Purification Technology*. 2021 Dec 1;276:119260.

10. Chen W, Fu X, Chan WP, Veksha A, Lisak G. Carbon nanosheet-carbon nanocage encapsulated Cu composite from chemical vapor deposition of real-world plastic waste for tailored CO₂ conversion to various products. *Applied Materials Today*. 2021 Dec 1;25:101207.
11. Lou YY, Fontmorin JM, Amrane A, Fourcade F, Geneste F. Metallic nanoparticles for electrocatalytic reduction of halogenated organic compounds: A review. *Electrochimica Acta*. 2021 May 1;377:138039.
12. Qian D, Li W, Chen F, Huang Y, Bao N, Gu H, Yu C. Voltammetric sensor for trichloroacetic acid using a glassy carbon electrode modified with Au@ Ag nanorods and hemoglobin. *Microchimica Acta*. 2017 Jul;184(7):1977-85.
13. Bashami RM, Soomro MT, Khan AN, Aazam ES, Ismail IM, El-Shahawi MS. A highly conductive thin film composite based on silver nanoparticles and malic acid for selective electrochemical sensing of trichloroacetic acid. *Analytica Chimica Acta*. 2018 Dec 7;1036:33-48.
14. Arai K, Kusu F, Noguchi N, Takamura K, Osawa H. Selective determination of chloride and bromide ions in serum by cyclic voltammetry. *Analytical biochemistry*. 1996 Aug 15;240(1):109-13.
15. Chiu MH, Cheng WL, Muthuraman G, Hsu CT, Chung HH, Zen JM. A disposable screen-printed silver strip sensor for single drop analysis of halide in biological samples. *Biosensors and Bioelectronics*. 2009 Jun 15;24(10):3008-13.
16. Bujes-Garrido J, Izquierdo-Bote D, Heras A, Colina A, Arcos-Martínez MJ. Determination of halides using Ag nanoparticles-modified disposable electrodes. A first approach to a wearable sensor for quantification of chloride ions. *Analytica chimica acta*. 2018 Jul 5;1012:42-8.
17. Niu P. Carbon Xerogel nanocomposite materials for electrochemical devices: application to heavy metal detection. *Universitat Autònoma de Barcelona*; 2015 Sep 18.
18. Deng J, Xiong T, Xu F, Li M, Han C, Gong Y, Wang H, Wang Y. Inspired by bread leavening: one-pot synthesis of hierarchically porous carbon for supercapacitors. *Green Chemistry*. 2015;17(7):4053-60.

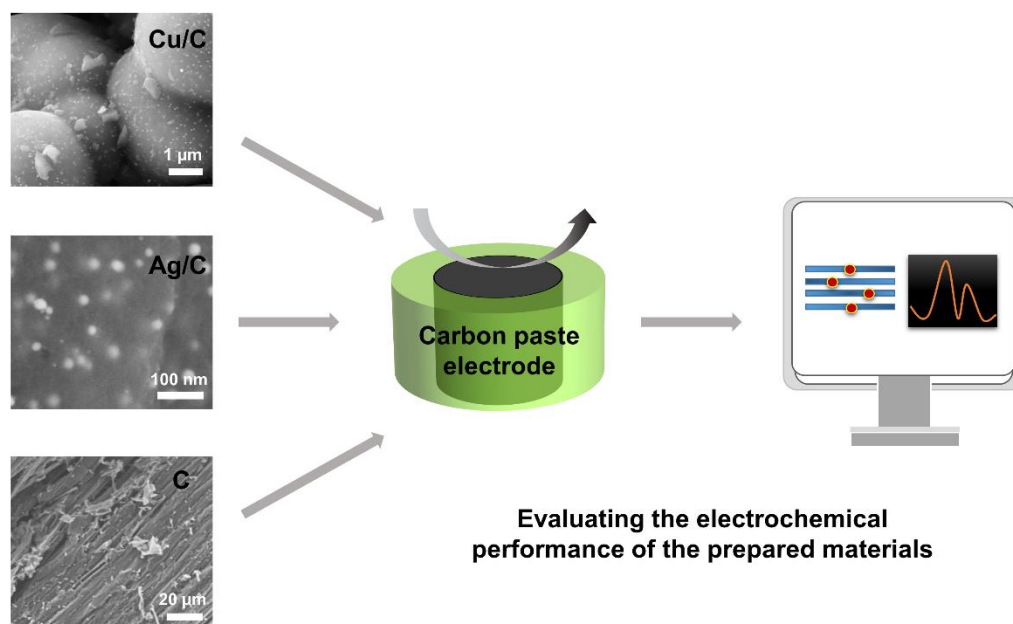
19. Torras M, Roig A. Copper Oxide Nanocubes Wrapping Metals by Microwave Synthesis. *Crystal Growth & Design*. 2021 Aug 13;21(9):5027-35.
20. Rouquerol J, Avnir D, Fairbridge CW, Everett DH, Haynes JM, Pernicone N, Ramsay JD, Sing KS, Unger KK. Recommendations for the characterization of porous solids (Technical Report). *Pure and applied chemistry*. 1994 Jan 1;66(8):1739-58.
21. Niu P, Fernández-Sánchez C, Gich M, Ayora C, Roig A. Electroanalytical assessment of heavy metals in waters with bismuth nanoparticle-porous carbon paste electrodes. *Electrochimica Acta*. 2015 May 20;165:155-61.
22. Moreno-Castilla C, Maldonado-Hódar FJ, Pérez-Cadenas AF. Physicochemical surface properties of Fe, Co, Ni, and Cu-doped monolithic organic aerogels. *Langmuir*. 2003 Jul 8;19(14):5650-5.
23. Duan W, Torras M, Roig A, Fernández-Sánchez C, Gich M. Composites of porous carbon and copper-based nanoparticles for the electrochemical analysis of chemical oxygen demand. *Materials Today Chemistry*. 2022 Jun 1;24:100899.
24. Rego F, Godinho-Ferreira P, Uva JS, Cunha J. Combination of structural and compositional factors for describing forest types using national forest inventory data. *Monitoring and Indicators of Forest Biodiversity in Europe—From Ideas to Operationality*. 2005;51:153-62.
25. Stokke DD, Wu Q, Han G. Introduction to wood and natural fiber composites. John Wiley & Sons; 2013 Oct 21.
26. Rego F, Dias AP, Casquilho M, Rosa FC, Rodrigues A. Fast determination of lignocellulosic composition of poplar biomass by thermogravimetry. *Biomass and bioenergy*. 2019 Mar 1;122:375-80.
27. Carrier M, Loppinet-Serani A, Denux D, Lasnier JM, Ham-Pichavant F, Cansell F, Aymonier C. Thermogravimetric analysis as a new method to determine the lignocellulosic composition of biomass. *Biomass and bioenergy*. 2011 Jan 1;35(1):298-307.
28. Díez D, Urueña A, Piñero R, Barrio A, Tamminen T. Determination of hemicellulose, cellulose, and lignin content in different types of biomasses by thermogravimetric analysis and pseudocomponent kinetic model (TGA-PKM method). *Processes*. 2020

Aug 27;8(9):1048.

29. Sun X, Shan R, Li X, Pan J, Liu X, Deng R, Song J. Characterization of 60 types of Chinese biomass waste and resultant biochars in terms of their candidacy for soil application. *Gcb Bioenergy*. 2017 Sep;9(9):1423-35.
30. Tuinstra F, Koenig JL. Raman spectrum of graphite. *The Journal of chemical physics*. 1970 Aug 1;53(3):1126-30.
31. Jawhari T, Roid A, Casado J. Raman spectroscopic characterization of some commercially available carbon black materials. *Carbon*. 1995 Jan 1;33(11):1561-5.
32. Tang X, Liu D, Wang YJ, Cui L, Ignaszak A, Yu Y, Zhang J. Research advances in biomass-derived nanostructured carbons and their composite materials for electrochemical energy technologies. *Progress in Materials Science*. 2021 May 1;118:100770.
33. Benny L, John A, Varghese A, Hegde G, George L. Waste elimination to porous carbonaceous materials for the application of electrochemical sensors: Recent developments. *Journal of Cleaner Production*. 2021 Mar 25;290:125759.

Chapter 4

Electroanalytical evaluation of metal nanoparticle-modified porous carbon nanocomposites for monitoring water pollutants



Summary

In this chapter, the three types of nanocomposites previously prepared, including copper-based nanoparticle-modified porous carbon, bread waste-derived Ag/C composite, and wood by-product-derived carbon material, were used to fabricate carbon paste electrodes. The electrochemical performance of the three types of materials was thoroughly evaluated through the electrochemical analysis of COD, halogenated compounds and redox species, respectively.

4.1 Introduction

4.1.1 Evaluating the performance of the nanomaterials with carbon paste electrodes

In recent years, nanomaterials have received increasing attention as potential electroanalytical probes, not only for providing an enhanced sensitivity but also for offering a stair change when being applied in the electrochemical analysis of water pollutants.^{1,2} These materials can be beneficial from their exceptional physicochemical properties, high adsorption and reactive capacity, high surface-to-volume ratio and other superior properties that are not present in the respective bulk material counterparts.^{1,2} In Chapter 3, we showed the production of nanocomposites of carbon modified with copper-based and silver nanoparticles, as well as the wood by-product-derived carbon matrix. In the present chapter, the material electrochemical performance is shown. For these studies, carbon paste electrodes (CPEs) were prepared.

CPEs can be easily prepared by mixing the functional materials with paraffin oil,³. The ease of fabrication and the low background currents that they show make them ideal in this context. Briefly, for the CPE preparation, 0.5 g of each material and 0.15 mL of spectroscopic grade liquid paraffin (Uvasol® from Merck) was mixed thoroughly to prepare a carbon paste. This paste was packed into a 3 mm-diameter well, defined at one end of a 6 mm-diameter Teflon body, into which a 3 mm diameter stainless steel rod was inserted to make the electrical contact (Figure 4.1).

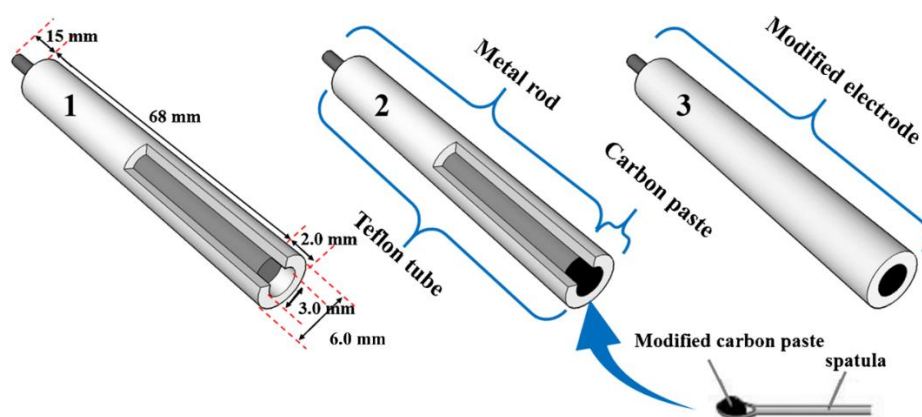


Figure 4.1. Schematic drawing of carbon paste electrode (CPE). (1) Lateral cut of the electrode with the respective scales, (2) Teflon® cylindrical tube, metal rod and the well to fill with the modified carbon paste, (3) CPE ready to use.⁴

The surface of the prepared carbon paste electrode was manually polished on A4 paper sheet. After each measurement, the carbon paste electrode was refilled with a fresh paste to ensure that all the analytical measurements were carried out under the same working conditions.

The prepared CPE was implemented in a conventional three-electrode electrochemical cell configuration, which included the 3 mm diameter carbon paste working electrode, described above, an Ag/AgCl reference electrode and a platinum counter electrode (both of them from Metrohm AG, Switzerland). An Autolab PGSTAT30 potentiostat (EcoChemie, the Netherlands) was used for all the electrochemical measurements.

4.2 Electrochemical performance of copper-based nanoparticle-modified carbon nanocomposites: analysis of chemical oxygen demand (COD)

Cyclic voltammetric experiments were performed to evaluate the electrochemical behavior of carbon paste electrodes prepared with the different composites mentioned in Chapter 3 (Figure 3.3 and Figure 3.5), including pure C (CPE_C), Cu₂O/C (CPE_{Cu₂O/C}), Cu/C_1 (CPE_{Cu/C_1}) and Cu/C_2 (CPE_{Cu/C_2}). Cyclic Voltammetry (CV) is the most common technique applied to initially assess the electrochemical performance of a device and details about it could be found in excellent electrochemistry books such as that written by Bard and Faulkner.⁵

All the voltammetric signals were recorded in a 0.1 M KNO₃ solution containing 1.0 mM ferrocene-methanol and revealed a quasi-reversible faradaic signal of the ferrocene/ferrocenium redox pair. The peak-to-peak potential separations (ΔE_p) were around 84 mV, 69 mV, 63 mV, and 68 mV for CPE_C, CPE_{Cu₂O/C}, CPE_{Cu/C_1} and CPE_{Cu/C_2}, respectively (Figure 4.2). In all cases, the ratio of the anodic to cathodic peak currents was close to one. Such values indicate good and fast electron transfer processes between the CPEs and the solution.^{5,6} In addition, peak-to-peak potential separation values (ΔE_p) obtained for pure amorphous carbon and for the nanocomposite materials (with lower ΔE_p values) indicate that the incorporation of the catalytic inorganic particles had a positive effect on the performance of the corresponding CPEs. Among them, the electrode made of Cu/C_1 presents the smallest ΔE_p value indicating a relatively faster electron transfer at the CPE solution interface.⁶⁻⁸

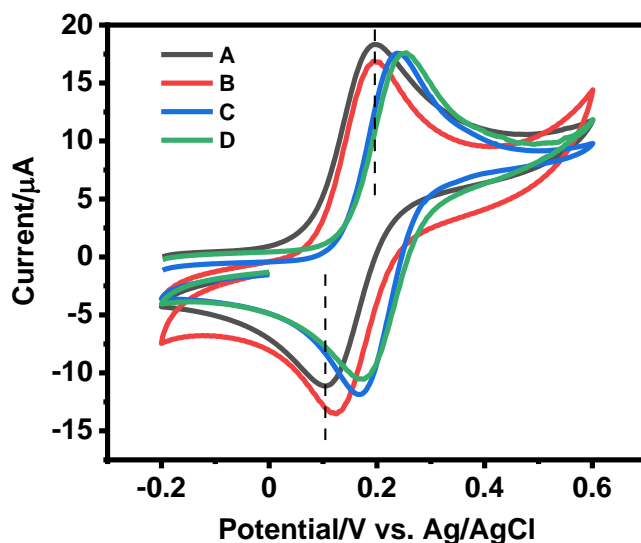


Figure 4.2. Cyclic voltammograms recorded in a 0.1M KNO_3 solution containing 1.0 mM ferrocene-methanol with the CPE sensors produced with pure C (A), $\text{Cu}_2\text{O}/\text{C}$ (B), Cu/C_1 (C) and Cu/C_2 (D). The scan rate is 100 mV s^{-1} .

4.2.1 Evaluation of the electrode response for COD analysis

The main composition of the soluble fraction of COD consists of organic molecules.⁹ Glucose is a pertinent standard analyte to be used for calibrating electrochemical sensors for COD.^{5,10–12} Thus, the CPE sensor performances were evaluated using glucose as the standard COD analyte.

First, CVs were recorded in a 0.1 M NaOH background electrolyte solution containing glucose standard analyte, in order to investigate the potential range at which the electrocatalytic oxidation of glucose took place (Figure 4.3 A and 4.3 B). From these measurements, a set potential value was chosen, at which glucose undergoes an oxidation process in order to set the conditions for applying the chronoamperometric technique for the measurement of COD.

Chronoamperometry is a time-dependent electrochemical technique in which a DC potential step is applied to the working electrode at which Faradaic processes of the target analyte under study take place. The resulting Faradaic current is monitored as a function of time and fluctuates according to the diffusion of the target from the bulk solution toward the electrode surface. A detailed description of this technique could be found in reference 5.¹³

Taking into account the well-known fact that carbon nanomaterials show good electrocatalytic performances under certain experimental conditions,^{14,15} the possible effect of the pure carbon powder on the electrocatalytic oxidation of glucose was initially tested. CPEs made of pure C were applied to record cyclic voltammetric measurements in 0.1 M NaOH solutions with and without glucose. The results presented in Figure 4.3 A reveal a negligible effect of the pure carbon material in the catalytic oxidation of glucose. Figure 4.3 B illustrates the cyclic voltammetric responses recorded with CPE_{Cu/C_1} in the absence (black curve) and presence of glucose (red curve). A clear electrocatalytic signal that is centered at around +0.6 V (vs. Ag/AgCl) is observed. From this study, an overpotential of +0.7 V was set for performing chronoamperometric measurements in solutions containing increasing glucose concentrations (Figure 4.3 C) and the current values recorded at 90 s in the chronoamperograms were used as the analytical signal. Afterward, the corresponding calibration of the CPE_{Cu/C_1} sensor was plotted (Figure 4.3 D). The extracted analytical parameters are displayed in Table 4.1.

The same process was carried out with the CPE_{Cu₂O/C} and CPE_{Cu/C_2} electrodes and the results are presented in Figures 4.4 and 4.5, and in Table 4.1. A very similar electrocatalytic performance was recorded for all the CPEs. As shown in the calibration curves and Table 4.1, the three CPES show different linear responses in a wide COD range. The wastewater treatment plants (WWTPs) have in the EU a legal limit of COD in the effluents, set to 125 mg L⁻¹ O₂,¹⁶ which falls within the linear ranges of the three CPEs studied in this work.

Table 4.1. Analytical parameters obtained from the Calibration Curves of different CPEs for COD analysis.

sensor	slope*10 ³ (μA mg ⁻¹ L ⁻¹ O ₂)	intercept (μA)	R ² (n=3)	LOD* (mgL ⁻¹ O ₂)	Linear range (mgL ⁻¹ O ₂)
CPE _{Cu₂O/C}	51.5 ± 1.1	13.2 ± 0.4	0.997	18.1	53 – 1292
CPE _{Cu/C_1}	27.1 ± 0.4	3.3 ± 0.4	0.998	25.4	53 – 1500
CPE _{Cu/C_2}	3.4 ± 0.1	2.8 ± 0.1	0.995	87.2	106 – 1500

*LOD is calculated using the 3σ IUPAC criterion.

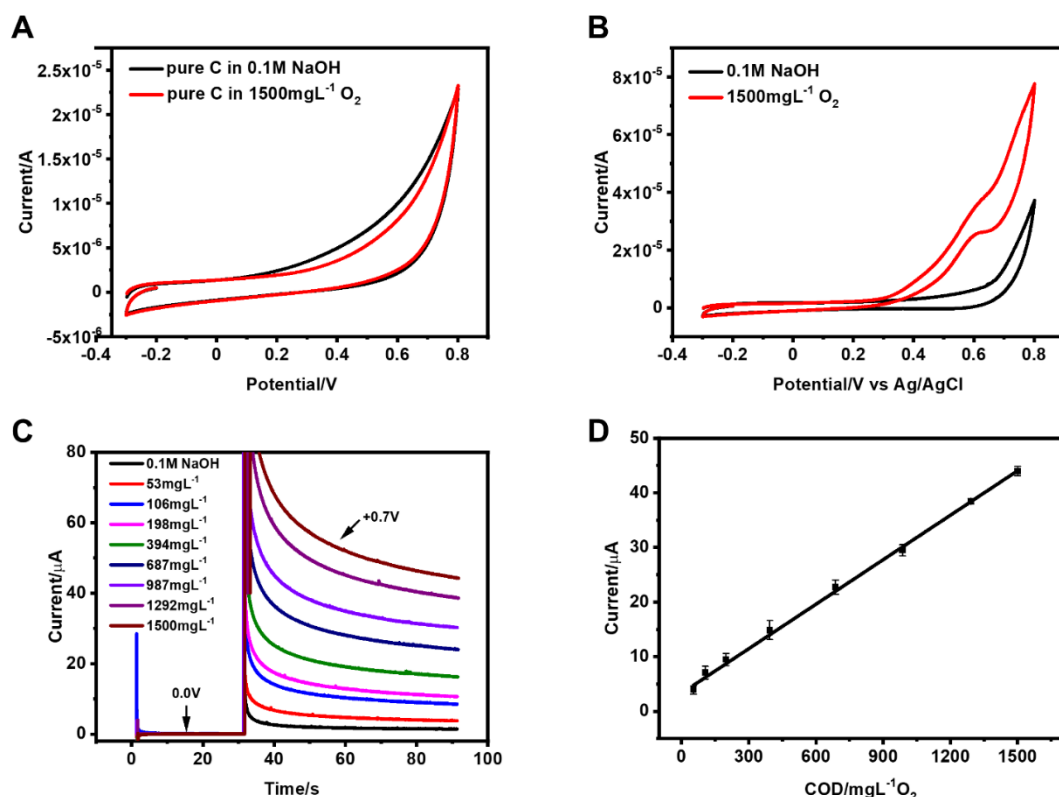


Figure 4.3. (A) Cyclic voltammograms recorded in a 0.1 M NaOH solution before and after the addition of glucose with the CPE based on the pure C powder. Scan rate = 100 mV s⁻¹. (B) Cyclic voltammograms recorded with CPE_{Cu/C_1} before (black curve) and after (red curve) the addition of glucose in a 0.1 M NaOH solution at a scan rate of 100 mV s⁻¹; (C) Chronoamperometric responses of the CPE_{Cu/C_1} recorded in solutions containing from 53 to 1500 mg L⁻¹ of O₂ (equivalent to 49.9 to 1330 mg L⁻¹ of glucose). In the chronoamperometric process, a potential of 0.0 V was initially set for 30 s, at which no redox reactions occurred and the current value tended to zero. Then, the potential was shifted to +0.7 V, at which the electrocatalytic oxidation of glucose took place and the anodic current was recorded for 60 s. (D) Calibration curve of the CPE_{Cu/C_1}. Each point represents the mean value of three measurements performed consecutively and the error bars are the corresponding standard deviation. A fresh CPE was used for each measurement.

The possible mechanism for the oxidation of organic matter by similar electrocatalysts in an alkaline medium has been previously reported.^{10,17–19} We also included a brief description of the most likely mechanism for the oxidation of organic compounds on the CPE_{Cu/C} electrode and the corresponding chemical reactions in the *Introduction* part (Chapter 1). The generation of Cu(III) radical species appears to be key in the effective electrocatalytic oxidation of organic matter in an alkaline medium. Although we have not found a paper describing the oxidation mechanism of organic matter by Cu₂O nanoparticles, we hypothesize that it could be similar to the one occurring with copper nanoparticles.

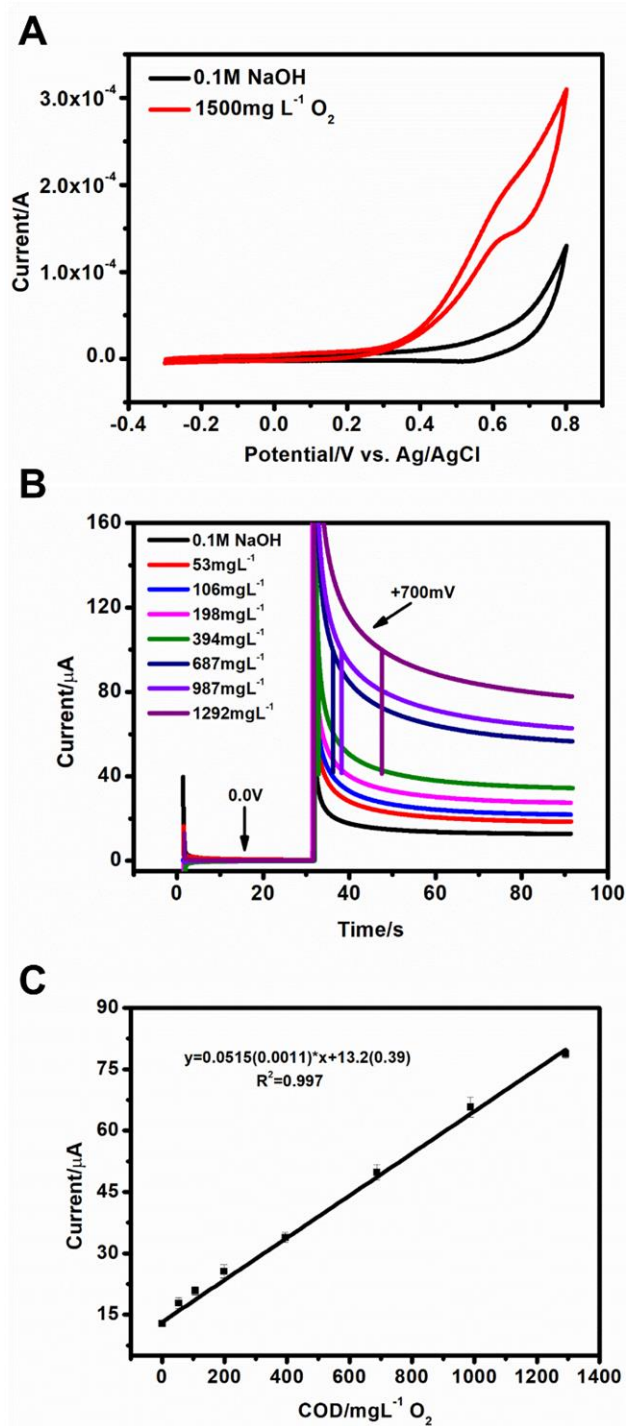


Figure 4.4. (A) Cyclic voltammograms recorded in a 0.1 M NaOH solution before and after the addition of glucose with CPE_{Cu2O/C} at a scan rate of 100 mV s⁻¹; (B) Chronoamperometric responses of the CPE_{Cu2O/C} recorded in solutions containing from 0 to 1292 mg L⁻¹ of O₂; (C) Calibration curve of the CPE_{Cu2O/C}. Each point represents the mean value of three measurements performed consecutively and the error bars are the corresponding standard deviation. A fresh CPE was used for each measurement.

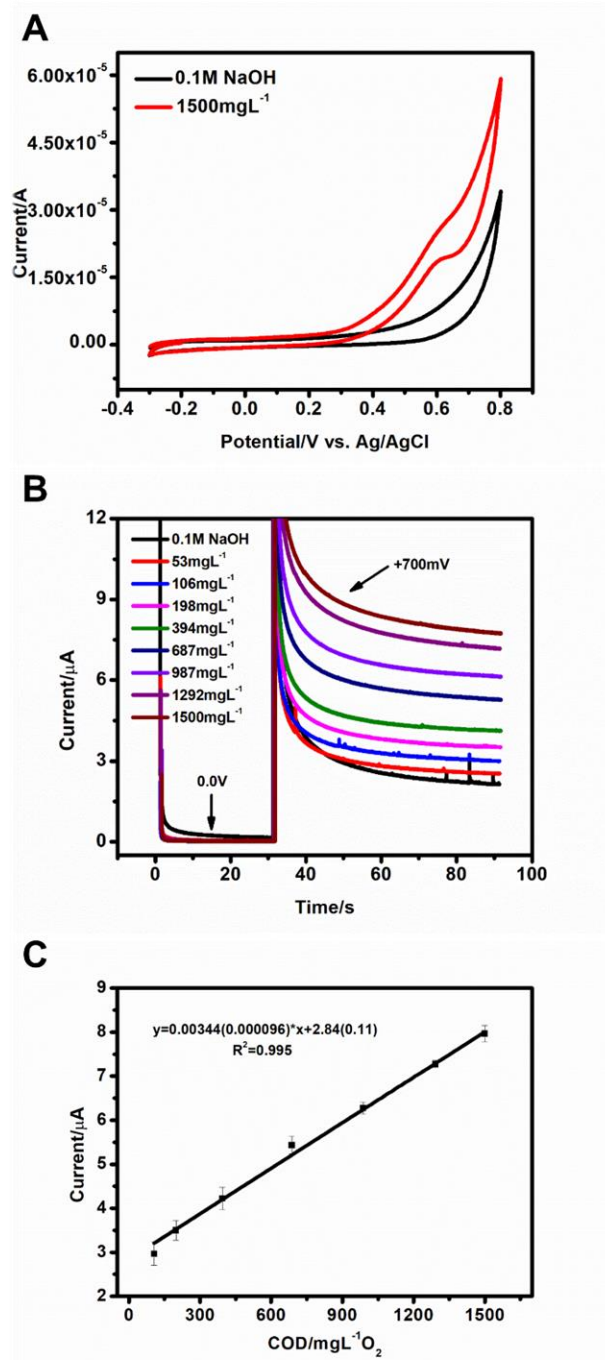


Figure 4.5. (A) Cyclic voltammograms recorded in a 0.1 M NaOH solution before and after the addition of glucose with CPE_{Cu/C₂} at a scan rate of 100 mV s⁻¹; (B) Chronoamperometric responses of the CPE_{Cu/C₂} recorded in solutions containing from 0 to 1500 mg L⁻¹ of O₂; (C) Calibration curve of the CPE_{Cu/C₂}. Each point represents the mean value of three measurements performed consecutively and the error bars are the corresponding standard deviation. A fresh CPE was used for each measurement.

The electrochemical performance reproducibility was studied by recording triplicate measurements using three freshly prepared CPEs with the same batch material. Relative standard deviations are below 5%, indicating good reproducibility of measurements. Thus, the analytical performance in standard glucose solutions makes the presented materials promising for the analysis of COD in wastewater.

4.2.2 Analysis of the wastewater samples

Three sets of real water samples were collected at the wastewater treatment plant (WWTP) of La Garriga (Barcelona, Spain) and kindly provided to us by Josefina Torán and Mercè Baldi. Upon receiving them, the samples were filtered by OlimPeak filters having a Nylon membrane of 0.45 μm pore size (Teknokroma, TR-200100) and immediately frozen at -20°C . The electrochemical analysis of the wastewater sample was completed within the next two weeks upon reception. The pH of these three samples was *circa* 7. To carry out the measurements, they were thawed and diluted with a 0.2 M NaOH solution to a ratio of 1:1, unless stated otherwise. Chronoamperometric measurements were performed in the resulting solutions. The current values recorded at 90 s in the chronoamperogram were interpolated in the corresponding calibration curve to obtain the COD value. COD analysis was also carried out using the dichromate standard method in an accredited laboratory (Laboratori Ambiental, Mina Pública Aigües de Terrassa, Terrassa, Spain), for comparative purposes.

The samples collected at the WWTP were from the pretreatment effluent, the clarifier effluent and the effluent at the plant exit. The values estimated with the three CPE sensors were compared with those measured with the standard dichromate method and the results are shown in Table 4.2. It can be seen that the $\text{CPE}_{\text{Cu}_2\text{O}/\text{C}}$ sensor shows superior performance and that the COD values of the three collected samples could be measured. By contrast, the $\text{CPE}_{\text{Cu}/\text{C}_2}$ sensor shows the poorest performance since two of the samples could not be measured under the set experimental conditions, meaning that those samples presented COD values below the limit of detection of the sensor. By comparing the sensor limit of detection (LOD) and the COD values of those samples provided by the standard method, it is clear that this material is not suitable for the development of commercial COD sensors to be applied in WWTPs.

The $\text{CPE}_{\text{Cu}/\text{C}_1}$ sensor shows a limit of detection that is well below the COD concentration

measured in the effluent sample by the standard method. However, since the sample was diluted 1:1 in 0.2 M NaOH solution (see experimental section), the concentration to be measured by the sensor falls below the limit of detection, and accordingly, no signal was detected. However, sample conditioning can be carried out using more concentrated NaOH solutions so that the sample is diluted to a less extent. This was carried out to better assess the performance of the CPE_{Cu/C_1} sensor. Indeed, the sample conditioning was carried out by diluting the three water samples in a 0.4 M NaOH solution at a volume ratio of 3:1. Even though a higher matrix effect could take place the COD was thus successfully analyzed with the CPE_{Cu/C_1} sensor even in the three samples, as shown in Table 4.2.

Table 4.2. COD detection of real water samples using CPE sensors and standard dichromate method.

Sample	$CPE_{Cu_2O/C}$ ($mgL^{-1}O_2$)	CPE_{Cu/C_1} ($mgL^{-1}O_2$)	CPE_{Cu/C_1} ($mgL^{-1}O_2$) [3:1 dilution]*	CPE_{Cu/C_2} ($mgL^{-1}O_2$)	Dichromate method ($mgL^{-1}O_2$)
1_ effluent	44 ± 7 (+19.4%)	out of detection range	40 ± 10 (+6.2%)	out of detection range	37 ± 8
2_ clarifier effluent	103 ± 9 (+21.3%)	98 ± 3 (+15.3%)	93 ± 9 (+9.8%)		85 ± 18
3_ pretreatment effluent	225 ± 5 (+7%)	223 ± 8 (+6.1%)	216 ± 12 (+3%)	216 ± 23 (+2.8%)	210 ± 25

* 3:1 dilution means that the samples were diluted in a 0.4 M NaOH solution at a volume ratio of 3:1.

As above, three measurements for the real sample analysis were performed using three freshly-prepared CPEs. The corresponding errors included in Table 4.2 are comparable to those associated with the standard dichromate method, revealing the good reproducibility of our sensor in the analysis of real water samples. Regarding the accuracy, the response of the produced sensors to COD is in good agreement with the COD values provided by the standard method.

Table 4.3. Previously reported data on the development and analytical performance of the COD electrochemical sensors.

Electrode type	Sensor fabrication	Linear range (mg L ⁻¹)	Sensitivity (μA mg ⁻¹ L ⁻¹)	limit of detection (mg L ⁻¹)	Ref
Home-made Screen printed electrode	Electrodeposition of Ni nanoparticles	0.1 – 400	6.107	0.02	23
CuO/Cu electrode (copper rod)	Electrochemical oxidation	50 – 1000	9.17*10 ⁻³	2.11	10
Copper electrical cable and pure Cu disk	Electrodeposition of nano_Cu film	2 – 595	3*10 ⁻⁴	2.4	18
Glassy carbon electrode	Electrodeposition of nano-copper	15 – 629	1.7	1.7	17
Cu wire	Electrodeposition of nano-copper	17.45 – 176	1.16	9.02	24
Graphite electrode	Electrodeposition of nano-copper	32 – 256	1.04	8.9	24
Electrochemical nanocomposite-derived sensor	CuO/AgO	53 – 1292	6.8*10 ⁻³	28	5
Carbon paste electrode	Physical mixing of Cu ₂ O NPs with C powder	53 – 1292	51.5*10 ⁻³	18.1	This work
Carbon paste electrode	One-pot method to prepare Cu/C ₁ composite	53 – 1500	27.1*10 ⁻³	25.4	

If we consider the COD value from the standard dichromate method as the “true” value, the sensor relative errors were calculated and are shown in Table 4.2 (values in red). It should be noted that the errors obtained with the CPE_{Cu/C₁} sensor applying the 3:1 dilution are less than 10% and comparable to the ones reported with other similar materials in the analysis

of real samples.¹²

As discussed above, $\text{CPE}_{\text{Cu}_2\text{O}/\text{C}}$ displayed the highest sensitivity and the lowest LOD of the three sensor approaches. This better performance might be related to the cubic geometry of Cu_2O nanoparticles, exposing specific crystalline planes with enhanced electrocatalytic activity, or to the increased presence of edges and corners, which could be the active sites to generate more hydroxyl radicals enhancing the efficiency to oxidize glucose.^{20–22} In spite of the fact that the copper nanoparticles in $\text{CPE}_{\text{Cu}/\text{C}_1}$ are smaller in size and are well distributed in the carbon matrix, $\text{CPE}_{\text{Cu}/\text{C}_1}$ exhibits a lower sensitivity and higher LOD, indicating that the particle geometry plays a more relevant role in the nanoparticle electrocatalytic behavior than its size. Let's finally note that since both $\text{CPE}_{\text{Cu}/\text{C}_1}$ and $\text{CPE}_{\text{Cu}/\text{C}_2}$ present similar amounts of Cu NPs of comparable sizes, the superior electrochemical performance of the former is likely related to its globular microstructure, which results in a larger surface area of macropores.

For comparative purposes, the analytical parameters of previously reported COD sensors making use of catalysts of the same nature are summarized in Table 4.3. In terms of analytical performance, some of these previously reported sensors show superior features compared with the ones presented here. However, in all those works the sensor fabrication involved nanoparticle electrodeposition or nanoparticle casting onto the surface of a commercial or previously-fabricated electrode. Such processes can hardly be adapted to a mass-production scenario, being a clear drawback for efficient large-scale industrial sensor production.

4.3 Electrochemical performance of silver nanoparticle-modified carbon nanocomposites: analysis of halides and organohalides

Cyclic voltammetric experiments were performed to evaluate the electrochemical behavior of CPEs prepared with the Ag/C composites described in Chapter 3 (Figure 3.13A). The produced electrodes were labeled as $\text{CPE}_{\text{Ag}/\text{C}}$.

4.3.1 Halide detection

Figure 4.6 shows a cyclic voltammogram (CV) recorded with the $\text{CPE}_{\text{Ag}/\text{C}}$ in 0.075 M phosphate buffer (PB) background solution (pH = 6.0) that visualizes the electrodic redox process that the AgNPs underwent. Two anodic peaks at +0.37 V (a_1) and +0.49 V (a_2), and

one cathodic peak centered at around 0 V (c_1) were recorded. The a_1 and a_2 can be ascribed to the formation of Ag_2O and AgO , respectively, in agreement with the reported literature.^{25–27} The c_1 may be related to the reduction of the Ag oxides and the formation of Ag^0 species on the electrode surface.^{25–27}

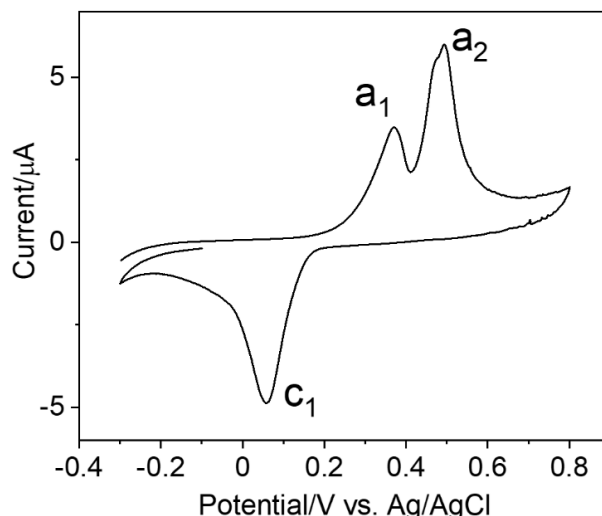


Figure 4.6. Cyclic voltammogram in PB solution (pH = 6.0) using the $\text{CPE}_{\text{Ag/C}}$ at scan rate of 100 mVs^{-1} .

The performance of $\text{CPE}_{\text{Ag/C}}$ was initially studied in the detection of halide ions. Figure 4.7 shows the CVs recorded in PB solutions of different pHs containing 0 and 5 mM Cl^- . The oxidation peaks at around 0.4 V and 0.5 V, which for most of the studied pH conditions appear in the CVs recorded in the absence of Cl^- (black curves) can be ascribed to the production of Ag oxides, described above.²⁵ In the presence of Cl^- (red curves), the oxidation peak at around +0.2 V is due to the reaction between Ag and Cl^- .^{28,29} The peaks related to the formation of Ag oxides became smaller when Cl^- was added to the electrolyte at pH 1.6, 6.0 and 7.5. This is because the formation of AgCl took place at lower anodic overpotentials in the anodic potential scan and thus was the predominant electronic process.³⁰ At pH 9.6, both the formation of AgCl and Ag oxides give rise to overlapped signals, with the latter being of high current intensity. This is likely due to the fact that the alkaline condition favors the formation of Ag oxides.^{25,27} From these measurements the detection of Cl^- appears to be more suitable at pH values of 6.0 and 7.5. At pH 1.6, the electrolyte is strongly acidic, while at pH of 9.6, the oxidation peaks of Ag (0) to Ag oxides are so significant that may interfere with the peak related to the formation of silver chloride.

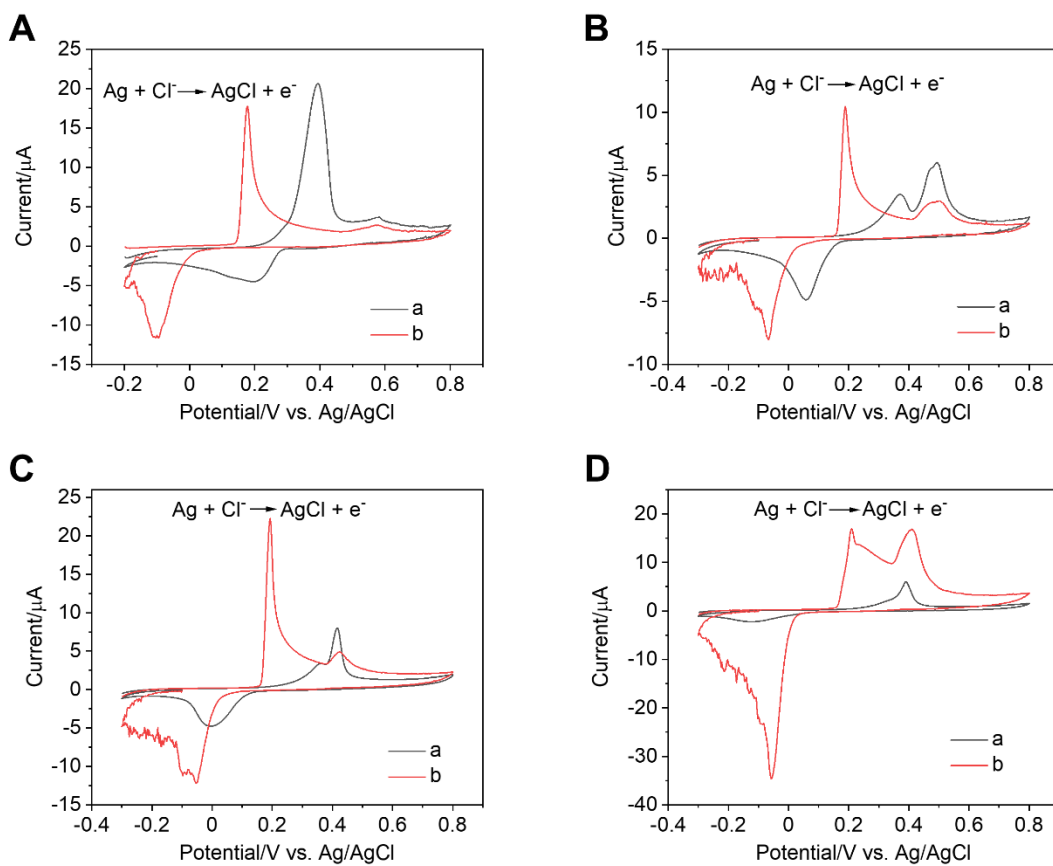


Figure 4.7. Cyclic voltammograms recorded with the $\text{CPE}_{\text{Ag/C}}$ in PB solutions in the absence of Cl^- (a) and presence of 5 mM Cl^- (b) at different pHs. (A) pH=1.6, (B) pH=6.0, (C) pH=7.5, (D) pH=9.6. Scan rate = 100 mV s^{-1} .

Similar studies were carried out for the detection of Br^- and I^- ions and the recorded voltammograms are shown in Figures 4.8 and 4.9. We recorded anodic peaks at $+0.07 \text{ V}$ and -0.15 V , which could be ascribed to the formation of AgBr and AgI , respectively. The relative peak current values related to the formation of the corresponding silver halides and silver oxides were also observed similarly to what was recorded in Cl^- detection. In order to avoid the interference of the AgO formation, a PB solution at pH 6 was selected as the background electrolyte for all the following studies.

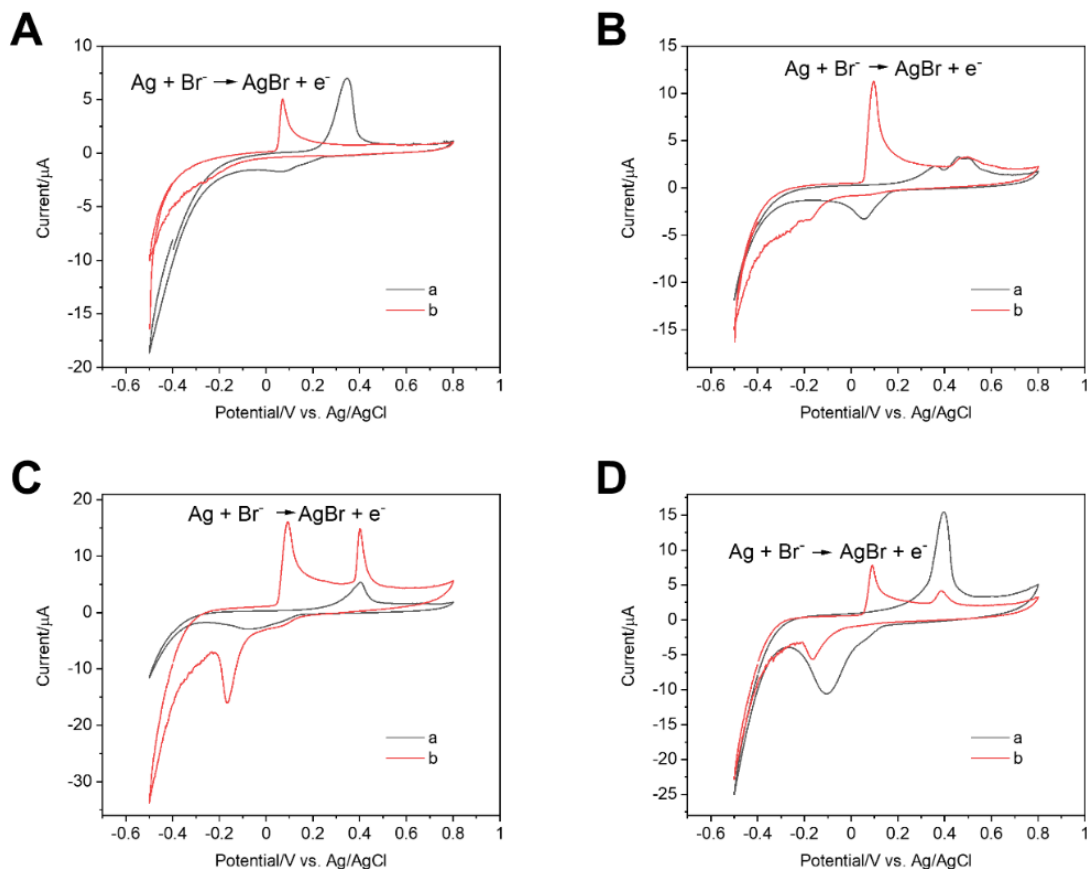


Figure 4.8. Cyclic voltammograms recorded with the $\text{CPE}_{\text{Ag/C}}$ in the absence of Br^- (a) and presence of 5 mM Br^- (b) at different pHs. (A) pH=1.6, (B) pH=6.0, (C) pH=7.5, (D) pH=9.6. Scan rate = 100 mV s^{-1} .

Pure carbon materials have previously shown good electrochemical/electrocatalytic properties when working under specific experimental conditions.^{14,15} Thus, we studied the response of CPEs made of pure carbon from pyrolyzed bread in solutions containing the target halides (Figure 4.10). When the concentration of Cl^- and Br^- was above 4.5 mM, very small oxidation peaks appeared at around +0.20 V and +0.35 V, respectively. For I^- , no oxidation peak was detected in the CVs in the tested concentration range. These results indicate that the carbon matrix did not contribute to the halide detection and just performed as the electrode conductive base material.

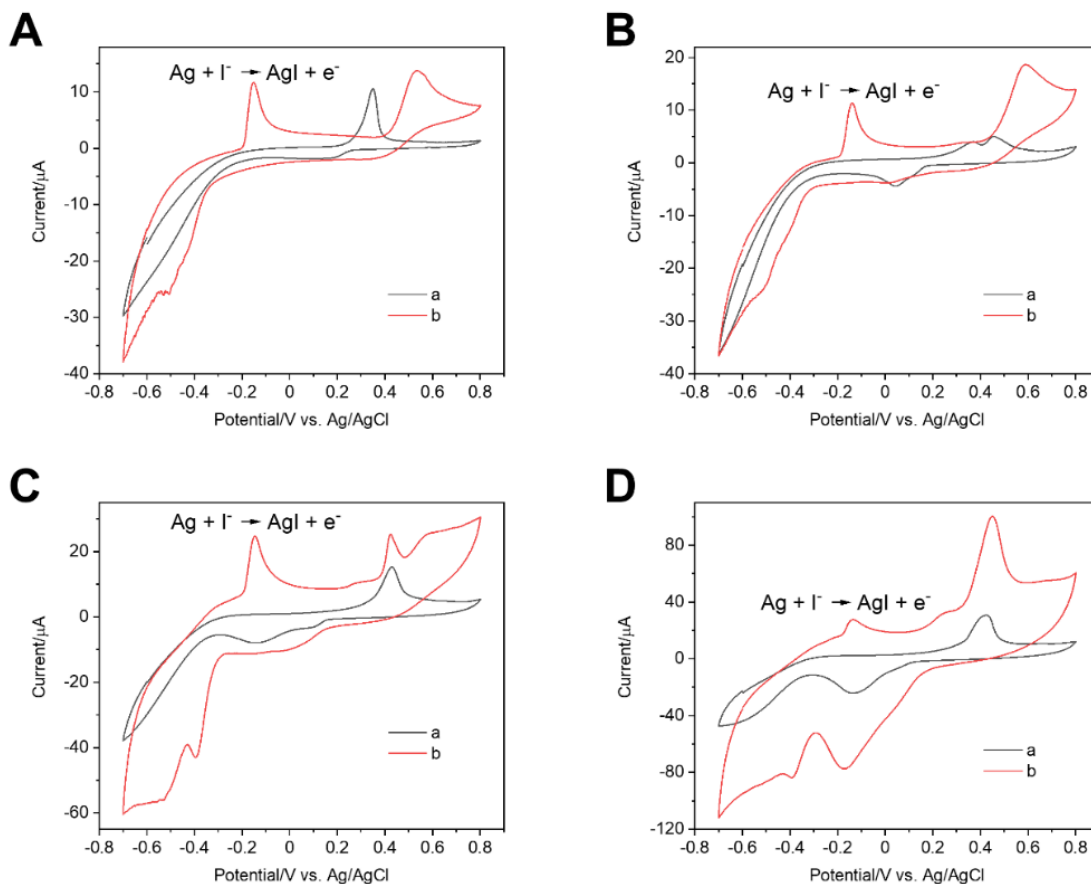


Figure 4.9. Cyclic voltammograms recorded with the $\text{CPE}_{\text{Ag/C}}$ in the absence of I^- (a) and presence of 5 mM I^- (b) at different pHs. (A) pH=1.6, (B) pH=6.0, (C) pH=7.5, (D) pH=9.6. Scan rate = 100 mV s^{-1} .

Figure 4.11 shows the cyclic voltammetric detection of the three halide ions using the $\text{CPE}_{\text{Ag/C}}$. Well-defined anodic peaks at potentials of +0.27, +0.14 and -0.11 V (vs. Ag/AgCl) were recorded, which can be respectively ascribed to Cl^- , Br^- and I^- . A silver halide precipitate forms on the surface of the Ag NPs and consequently generates an oxidation current on the voltammogram, which is in line with the equation of $\text{Ag} + \text{X}^- \rightarrow \text{AgX} + \text{e}^-$ ($\text{X} = \text{Cl}^-$, Br^- and I^-).^{29,31} The well-distinguished peak potentials do not overlap and can be related to the different solubility products (K_{sp}) of the Ag halides, which determines thermodynamically the strength of the interaction between the surface silver atoms and the halide anions.^{28,29}

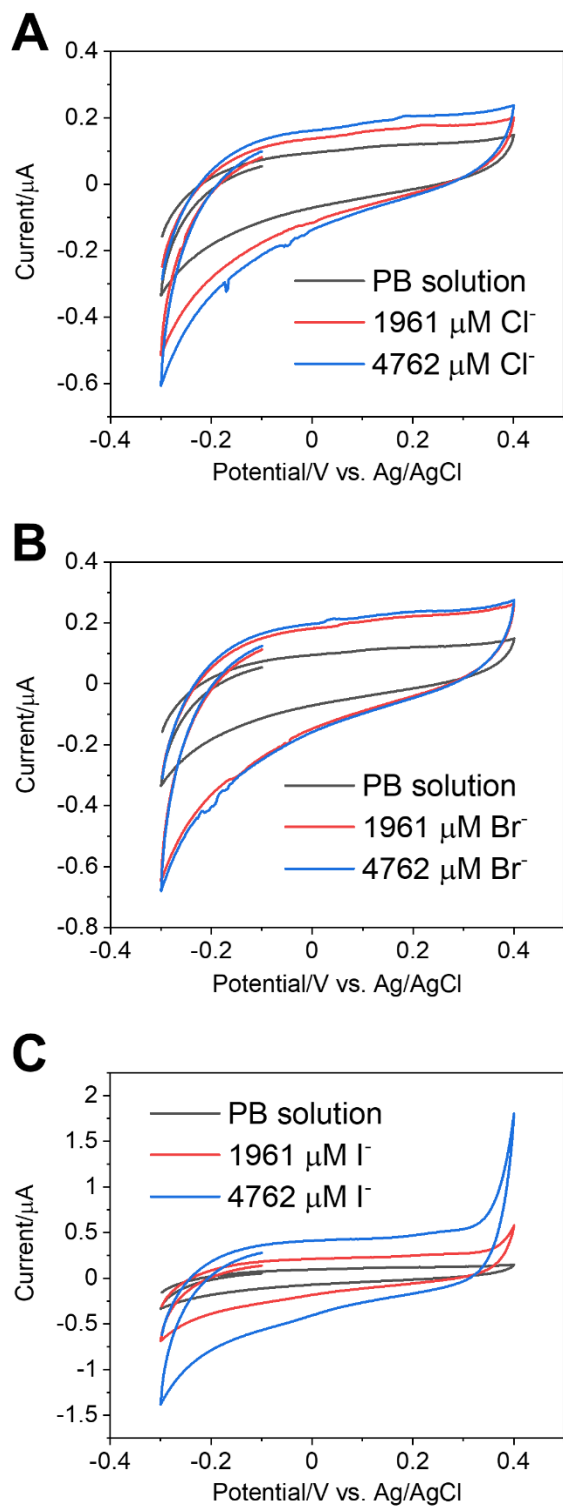


Figure 4.10. (A) Cyclic voltammograms recorded with the CPE made of pure C powder in PB solution (pH=6) before and after the addition of different concentrations of Cl⁻ (A), Br⁻ (B) and I⁻ (C). Scan rate = 100 mV s⁻¹.

The potential barrier required to form silver compounds (AgCl, AgBr and AgI) by the formation of Ag-anion bonds would affect the oxidation/reduction potential. It is worth noting that the K_{sp} value for the Ag halides increases in the order of $Cl^- > Br^- > I^-$ ($AgCl=1.76 \cdot 10^{-10}$, $AgBr=5.32 \cdot 10^{-13}$ and $AgI=8.49 \cdot 10^{-17}$).²⁹ The smaller the K_{sp} , the stronger the chemical affinity between the silver surface atoms and the halide anions and so the lower the overpotential required to produce the corresponding Ag halides. Thus, the significantly different K_{sp} values contribute to their well-separated oxidation peak potentials.

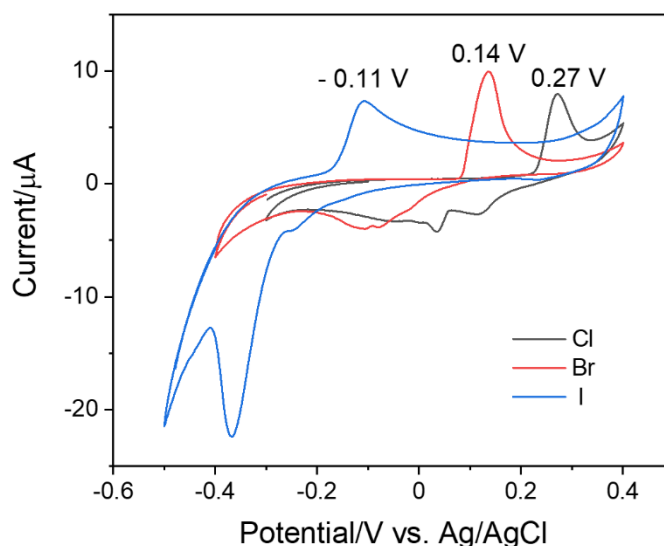


Figure 4.11. Cyclic voltammograms were obtained with the $CPE_{Ag/C}$ in phosphate buffer solution (pH =6) containing 395 μM chloride, bromide, and iodide, respectively, in a separated solution at a scan rate of 100 mV/s.

Figure 4.12 A presents the voltammetric responses recorded in PB solutions containing increasing concentrations of Cl^- and Figure 4.12 B is a zoomed-in image of the oxidation peaks recorded between +0.2 V and +0.4 V. As expected, the peak current increases with the Cl^- concentration. Also, the oxidation peak shifts to lower potentials when the Cl^- concentration increases, as expected from the Nernst equation.³² The calibration curve obtained by plotting the peak current vs the Cl^- concentration (Figure 4.12 C) shows a linear response albeit with a decreased slope for concentrations above 500 μM . The limit of detection is 16 μM estimated using 3σ IUPAC criterion. This value is below the maximum allowable concentration of 250 ppm (~ 7 mM) in drinking water set by the USA EPA.³³

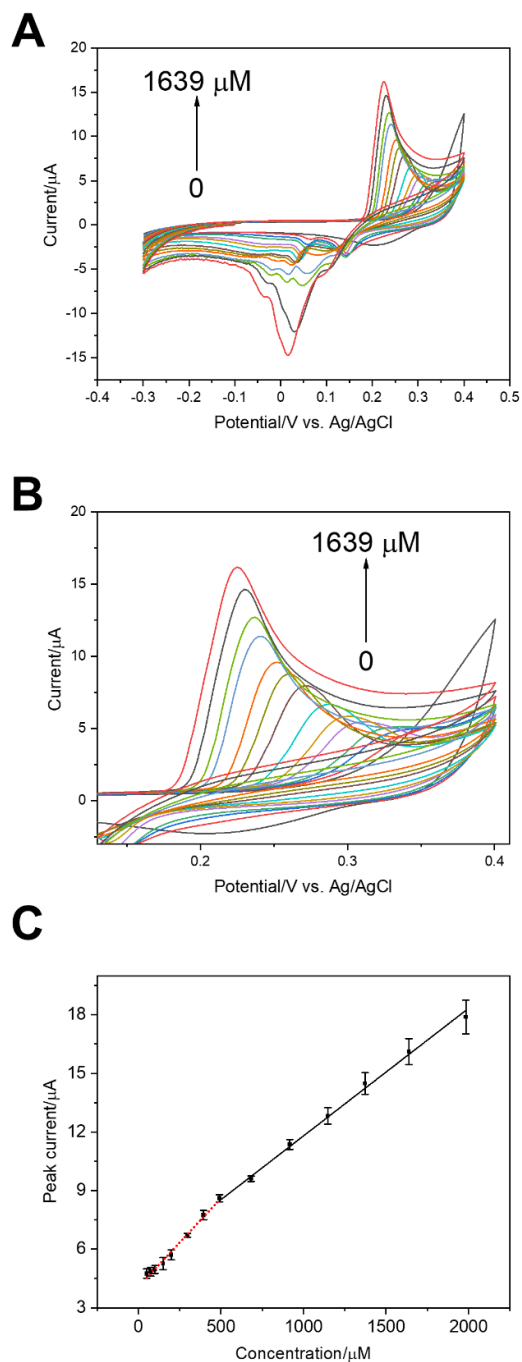


Figure 4.12. (A) Cyclic voltammograms of Cl^- solutions in PB of concentrations ranging from 0 to 1639 μM recorded with $\text{CPE}_{\text{Ag/C}}$ (from bottom to top signals: 0, 50, 74, 100, 149, 199, 297, 395, 491, 682, 917, 1147, 1373 and 1639 μM), (B) The enlarged oxidation peak curve of cyclic voltammograms shown in (A), (C) Calibration curve of the $\text{CPE}_{\text{Ag/C}}$ for measurement of Cl^- . Each point represents the mean value of three measurements performed consecutively and the error bars are the corresponding standard deviation. A fresh CPE was used for each measurement.

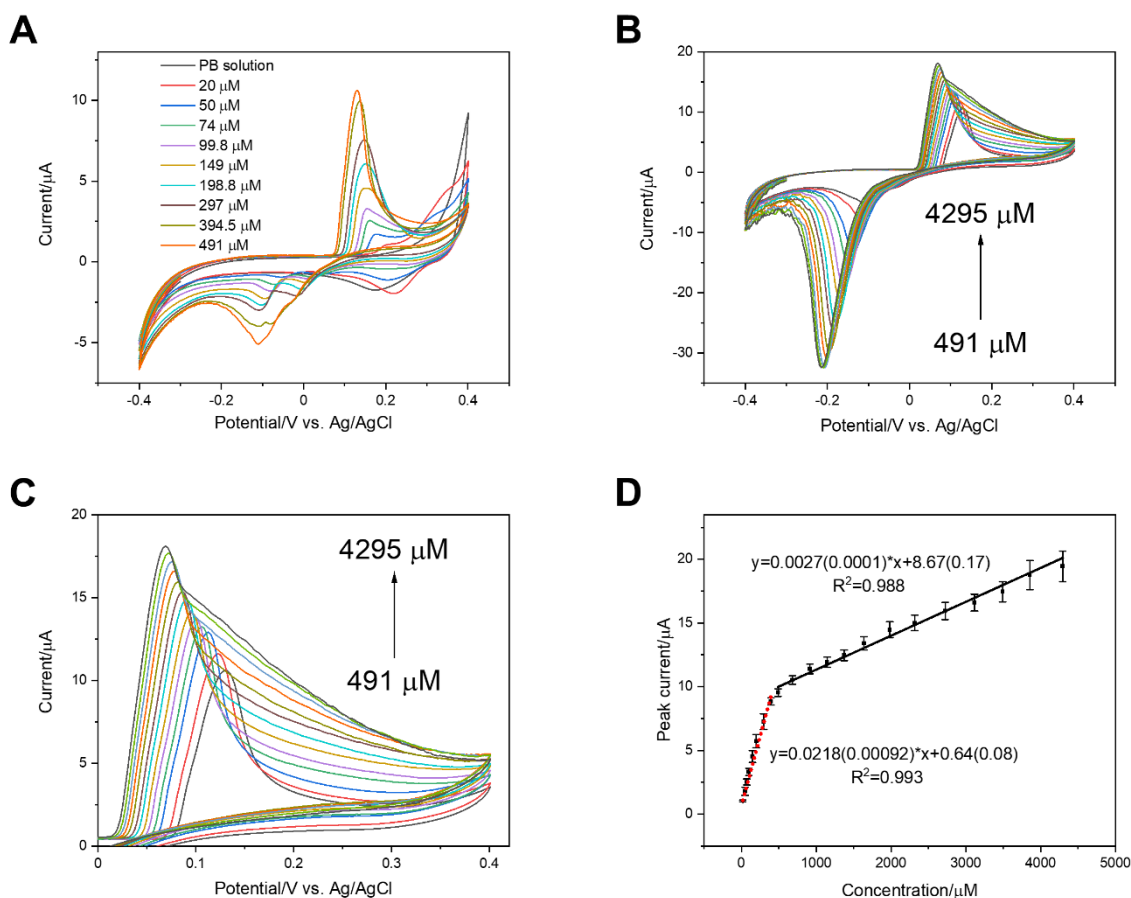


Figure 4.13. (A) CVs recorded with $\text{CPE}_{\text{Ag/C}}$ in PB solutions containing from 0 μM to 491 μM Br^- . (B) CVs recorded with $\text{CPE}_{\text{Ag/C}}$ in PB solutions containing from 491 μM to 4295 μM Br^- (from bottom to top signals: 491, 682, 917, 1147, 1373, 1639, 1983, 2318, 2723, 3114, 3491, 3856 and 4295 μM). (C) The enlarged oxidation peak curve of cyclic voltammograms shown in (B). (D) Calibration curve. Each point represents the mean value of three measurements performed consecutively and the error bars are the corresponding standard deviation. A fresh CPE was used for each measurement. Scan rate = 100 mV s^{-1} .

Similar studies were carried out for Br^- and I^- target analytes (Figures 4.13 and 4.14). Two linear ranges were also estimated in the detection of both species, showing higher sensitivity at lower analyte concentrations. The decreased sensitivity above a critical concentration could be indicative of Langmuir-type adsorption of halides at the electrode surface.^{34,35} Similar behaviors were reported for the electrochemical analysis of other chemical species.^{34,36} The analytical parameters obtained from the calibration curves of the different halides are summarized in Table 4.4. Figure 4.15 shows CVs recorded in a PB solution containing the same concentration of Cl^- , Br^- and I^- . The peak potentials are well separated and in agreement with those observed in Figures 4.11, 4.12, as well as in Figures 4.13, 4.14.

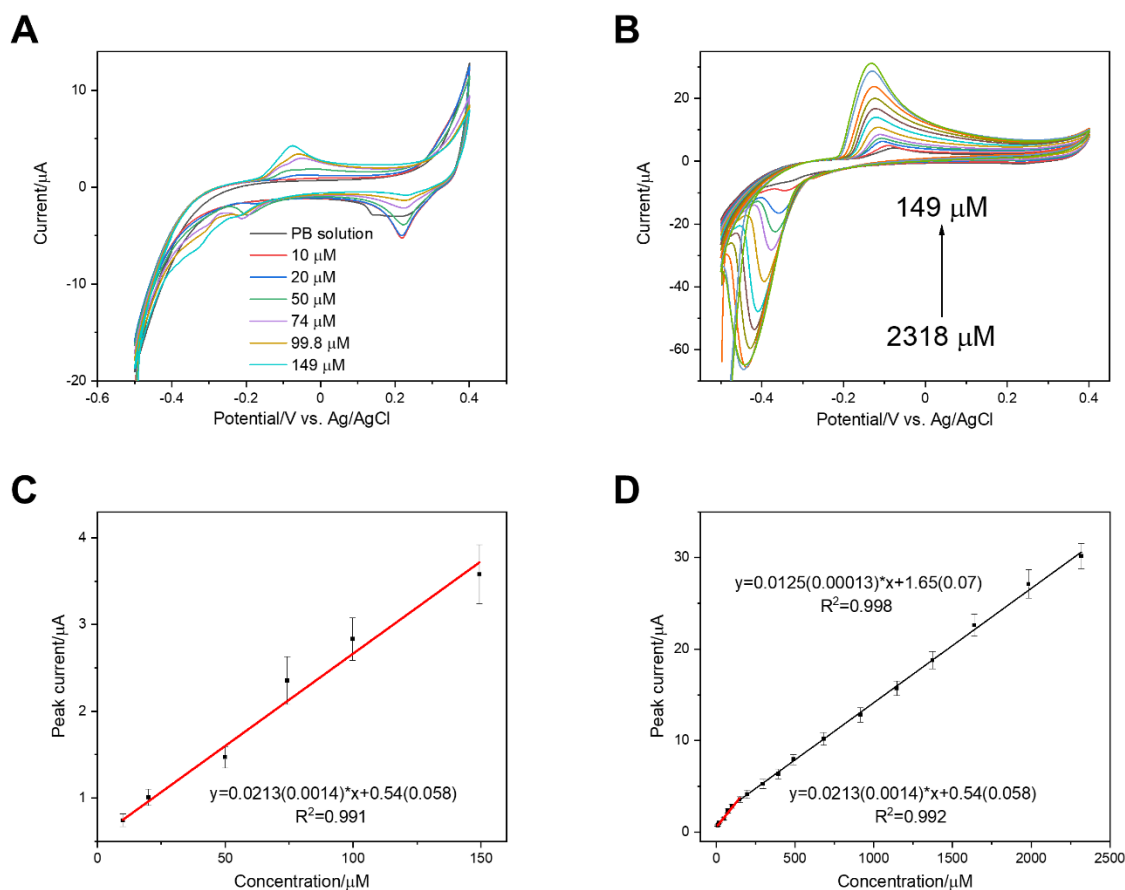


Figure 4.14. (A) Cyclic voltammograms recorded with CPE_{Ag/C} in PB solutions containing from 0 μM to 149 μM I^- . (B) Cyclic voltammograms recorded with CPE_{Ag/C} in PB solutions containing from 149 μM to 2318 μM I^- (from bottom to top signals: 149, 199, 297, 395, 491, 682, 917, 1147, 1373, 1639, 1983 and 2318 μM). (C) Calibration curve plotted in the I^- concentration range from 10 μM to 149 μM . (D) Calibration curve plotted in the I^- concentration range from 10 μM to 2318 μM . Each point represents the mean value of three measurements performed consecutively and the error bars are the corresponding standard deviation. A fresh CPE was used for each measurement. Scan rate = 100 mV s⁻¹.

This allows those ions to be simultaneously identified and is related to the different K_{sp} values, as described above. In this regard, it is not surprising that the largest peak current is associated with the formation of AgI. It is also worth mentioning that the oxidation peaks for Br^- and I^- are already visible from the second cycle, while the Cl^- peak only appears after several cycles. This can result from the competition between the different halide anions for interacting with the surface of Ag NPs. Initially, there is the same concentration of Cl^- , Br^- and I^- around silver NP surfaces but due to the stronger interaction of I^- and Br^- with the silver surface atoms, the oxidation peaks of Br^- and I^- appear firstly. However, after several scans, the concentration of Cl^- becomes comparatively larger than that of the already depleted Br^- and I^- , and thus the oxidation peak for Cl^- becomes visible.

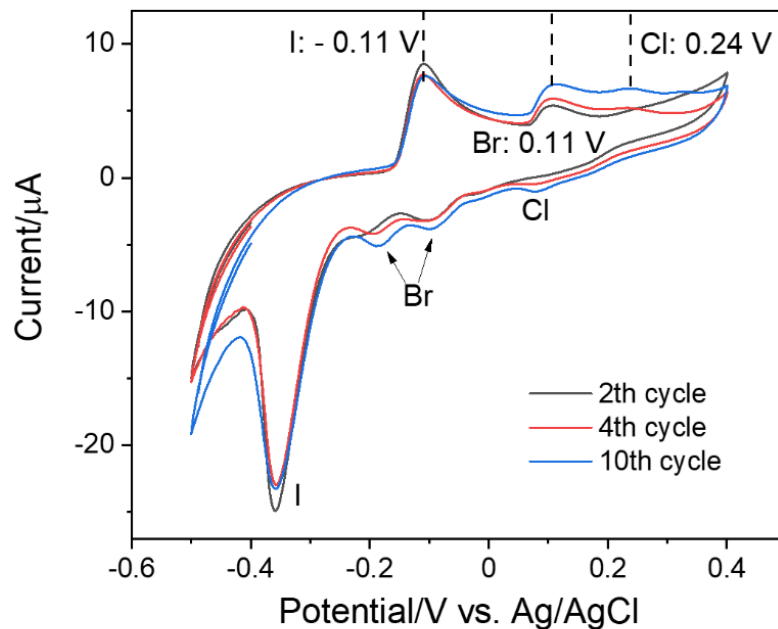


Figure 4.15. Cyclic voltammograms recorded with the $\text{CPE}_{\text{Ag/C}}$ in phosphate buffer solution (pH = 6) containing 395 μM chloride, bromide and iodide, respectively, in a mixed solution at a scan rate of 100 mV/s.

4.3.2 Analysis of organohalide molecules in water

Encouraged by the positive analytical response of Ag/C nanocomposites for the analysis of halide anions reported in the previous sections, we decided to assess their potential for analyzing organohalide molecules that have been identified to be water pollutants. The electrocatalytic activity of Ag NPs for inducing the cleavage of carbon-halide bonds in this family of molecules has been previously reported³⁷ and already detailed in Chapter 3???. This could be exploited to electrochemically detect different target molecules following the same experimental procedure as above. Two organohalides were selected in this work: sucralose and trichloroacetic acid.

Table 4.4. Analytical parameters obtained from the calibration curves of CPE_{Ag/C} for halides, sucralose and TCA analysis.

Sensor	Analyte	Method	Slope·10 ³ ($\mu\text{A } \mu\text{M}^{-1}$)	Intercept (μA)	R ² (n=3)	LOD (μM)	Linear range (μM)
CPE _{Ag/C}	Cl ⁻	CV	9.1±0.3	4.1±0.1	0.993	16	50 – 491
			6.5±0.2	5.3±0.2	0.995	–	491 – 1983
	Br ⁻	CV	21.8±0.9	0.6±0.08	0.993	8	20 – 491
			2.7±0.1	8.7±0.2	0.988	–	491 – 4295
	I ⁻	CV	21±1.4	0.5±0.06	0.992	7	10 – 149
			12.5±0.1	1.7±0.07	0.998	–	149 – 2318
	Sucralose	CV	1.2±0.2	2.6±0.1	0.946	141	200 – 990
			0.18±0.005	3.5±0.04	0.995	–	990 – 16700
	TCA	CV	1.15±0.03	2.5±0.1	0.996	326	3114 – 5508
		SWV	1.62±0.06	0.9±0.09	0.994	167	395 – 3114

LOD is calculated using the 3 σ IUPAC criterion.

4.3.2.1 Sucralose detection. Figures 4.16 A and B show the CVs recorded with CPE_{Ag/C} in PB solutions containing sucralose concentrations in the range from 0.2 mM to 16.7 mM. The peak current intensity increased with the concentration of sucralose, showing a linear dependence in the studied concentration range. Similar to the calibration curves obtained for the halide ions, two distinct slopes were obtained (Figure 4.16 C), which again may be indicative of the Langmuir type adsorption of sucralose at the surface of the electrode.^{34,35} The analytical parameters related to the calibration curves are displayed in Table 4.4.

As introduced in Chapter 1, the mechanism that may be governing the electrochemical detection of sucralose with the Ag/C nanocomposite comprises two steps, namely, the initial dehalogenation of the sucralose molecule followed by the formation of AgCl.^{29,30,37} Dehalogenation processes catalyzed by silver have widely been investigated.^{38–40} These are known to proceed by the adsorption on the surface of Ag of the halogenated compound “RX” (where R is an organic radical and X a halide), producing an “attenuated radical” intermediate of the kind $R\cdots X\cdots Ag$ (see Figure 4.17 A).³⁸ The strong interaction of RCl with Ag NPs improves the kinetics of the dehalogenation reaction because the C-Cl bond is greatly weakened due to the $Cl\cdots Ag$ and $R\cdots Ag$ interactions, facilitating the cleavage of the C-Cl bond and the transfer of electrons (see Figure 4.17 B).^{37,40} After the dehalogenation process (Figure 4.17 C), the free Cl^- ion is released and it can adsorb onto the surface of Ag NPs. Then, the free ion Cl^- can react with Ag to form AgCl, releasing an electron which is collected by the Ag/C electrode and contributes to the analysis signal (Figure 4.17 D) in a process analogous to that of the previously discussed halide anions in solution.

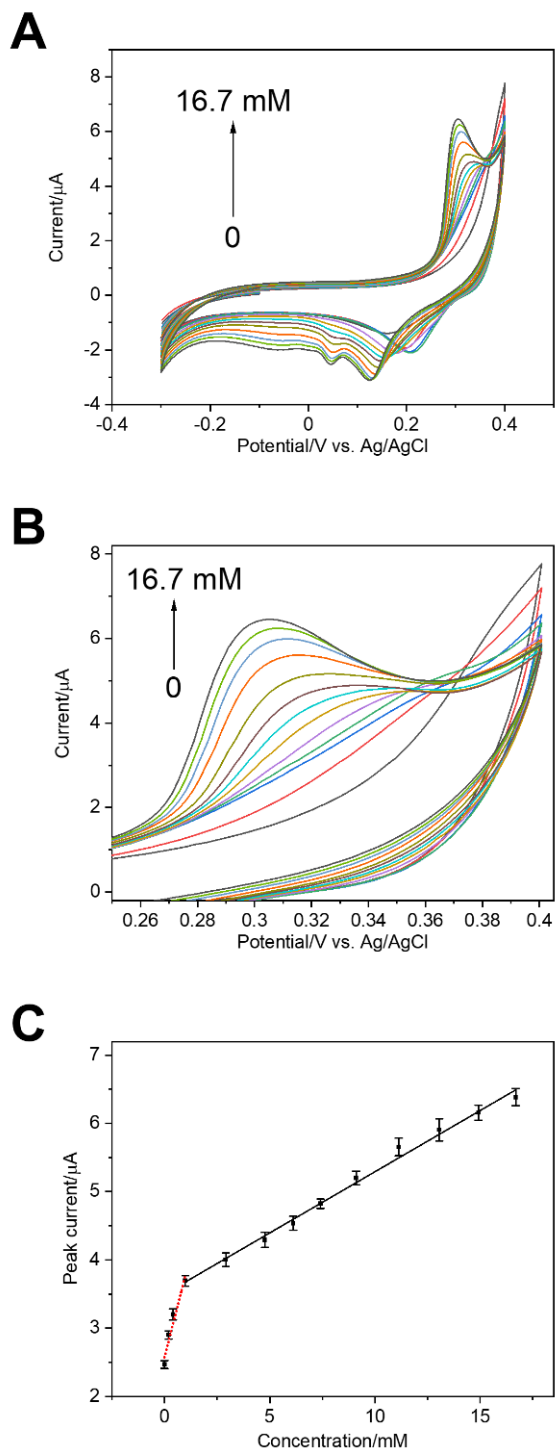


Figure 4.16. (A) Cyclic voltammograms recorded with CPE_{Ag/C} in PB solutions containing from 0 mM to 16.7 mM sucralose (from bottom to top signals: 0, 0.2, 0.4, 0.99, 2.92, 4.77, 6.12, 7.42, 9.11, 11.13, 13.07, 14.92 and 16.7 Mm). **(B)** The amplified peak curve of cyclic voltammograms shown in (A). **(C)** Calibration curve of the CPE_{Ag/C} for measurement of sucralose. Each point represents the mean value of three measurements performed consecutively and the error bars are the corresponding standard deviation. A fresh CPE was used for each measurement.

One sucralose molecule contains three Cl atoms and whether the dehalogenation process was complete, the LOD may theoretically be three times lower than that achieved in the detection of Cl^- ions. However, the LOD for measuring sucralose is $141\text{ }\mu\text{M}$ ($\sim 5\text{ ppm}$), which is significantly larger than the one obtained for the detection of Cl^- in solutions ($16\text{ }\mu\text{M}$). This could be due to a partial release of Cl^- from the sucralose molecules through the dehalogenation processes, discussed above.

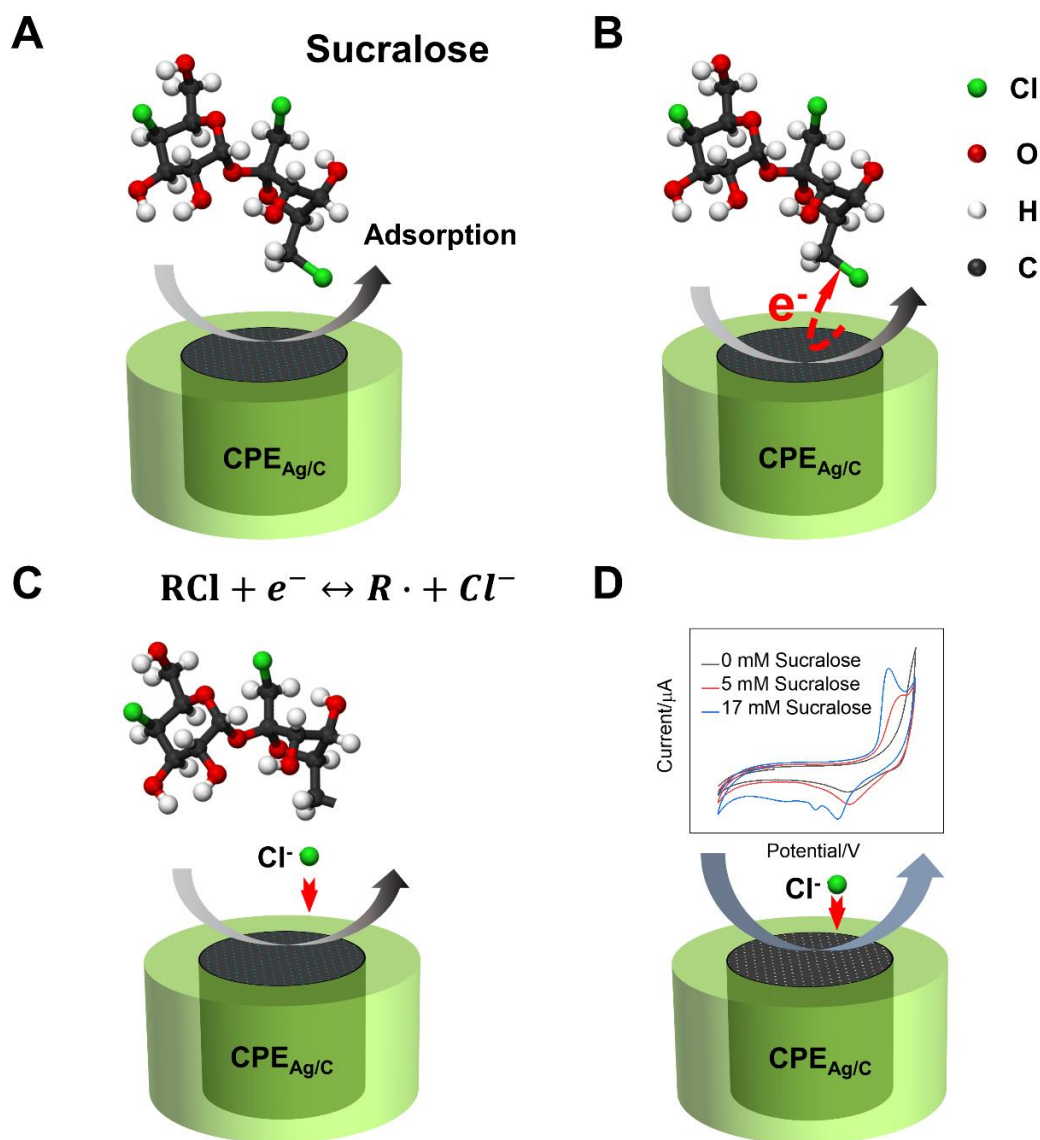


Figure 4.17. A schematic diagram of the possible underlying mechanisms in the electrochemical analysis of sucralose with $\text{CPE}_{\text{Ag/C}}$.

4.3.2.2 Trichloroacetic acid determination

To further assess the performance of the $\text{CPE}_{\text{Ag/C}}$ electrode, we also carried out the analysis of trichloroacetic acid (TCA) by CV. The possible mechanism for analyzing TCA with $\text{CPE}_{\text{Ag/C}}$ could be similar to that of the already discussed sucralose analysis. Figures 4.18 A and 4.18 B show the CV responses for solutions with increasing concentrations of TCA. Using the corresponding peak currents, the calibration curve (Figure 4.18 C) was obtained and the estimated analytical parameters are summarized in Table 4.4. It was found that the linear range is limited and can only be obtained for high TCA concentrations, thus giving rise to a high limit of detection. A similar poor response had been previously reported when applying CV measurements⁴¹, showing linear dynamic ranges between 2500 and 22500 μM . However, previous works have shown that using Square Wave Voltammetry (SWV) electrochemical technique, a linear calibration curve could be obtained at lower concentration ranges.^{42,43}

SWV technique applies a potential waveform at which the recording of the capacitive current is minimized so that the Faradaic to capacitive current ratio is greatly enhanced looking at improving significantly improving the sensitivity of the electrochemical analysis. A detailed description can also be found in reference 5.⁵

Here, we applied the SWV method and, as shown in Figure 4.19, the recorded SWV signals at different TCA concentrations and the corresponding calibration were obtained. The calculated analytical parameters are also displayed in Table 4.4. A linear range of 395 – 3114 μM and a LOD of 167 μM were obtained.

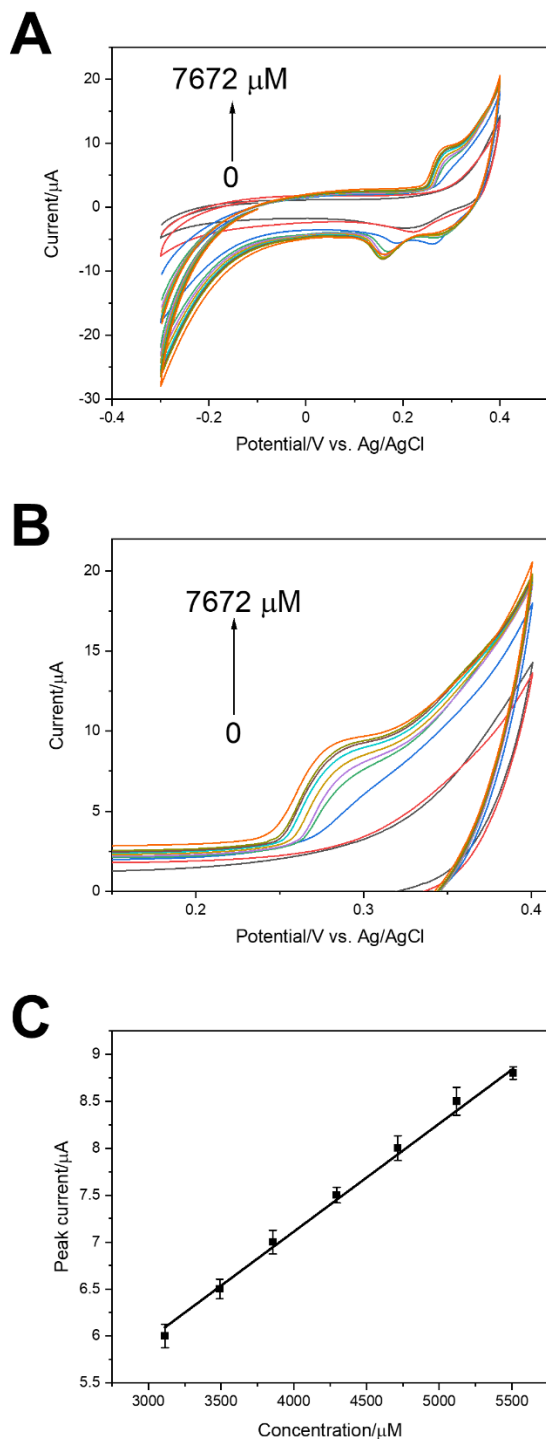


Figure 4.18. (A) Cyclic voltammograms recorded with $\text{CPE}_{\text{Ag/C}}$ in PB solutions containing from 0 μM to 7672 μM trichloroacetic acid (from bottom to top signals: 0, 2723, 3114, 3491, 3856, 4295, 4715, 5119, 5508 and 7672 μM). (B) Zoomed image of the CVs shown in (A). (C) Corresponding calibration curve. Each point represents the mean value of three measurements performed consecutively and the error bars are the corresponding standard deviation. A fresh CPE was used for each measurement.

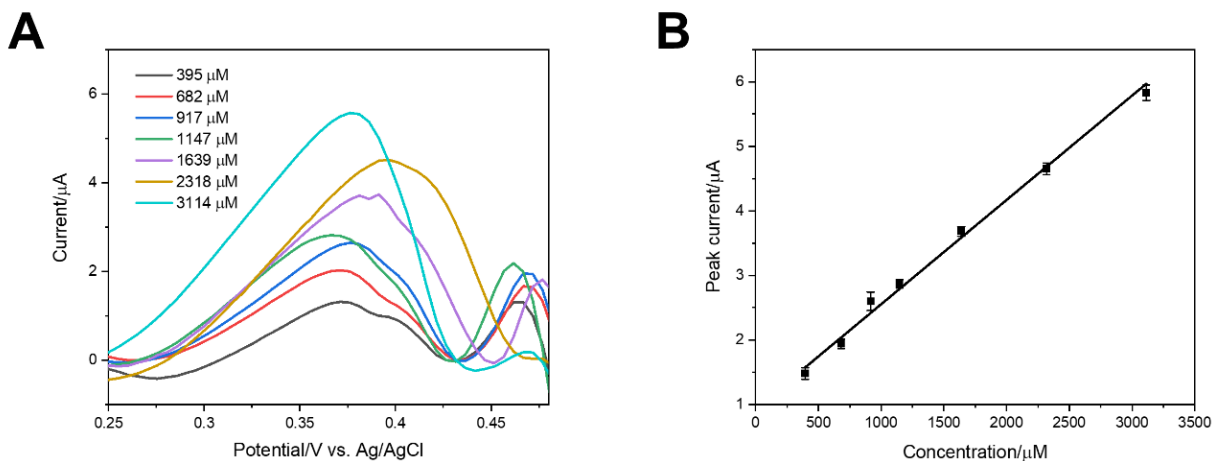


Figure 4.19. (A) SWVs recorded with CPE_{Ag/C} in solutions containing different concentrations of TCA. (B) Corresponding calibration curve. Each point represents the mean value of three measurements performed consecutively and the error bars are the corresponding standard deviation. A fresh CPE was used for each measurement.

For comparative purposes, the analytical performance of electrochemical sensors of halides and TCA previously reported in the literature are summarized in Tables 4.5 and 4.6, respectively. Compared with the sensors introduced in this work, these previously reported sensors show certain advantages in terms of analytical performance. However, most of these sensors rely on the electrodeposition or casting of nanoparticles on the surface of the electrodes. This is a sensor preparation process that is difficult to adapt to mass production and not suitable for translation to the industry. In the case of sucralose, as far as we know, only one research focused on the development of electrochemical sensors for its analysis. Nikolelis et al.⁴⁴ reported an electrochemical device for the monitoring of sucralose, taking advantage of the interactions between the sucralose and bilayer lipid membranes. The adsorption of sucralose to the membranes generates an increase in the ionic current, which is ascribed to the alteration of electrostatic fields of the lipid membrane. However, sensor manufacturing is very complex. Our work shows that Ag/C electrodes are produced from bread waste in a very simple and upscalable fabrication process that can be applied to the electrochemical analysis of halides and different organohalide molecules in waters.

Table 4.5. Analytical parameters of the previously reported sensors for halide detection.

Modified electrodes	Halides	Linear range (μM)	LOD (μM)	Ref.
Ag NPs-modified SPE	Cl^-	5-90	5	30
	Br^-	5-80	5	
	I^-	-	-	
Ag NWs-modified Pt electrode	Cl^-	200-20200	20	28
	Br^-	50-20200	10	
	I^-	50-20200	10	
Screen-printed silver strip sensor	Cl^-	100-20000	18.83	45
	Br^-	10-20000	2.95	
	I^-	10-20000	3.05	
Silver films on polycrystalline gold	Cl^-	0.5-20	-	46
Nano-silver modified indium-tin oxide thin electrodes	Cl^-	0.01-1	0.0052	47
Ag/dopamine modified poly(γ - glutamic acid) NPs	Cl^-	0.01-1000	0.0033	48
$\text{CPE}_{\text{Ag/C}}$	Cl^-	50-491, 491-1983	16	This work
	Br^-	20-491, 491-4295	8	
	I^-	10-149, 149-2318	7	

Table 4.6. Analytical parameters of previously reported sensors for TCA detection.

Modified electrodes	Linear range (μM)	LOD (μM)	Ref.
Ag NPs-MA/GCE (SWV)	0.1-2, 4-100	0.030, 0.079	42
SNP-CS/GCE (CA)	3-56	1.1	49
Ag-MWCNT/GCE (SWV)	5-120	1.9	43
MWCNTs/Pc/Fe(CA)	8-2000	2.0	50
Hg-Ag@GNR-PSS-PDDA/GCE (CA)	0.16-1.7	0.12	51
np-Ag (CA)	2500-22500	25.4	41
Porphyrin/SWNTs-[BMIM][PF ₆]/GCE (CA)	0.9-140	0.38	52
TH/TNTs/CS/GCE (CV)	15-1500	-	53
CPE _{Ag/C} (CV)	3114 – 5508	326	This work
CPE _{Ag/C} (SWV)	395 – 3114	167	

4.4 Electrochemical performance of wood-derived carbon material: analysis of redox species

4.4.1 Electrochemical assessment of the wood-derived carbon paste electrodes

Three types of carbon materials (shown in chapter 3, Figure 3.20) were previously produced from the pyrolysis of wood by-products, and labeled as C_p (carbon derived from the Pine tree), C_c (carbon derived from the Chestnut tree), and C_o (carbon derived from the Oak tree).

The C_p, C_c, and C_o carbons were used to fabricate carbon paste electrodes (CPEs), which were labeled as CPE_C_p, CPE_C_c, and CPE_C_o. The electrochemical performance of the CPEs was evaluated by CV measurements in solutions containing different representative

redox species showing inner-sphere and outer-sphere redox mechanisms.⁵⁴ The design of this study takes into account the kinetic sensitivity of different redox probes to the carbon electrode surface composition and structure. The electron transfer (ET) on different carbon electrodes is greatly influenced by different aspects of their surface chemistry, such as the density of surface oxides or other functional groups or impurities, and the surface electronic density of states (DOS) at the redox species formal potential. Inner-sphere redox probes such as ferricyanide are quite sensitive to the presence of defects which may act as electrocatalytic active sites to enhance the ET kinetics at the electrode surface. By contrast, the electrode response to outer-sphere redox probes such as ferrocene is insensitive to the presence of defects and their electrochemical behavior only depends on the DOS of the carbon material.^{54,55}

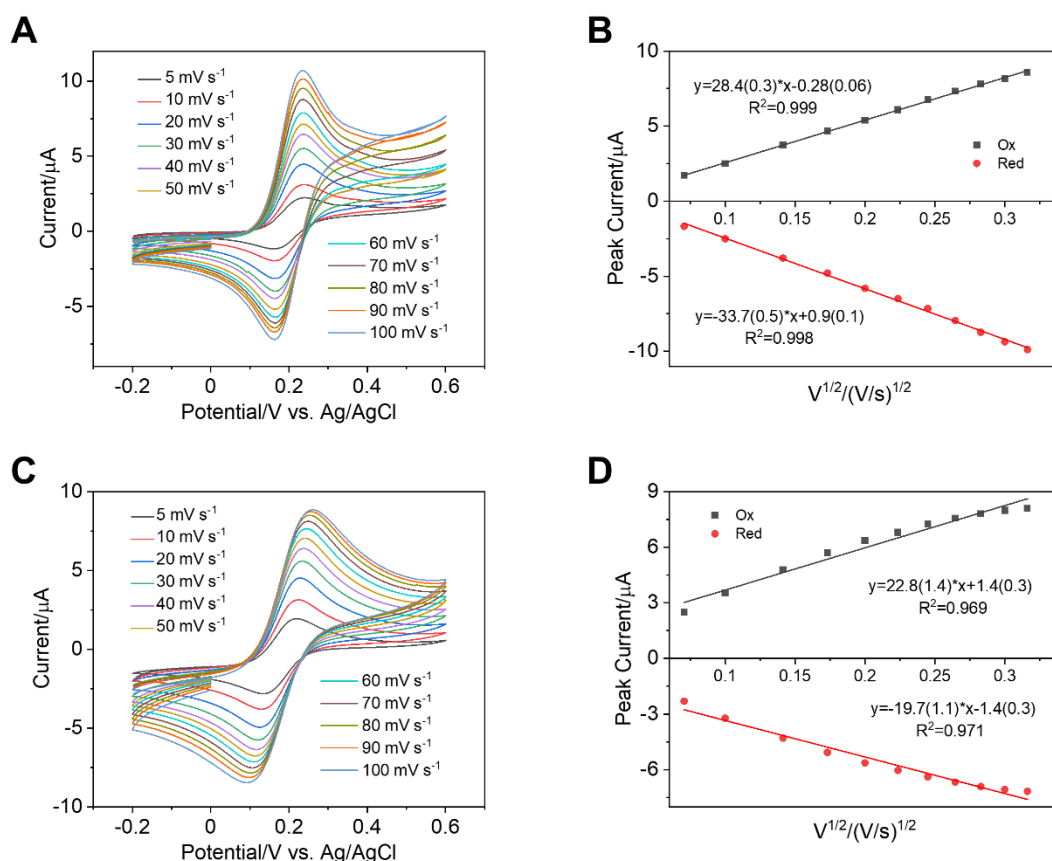


Figure 4.20. Cyclic voltammograms recorded with CPE_Cc at different scan rates, in a 0.1 M KNO₃ solution containing 1 mM ferrocene redox species (A) and 1 mM ferricyanide redox pair (C), and plots of anodic peak and cathodic peak currents vs. the square root of the scan rate (B and D). (B) is plotted from the measurements of ferrocene redox species and (D) is obtained from the measurements of ferricyanide redox pair.

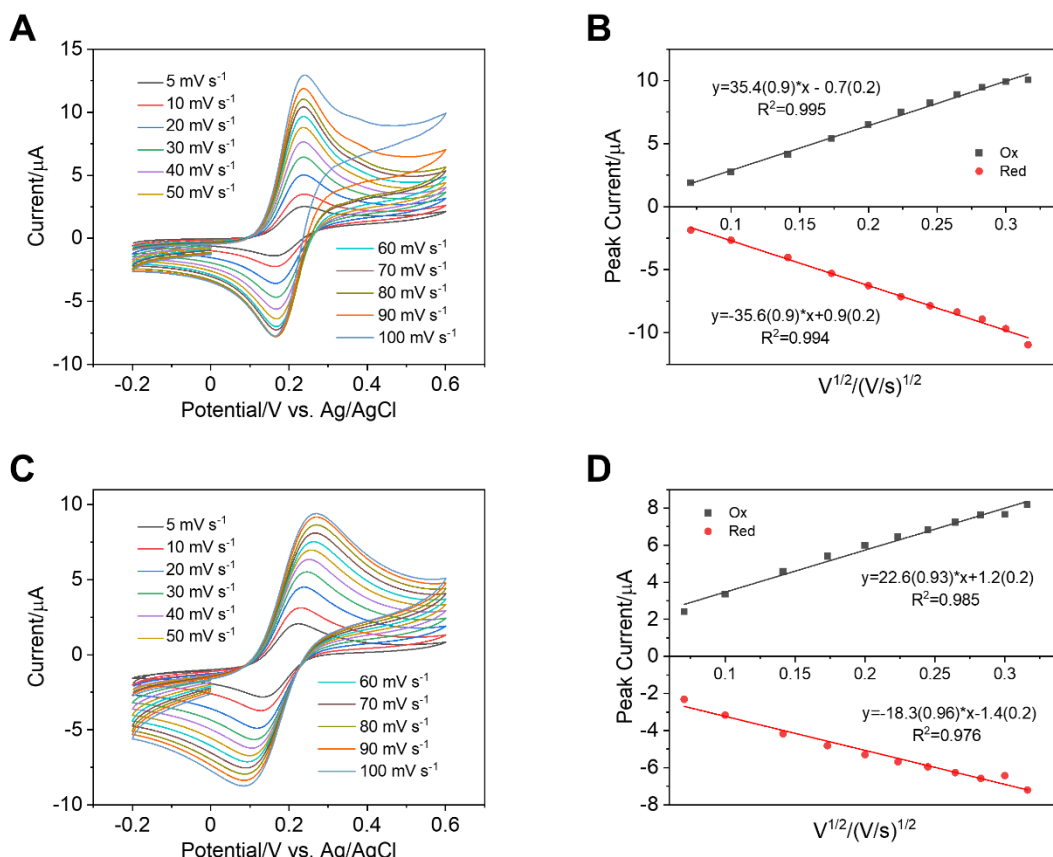


Figure 4.21. Cyclic voltammograms recorded with CPE_{Cp} at different scan rates, in a 0.1 M KNO₃ solution containing 1 mM ferrocene redox species (A) and 1 mM ferricyanide redox pair (C), and plots of anodic peak and cathodic peak currents vs. the square root of the scan rate (B and D). (B) is plotted from the measurements of ferrocene redox species and (D) is obtained from the measurements of ferricyanide redox pair.

Figure 4.20 shows the cyclic voltammograms recorded with CPE_{Cc} at scan rates from 5 to 100 mV s⁻¹, in a 0.1 M KNO₃ solution containing 1 mM ferrocene redox species (Figure 4.20 A) and 1 mM ferricyanide redox pair (Figure 4.20 C). Similar measurements were performed with CPE_{Cp} (Figure 4.21) and CPE_{Co} (Figure 4.22).

Both outer-sphere and inner-sphere redox species show quasi-reversible voltammetric signals with all the CPEs. It is worth noting that for the three CPEs, the values of peak-to-peak potential separation (ΔE_p) obtained from the outer-sphere redox probe of ferrocene are around 63 mV at 50 mV s⁻¹ scan rate (Table 4.7). These values are very close to the 59 mV expected for 1-*e*⁻ electrochemical process, indicating that there is a high DOS on the surface of all the materials.^{54,56} The ΔE_p values obtained from the inner-sphere redox probe of ferricyanide redox pair are between 110 and 170 mV at 50 mV s⁻¹ scan rate (Table 4.7),

which indicates a quasi-reversible electrochemical process.^{54,56} In addition, the ΔE_p values acquired with the three produced CPEs for the ferricyanide redox pair are in the order of $CPE_{C_c} < CPE_{C_p} < CPE_{C_o}$, indicating that their respective electrochemical performances decrease in the following order: $CPE_{C_c} > CPE_{C_p} > CPE_{C_o}$.

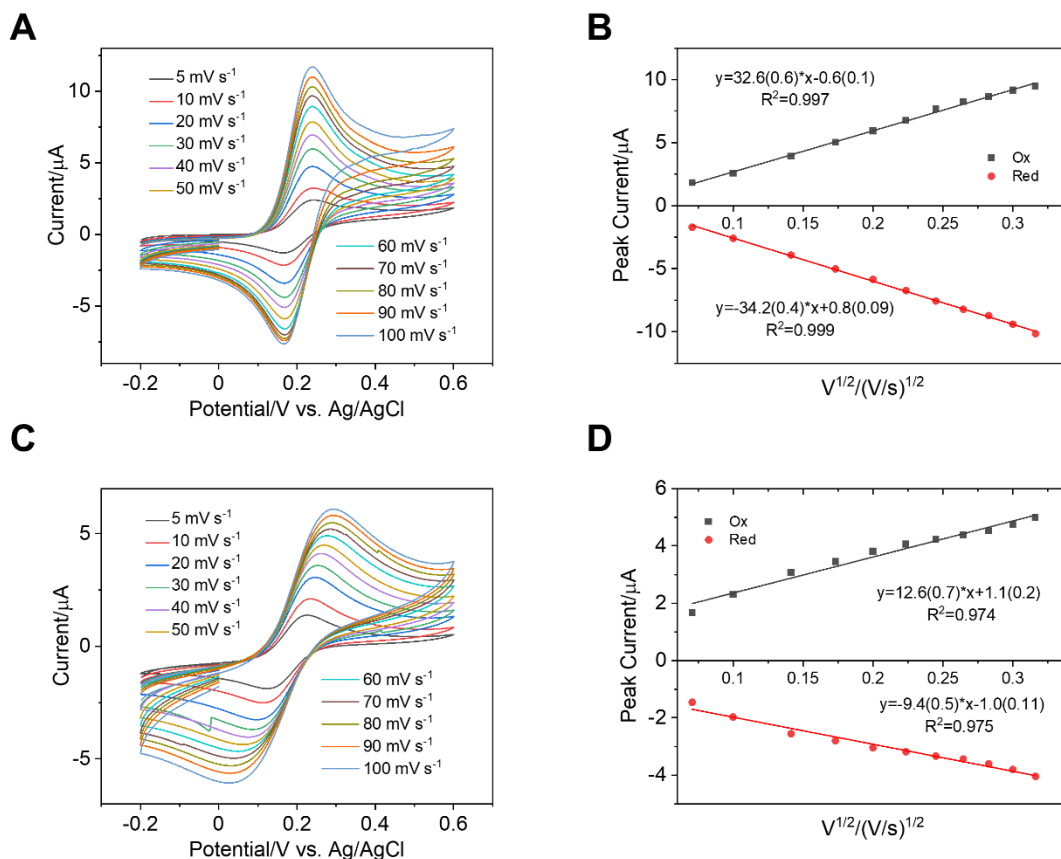


Figure 4.22. Cyclic voltammograms recorded with CPE_{C_o} at different scan rates, in a 0.1 M KNO₃ solution containing 1 mM ferrocene redox species (A) and 1 mM ferricyanide redox pair (C), and plots of anodic peak and cathodic peak currents vs. the square root of the scan rate (B and D). (B) is plotted from the measurements of ferrocene redox species and (D) is obtained from the measurements of ferricyanide redox pair.

The peak currents for both anodic and cathodic signals obtained from the inner-sphere and outer-sphere redox species recorded at scan rates in the range from 5 to 100 mV s⁻¹ show a linear dependence with the square root of the scan rate (Figure 4.20, Figure 4.21, and Figure 4.22), pointing out that the redox processes for all the CPEs prepared with the C_p, C_c, and C_o materials are controlled by diffusion.⁶

Table 4.7. Peak-to-peak potential separation (ΔE_p) at a scan rate of 50 mV s^{-1} for different CPEs in a 0.1 M KNO_3 solution containing 1 mM ferrocene redox species and 1 mM ferricyanide redox pair.

	Redox Species	CPE_C _p	CPE_C _c	CPE_C _o	CPE_C _g
ΔE_p (mV)	ferrocene	61	63	63	66
	ferricyanide	137	112	166	134

For comparative purposes, a CPE made of commercial graphite powder (labeled as CPE_C_g) was characterized following the same study shown above (Figure 4.23). The recorded ΔE_p values of 66 mV for ferrocene and 134 mV for ferricyanide (Table 4.7) are quite similar to those obtained for CPE_C_p, CPE_C_c, and CPE_C_o. This confirms that the C_p, C_c, and C_o materials exhibit excellent electrochemical performance.

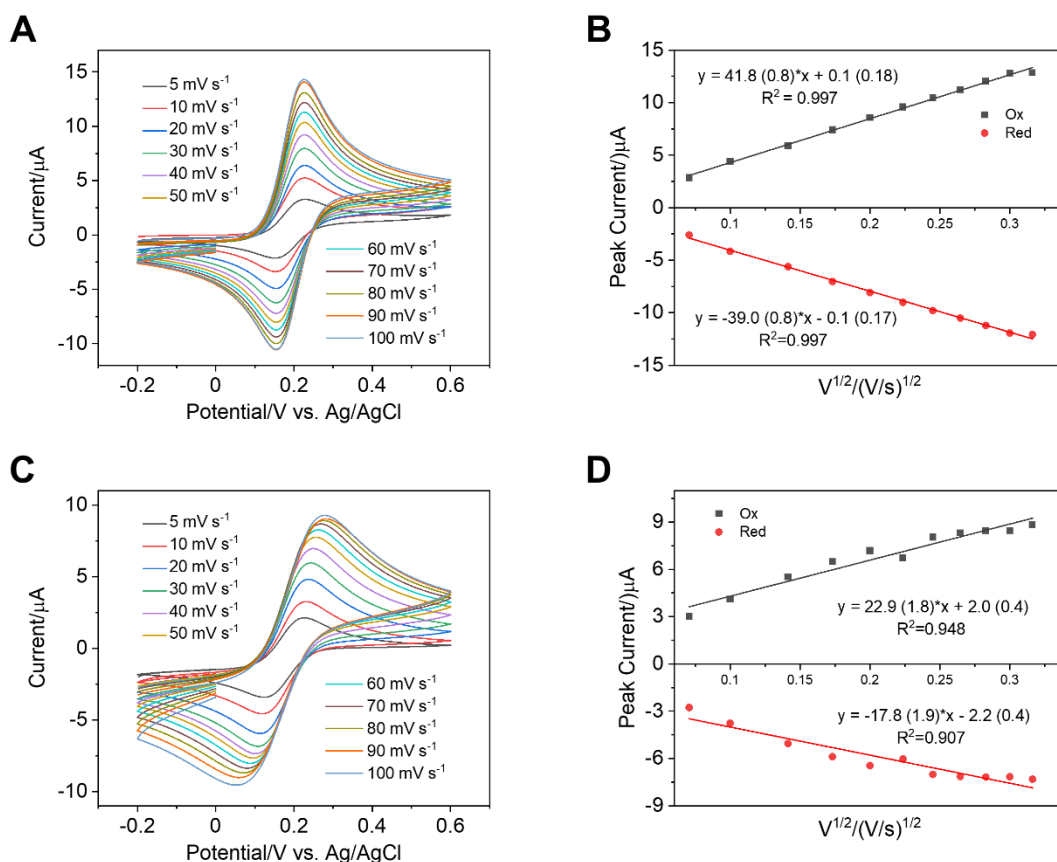


Figure 4.23. Cyclic voltammograms recorded with CPE_C_g at different scan rates, in a 0.1 M KNO_3 solution containing 1 mM ferrocene redox species (A) and 1 mM ferricyanide redox pair (C), and plots of anodic peak and cathodic peak currents vs. the square root of the scan rate (B and D). (B) is plotted from the measurements of ferrocene redox species and (D) is obtained from the measurements of ferricyanide redox pair.

To better assess the electrochemical performance displayed by the different carbon materials, we calculated their apparent heterogeneous electron transfer rate constants (K_{app}^0) from cyclic voltammograms recorded at different scan rates (Table 4.8). This was done without correcting double-layer effects and following the Nicholson method as described in detail in our previous work.⁵⁴ The largest K_{app}^0 values, from both the outer-sphere redox probe of ferrocene and inner-sphere redox probe of ferricyanide redox pair were obtained for C_c, while C_o exhibited the lowest electron transfer rates.

The electrochemical performance of the different wood-based carbons can be correlated to the wood characteristics by considering the results obtained from Thermogravimetry, Raman spectroscopy, BET measurements, shown in Chapter 3, together with the electrochemical characterization that was just shown (Table 4.8).

Table 4.8. The data comparison of the results from TG analyses, Raman spectrum analyses, BET analyses and electrochemical measurements.

		C _p	C _c	C _o
TG analysis	Percentage of hemicellulose in the wood by-product material	45%	33%	51%
	Percentage of cellulose + lignin in the wood by-product material	55%	67%	49%
Raman spectrum analysis	I_G/I_D	0.43	0.59	0.31
BET analysis	Surface area (m²g⁻¹)	31.0 ± 0.2	32.8 ± 0.1	18.9 ± 0.1
	Total pore volume (*10⁻³ cm³g⁻¹)	31 ± 1	41 ± 1	22 ± 1
Electrochemical performance	K_{app}⁰[*10⁻⁴ cm s⁻¹]_{ferrocene}	410±74	510±76	380±51
	K_{app}⁰[*10⁻⁴ cm s⁻¹]_{ferricyanide}	18±3	27±2	10±3

The TG analysis revealed that the wood by-products under study presented different proportions of hemicellulose, cellulose and lignin. These polymers will determine the carbon sp² content, 3D structure, and defect distribution that in turn define the material electronic conductivity, surface area and porosity as well as the catalytic activity.^{57,58} Our study shows

that the electrochemical response of the wood-derived carbons is negatively impacted by hemicellulose but positively correlated with the presence of cellulose and lignin, in agreement with previous literature.⁵⁹ This result can be attributed to the molecular composition of hemicellulose, cellulose and lignin.^{60–62} Hemicellulose is an amorphous polymer made of heterogeneous monosaccharide units (arabinoxylans, arabinogalactans, β -glucans, *etc.*).⁶⁰ After the thermal depolymerization of hemicellulose into a variety of monosaccharides, thermal degradation and ring rearrangement occur. Due to the differences in the thermal stability of each monosaccharide unit, the carbon rearrangement could be hindered and result in a low degree of sp^2 carbon.⁵⁹ On the other hand, cellulose is composed of β -glucose single monomer.⁶¹ Such a uniform composition may facilitate the recombination of carbon rings into carbon sheets with sp^2 arrangements.^{59,63} Lignin is a highly thermally-resistant component due to its rich amount of crosslinked bonds.⁶² With the slow kinetics of its thermal decomposition and a higher pyrolytic temperature, the formation of sp^2 structure could be favored in lignin.⁶³ In turn, graphite-like sp^2 bonds improve the electrical transport properties of the material,^{64,65} which results in a better electrochemical performance. Indeed, the electrodes prepared from the wood with the lowest hemicellulose content, CPE_C_c, show an excellent electrochemical response considering the measurements carried out with the representative redox species. The obtained K^0_{app} values are almost 2 times larger than that of commercial graphite powder, which has the K^0_{app} values of $220 \pm 60 \cdot 10^{-4} \text{ cm s}^{-1}$ for ferrocene and $15 \pm 3 \cdot 10^{-4} \text{ cm s}^{-1}$ for ferricyanide. Thus, sample C_c was selected to further explore the potential of chestnut wood-derived material in electrochemical sensor applications.

4.5 Conclusion

We demonstrated the excellent electrochemical performance of the produced composites consisting of a porous C matrix and Cu₂O or Cu nanoparticles for the reliable detection of COD in real wastewater samples. All of them were analytically validated in the detection of COD using glucose as a standard analyte and the analysis of water samples collected at three different locations of a WWTP gave COD values quite similar among the different materials and in agreement with those obtained by the standard dichromate method. The Cu/C₁ material, prepared by a one-pot synthesis, is the most promising material considering both the ease of manufacturing and its analytical performance.

The potential of the Ag/C nanocomposite for analyzing halides (Cl^- , Br^- and I^-) and organohalides (sucralose and trichloroacetic acid) was evaluated and the achieved results indicate that bread waste can be upcycled to high-added-value materials by doping with specific nanoparticles and application for electrochemical sensor purposes, thus contributing to the circular bio-economy.

The electrochemical performance of the carbon materials derived from wood by-products was successfully assessed. The biomass-carbon-electrochemistry correlations were also unlocked. The carbon material derived from the Chestnut wood shows better electrochemical performance and will be further explored for electrochemical sensor applications.

The preparation approaches for the three types of materials are compatible with upscaling processes for mass manufacturing and cost-effective fabrication of electrochemical sensors using screen-printing fabrication approaches. This opens up new opportunities for the development of portable, low-cost electrochemical sensors, offering the possibility of on-site detection of water pollutants.

References

1. Maduraiveeran G, Jin W. Nanomaterials based electrochemical sensor and biosensor platforms for environmental applications. *Trends in Environmental Analytical Chemistry*. 2017 Jan 1;13:10-23.
2. Waheed A, Mansha M, Ullah N. Nanomaterials-based electrochemical detection of heavy metals in water: Current status, challenges and future direction. *TrAC Trends in Analytical Chemistry*. 2018 Aug 1;105:37-51.
3. Svancara I, Kalcher K, Walcarius A, Vytras K. *Electroanalysis with carbon paste electrodes*. Crc Press; 2012 Mar 9.
4. Santos AM, Wong A, Vicentini FC, Fatibello-Filho O. Simultaneous voltammetric sensing of levodopa, piroxicam, ofloxacin and methocarbamol using a carbon paste electrode modified with graphite oxide and β -cyclodextrin. *Microchimica Acta*. 2019 Mar;186(3):1-9.
5. Gutiérrez-Capitán M, Baldi A, Gómez R, García V, Jiménez-Jorquera C, Fernández-Sánchez C. Electrochemical nanocomposite-derived sensor for the analysis of chemical oxygen demand in urban wastewaters. *Analytical chemistry*. 2015 Feb 17;87(4):2152-60.
6. Niu P, Asturias-Arribas L, Jordà X, Goñi AR, Roig A, Gich M, Fernández-Sánchez C. Carbon-Silica Composites to Produce Highly Robust Thin-Film Electrochemical Microdevices. *Advanced Materials Technologies*. 2017 Dec;2(12):1700163.
7. Hammerich O, Speiser B, editors. *Organic electrochemistry*. Boca Raton, FL: CRC press; 2016.
8. Feeney R, Kounaves SP. Determination of heterogeneous electron transfer rate constants at microfabricated iridium electrodes. *Electrochemistry communications*. 1999 Oct 1;1(10):453-8.
9. Zhang J, Shao Y, Liu G, Qi L, Wang H, Xu X, Liu S. Wastewater COD characterization: RBCOD and SBCOD characterization analysis methods. *Scientific reports*. 2021 Jan 12;11(1):1-0.

10. Carchi T, Lapo B, Alvarado J, Espinoza-Montero PJ, Llorca J, Fernández L. A Nafion film cover to enhance the analytical performance of the CuO/Cu electrochemical sensor for determination of chemical oxygen demand. *Sensors*. 2019 Feb 6;19(3):669.
11. Wang Q, Del Valle M. Determination of chemical oxygen demand (COD) using nanoparticle-modified voltammetric sensors and electronic tongue principles. *Chemosensors*. 2021 Feb 27;9(3):46.
12. Silva CR, Conceição CD, Bonifácio VG, Teixeira MF. Determination of the chemical oxygen demand (COD) using a copper electrode: a clean alternative method. *Journal of Solid State Electrochemistry*. 2009 May;13(5):665-9.
13. Bard AJ, Faulkner LR, White HS. *Electrochemical methods: fundamentals and applications*. John Wiley & Sons; 2022 May 3.
14. Byers JC, Güell AG, Unwin PR. Nanoscale electrocatalysis: visualizing oxygen reduction at pristine, kinked, and oxidized sites on individual carbon nanotubes. *Journal of the American Chemical Society*. 2014 Aug 13;136(32):11252-5.
15. Cao Y, Yu H, Peng F, Wang H. Selective allylic oxidation of cyclohexene catalyzed by nitrogen-doped carbon nanotubes. *ACS Catalysis*. 2014 May 2;4(5):1617-25.
16. Directive EU. Council Directive of 21. May 1991 concerning urban waste water treatment (91/271/EEC). *J. Eur. Commun.* 1991;34:40.
17. Badr IH, Hassan HH, Hamed E, Abdel-Aziz AM. Sensitive and Green Method for Determination of Chemical Oxygen Demand Using a Nano - copper Based Electrochemical Sensor. *Electroanalysis*. 2017 Oct;29(10):2401-9.
18. Hassan HH, Badr IH, Abdel-Fatah HT, Elfeky EM, Abdel-Aziz AM. Low cost chemical oxygen demand sensor based on electrodeposited nano-copper film. *Arabian Journal of Chemistry*. 2018 Feb 1;11(2):171-80.
19. Huang X, Zhu Y, Yang W, Jiang A, Jin X, Zhang Y, Yan L, Zhang G, Liu Z. A self-supported CuO/Cu nanowire electrode as highly efficient sensor for COD measurement. *Molecules*. 2019 Aug 28;24(17):3132.
20. Hong BD, Lee CL. Specific activities of rhombic dodecahedral, octahedral, and cubic Cu₂O nanocrystals as glucose oxidation catalysts. *Chemical Engineering Journal*. 2020 Feb 15;382:122994.

21. Xu H, Wang W, Zhu W. Shape evolution and size-controllable synthesis of Cu₂O octahedra and their morphology-dependent photocatalytic properties. *The Journal of Physical Chemistry B*. 2006 Jul 20;110(28):13829-34.
22. Huang WC, Lyu LM, Yang YC, Huang MH. Synthesis of Cu₂O nanocrystals from cubic to rhombic dodecahedral structures and their comparative photocatalytic activity. *Journal of the American Chemical Society*. 2012 Jan 18;134(2):1261-7.
23. Li X, Lin D, Lu K, Chen X, Yin S, Li Y, Zhang Z, Tang M, Chen G. Graphene oxide orientated by a magnetic field and application in sensitive detection of chemical oxygen demand. *Analytica Chimica Acta*. 2020 Jul 25;1122:31-8.
24. Diksy Y, Rahmawati I, Jiwanti PK, Ivandini TA. Nano-Cu modified Cu and nano-Cu modified graphite electrodes for chemical oxygen demand sensors. *Analytical Sciences*. 2020:20P069.
25. Droog JM, Alderliesten PT, Bootsma GA. Initial stages of anodic oxidation of silver in sodium hydroxide solution studied by potential sweep voltammetry and ellipsometry. *Journal of Electroanalytical Chemistry and Interfacial Electrochemistry*. 1979 May 25;99(2):173-86.
26. Bayesov A, Tuleshova E, Tukibayeva A, Aibolova G, Baineysheva F. Electrochemical behavior of silver electrode in sulphuric acidic solution during anodic polarization. *Oriental journal of Chemistry*. 2015;31(4):1867.
27. Stonehart P, Portante FP. Potentiodynamic examination of surface processes and kinetics for the Ag₂O/AgO/OH⁻ system. *Electrochimica Acta*. 1968 Aug 1;13(8):1805-14.
28. Qin X, Wang H, Miao Z, Wang X, Fang Y, Chen Q, Shao X. Synthesis of silver nanowires and their applications in the electrochemical detection of halide. *Talanta*. 2011 May 15;84(3):673-8.
29. Chiu MH, Cheng WL, Muthuraman G, Hsu CT, Chung HH, Zen JM. A disposable screen-printed silver strip sensor for single drop analysis of halide in biological samples. *Biosensors and Bioelectronics*. 2009 Jun 15;24(10):3008-13.
30. Bujes-Garrido J, Izquierdo-Bote D, Heras A, Colina A, Arcos-Martínez MJ. Determination of halides using Ag nanoparticles-modified disposable electrodes. *A*

first approach to a wearable sensor for quantification of chloride ions. *Analytica chimica acta*. 2018 Jul 5;1012:42-8.

31. Arai K, Kusu F, Noguchi N, Takamura K, Osawa H. Selective determination of chloride and bromide ions in serum by cyclic voltammetry. *Analytical biochemistry*. 1996 Aug 15;240(1):109-13.
32. Patella B, Aiello G, Drago G, Torino C, Vilasi A, O'Riordan A, Inguanta R. Electrochemical detection of chloride ions using Ag-based electrodes obtained from compact disc. *Analytica Chimica Acta*. 2022 Jan 15;1190:339215.
33. Singare PU, Ansari MV, Dixit NN. Water pollution along the Mahul Creek of Mumbai, India—Study of physico-chemical properties. *International Letters of Natural Sciences*. 2014;11(1).
34. Yadav M, Ganesan V, Gupta R, Yadav DK, Sonkar PK. Cobalt oxide nanocrystals anchored on graphene sheets for electrochemical determination of chloramphenicol. *Microchemical Journal*. 2019 May 1;146:881-7.
35. Guo X, Wang J. Comparison of linearization methods for modeling the Langmuir adsorption isotherm. *Journal of Molecular Liquids*. 2019 Dec 15;296:111850.
36. Peng D, Li Y, Huang Z, Liang RP, Qiu JD, Liu J. Efficient DNA-catalyzed porphyrin metalation for fluorescent ratiometric Pb²⁺ detection. *Analytical chemistry*. 2019 Aug 15;91(17):11403-8.
37. Lou YY, Fontmorin JM, Amrane A, Fourcade F, Geneste F. Metallic nanoparticles for electrocatalytic reduction of halogenated organic compounds: A review. *Electrochimica Acta*. 2021 May 1;377:138039.
38. Foresti ML, Innocenti M, Forni F, Guidelli R. Electrosorption valency and partial charge transfer in halide and sulfide adsorption on Ag (111). *Langmuir*. 1998 Nov 24;14(24):7008-16.
39. Yin H, Cao X, Lei C, Chen W, Huang B. Insights into electroreductive dehalogenation mechanisms of chlorinated environmental pollutants. *ChemElectroChem*. 2020 Apr 17;7(8):1825-37.
40. Isse AA, Mussini PR, Gennaro A. New insights into electrocatalysis and dissociative electron transfer mechanisms: the case of aromatic bromides. *The Journal of Physical*

Chemistry C. 2009 Aug 20;113(33):14983-92.

41. Chen T, Liu Z, Lu W, Zhou X, Ma H. Fabrication of free-standing nanoporous silver by selectively dissolving gold from gold–silver alloys via a novel converse dealloying method. *Electrochemistry communications*. 2011 Oct 1;13(10):1086-9.
42. Bashami RM, Soomro MT, Khan AN, Aazam ES, Ismail IM, El-Shahawi MS. A highly conductive thin film composite based on silver nanoparticles and malic acid for selective electrochemical sensing of trichloroacetic acid. *Analytica Chimica Acta*. 2018 Dec 7;1036:33-48.
43. Liu B, Hu X, Deng Y, Yang S, Sun C. Selective determination of trichloroacetic acid using silver nanoparticle coated multi-walled carbon nanotubes. *Electrochemistry communications*. 2010 Oct 1;12(10):1395-7.
44. Nikolelis DP, Pantoulis S. A minisensor for the rapid screening of sucralose based on surface-stabilized bilayer lipid membranes. *Biosensors and Bioelectronics*. 2000 Nov 1;15(9-10):439-44.
45. Chiu MH, Cheng WL, Muthuraman G, Hsu CT, Chung HH, Zen JM. A disposable screen-printed silver strip sensor for single drop analysis of halide in biological samples. *Biosensors and Bioelectronics*. 2009 Jun 15;24(10):3008-13.
46. Choi HG, Laibinis PE. Electrochemical detection of chloride by underpotentially deposited silver films on polycrystalline gold. *Analytical chemistry*. 2004 Oct 1;76(19):5911-7.
47. Chu L, Zhang X. Electrochemical detection of chloride at the multilayer nano-silver modified indium-tin oxide thin electrodes. *Journal of Electroanalytical Chemistry*. 2012 Jan 15;665:26-32.
48. Zhang R, Xu S, Zhu Y, Luo J, Liu X, Tang D. One-pot facile preparation of Ag nanoparticles for chloride ion sensing. *Colloid and Polymer Science*. 2016 Oct;294(10):1643-9.
49. Liu B, Deng Y, Hu X, Gao Z, Sun C. Electrochemical sensing of trichloroacetic acid based on silver nanoparticles doped chitosan hydrogel film prepared with controllable electrodeposition. *Electrochimica acta*. 2012 Aug 1;76:410-5.
50. Kurd M, Salimi A, Hallaj R. Highly sensitive amperometric sensor for micromolar

detection of trichloroacetic acid based on multiwalled carbon nanotubes and Fe (II)–phtalocyanine modified glassy carbon electrode. *Materials Science and Engineering: C*. 2013 Apr 1;33(3):1720-6.

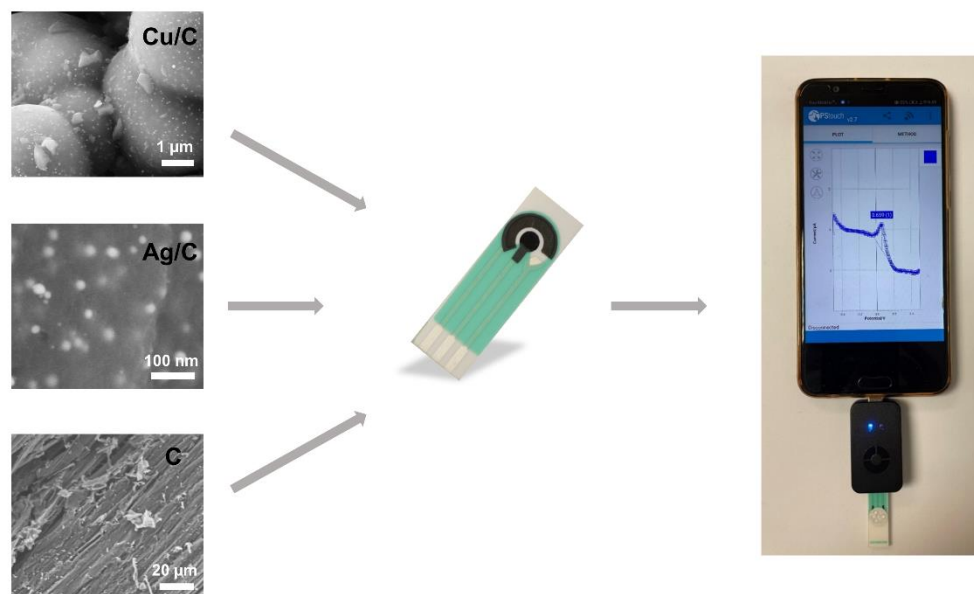
51. Qian D, Li W, Chen F, Huang Y, Bao N, Gu H, Yu C. Voltammetric sensor for trichloroacetic acid using a glassy carbon electrode modified with Au@ Ag nanorods and hemoglobin. *Microchimica Acta*. 2017 Jul;184(7):1977-85.
52. Tu W, Lei J, Ju H. Functionalization of carbon nanotubes with water -insoluble porphyrin in ionic liquid: direct electrochemistry and highly sensitive amperometric biosensing for trichloroacetic acid. *Chemistry – A European Journal*. 2009 Jan 5;15(3):779-84.
53. Dai H, Xu H, Wu X, Lin Y, Wei M, Chen G. Electrochemical behavior of thionine at titanate nanotubes-based modified electrode: A sensing platform for the detection of trichloroacetic acid. *Talanta*. 2010 Jun 15;81(4-5):1461-6.
54. Niu P, Asturias-Arribas L, Jordà X, Goñi AR, Roig A, Gich M, Fernández-Sánchez C. Carbon–Silica Composites to Produce Highly Robust Thin -Film Electrochemical Microdevices. *Advanced Materials Technologies*. 2017 Dec;2(12):1700163.
55. Chen P, Fryling MA, McCreery RL. Electron transfer kinetics at modified carbon electrode surfaces: the role of specific surface sites. *Analytical Chemistry*. 1995 Sep 1;67(18):3115-22.
56. Niu P, Asturias-Arribas L, Gich M, Fernández-Sánchez C, Roig A. Electrochemically active thin carbon films with enhanced adhesion to silicon substrates. *ACS Applied Materials & Interfaces*. 2016 Nov 16;8(45):31092-9.
57. Tabac S, Eisenberg D. Pyrolyze this paper: can biomass become a source for precise carbon electrodes?. *Current Opinion in Electrochemistry*. 2021 Feb 1;25:100638.
58. Sun X, Shan R, Li X, Pan J, Liu X, Deng R, Song J. Characterization of 60 types of Chinese biomass waste and resultant biochars in terms of their candidacy for soil application. *Gcb Bioenergy*. 2017 Sep;9(9):1423-35.
59. Feng Y, Tao L, He Y, Jin Q, Kuai C, Zheng Y, Li M, Hou Q, Zheng Z, Lin F, Huang H. Chemical-enzymatic fractionation to unlock the potential of biomass-derived carbon materials for sodium ion batteries. *Journal of Materials Chemistry A*.

2019;7(47):26954-65.

60. Swennen K, Courtin CM, Delcour JA. Non-digestible oligosaccharides with prebiotic properties. *Critical reviews in food science and nutrition*. 2006 Sep 1;46(6):459-71.
61. Pizzi A, Eaton N. The structure of cellulose by conformational analysis. 2. The cellulose polymer chain. *Journal of Macromolecular Science—Chemistry*. 1985 Jan 1;22(1):105-37.
62. Zhou X, Li W, Mabon R, Broadbelt LJ. A critical review on hemicellulose pyrolysis. *Energy Technology*. 2017 Jan;5(1):52-79.
63. Qin C, Wang H, Yuan X, Xiong T, Zhang J, Zhang J. Understanding structure-performance correlation of biochar materials in environmental remediation and electrochemical devices. *Chemical Engineering Journal*. 2020 Feb 15;382:122977.
64. Dwivedi N, Kumar S, Malik HK, Rauthan CM, Panwar OS. Correlation of sp³ and sp² fraction of carbon with electrical, optical and nano-mechanical properties of argon-diluted diamond-like carbon films. *Applied surface science*. 2011 May 15;257(15):6804-10.
65. Tomidokoro M, Tunmee S, Rittihong U, Euaruksakul C, Supruangnet R, Nakajima H, Hirata Y, Ohtake N, Akasaka H. Electrical conduction properties of hydrogenated amorphous carbon films with different structures. *Materials*. 2021 May 1;14(9):2355.

Chapter 5

Preparation and characterization of metal nanoparticle-modified carbon nanocomposite screen-printed electrodes



Summary

In this chapter, the three types of previously prepared materials, namely copper-based nanoparticle-modified porous carbon, bread waste-derived Ag/C composite, and carbon derived from wood by-products, were used to fabricate thick-film electrodes by screen-printing integrated in a common three-electrode electrochemical cell configuration. The electrochemical performance of the resulting electrochemical devices was thoroughly evaluated and applied to the detection of chemical oxygen demand (COD), halogenated compounds or heavy metals. Furthermore, a modified paper disk component was implemented in the devices with the aim of producing miniaturized sample-to-result electrochemical sensors of potential application to in-field analytical studies.

5.1 Introduction

Progress in the field of analytical chemistry is directed toward generating analytical data at the point of need.^{1–3} More and more fast, user-friendly, and portable devices that replace or complement bulky and expensive bench-top equipment are broadly demanded for many analytical applications, including environmental monitoring of chemical parameters used as water quality indicators. Such device approaches overcome different drawbacks related to the sample collection, transport, storage and measurement in centralized laboratories.⁴ In this context, electroanalytical tools have become a promising alternative due to the merits of sensitivity, miniaturization, portability, cost-effectiveness and low-power instrumentation requirements.^{1,4}

Screen-printing (thick film) fabrication technology is widely used for the large-scale manufacturing of low-cost electrochemical cells of a variety of configurations used for chemical sensor purposes.^{1,5,6} Screen-printed electrodes (SPEs) are commonly used as sensor platforms on a daily basis in many fields for carrying out discrete measurements where they are very often applied as single-use devices. This is an important feature to circumvent several drawbacks associated with conventional electrochemical devices such as glassy carbon or solid metal electrodes that are affected by electrode fouling when used repeatedly, frequent calibration and tedious pretreatment processes.⁷

In a scenario where discrete on-site measurements are to be carried out, a much simpler device that does not require any maintenance and can be operated by non-specialists would be the ideal solution. Hence, in this chapter, we develop a sample-to-result miniaturized electrochemical sensor approach for measuring water pollutants. The sensor incorporates a paper filtering disk component loaded with an electrolyte that, upon addition of a small sample volume, enables sample preconditioning and subsequent electrochemical measurement without any user intervention. Measurements can be carried out with compact, low-power instrumentation connected to a mobile device for in-field analytical studies.

5.2 Fabrication and electrochemical characterization of Cu/C screen-printed electrodes

5.2.1 Preparation of Cu/C ink and screen-printing fabrication of Cu/C composite electrodes

The synthesis method of Cu/C material is very similar to that of Cu/C₁ introduced in Chapter 3 (Figure 3.3B), with slight differences. The main one is the adjustment of the pH of the sol solution during the synthesis process which effectively improved the conductivity of the resulting material. The Cu/C nanocomposite powder with the desired particle size was mixed with a 15-20 wt.% nitrocellulose binder solution prepared in 2-Butoxyethyl acetate. The weight ratio of the material to binder was 3:1. Afterward, the mixture was stirred thoroughly with the assistance of 2.0 mm ZrO₂ balls until the resulting paste presented a honey-like texture. The ZrO₂ balls are used to enhance the dispersion of the Cu/C powder to avoid agglomeration. Afterward, the ink was used to fabricate the working electrode of the Cu/C composite screen-printed electrochemical device (SPE_Cu/C).

Electrochemical devices showing a three-electrode cell configuration (Figure 5.1) were manually screen printed on a polyethylene terephthalate (PET) substrate using a home-made screen-printing machine.⁸ The principles of the screen-printing process were described in Chapter 1, section 1.5. Firstly, Ag conducting tracks and the pseudo-reference electrode (725A silver pastes) were printed. Next, the ink made of Cu/C nanocomposite was applied to print the auxiliary and working electrodes. Finally, a dielectric layer (Electrodag PF-455B photocurable dielectric) was printed to cover the conducting silver tracks. 12 screen-printed electrodes printed on the same PET substrate could be obtained using around 0.4 g Cu/C material in one process and around 120 screen-printed electrodes could be printed in one batch with around 6 g Cu/C material. Then they were cut into individual electrodes using a CO₂ laser cutter (Figure 5.1).

Figure 5.2 A shows the SEM images of the rough surface of a screen-printed working electrode made of Cu/C nanocomposite. Surface morphology is similar to the surface of any carbon (graphite) screen-printed electrode on the market. The higher magnification SEM image (Figure 5.2 B) reveals that both the carbon and the particle components were dispersed in the ink. EDX analysis of the electrode surface in which the relative content of C and Cu were quantified indicates the presence of 4.3 wt.% Cu for a 95.7 wt. % of C.

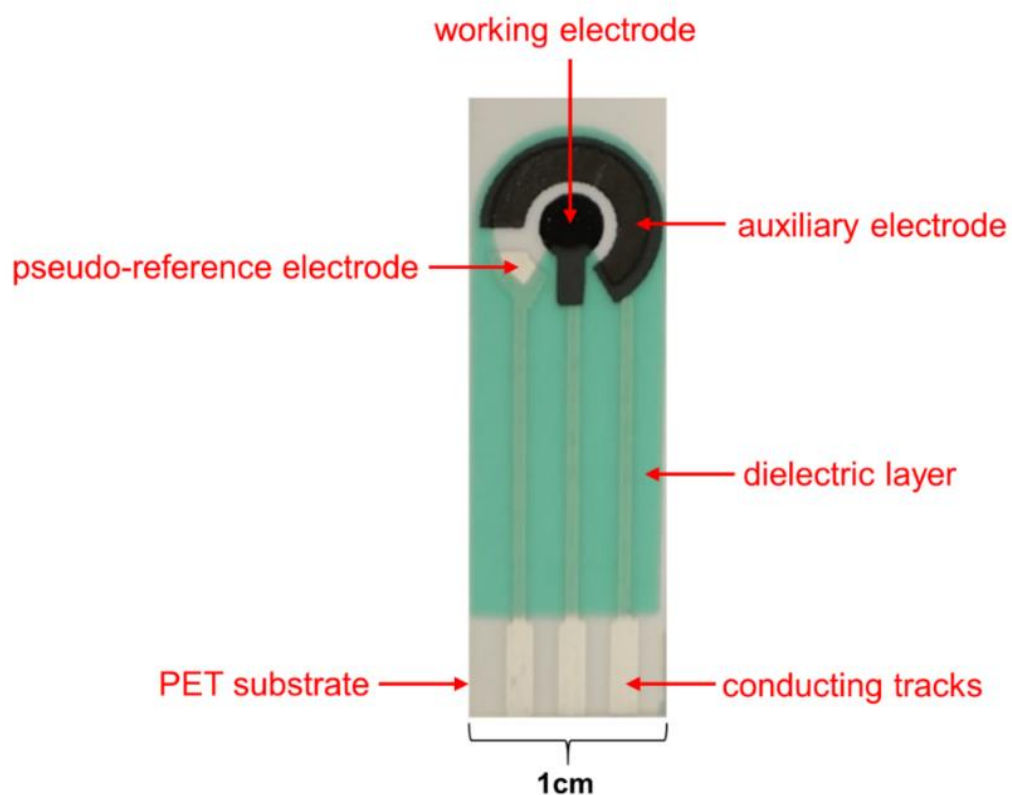


Figure 5.1. Optical image showing the different components of the screen-printed electrode.

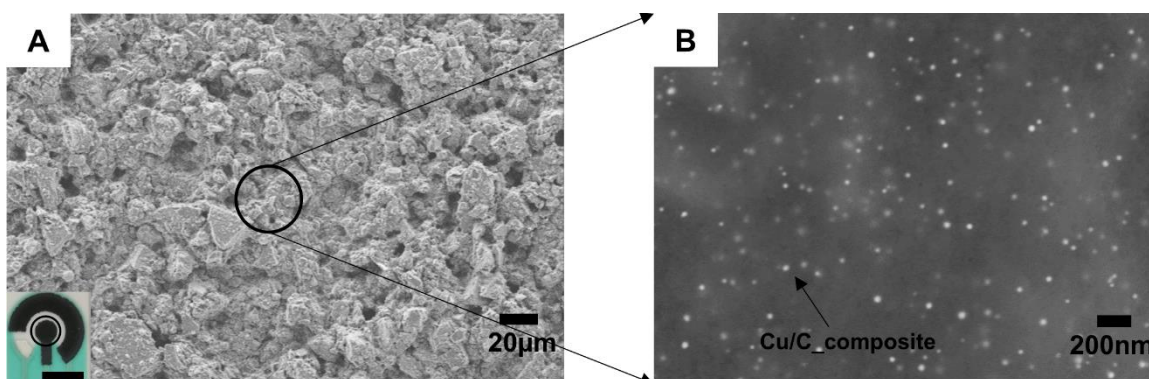


Figure 5.2. SEM images of the surface of a screen-printed Cu/C composite electrode. The inset in (A) is the photograph of the three-electrode cell of the SPE, where the scale bar is 0.5 cm.

5.2.2 Electrochemical assessment of SPE_Cu/C: analysis of COD

CV measurements were recorded in a 0.1 M KNO₃ solution containing 1 mM ferrocene-methanol to study the electrochemical performance of SPE_Cu/C (Figure 5.3 and Table 5.1). They exhibited a good electrochemical behavior assessed by considering the peak-to-peak potential separation of 139±12 mV and the anodic to cathodic peak current ratio of ca. 1.13±0.02. This performance reveals that the good conductivity of the Cu/C composite materials is not greatly affected when being used in the form of ink where the percentage of material is just 75 %.

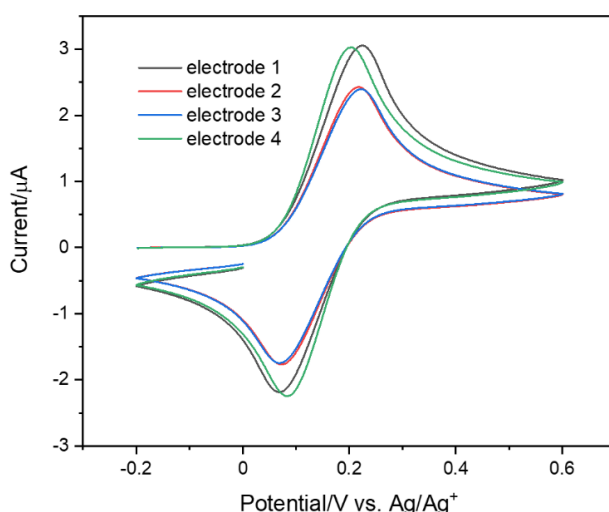


Figure 5.3. Cyclic voltammograms recorded in a 0.1 M KNO₃ solution containing 1 mM ferrocene- methanol using four different SPEs_Cu/C. The scan rate is 100 mV s⁻¹.

Table 5.1. Peak to peak potential separation and ratio of anodic to cathodic peak currents for the 4 electrodes tested.

	Electrod e 1	Electrod e 2	Electrod e 3	Electrod e 4	Mean Value	Standard Deviation
peak to peak separation (V)	0.149	0.139	0.146	0.122	0.139	0.012
anodic to cathodic peak current ratio	1.15	1.13	1.12	1.11	1.13	0.02

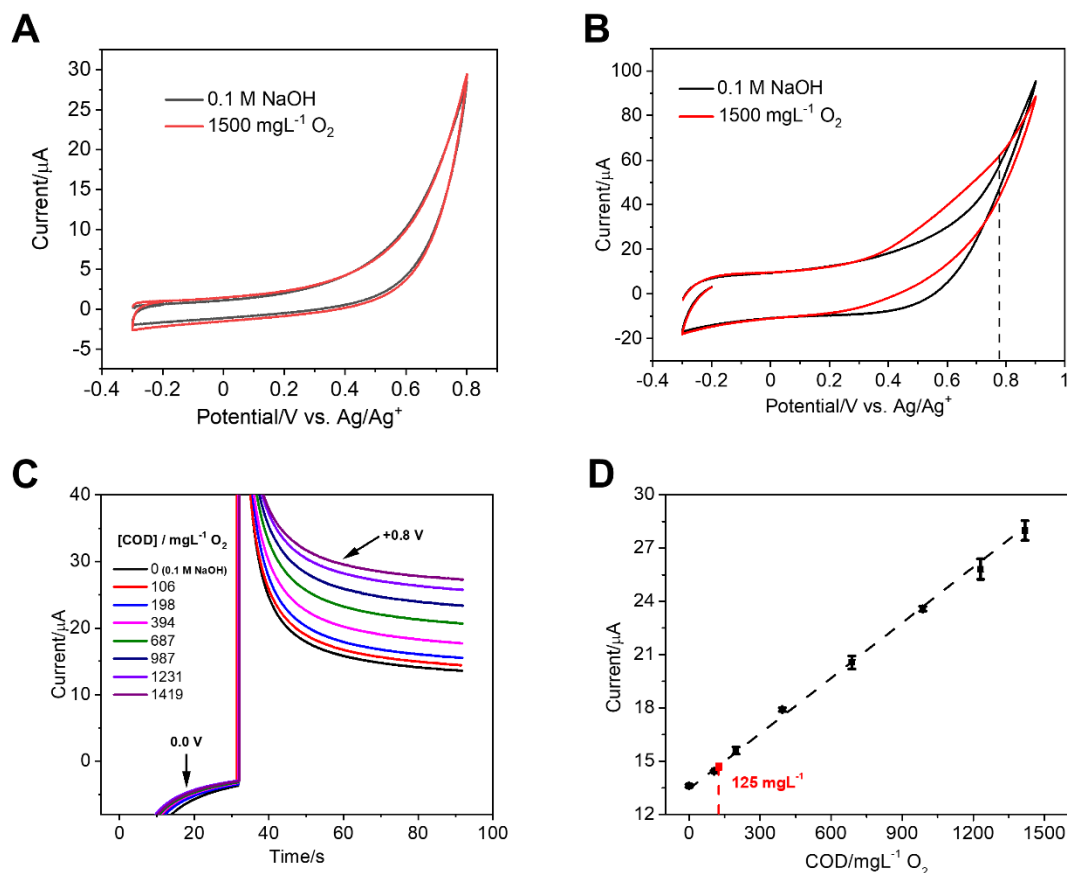


Figure 5.4. Cyclic voltammograms recorded in a 0.1 M NaOH solution before and after the addition of glucose using, (A) the SPE made of pure C and, (B) the SPE_Cu/C electrode, at a scan rate of 100 mV s⁻¹. The dotted line shows the overpotential chosen for carrying out the chronoamperometric studies. (C) Chronoamperometric responses of the screen-printed Cu/C electrode recorded in solutions ranging from 0 to 1419 mg L⁻¹ O₂ (equivalent to 0 to 1258 mg L⁻¹ of glucose). (D) Calibration curve of the screen-printed Cu/C electrode in the range between 0 and 1419 mg L⁻¹ O₂. The standard deviation of three measurements carried out consecutively and depicted as an error bar for each concentration.

The performance of the SPE_Cu/C as an electrochemical sensor for measuring COD was assessed using glucose as the standard analyte.^{9–11} First, a comparative study on the response of SPE electrodes produced with just the carbon material and with the Cu/C composite was carried out by cyclic voltammetry. We aim to investigate the possible contribution of the C component to the sensor response, considering the previously reported electrocatalytic response of some C materials to different target analytes under certain experimental conditions^{12,13}. The CVs shown in Figure 5.4 A were recorded in 0.1 M NaOH solutions with and without glucose. Since both curves are nearly identical, it is evidenced that no electrocatalytic processes due to the C material took place.

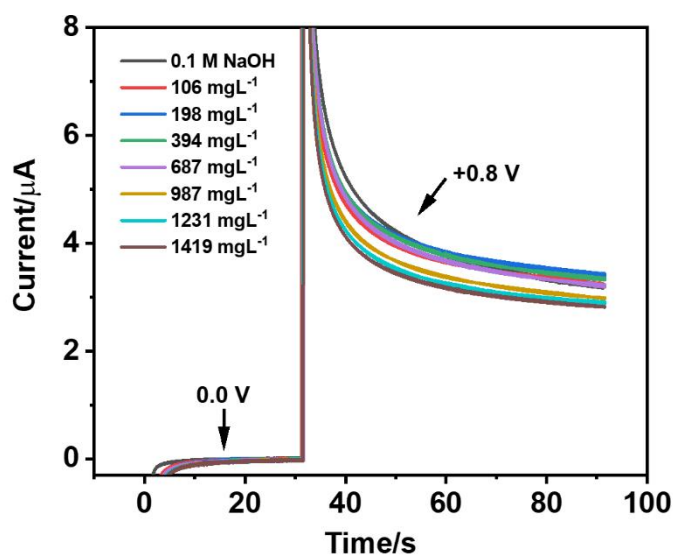


Figure 5.5. Chronoamperometric responses of the screen-printed C electrode recorded in solutions ranging from 0 to 1419 mg L⁻¹ O₂ (equivalent to 0 to 1258 mg L⁻¹ of glucose).

Table 5.2. Analytical parameters obtained from the calibration curves recorded with the different SP sensor approaches using glucose as standard analyte.

Sensor	Slope (nA mg ⁻¹ L O ₂)	intercept (μA)	R ² (n=3)	Linear range (mgL ⁻¹ O ₂)	LOD* (mgL ⁻¹ O ₂)
SPE_Cu/C	10.4±0.3	13.4±0.1	0.995	53-1419	23.6
SPE_Cu/C_paper	5.9±0.2	5.8±0.2	0.996	53-394	24.4
SPE_Cu/C_paper _{NaOH}	1.6±0.1	1.2±0.1	0.997	53-394	26.0

*LOD is calculated using the 3σ IUPAC criterion.

Figure 5.4 B shows the corresponding signals recorded with the SPE_Cu/C. Here, an oxidation wave at around +0.7 V vs Ag/AgCl was recorded in the glucose solution, which can be ascribed to the electrocatalytic effect of the Cu nanoparticles on the oxidation of this target analyte. An overpotential of +0.8 V vs Ag/AgCl was selected to carry out chronoamperometric measurements. These were also carried out with the SPE made of pure C. Figure 5.5 shows the chronoamperometric responses of the screen-printed C electrode recorded in solutions ranging from 0 to 1419 mg L⁻¹ O₂ (0 – 1258 mg L⁻¹ of glucose). The acquired curves tend to overlap in the range of lower glucose concentrations and the current will decrease as the concentration of glucose increases, confirming a negligible

contribution of the pure carbon material to the catalytic oxidation of glucose. The possible mechanism for the oxidation of organic chemical species by the Cu nanoparticles in an alkaline medium has been well explained in previous reports and details have been given in Chapter 1 of this thesis.^{14–17}

Figure 5.4 C shows the chronoamperometric response of SPE_Cu/C to different concentrations of glucose. The recorded current clearly increases with the glucose concentration in the solution. In these measurements, a potential of 0.0 V was initially set for 30 s, at which no redox reactions occurred and the current tended to zero. Then the potential was shifted to +0.8 V, at which the Cu nanoparticle electrocatalytic oxidation of glucose took place, and the anodic current was recorded for 60 s. The total time for one measurement was 90 s. Based on these chronoamperograms, the value of the current recorded at the 90 s time was used as the analytical signal. The corresponding calibration curve is presented in Figure 5.4 D, and the analytical parameters obtained from it are summarized in Table 5.2. The WWTPs have in the EU a legal limit of COD in the effluents, set to 125 mg L⁻¹ O₂, or a minimum 75% reduction of the organic load of the influent.^{9,18} Hence, the presented SPE_Cu/C sensor, with a LOD well below 125 mg L⁻¹ O₂, can be an excellent option for measuring the COD in wastewater.

5.2.3 Integration of a paper disk with the SPE_Cu/C sensor for one-step COD measurements

An excellent way to make the COD sensors more user-friendly is by reducing the number of manual steps required to perform an analysis, making it more amenable to be applied as an on-site sample-to-result device. To this aim, we devised a way to eliminate the sample filtering and pH conditioning steps by introducing a disk of filtering paper loaded with NaOH over the electrode area. The paper disk (Whatman® membrane filters nylon, WHA7404004) was laser cut to a suitable size. An adhesive vinyl plastic layer having several evenly distributed circular holes was also laser cut to be placed over the paper. The paper disk was used bare or loaded with NaOH. For this, 20 µl of a 0.5 M NaOH electrolyte solution was cast on the disk and left to dry at RT. The estimated NaOH mass was 0.4 mg. Then, the paper disk was integrated into the SPE, by fixing it on the electrode area with the aid of the vinyl plastic layer. The paper disk and the plastic layer were aligned, covering the entire electrode area (Figure 5.6 and 5.7).

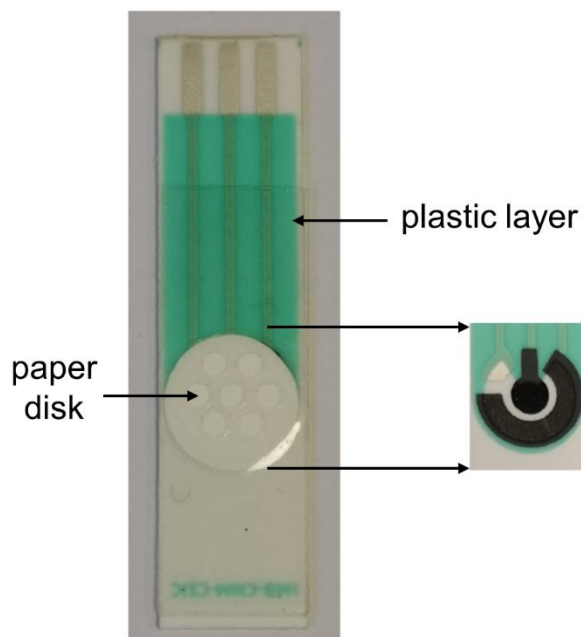


Figure 5.6. Representative image of the SPE_Cu/C with an integrated paper disk.

This paper disk enables sample preconditioning, which includes filtering and adjusting its pH and conductivity, so that the COD amperometric measurement can be done without any user intervention other than adding the required sample volume. Figure 5.6 and Figure 5.7 show an optical image and schematic representation of the implementation of the paper disk, respectively. Each measurement required the addition of 20 μL of solution carefully drop-cast over the holed plastic area. The solution was left to flow through the paper. It was shown that a 10-min time was sufficient for the solution to reach the electrode area before carrying out the chronoamperometric measurement.

We carried out a sequential assessment procedure to show that the paper disk did not compromise the sensor performance. First, chronoamperometric measurements were performed by introducing a bare paper disk without NaOH. The corresponding calibration curve was constructed using a 0.1 M NaOH solution containing different glucose concentrations (Figure 5.8).

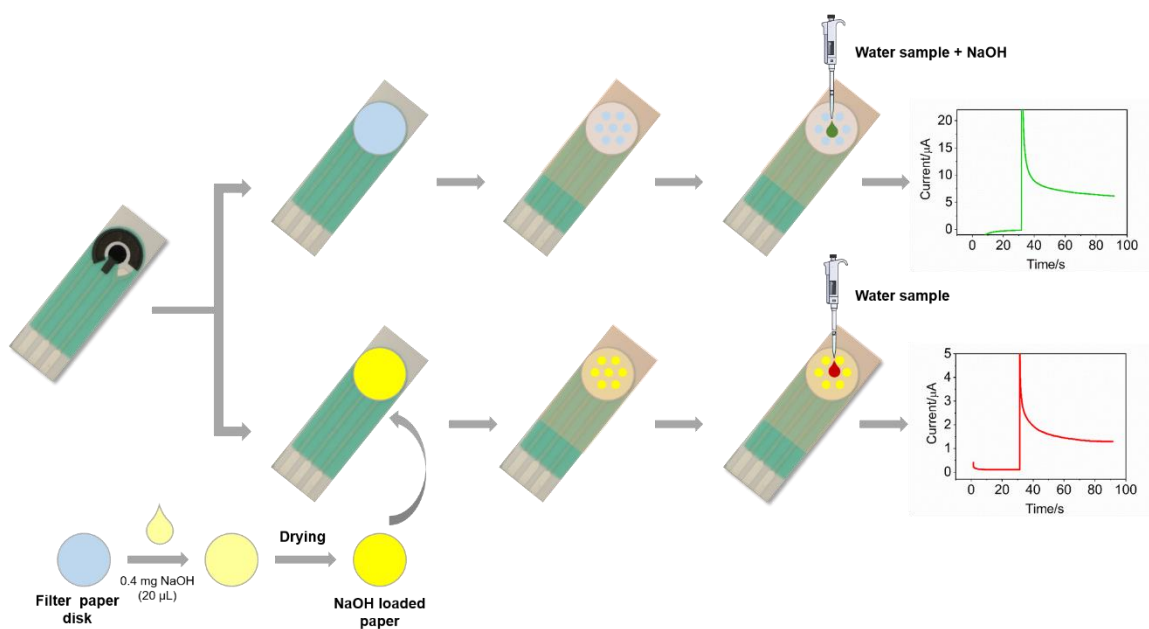


Figure 5.7. Schematic representation of the fabrication and analytical response of SPE_{Cu/C} with an integrated paper disk (top) and with an integrated paper disk loaded with NaOH (bottom).

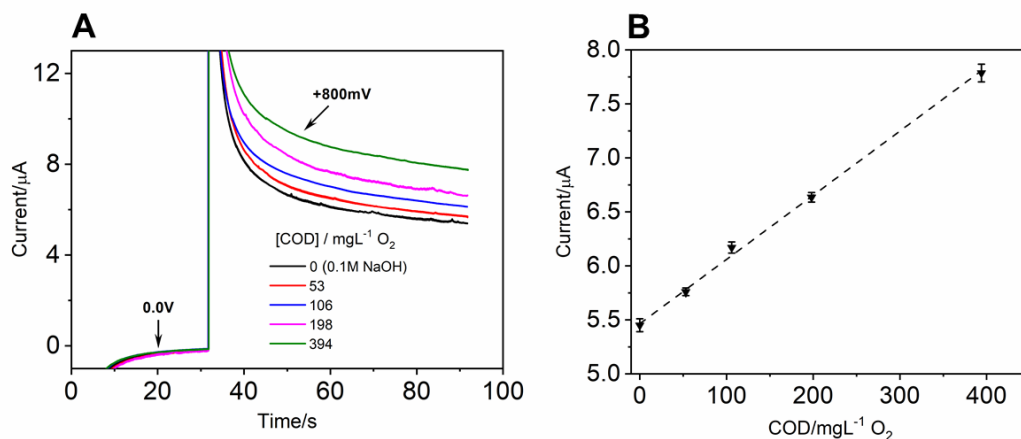


Figure 5.8. (A) Chronoamperometric responses of the SPE_{Cu/C} covered with the paper disk not loaded with NaOH were recorded in 0.1 M NaOH solutions containing different glucose amounts to set COD levels from 0 to 394 mg L⁻¹ O₂. For recording these signals, the potential was shifted from 0.0 V to +0.8 V vs Ag pseudo-reference electrode; (B) Corresponding calibration curve. The standard deviation of three measurements carried out consecutively and drawn as an error bar.

The total time for one measurement was 690 s (600 s for the sample to flow through the paper plus 90 s for recording the chronoamperometric signal). Figure 5.8 A displays the corresponding chronoamperometric signals for different concentrations of glucose, used as

an organic standard analyte. The value of the current recorded at 90 s was chosen as the analytical signal, as in the previous studies. The signal increases linearly with the glucose concentration. The corresponding calibration curve is presented in Figure 5.8 B, and the analytical parameters extracted from it are included in Table 5.2, for comparison purposes.

Second, the same study was repeated using a paper disk loaded with NaOH. Figure 5.9 shows the chronoamperograms and the calibration curve of the SPE_Cu/C covered with the filter paper loaded with NaOH (SPE_Cu/C_{paperNaOH}). The corresponding analytical parameters resulting are also included in Table 5.2.

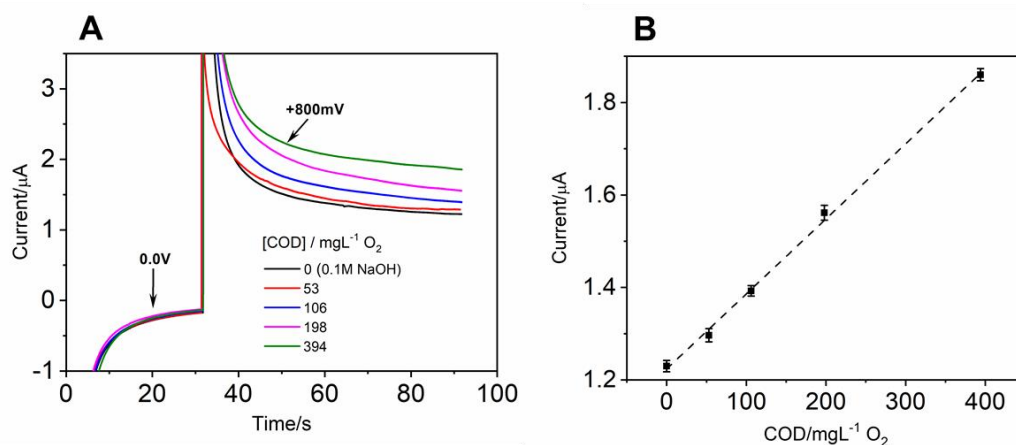


Figure 5.9. (A) Chronoamperometric responses of the SPE_Cu/C covered by the filter paper loaded with NaOH were recorded in water solutions containing different glucose amounts to set COD levels from 0 to 394mg L⁻¹O₂. For recording these signals, the potential was shifted from 0.0 V to 0.8 V vs Ag pseudo-reference electrode; (B) Corresponding calibration curve. The standard deviation of three measurements was carried out consecutively and drawn as an error bar.

From the values in Table 5.2, it can be seen that the sensitivity decreases upon implementation of the paper disk and the paper disk loaded with NaOH. It is also observed that the introduction of the paper shortens the linear range. However, the detection limit is maintained, and the value achieved with the complete COD sensor device is 26 mg L⁻¹O₂. As mentioned several times in the previous chapter, water samples from effluents of urban wastewater treatment plants cannot show organic matter concentrations above the legal limit of COD, set to 125 mg L⁻¹ O₂, or have to decrease by at least 75% with respect to the organic load of the influent.¹⁸ Thus, the SPE_Cu/C_{paperNaOH} sensor is very simple and user-friendly and could be applied to carry out discrete measurements of COD in-field in wastewater treatment plants, as shown below.

5.2.4 Analysis of water samples in the laboratory

In order to explore the practical application of the developed screen-printed electrodes, three sets of real water samples were collected at the urban WWTPS in La Garriga (Barcelona, Spain) and analyzed following a protocol previously set by our group.⁹ Upon reception of the real water samples, a certain volume of each sample was filtered using an OlimPeak filter, including a 0.45 μm Nylon membrane (Teknokroma, TR-200100). Then, both filtered and unfiltered samples were frozen at -20°C . During the following two weeks, samples were analyzed to avoid any errors coming from the possible alteration of the sample composition. The pH of these three samples was about 8. To carry out the measurements, they were thawed at room temperature and then diluted 1:1 with a 0.2 M NaOH solution to adjust the pH and ionic conductivity conditions at which the desired electrocatalytic process was favored, which is very similar to those used for plotting the calibration curves. Then, the three filtered water samples were analyzed using SPE_Cu/C, and both filtered and unfiltered samples were analyzed using the SPE_Cu/C_paper and SPE_Cu/C_paper_{NaOH} sensors. The recorded current intensities were interpolated into the corresponding calibration curve to calculate the COD value. COD analyses obtained with the dichromate standard method of the same samples were also conducted at an accredited laboratory (Applus Norcontrol, S.L.U, Laboratorio Análisis Químicos de Sada, A Coruña, Spain).⁹

As can be seen in Table 5.3, the values recorded with the three sensor approaches were quite similar, demonstrating that the paper component successfully performed in the filtering and preconditioning of the sample before the measurement. Moreover, the values recorded with the sensors are, within the error limits, consistent with the values obtained with the standard dichromate method carried out at a certified laboratory. By considering the COD value from the standard dichromate method as the “true” value, the relative error of the measurement provided by the sensors could be estimated (Table 5.3, red values). This is between 4 and 18 % for all the analyzed samples. These values are similar to the ones reported in previous works,¹⁹ demonstrating the potential of our sensor approach to quantitatively detect the soluble COD in real water samples.

Table 5.3. COD analysis of real water samples coming from a WWTP using SPE sensors and the standard dichromate method. Sample 1 – Exit effluent; Sample 2- Clarifier effluent; Sample 3 – Pretreatment effluent.

Electrodes	Sample 1 (mgL ⁻¹ O ₂)	Sample 2 (mgL ⁻¹ O ₂)	Sample 3 (mgL ⁻¹ O ₂)	Analysis Time	Pre- filtered
SPE_Cu/C	39±5 (+5.4%)	99±7 (+16.5%)	220±11 (+4.8%)	15 min	Yes
SPE_Cu/C_paper	40±4 (+8.1%)	96±7 (+12.9%)	218±11 (+3.8%)	10 min	Yes
SPE_Cu/C_paper	41±4 (+10.8%)	99±5 (+16.5%)	222±14 (+5.7%)	10 min	No
SPE_Cu/C_paper _{NaOH}	40±5 (+8.1%)	98±7 (+15.2%)	221±14 (+5.2%)	10 min	Yes
SPE_Cu/C_paper _{NaOH}	42±6 (+13.5%)	100±2 (+17.6%)	228±18 (+8.6%)	10 min	No
Dichromate method	37±8	85±18	210±25		Yes

In Table 5.4, the analytical performance of the very few electrochemical sensor devices based on screen-printed technology, previously reported for measuring COD, are summarized for comparative purposes. Basically, there are two previous reports of SPE sensors based on the use of Ni nanoparticles as electrocatalysts, electrodeposited on the surface of a carbon screen-printed electrode previously modified by drop-casting with graphene oxide. Such configuration is rather complex to be mass-produced. Moreover, COD analysis required manual sample conditioning using an electrolyte solution. Other SPE based on the use of Cu nanoparticles but not applied to the detection of COD have been studied and their main features are presented in Table 5.5. By contrast, and to the best of our knowledge, our work represents the first application of a sample-to-result miniaturized electrochemical sensor for measuring COD based on a screen-printed electrode that incorporates a paper disk component loaded with an electrolyte and just requires the addition of a small sample volume. The SPE is made of a Cu/C nanocomposite material prepared by a one-pot sol-gel synthesis approach. This one-pot method shows

unprecedented advantages for mass production and large-scale manufacturing of cost-effective electrochemical sensors.

Table 5.4. Comparative analytical features of previously reported electrochemical sensors for COD detection in wastewater and this thesis. COD standard analyte in [13, 14] was glycine, whereas glucose was used in this thesis.

Electrode type	Particle preparation method	Linear range (mgL ⁻¹); sensitivity (nA mg ⁻¹ L ⁻¹); limit of detection (mgL ⁻¹)	Comments	Ref.
Home-made C SPE modified with graphene oxide	Electrodeposition of Ni NPs	0.1-400; 6107; 0.02	Not suitable for mass production	13
Home-made C SPE modified with graphene oxide	Electrodeposition of Ni NPs	0.1-400; 3850; 0.05	Not suitable for mass production	14
SPE_Cu/C	One-pot synthesis of Cu/C composite	53-1419; 10.4±0.3; 23.6	Amenable for mass production.	This work
SPE_Cu/C_paper		53-394; 5.9±0.2; 24.4	User-friendly device for on-site application	
SPE_Cu/C_paper _{NaOH}		53-394; 1.62±0.04; 26.0		

Table 5.5 Analytical parameters of screen-printed electrode electrochemical sensors for glucose analysis from previous reports.

Electrode type	Particles	Notes	Linear range, sensitivity and limit of detection	Ref
Home-made screen-printed electrode	Commercial copper(II) oxide powder (physical mixing)	First example of a copper(II) oxide screen-printed electrode	50 μM to 1.2 mM, 4 (\pm 1) μM	19
Home-made screen-printed electrode	Electrodeposition of copper nanoparticles	Applied in blood samples	0.5 μM to 15 mM, 3225 $\mu\text{A mM}^{-1}\text{cm}^{-2}$, 0.06 μM	20
Home-made screen-printed electrode	Pd-CuO with reduced graphene (drop cast)	Applied in blood serum	6 μM to 22mM, 3355 $\mu\text{A mM}^{-1}\text{cm}^{-2}$, 0.03 μM	21
Home-made screen-printed electrode	Cu nanobelt (electrodeposition)		10 μM –1.13 mM, 79.8 $\mu\text{A mM}^{-1}\text{cm}^{-2}$, 10 μM	22
Screen-printed electrode from DropSens	In-situ grown flower-like nanostructured CuO	Commercial generic device	40 μM –2mM, 1460 $\mu\text{A mM}^{-1}\text{cm}^{-2}$, 2.5 μM	23
Screen-printed electrode from DropSens	Wet precipitation method to prepare Cu ₂ O-nanocubes (drop cast)	Commercial generic device	7 μM to 4.5 mM, 1040 $\mu\text{A mM}^{-1}\text{cm}^{-2}$, 3.1 μM	24
Home-made screen-printed electrode	Flower-like CuO and CuO/ MWCNTs (physical mixing)		4 μM to 14.5mM, 1211 $\mu\text{A mM}^{-1}\text{cm}^{-2}$, 4 μM	25

5.2.5 In-field analysis of COD in an urban WWTP

An analytical assessment of the COD sensor performance was carried out in-field at a WWTP (Figure 5.10). The Sensit Smartphone Minipotentiostat (PalmSens BV, Houten, The Netherlands) controlled by PStouch software for Android, was connected to a smartphone to carry out the measurements. Figure 5.10 A shows a picture of the COD instrument, using a compact potentiostat that allowed the direct connection of the sensor without the need for any additional wiring.



Figure 5.10. (A) Photograph of COD detection setup using a smartphone-based Chronoamperometric method; (B) photograph of in-field measurement of COD in the wastewater treatment plant.

Three sampling points (see Figure 5.11) were selected that were located in (1) the pretreatment effluent, (2) after the clarifier effluent and (3) at the exit (effluent). The three representative samples were collected at the same points as those previously analyzed in the lab. For performing an analysis, 20 μL of the sample was carefully drop-cast over the holed plastic area of the sensor and the solution was left to be filtered and flow through the paper disk for just 6 min to reach the electrode area. During these experiments, we could see that analysis times significantly shorter than those used previously were more adequate. This was important to prevent the effect that evaporation may have had on the sensor performance when measurements were carried out under sunny and windy weather conditions. Considering that the chronoamperometric measurements took 90 seconds, as in the measurements above, the overall analysis time was 450 s. The value of the current recorded at 90 s time was chosen as the analytical signal.



Figure 5.11. Photographs of the in-field COD measurements carried out at the urban wastewater treatment plant. (A) Sampling point at the pretreatment effluent, (B) Sampling point at the clarifier effluent, (C, and D) Sampling point at the exit (effluent).

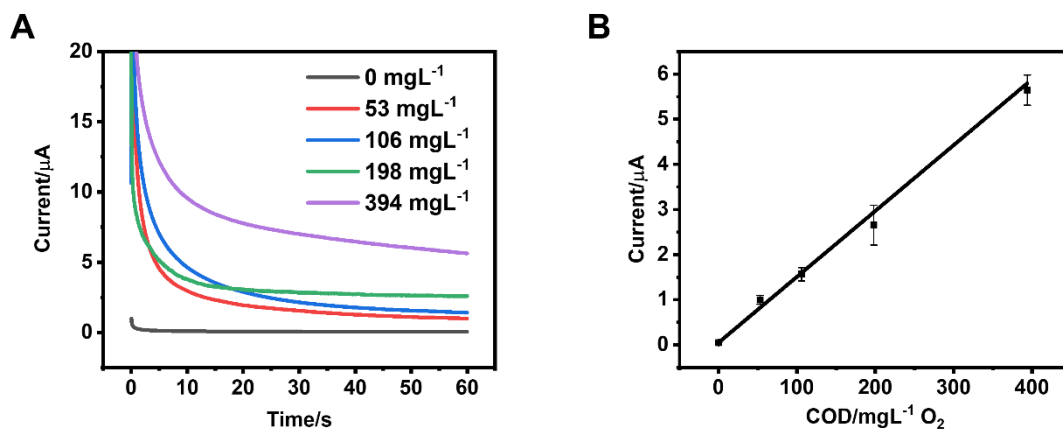


Figure 5.12. (A) Chronoamperometric responses of the SPE_Cu/C covered by the paper disk loaded with NaOH were recorded using the minipotentiostat in water solutions containing from 0 to 394 mg L⁻¹ O₂. To record these signals, the potential was applied as +0.8 V vs. Ag pseudo-reference electrode after pretreatment at 0.0 V for 30 s; (B) Corresponding calibration curve. Each point represents the mean value of three measurements performed consecutively and the error bars are the corresponding standard deviation.

COD values were estimated by interpolation of the recorded currents in the corresponding calibration curve (Figure 5.12). Calibration curves should be acquired for each batch of fabricated electrodes. This is carried out to compensate for any potential biases originating in any of the different sensor manufacturing steps. The automation of the sensor mass production may minimize these undesired effects. The COD values of the samples were 28 ± 6 , 57 ± 8 , and 195 ± 61 mg/L O₂ for the sampling points at the effluent, primary treatment, and solid sedimentation locations of the plant, respectively. These are consistent with the previous results recorded in the lab. These results point out that our integrated screen-printed electrochemical sensor successfully performed for analyzing COD in-field.

5.3 Fabrication and electrochemical characterization of screen-printed Ag/C electrodes

5.3.1 Preparation of Ag/C ink and screen-printing fabrication of Ag/C electrodes

The ink was prepared following the formulation of Cu/C ink described above, the difference being just the Ag/C powdered material. Briefly, this material was mixed with nitrocellulose binder solution (15-20 wt%) prepared in 2-Butoxyethyl acetate. The weight ratio of the Ag/C material to binder is 3:1. Then, the mixture was stirred thoroughly with the assistance of 2.0 mm ZrO₂ balls until the resulting paste presented a honey-like texture. The ZrO₂ balls are used to enhance the dispersion of the Ag/C powder to avoid agglomeration. Finally, the ink was used to print the working electrode of the Ag/C screen-printed electrochemical device (SPE_Ag/C).

Three-electrode electrochemical cells (Figure 5.13) were manually screen printed on PET substrates in the same fashion as with the SPE_Cu/C, described in section 5.2.1. Here, the pseudo-reference and auxiliary electrodes were printed using a commercial C ink (C2030519P4). Ag was avoided in the fabrication of the pseudo-reference electrode to avoid any leaching that could take place when in contact with the measuring solution and that could interfere with the Ag NPs performance. The produced Ag/C ink was used to print the working electrode. The produced SPEs are shown in (Figure 5.13 and 5.14). It should be noted that the pseudo-reference electrode clearly differed to that shown in Figure 5.1.

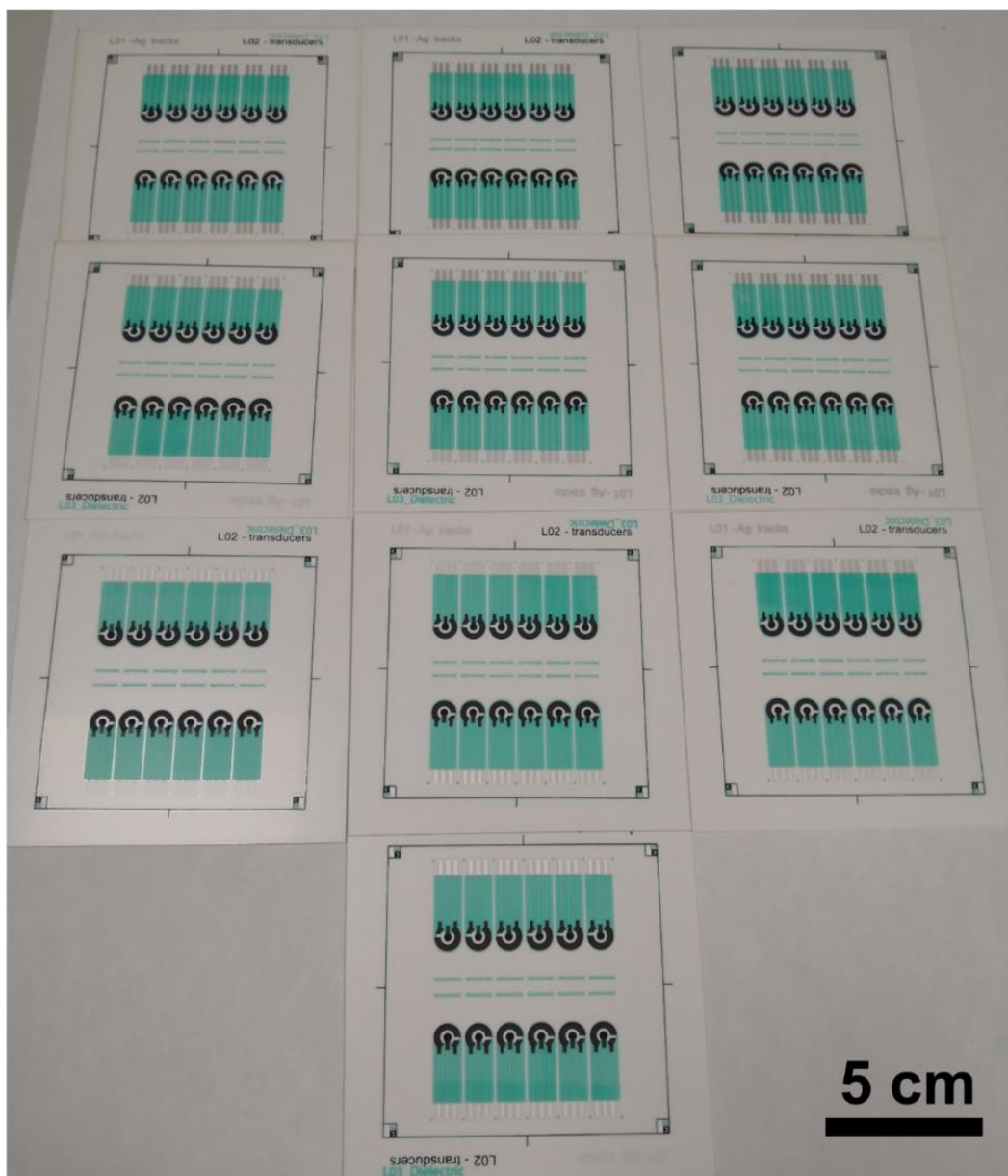


Figure 5.13. Optical image of the produced screen-printed electrodes.

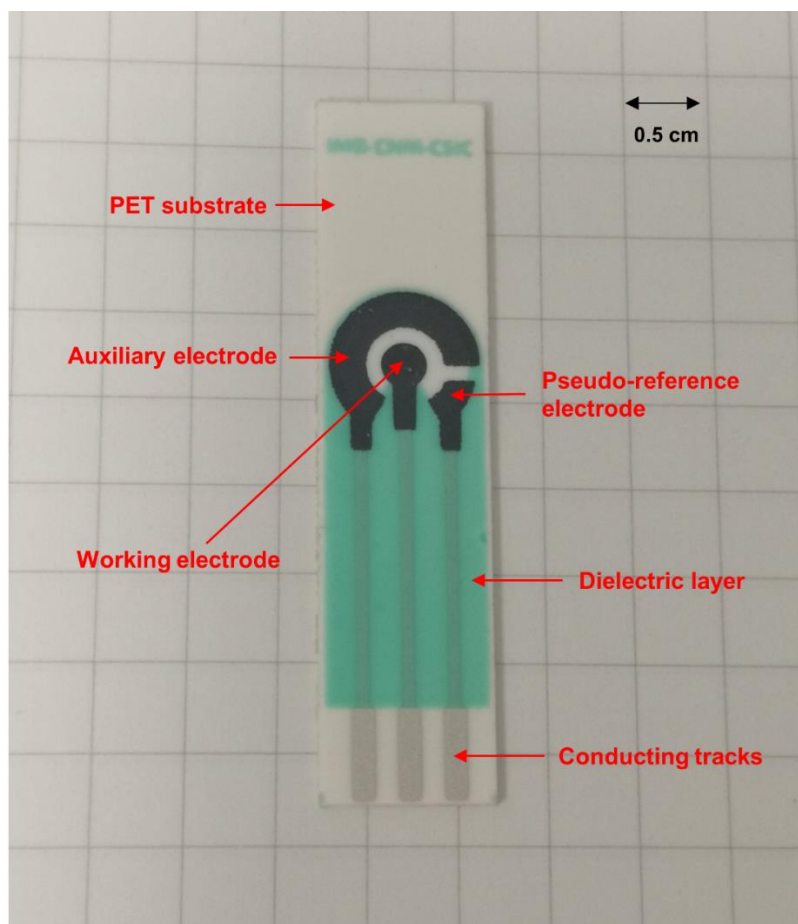


Figure 5.14. Optical image showing the different components of the screen-printed electrode.

Figure 5.15 depicts the SEM images of the rough surface of the screen-printed working electrode produced with the Ag/C nanocomposite ink. The surface morphology is similar to the surface of commercial carbon (graphite) screen-printed electrodes and the Ag/C material appears uniformly dispersed. The higher magnification SEM image in the secondary electron mode shown in Figure 5.15C reveals the existence of small bright particles on the surface and within the bulk of the material, which can be ascribed to the Ag NPs and the C component, respectively. The size distribution of the Ag NPs is between 12 nm and 18 nm, measured with the Image J software (Figure 5.16) on a detailed study of different SEM images. The Ag to C mass ratio on the electrode surface is around 10.8 wt% based on the EDX analysis (Figure 5.17 and Table 5.6).

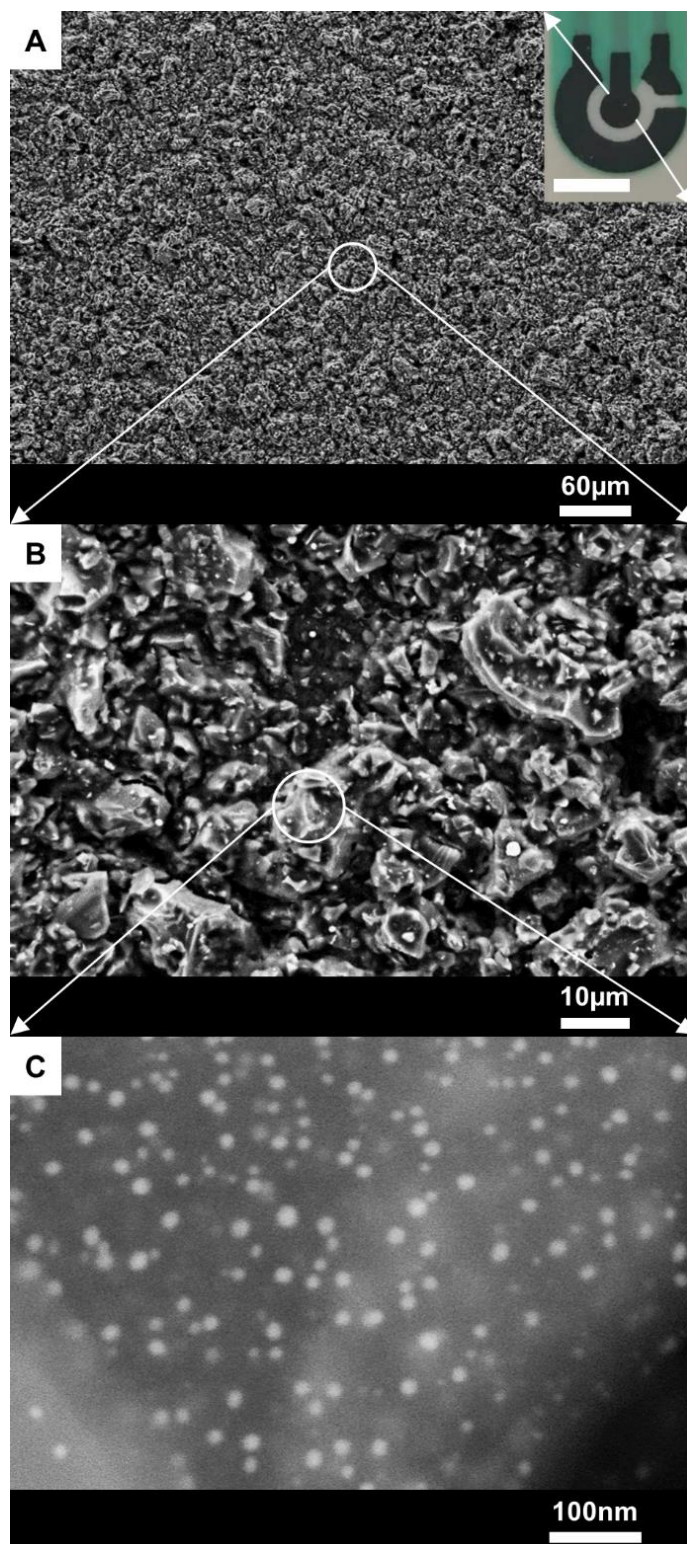


Figure 5.15. SEM images of the surface of a screen-printed Ag/C composite electrode. The inset in (A) is the photograph of the SPE three-electrode cell, where the scale bar is 0.5 cm.

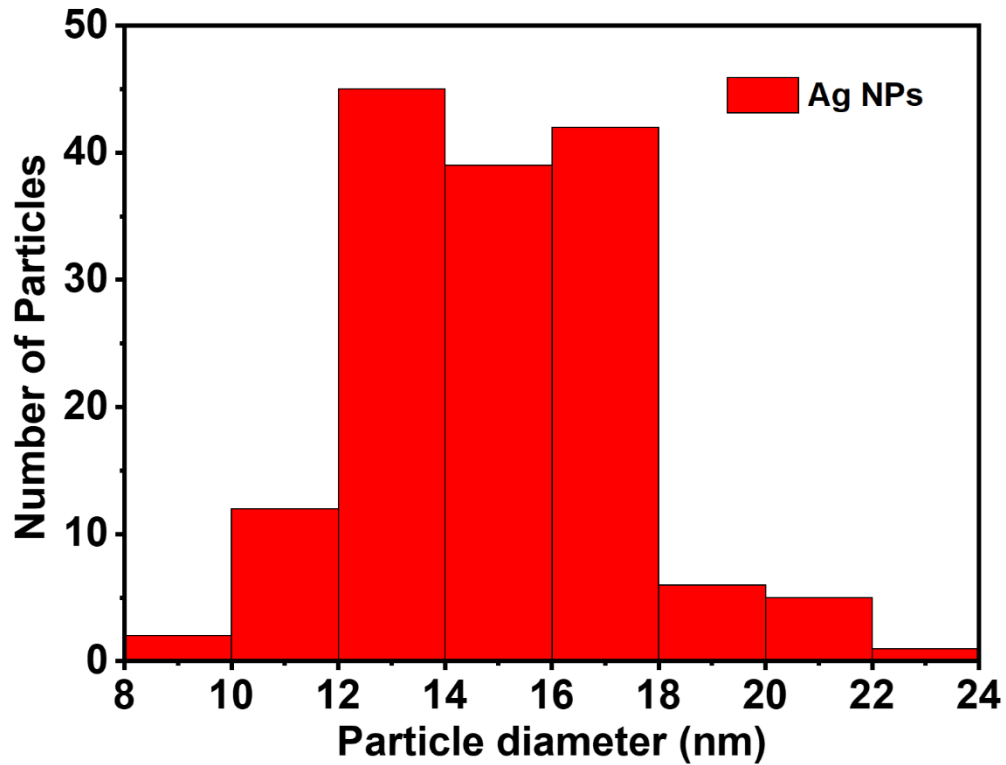


Figure 5.16. Ag nanoparticle size distribution histogram in SPE_Ag/C.

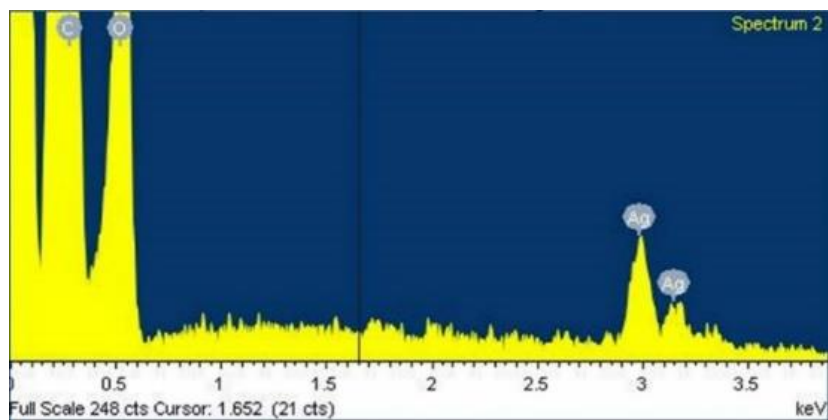


Figure 5.17. Energy dispersive spectroscopy (EDX) spectra of the working electrode material in SPE_Ag/C. The EDX analysis revealed the percentage of silver (Ag) and carbon (C) in the material.

Table 5.6. Composition of the working electrode material in SPE_Ag/C based on the EDX analysis.

Element	Wt.%	At.%
C	55.1	67.27
Ag	10.79	1.47
O	34.11	31.27

5.3.2 Electrochemical assessment of SPE_Ag/C: Analysis of Chloride

In order to evaluate the electrochemical performance of the produced SPE_Ag/C, 20 units from the same batch were tested in a 0.1M KNO₃ solution containing 1mM ferrocene-methanol electroactive redox species at a potential scan rate of 100 mVs⁻¹. 15 SPEs_Ag/C provide comparable signals, showing a peak-to-peak separation (ΔE_p) and anodic to cathodic peak current ratio of 187 ± 7 mV and 0.94 ± 0.02 , respectively (Table 5.7). Thus the fabrication yield was estimated to be 75%.

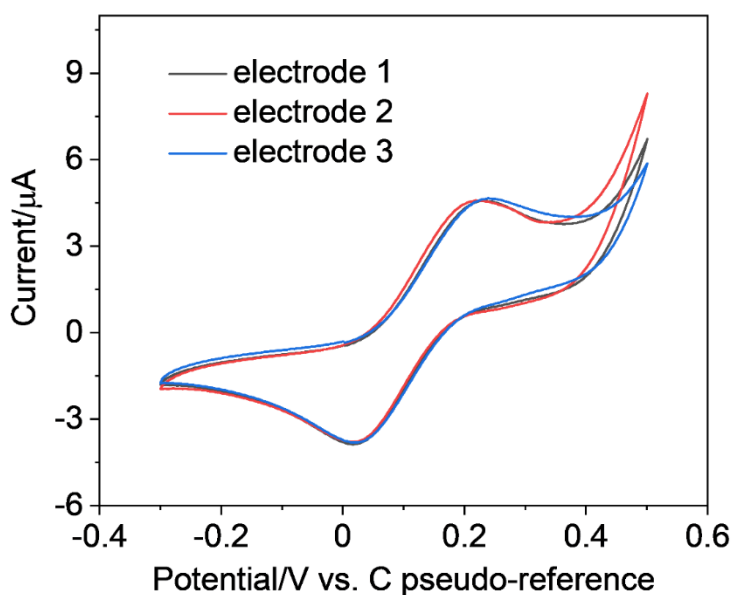


Figure 5.18. Cyclic voltammograms recorded in a 0.1M KNO₃ solution containing 1mM ferrocene-methanol using three different SPEs_Ag/C. The scan rate is 100 mV s⁻¹.

Table 5.7. Peak to peak separation and anodic to cathodic peak current ratio for different screen-printed Ag/C composite electrodes in a 0.1M KNO₃ solution containing 1mM ferrocene-methanol redox probe. The scan rate is 100 mV s⁻¹.

Electrodes	Peak to peak separation(mV)	Anodic peak current (μA)	Cathodic peak current (μA)	Anodic to cathodic peak current ratio
1	180	3.6	3.8	0.95
2	186	3.54	3.65	0.97
3	190	3.52	3.7	0.95
4	175	3.55	3.68	0.96
5	193	3.64	3.77	0.97
6	198	3.52	3.66	0.96
7	183	3.57	3.79	0.94
8	187	3.32	3.76	0.88
9	194	3.58	3.69	0.97
10	193	3.54	3.77	0.94
11	190	3.63	3.85	0.94
12	190	3.52	3.74	0.94
13	185	3.36	3.68	0.91
14	173	3.53	3.75	0.94
15	190	3.35	3.75	0.89
mean value	187	3.52	3.74	0.94
standard deviation	7	0.1	0.06	0.027
RSD	4%	3%	1.5%	2.8%

Figure 5.18 shows three examples of the cyclic voltammograms (CV) recorded with the SPE_Ag/C. The fabrication yield could be improved by optimizing different aspects of the material synthesis, such as the mixing of bread waste and Ag precursor, or using an automatic screen-printing machine.

A cyclic voltammogram was recorded in 0.075 M phosphate-buffered background solution pH 6 (PB) with a SPE_Ag/C to monitor the electrochemical redox process of Ag NPs (Figure 5.19). The recorded anodic peak at + 0.27 V could be ascribed to the oxidation of Ag and

the formation of Ag_2O .^{26–28} The cathodic peak centered at around -0.15 V could be related to the reduction of the Ag oxides and the formation of Ag^0 species on the electrode surface.^{26–28} Also, there is a sort of wave at around +0.45 V that could be ascribed to the formation of AgO, following a similar behavior to the one recorded in the characterization of the material using CPEs (Chapter 4, section 4.3.1). The peaks are not that nicely defined and this is likely to be due to the ink composition used for printing the electrode that shows a mass percentage of Ag/C material of just 75%, which influences the electrochemical performance of the electrode. This is commonplace with all commercial SPEs when compared with the conventional bulky electrode counterparts (screen-printed graphite electrodes versus glassy carbon or pyrolytic graphite electrodes).

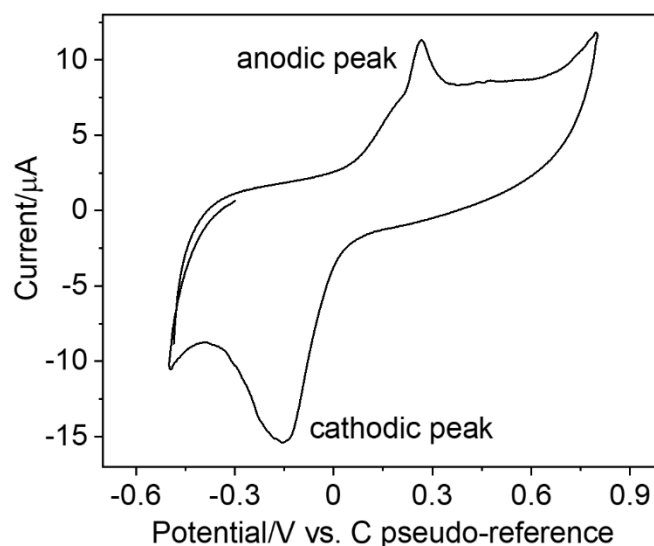


Figure 5.19. Cyclic voltammogram in PB solution (pH = 6.0) using screen-printed Ag/C composite electrode at scan rate of 100 mVs^{-1} .

Figure 5.20 shows the CV signals recorded in PB containing Cl^- concentrations in a range from $50 \mu\text{M}$ to $2723 \mu\text{M}$. A peak appears at $+0.19 \text{ V}$ (vs. C pseudo-ref. electrode), whose peak current steadily increases with the Cl^- concentration in the solution. This peak is produced by the oxidation of Ag^+ and the production of a AgCl precipitate. Also, the oxidation peak shifts to lower potentials when the Cl^- concentration increases, as expected from the Nernst equation.^{29,30} This is a similar phenomenon in the carbon paste electrodes (Chapter 4, section 4.3.1). A calibration curve was plotted, and the corresponding analytical

parameters were summarized in Table 5.8. Two linear ranges were observed, similar to those recorded with the CPEs in Chapter 4. Limits of detection in the low μM range were estimated. The measurements presented a good reproducibility reflected in small standard deviations obtained for each tested Cl^- concentration, the corresponding error bars being below 5%, in all cases. Here, Cl^- standard analyte was initially used to show the potential performance of the SPE_Ag/C for detecting chlorinated species. Then, the analysis of sucralose and trichloroacetic acid in waters was carried out in a similar fashion to the studies carried out in Chapter 4.

Table 5.8. Analytical parameters obtained from the calibration curves for Cl^- , sucralose and TCA analysis.

Sensor	Analyte	Method	Slope ($\text{nA } \mu\text{M}^{-1}$)	Intercept (μA)	R^2 (n=3)	LOD (μM)	Linear Range (μM)
SPE_Ag/C	Cl^-	CV	3.0 ± 0.1	0.030 ± 0.006	0.991	15.2	50-491
			0.50 ± 0.02	1.20 ± 0.02	0.994	-	491-2723
	sucralose	CV	0.20 ± 0.01	1.80 ± 0.01	0.993	145	200-2920
			0.030 ± 0.001	2.20 ± 0.01	0.991	-	3850-16690
	TCA	SWV	0.300 ± 0.003	0.70 ± 0.01	0.999	19.8	100-5508
SPE_Ag/C_paper	sucralose	CV	0.200 ± 0.004	0.200 ± 0.008	0.994	240	400-2920
			0.070 ± 0.001	0.70 ± 0.02	0.998	-	3850-13070
	TCA	SWV	0.200 ± 0.002	0.3000 ± 0.0007	0.999	23.8	100-4295

*Limit of detection (LOD) is calculated using the 3σ IUPAC criterion.

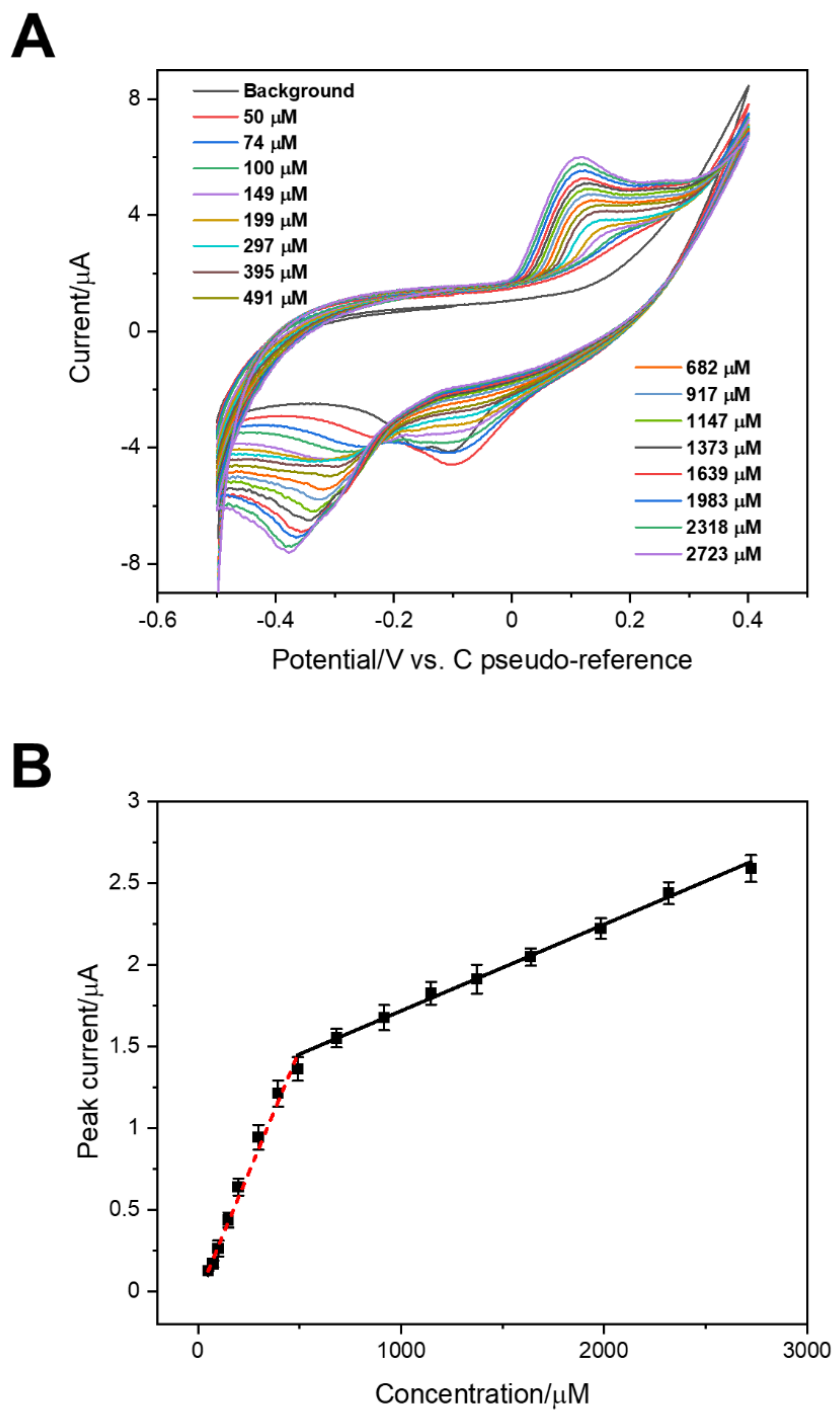


Figure 5.20. (A) Cyclic voltammograms recorded with SPE_Ag/C in PB solutions containing from 50 μM to 2723 μM Cl^- , (B) Calibration curve of the SPE_Ag/C for measurement of Cl^- . Each point represents the mean value of three measurements carried out with three electrochemical sensors from the same batch, the error bars being the corresponding standard deviation.

5.3.3 Application of the SPE_Ag/C to the analysis of sucralose and TCA

5.3.3.1 Electrochemical detection of sucralose and TCA with bare SPE_Ag/C

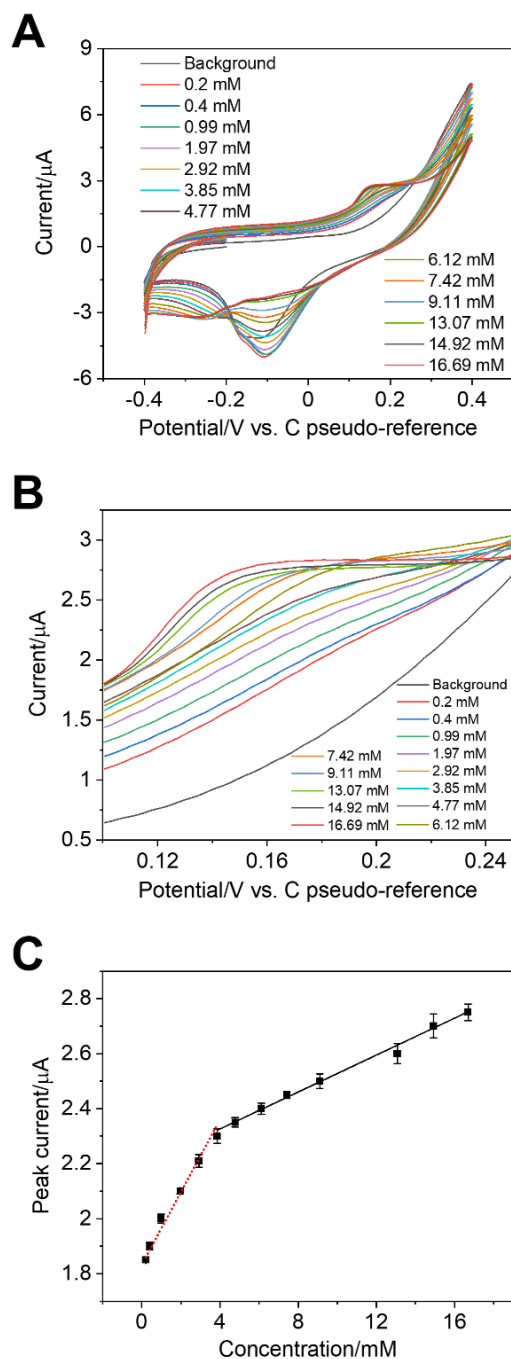


Figure 5.21. (A) Cyclic voltammograms recorded with SPE_Ag/C in PB solutions from 0 mM to 16.69 mM of sucralose. (B) Zoomed-in image of the cyclic voltammograms shown in (A). (C) Calibration curve of the SPE_Ag/C for sucralose. Each point represents the mean value of three measurements carried out with three electrochemical sensors from the same batch, the error bars being the corresponding standard deviation.

Figure 5.21 shows the cyclic voltammograms recorded with SPE_Ag/C in PB solutions containing increasing concentrations of sucralose. A peak at around +0.18 V was recorded, which increased its current intensity with the sucralose concentration in the solution. The corresponding calibration curve was constructed, and the extracted analytical parameters are displayed in Table 5.8. As in the case of the Cl^- analysis, the calibration curve shows two linear ranges, but a significantly higher detection limit of around 145 μM was estimated in this case.

A previous work reported the difficulty of detecting concentrations of TCA in the sub-mM range by CV.³¹ It was described that the sensor sensitivity could be improved by using the square-wave voltammetric technique (SWV), with which a calibration curve showing a linear concentration range of 5-120 μM could be achieved.³² Therefore, SWV was applied with the developed sensor to measure TCA. Figure 5.22 shows the SWV measurement recorded with the SPE_Ag/C in PB. An anodic peak at around +0.28 V was observed, which can be ascribed to the oxidation of Ag NPs. This result is in agreement with the CV measurement shown in Figure 5.19.

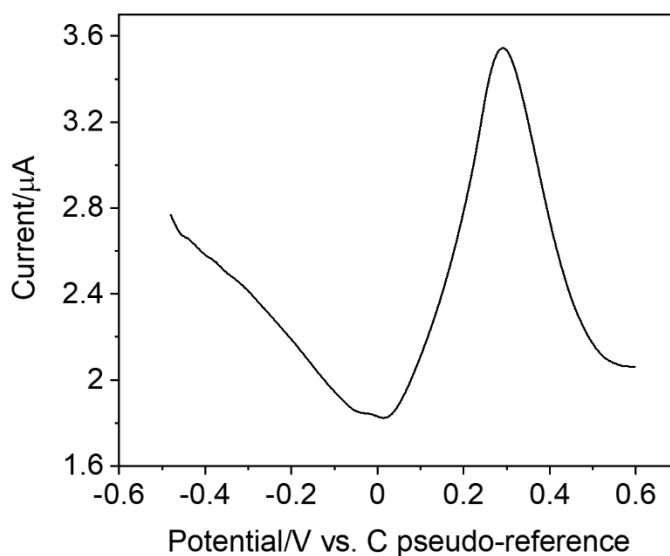


Figure 5.22. Square wave voltammetry in PB solution (pH = 6.0) using screen-printed Ag/C composite electrode.

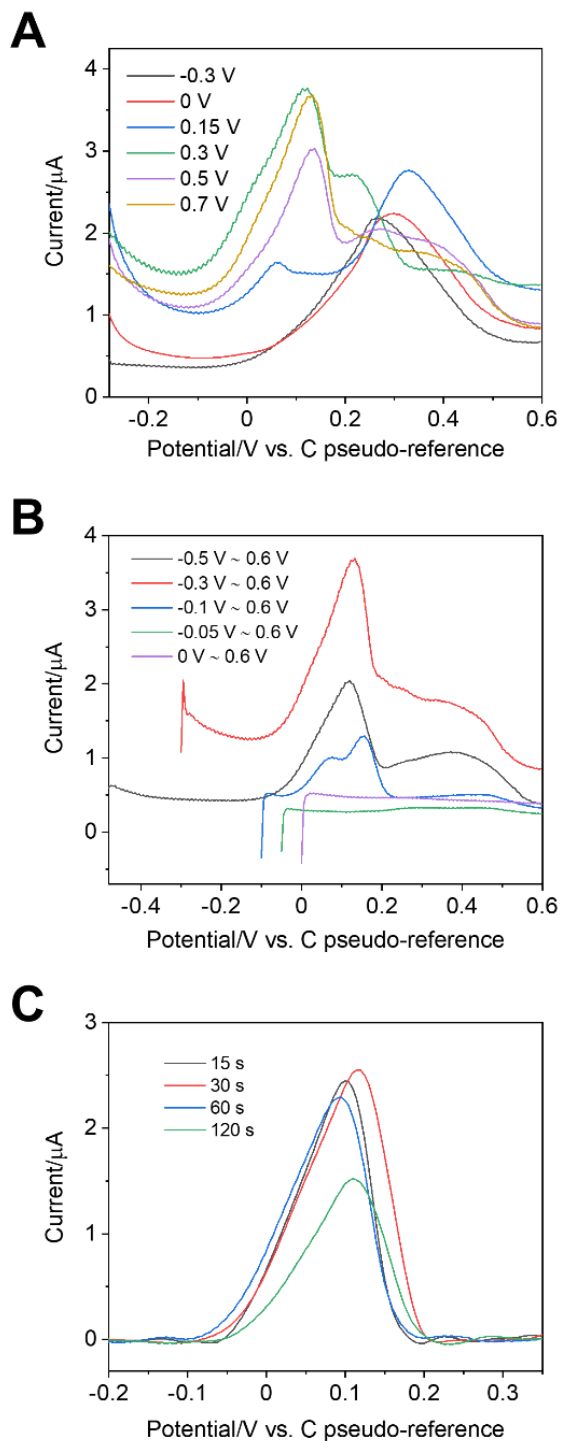


Figure 5.23. Optimization of the electrochemical condition for the measurement of TCA. (A) SWV curves recorded at different applied potentials. The scan range is -0.3 V – 0.6 V and the conditioning potential time is 15 s. **(B)** SWV curves recorded at different scan ranges. The applied conditioning potential is 0.5 V and the conditioning potential time is 15 s. **(C)** SWV curves recorded for different durations of the conditioning potential. The applied conditioning potential is 0.5 V and the scan range is -0.5 V – 0.6 V. The concentration of TCA is 500 μM . The SWV parameters were 5 mV step, 25 mV amplitude and 20 Hz frequency.

Then, the square wave voltammograms were recorded in PB solutions containing TCA. First, three parameters influencing the SWV response were optimized. These were the applied conditioning potential and its duration, together with the starting potential (Figure 5.23). An anodic peak at around +0.12 V (vs. C pseudo-reference) was ascribed to the reaction of TCA with the electrochemical sensor, while the peak at around +0.28 V corresponds to the direct oxidation of Ag NPs on the electrode surface, as mentioned above. However, the peak related to the TCA detection was not observed when the applied conditioning potential was below 0 V (Figure 5.23A). As this potential value increased steadily from +0.15 V to +0.7 V, the recorded peak at +0.12 V appeared and its peak current increased, becoming predominant at potentials values $\geq +0.3$ V. A clear explanation for this behavior cannot be given. However, we hypothesized that the application of these conditioning potential values might induce an activation of the Ag NPs. That is, Ag NPs were oxidized to a certain extent, generating Ag^+ species required for the effective interaction with the Cl^- residues of the TCA target analyte. From the voltammograms shown in Figure 5.23A, we selected potential of +0.5 V for further experiments. Regarding the influence of the starting potential, Figure 5.23B shows that this potential should be higher than -0.05 V for recording the TCA peak. Two separated small peaks appeared when the starting potential was set to -0.1 V. By decreasing this value to -0.3 V or -0.5 V, the TCA peak increased and was better defined. Thus, the selected potential scan range was between -0.5 V and +0.6 V. Next, the conditioning potential time was optimized and experiments are shown in Figure 5.23C. As the time increased from 15 s to 30 s, 60 s and 120 s, the peak intensity for measuring TCA first increased and then decreased. Thus, 30 s was used for further measurements.

After the optimization of the set parameters, square-wave voltammograms were recorded in solutions containing different TCA concentrations. Figure 5.24A shows how the sensor response increases with the TCA concentration. The calibration curve was then plotted (Figure 5.24B) and the corresponding parameters are included in Table 5.8. A linear response in the concentration range of 100 - 5508 μM TCA was obtained, with a sensitivity of $0.300 \pm 0.003 \text{ nA } \mu\text{M}^{-1}$. The LOD was 19.8 μM , estimated using the 3σ IUPAC criterion.³³

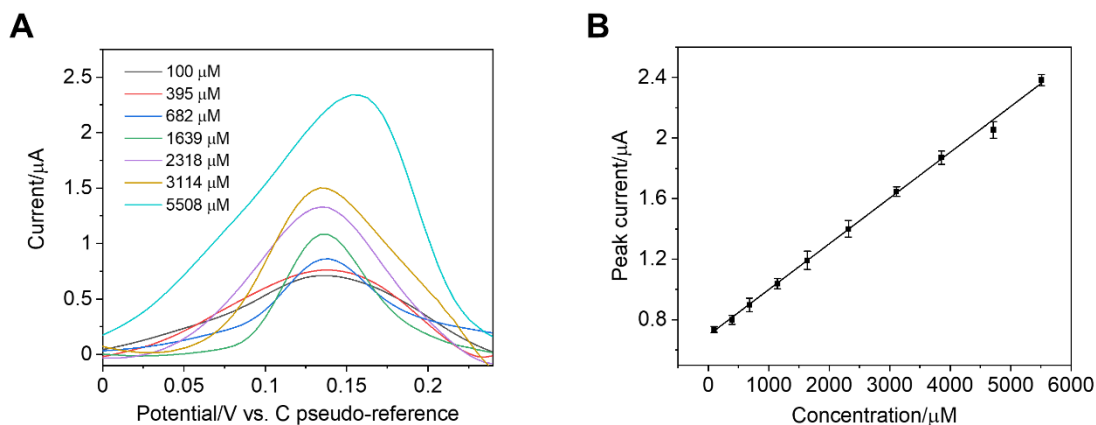


Figure 5.24. (A) Square-wave voltammograms of some representative concentrations of TCA recorded with SPE_Ag/C electrode, (B) Calibration curve for the measurement of trichloroacetic acid using SWV method. Each point represents the mean value of three measurements performed with three SPE_Ag/C devices and the error bars are the corresponding standard deviation. Voltammograms in (A) just represent some examples of all the measurements carried out at different TCA concentrations.

5.3.3.2 Electrochemical detection of sucralose and TCA using a sample-to-result SPE_Ag/C approach

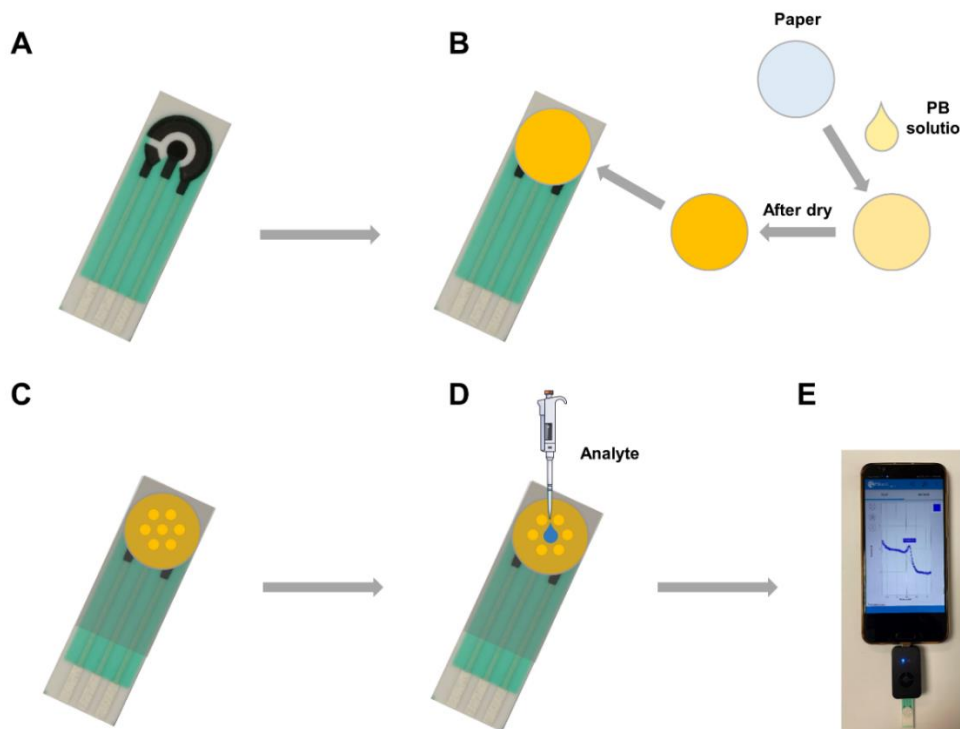


Figure 5.25. Schematic representation of the fabricated SPE_Ag/C miniaturized analysis platform and the analytical response applied to the compact low-power instrument connected to a mobile phone.

In order to make the SPE_Ag/C of potential use for on-site analysis, a paper disk loaded with the reagents required for sample conditioning, was implemented over the sensor area (SPE_Ag/C_paper). The fabrication process is similar to the one of the SPE_Cu/C_paper_{NaOH} electrodes. In detail, a 1 cm diameter paper disk (Whatman® nylon membrane filter, 0.45 μm pore size) and a vinyl plastic layer showing a holed structure (Figure 5.25) were cut using a laser (Epilog Mini 24, Epilog Laser). The paper disk was loaded with phosphate salts. For this, 20 μl of the 0.075 M phosphate buffer (pH 6) solution was drop-cast on the disk and left to dry at room temperature (Figure 5.25 B). Then, the modified paper disk was placed to cover the electrode area and was tightly fixed with a vinyl plastic layer (Figure 5.25 C). Once the SPE_Ag/C_paper was connected to a compact low-power minipotentostat operated by a smartphone, the sensor platform was ready to use. This only requires the addition of 20 μl of the just collected water sample without any additional processing, making it very convenient for on-site analytical measurements (Figure 5.25 D, E). Figure 5.26 shows the photos as the sensor is working.

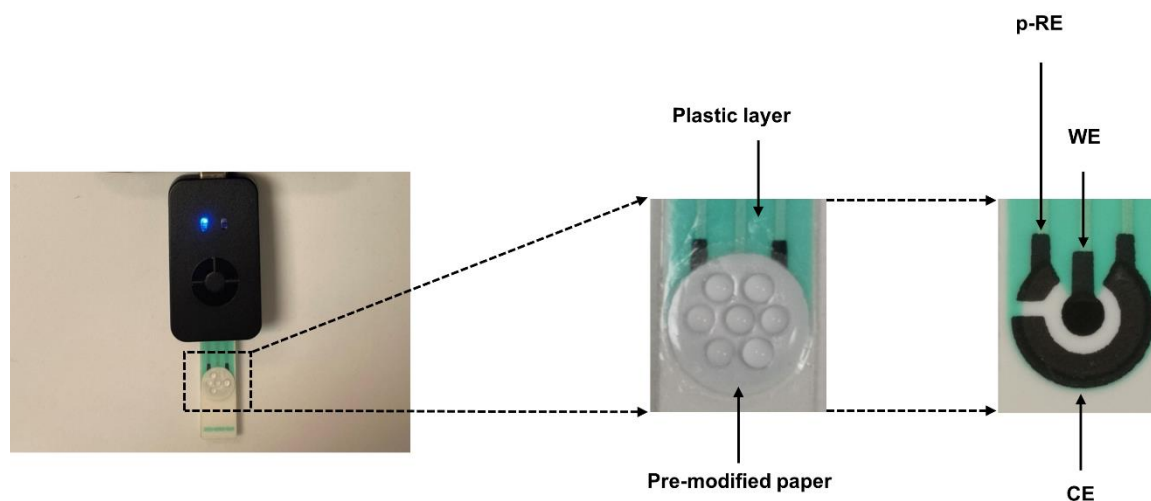


Figure 5.26. Photograph of the measurement with SPE_Ag/C_paper sensor connected to the compact low-power minipotentostat.

Figure 5.27 shows CVs for different concentrations of sucralose recorded using the described platform. It can be seen that the current of the anodic peak ascribed to sucralose increased with the sucralose concentration. Accordingly, the calibration curve was obtained and the corresponding analytical parameters are summarized in Table 5.8. The calibration curve also shows two linear ranges. The range at low concentrations between 0.4 mM and

2.92 mM, shows a higher slope than the second range between 3.85 mM to 13.07 mM. These values are in the same range as those obtained with the SPE_Ag/C device.

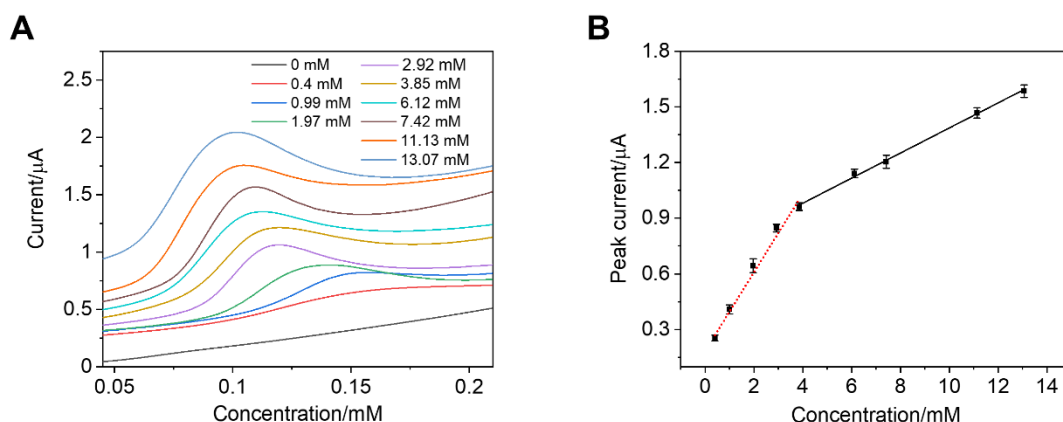


Figure 5.27. (A) CVs recorded with SPE_Ag/C_paper sensor connected to the smartphone-based minipotentiostat at different concentrations of sucralose; (B) Corresponding calibration curve of the measurement. The reproducibility of the electrochemical characteristics was studied by carrying out triplicate measurements using three SPEs from the same batch. Each point represents the mean value of three measurements performed consecutively and the error bars are the corresponding standard deviation. Scan rate: 100 mV/s.

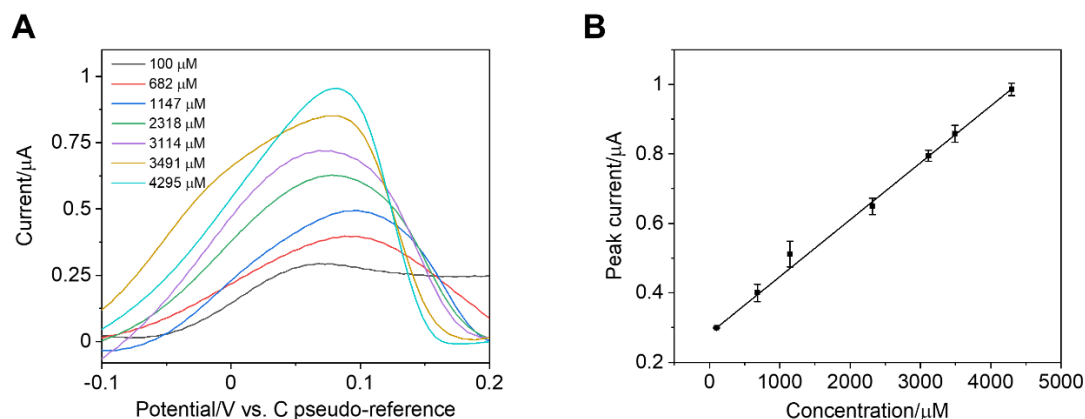


Figure 5.28. (A) SWVs recorded with SPE_Ag/C_paper sensor connected to the smartphone-based minipotentiostat at different concentrations of TCA, (B) Calibration curve for the measurement of trichloroacetic acid. The reproducibility of the electrochemical characteristics was studied by carrying out triplicate measurements using three SPEs from the same batch. Each point represents the mean value of three measurements performed consecutively and the error bars are the corresponding standard deviation. The SWV parameters were 5 mV step, 25 mV amplitude and 20 Hz frequency.

The same platform was used to analyze TCA by SWV. Figure 5.28 A and 5.28 B show the SWV curves at different concentrations of TCA and the corresponding calibration. The analytical parameters (see Table 5.8) are similar to those obtained with the SPE_Ag/C sensor.

Table 5.9. Analytical parameters of the developed sensors for TCA determination.

Modified electrodes	Linear range (μM)	LOD (μM)	Ref
Ag NPs-MA/GCE (SWV)	0.1-2, 4-100	0.030, 0.079	34
Hg-Ag@GNR-PSS-PDDA/GCE (CA)	0.16-1.7	0.12	35
Porphyrin/SWNTs-[BMIM][PF ₆]/GCE (CA)	0.9-140	0.38	36
SNP-CS/GCE (CA)	3-56	1.1	37
Ag-MWCNT/GCE (SWV)	5-120	1.9	32
MWCNTs/Pc/Fe(CA)	8-2000	2.0	38
TH/TNTs/CS/GCE (CV)	15-1500	-	39
np-Ag (CA)	2500-22500	25.4	31
SPE_Ag/C (SWV)	100-5508	19.8	This work
SPE_Ag/C_paper (SWV)	100-4295	23.8	

Previous reports describing similar sensor approaches were sought for comparative purposes. To the best of our knowledge, the detection of sucralose using an electrochemical sensor platform was just reported in one paper by Nikolelis et al.⁴⁰ Their sensor incorporated a surface-stabilized bilayer lipid membrane. The adsorption of the target analyte produced a change in the ionic conductivity of the membrane which transduced into a faradaic current directly proportional to the analyte concentration in the solution. This work just reports a proof-of-concept of a sensor transduction mechanism using lipid membrane receptors, which was not explored further. Moreover, since the sensor lifetime was short, it doesn't seem very convenient to implement it in decentralized analytical studies.

Electrochemical sensor approaches for TCA detection were previously reported and are summarized in Table 5.9. Some of these outperform the sensor described in this work in terms of linear range and limit of detection. However, most of them are based on complex sensor architectures, thus making the manufacturing process unsuitable for mass production. In addition, the use in some of these studies of conventional electrochemical cells comprising commercial working electrodes such as glassy carbon, restricted their use in analytical laboratories.

5.4 Fabrication and electrochemical characterization of wood-derived screen-printed carbon electrodes

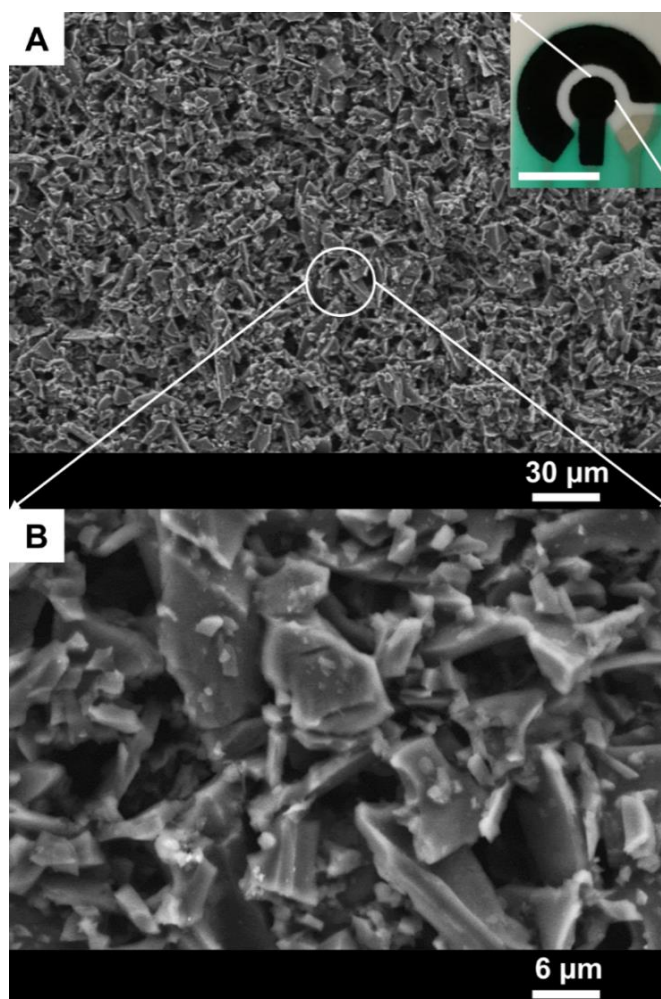


Figure 5.29. SEM images of the surface of the SPE_{Cc}. The inset in (A) is the photograph of the three-electrode cell of the SPE, with a scale bar of 0.5 cm.

The wood-derived C ink preparation and the screen-printing process of the three-electrode configuration were the same as those described in sections 5.2 and 5.3. Here, the reference electrode was prepared using a silver paste whereas de auxiliary and carbon paste electrodes were simultaneously printed using wood-derived ink.

Batches of 120 screen-printed working electrodes (SPE_C_c) were prepared from 20 ml of C ink made of Chestnut wood by-product (C_c). Figure 5.29 shows the SEM images of a working electrode rough surface, which displays a morphology similar to that of the surface of any carbon (graphite) screen-printed electrode found on the market.

The SPE_C_c electrochemical performance was assessed by CV in 0.1 M KNO₃ solutions containing 1 mM ferrocene outer-sphere or 1 mM ferricyanide inner-sphere redox species. Figure 5.30A shows the CVs recorded with SPE_C_c at scan rates from 5 to 100 mV s⁻¹ in the ferrocene solution. The ΔE_p values at 50 mV s⁻¹ scan rate and the K^0_{app} values, summarized in Table 5.10, indicate that the SPE_C_c electrodes show quasi-reversible voltammetric signals. The anodic and cathodic peak current signals recorded at scan rates in the range from 5 to 100 mV s⁻¹ show a linear relation with the square root of the scan rate (Figure 5.30B), unambiguously revealing diffusion-controlled redox processes.

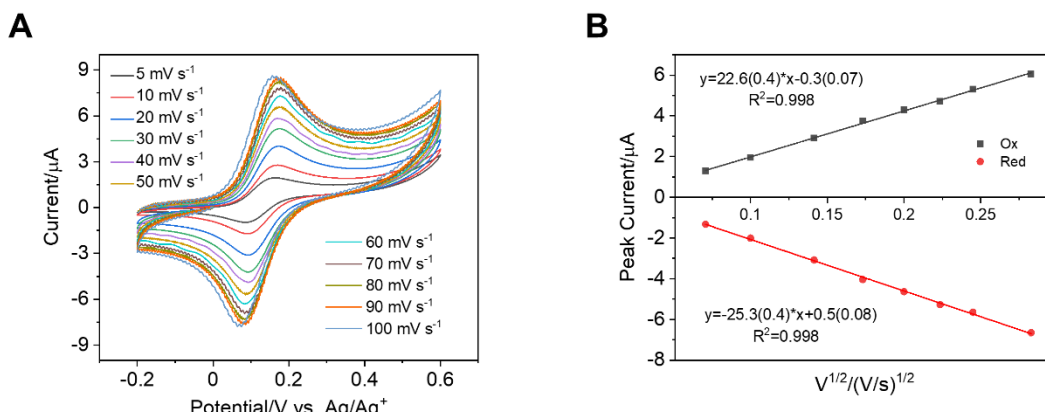


Figure 5.30. Cyclic voltammograms recorded with the SPE_C_c at different scan rates, in a 0.1 M KNO₃ solution containing 1 mM ferrocene redox species (A), and plots of anodic peak and cathodic peak currents vs. the square root of the scan rate (B).

Similar measurements carried out with a SPE fabricated using a commercial graphite ink (SPE_C_g), revealed that the electrochemical performance of SPE_C_c is comparable to that of the SPE_C_g (see Table 5.10 and Figure 5.31).

Table 5.10. Peak-to-peak potential separation (ΔE_P) at a scan rate of 50 mV s^{-1} and the electron transfer rate k^0_{app} values for SPE_C_c and SPE_C_g in a 0.1 M KNO_3 solution containing 1 mM ferrocene redox species.

Samples	redox species	ΔE_P (mV)	$K^0_{\text{app}} [^*10^{-4} \text{ cm s}^{-1}]$
SPE_C _c	Ferrocene	78	90±16
SPE_C _g		71	130±29

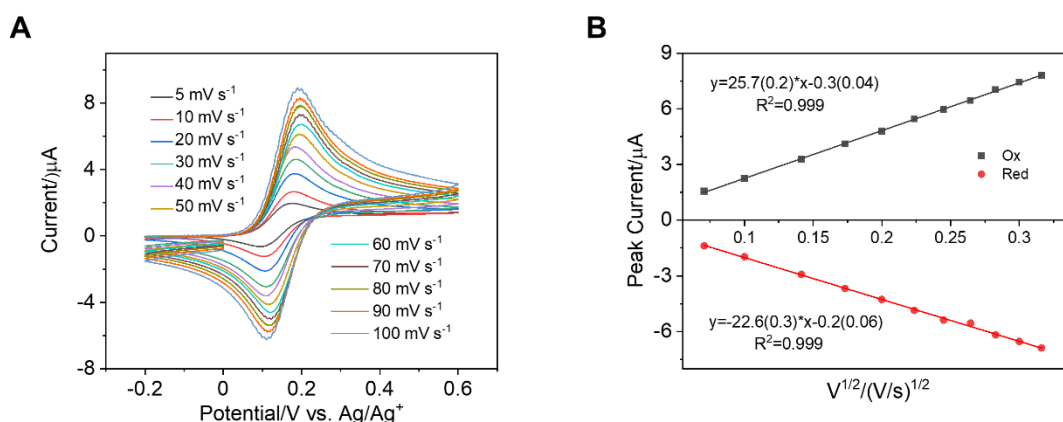


Figure 5.31. Cyclic voltammograms recorded with the SPE_C_g at different scan rates, in a 0.1 M KNO_3 solution containing 1 mM ferrocene redox species (A), and plots of anodic peak and cathodic peak currents vs. the square root of the scan rate (B).

CVs were recorded with SPE_C_c (Figure 5.32A) and SPE_C_g (Figure 5.32B) at 50 mV s^{-1} scan rate, in a 0.1 M KNO_3 solution with and without 1 mM Ferricyanide redox species. The oxidation and the reduction peaks obtained from the SPE_C_c are very small. It was not investigated any further and this behavior could be related to the surface chemistry of the SPE_C_c. In the case of SPE_C_g, the ΔE_P is 394 mV , which is very large revealing a low electron transfer kinetics.⁴¹

Even though the surface chemistry of the fabricated SPE_C_c limits the analytical performance with a surface-sensitive redox species (Ferricyanide), they show an excellent behavior when measuring ferrocene redox species, which present a surface-insensitive electrochemical response. This encouraged us to use these devices for electrochemical sensing purposes, as shown in the section below.

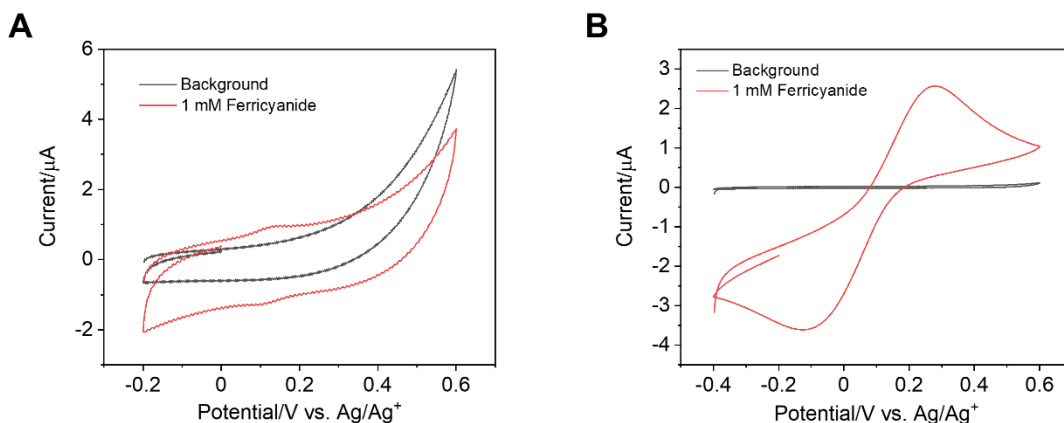


Figure 5.32. Cyclic voltammetric responses of SPE_C_c and SPE_C_g recorded in 0.1 M KNO₃ supporting electrolyte solutions containing 1 mM Ferricyanide redox probe. Background signals recorded in the 0.1 M KNO₃ supporting electrodes are also included. Scan rate: 50 mV s⁻¹.

5.4.1 Electrochemical performance of Bi or Sb modified SPE_C_c devices: Analysis of heavy metals

SPE_C_c were assessed for the analysis of Pb(II) and Cd (II) heavy metal ion pollutants in water. Both have been listed by different governmental agencies as priority pollutants to be analyzed in surface waters and their maximum allowable concentrations according to different regulations are summarized in Table 5.11.^{42–45} We adopted Bi and Sb as active materials for detecting Pb(II) and Cd (II). The latter can be electrochemically reduced on the surfaces of the Group 15 metals and later re-oxidized and quantified by anodic stripping voltammetry. Two approaches were followed using Bi(III) or Sb(III), co-electrodeposited with the Pb(II) and Cd (II) by in-situ plating on the surface of the SPE_C_c. Then the Pb(II) and Cd (II) were stripped using the differential pulse anodic stripping voltammetric (DPASV) technique. DPASV is based on the accumulation of redox species on the surface of an electrochemical device by electrodeposition at a controlled DC potential for a certain period of time. This is followed by the application of a potential scan at which the deposited species are stripped off the surface. The potential waveform is in this case a differential potential pulse, which allows for discrimination of the recorded Faradaic to capacitive currents for enhanced sensitivity purposes. The stripping peak currents recorded in the electrochemical signals were used to analyze the concentration of the heavy metals in the water solution.

Table 5.11. Maximum allowable concentrations of heavy metal ions in drinking water.

Heavy metals	WHO (ppb)	EU-WFD (ppb)	US-EPA (ppb)	C-MEP (ppb)
Lead (Pb)	10	14	15	10
Cadmium (Cd)	3	0.45-1.5	5	5

World Health Organization: WHO; the European Union Water Framework Directive: EU-WFD; the US Environmental Protection Agency: US-EPA; and the Ministry of Environmental Protection of China (C-MEP).

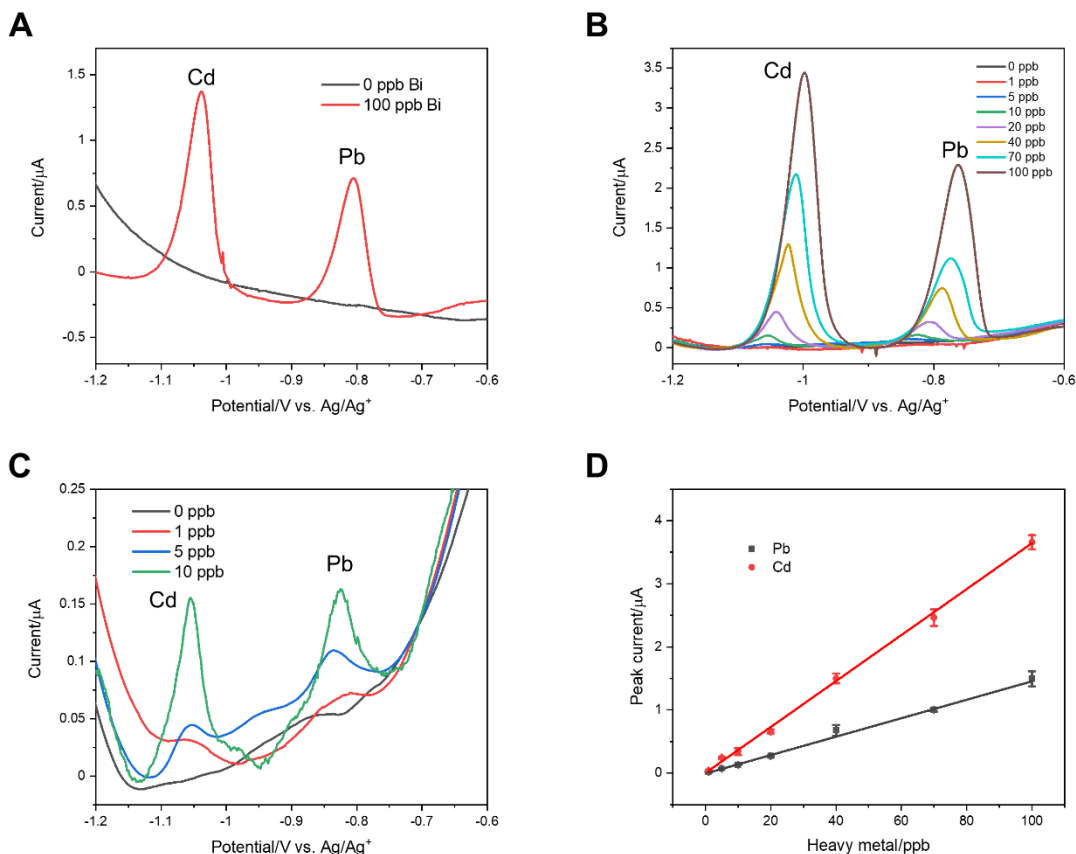


Figure 5.33. (A) DPASV signals recorded in acetate buffer solutions (pH 4.5) containing 100 ppb Pb (II) and Cd (II) with and without active materials of Bi (III). (black line) No addition of Bi (III); (red line) addition of 100 ppb Bi; (B and C) DPASV signals recorded in 0.1 M acetate buffer solutions pH 4.5, containing different concentrations of Pb (II) and Cd (II) on the Bi-SPEs with the in-situ plating method. (D) Calibration curves for both heavy metals. Each point represents the mean value of three measurements and the error bars indicate the corresponding standard deviation.

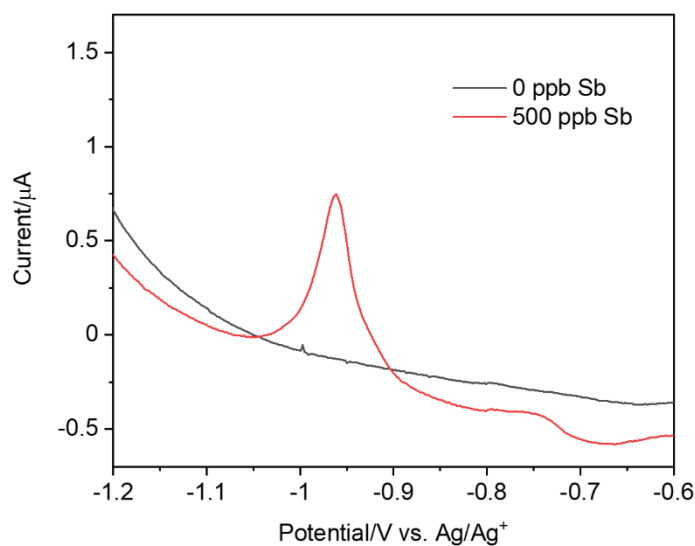


Figure 5.34. DPASV signals recorded in acetate buffer solutions (pH 4.5) containing 100 ppb Pb (II) and Cd (II) with and without active materials of Sb (III). (black line) No addition of Sb (III); (red line) addition of 500 ppb Sb (III).

Considering that some carbon material may show electrocatalytic behavior under certain experimental conditions,^{12,13} we performed a comparative study using the SPEs with and without the addition of Bi (III) or Sb (III). As shown in Figure 5.33A and Figure 5.34, the peaks for Pb(II) and Cd (II) do not appear without the addition of Bi (III) or Sb (III). On the contrary, when the Bi (III) is present (Figure 5.33A), two peaks at around -0.8 V and -1 V (vs. Ag/Ag⁺ pseudo-ref.) are clearly visible that can be assigned to Pb and Cd stripping processes, respectively.^{46,47} When Sb (III) is present (Figure 5.34), the peak of Cd (II) is very clear but the one corresponding to Pb(II) is very weak. Thus, Bi (III) or Sb (III) should be applied as the active material in the performance of the electrochemical device for heavy metal detection.

The experimental conditions for the detection of Cd(II) and Pb(II) with Bi (III) as active material were optimized. As shown in Figures 5.35 and 5.36, three parameters (concentration of Bi, applied potential for co-deposition and accumulation time) are respectively optimized in solutions containing both heavy metals at concentrations in the low (20 ppb) and high (100 ppb) range. The optimized conditions of 100 ppb Bi (III), -1.6 V applied DC potential and 5 min accumulation time were further applied to detect the Pb(II) and Cd (II) with the SPE_Cc.

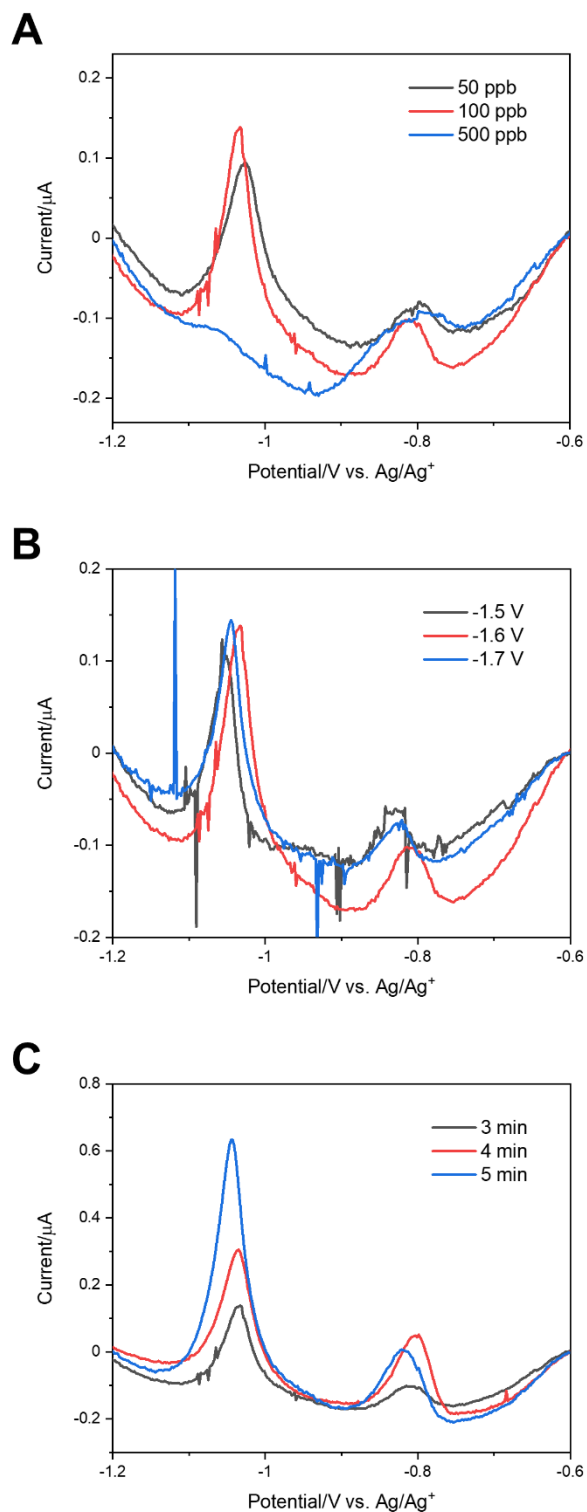


Figure 5.35. Optimization of the electrochemical condition for the analysis of Cd and Pb with Bi as active material by the in-situ plating method. (A) different addition amounts of Bi; (B) different applied potential; (C) different accumulation time. The concentration of Pb and Cd is 20 ppb.

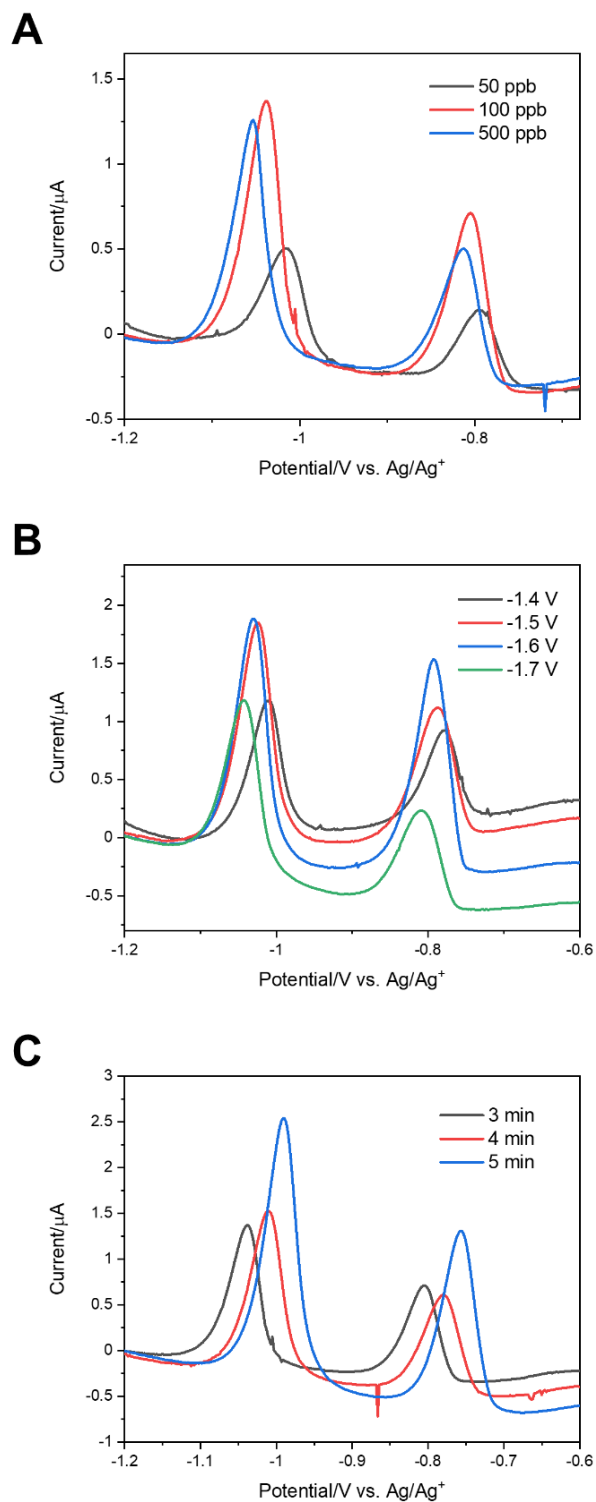


Figure 5.36. Optimization of the electrochemical condition for the analysis of Cd and Pb with Bi as active material by the in-situ plating method. (A) different addition amounts of Bi; (B) different applied potential; (C) different accumulation time. The concentration of Pb and Cd is 100 ppb.

Figure 5.33B and Figure 5.33C depict the DPASV signals recorded in solutions containing different concentrations of Pb(II) and Cd (II). The peak currents increased with the heavy metal concentration and the peak potential shifted toward more positive values. Figure 5.33D shows the calibration curves of Pb(II) and Cd (II) and the analytical parameters extracted from them are summarized in Table 5.12. The maximum allowable Pb(II) and Cd (II) concentrations in drinking water set by different government agencies fall within the linear ranges of our electrode except for the Cd (II) concentration provided by EU-WFD. These results indicate that our sensor could be a promising cost-effective alternative for monitoring Pb(II) and Cd (II) in drinking water. The reproducibility of the electrochemical analysis was studied by recording triplicates using three SPEs_C_c from the same batch, and the standard deviation was drawn as the error bar in the calibration curves (Figure 5.33D). The error bar is around 5%, revealing the good reproducibility of the analysis of Pb(II) and Cd (II).

Table 5.12. Parameters of calibration curves for the different heavy metals.

Heavy metals	Linear range (ppb)	Sensitivity ($\mu\text{A/ppb}$)	Limit of detection (ppb)	Correlation coefficient (R)
Pb	1-100	0.015 ± 0.0005	0.37	0.994
Cd	1-100	0.036 ± 0.002	0.15	0.991

LOD is calculated using the 3σ IUPAC criterion.

Similarly, the Sb (III) was also used as the active material to analyze Pb(II) and Cd (II). After optimization of the electrochemical condition (Figure 5.37 and 5.38), 500 ppb of additional amount of Sb (III), applied potential of -1.4 V and accumulation time of 4 min were used to analyze the Pb(II) and Cd (II). Figure 5.39 shows the analysis result of the measurement for different concentrations of Pb(II) and Cd (II). It is obvious that the peaks for the Pb(II) and Cd (II) are difficult to obtain when the concentrations of the heavy metal are below 20 ppb. This confirms that Bi (III) is a better active material to analyze Pb(II) and Cd (II) compared to Sb (III).

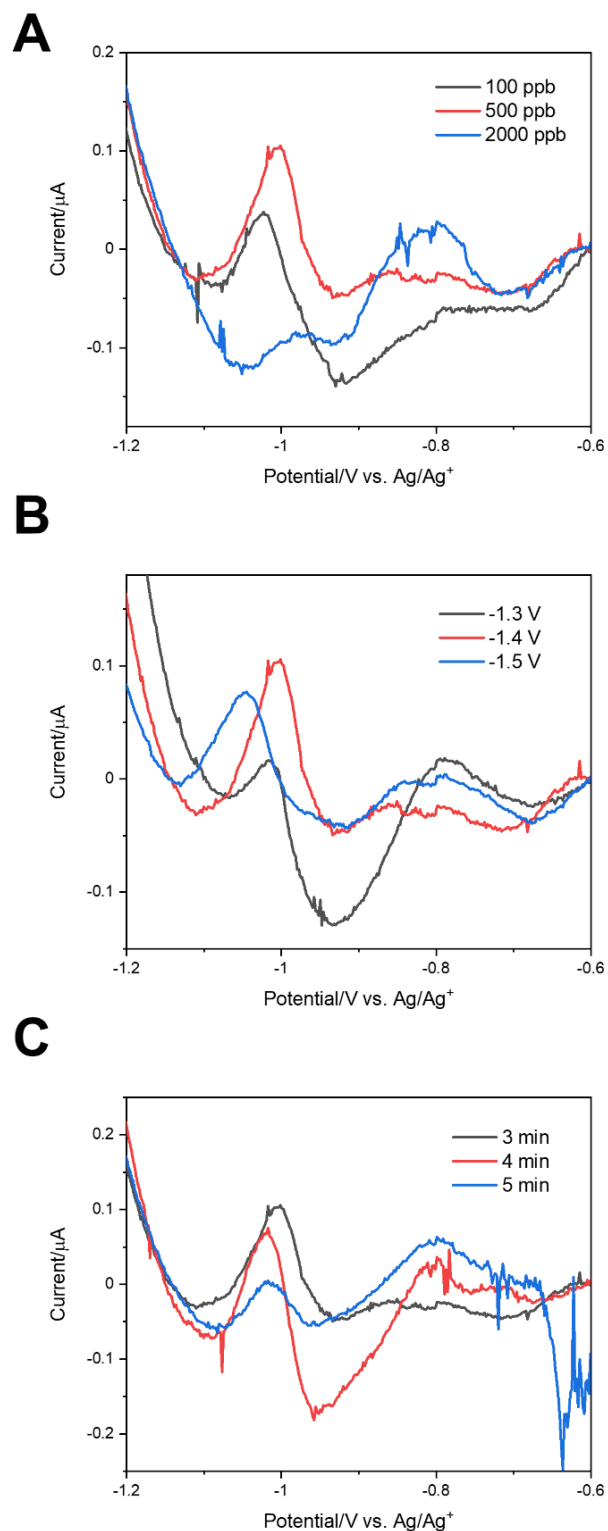


Figure 5.37. Optimization of the electrochemical condition for the analysis of Cd and Pb with Sb as active material by the in-situ plating method. (A) different addition amounts of Sb; (B) different applied potential; (C) different accumulation time. The concentration of Pb and Cd is 40 ppb.

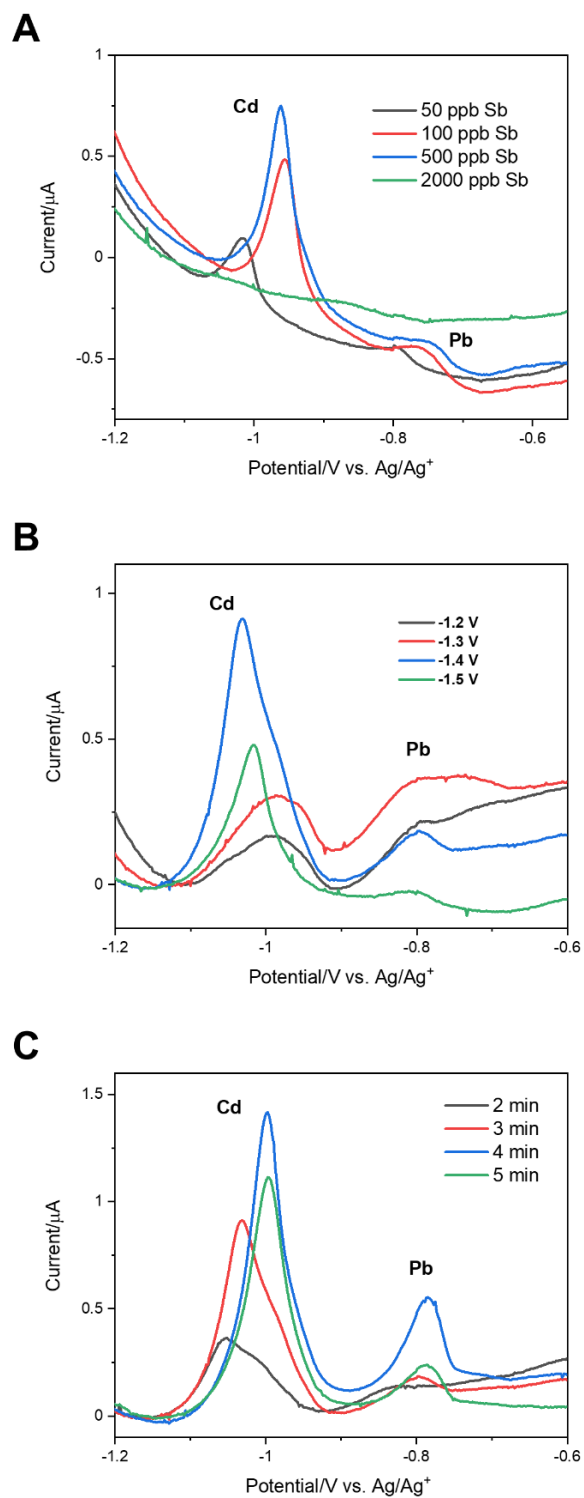


Figure 5.38. Optimization of the electrochemical condition for the analysis of Cd and Pb with Sb as active material by the in-situ plating method. (A) different addition amounts of Sb; (B) different applied potential; (C) different accumulation time. The concentration of Pb and Cd is 100 ppb.

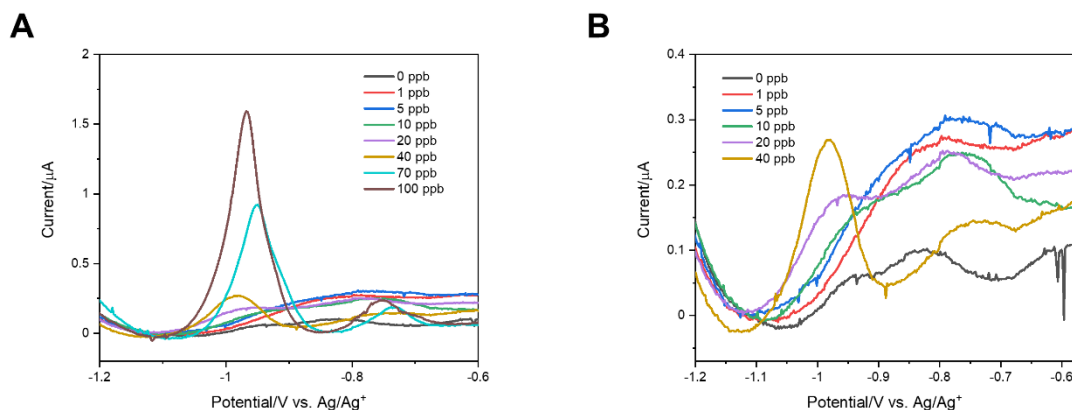


Figure 5.39. DPASV signals recorded in acetate buffer solutions (pH 4.5) containing different concentrations of Pb (II) and Cd (II) on Sb-SPEs by the in-situ plating method. Electrodeposition was carried out at -1.4 V for 4 min.

5.5 Conclusion

The Cu/C and Ag/C nanocomposites prepared in this Thesis (Chapter 3) were used to fabricate screen-printed electrodes that displayed a good performance for specific analytes of interest (COD and halogenated compounds, respectively). The screen-printing process is a convenient method for the eventual mass production and manufacturing of low-cost ready-to-use electrochemical devices. Integrating the SPEs with a paper disk loaded with an electrolyte enabled automatic sample preconditioning. This includes filtering and conductivity and pH tuning, making possible an electrochemical analysis by the simple addition of the required sample volume. As a result, the sample-to-result single-use screen-printed sensors for in-field analysis of COD and halogenated compounds were successfully produced.

The pure carbon material derived from the pyrolyzed wood by-product was adopted for the fabrication of screen-printed electrodes. These screen-printed electrodes were successfully applied to analyze heavy metals by modification of bismuth active species using the in-situ plating method.

References

1. Ferrari AG, Rowley-Neale SJ, Banks CE. Screen-printed electrodes: Transitioning the laboratory in-to-the field. *Talanta Open*. 2021 Aug 1;3:100032.
2. Kanoun O, Lazarević-Pašti T, Pašti I, Nasraoui S, Talbi M, Brahem A, Adiraju A, Sheremet E, Rodriguez RD, Ben Ali M, Al-Hamry A. A review of nanocomposite-modified electrochemical sensors for water quality monitoring. *Sensors*. 2021 Jun 16;21(12):4131.
3. Workman Jr J, Lavine B, Chrisman R, Koch M. Process analytical chemistry. *Analytical chemistry*. 2011 Jun 15;83(12):4557-78.
4. Hayat A, Marty JL. Disposable screen printed electrochemical sensors: Tools for environmental monitoring. *Sensors*. 2014 Jun 13;14(6):10432-53.
5. Beitollahi H, Mohammadi SZ, Safaei M, Tajik S. Applications of electrochemical sensors and biosensors based on modified screen-printed electrodes: a review. *Analytical Methods*. 2020;12(12):1547-60.
6. Suresh RR, Lakshmanakumar M, Arockia Jayalatha JB, Rajan KS, Sethuraman S, Krishnan UM, Rayappan JB. Fabrication of screen-printed electrodes: opportunities and challenges. *Journal of Materials Science*. 2021 May;56(15):8951-9006.
7. Mohamad Nor N, Ramli NH, Poobalan H, Qi Tan K, Abdul Razak K. Recent Advancement in Disposable Electrode Modified with Nanomaterials for Electrochemical Heavy Metal Sensors. *Critical reviews in analytical chemistry*. 2021 Jul 5:1-36.
8. Ruiz-Vega G, Kitsara M, Pellitero MA, Baldrich E, del Campo FJ. Electrochemical lateral flow devices: towards rapid immunomagnetic assays. *ChemElectroChem*. 2017 Apr;4(4):880-9.
9. Gutiérrez-Capitán M, Baldi A, Gómez R, García V, Jiménez-Jorquera C, Fernández-Sánchez C. Electrochemical nanocomposite-derived sensor for the analysis of chemical oxygen demand in urban wastewaters. *Analytical chemistry*. 2015 Feb 17;87(4):2152-60.

10. Silva CR, Conceição CD, Bonifácio VG, Teixeira MF. Determination of the chemical oxygen demand (COD) using a copper electrode: a clean alternative method. *Journal of Solid State Electrochemistry*. 2009 May;13(5):665-9.
11. Duan W, Torras M, Roig A, Fernández-Sánchez C, Gich M. Composites of porous carbon and copper-based nanoparticles for the electrochemical analysis of chemical oxygen demand. *Materials Today Chemistry*. 2022 Jun 1;24:100899.
12. Byers JC, Güell AG, Unwin PR. Nanoscale electrocatalysis: visualizing oxygen reduction at pristine, kinked, and oxidized sites on individual carbon nanotubes. *Journal of the American Chemical Society*. 2014 Aug 13;136(32):11252-5.
13. Cao Y, Yu H, Peng F, Wang H. Selective allylic oxidation of cyclohexene catalyzed by nitrogen-doped carbon nanotubes. *ACS Catalysis*. 2014 May 2;4(5):1617-25.
14. Badr IH, Hassan HH, Hamed E, Abdel-Aziz AM. Sensitive and Green Method for Determination of Chemical Oxygen Demand Using a Nano - copper Based Electrochemical Sensor. *Electroanalysis*. 2017 Oct;29(10):2401-9.
15. Hassan HH, Badr IH, Abdel-Fatah HT, Elfeky EM, Abdel-Aziz AM. Low cost chemical oxygen demand sensor based on electrodeposited nano-copper film. *Arabian Journal of Chemistry*. 2018 Feb 1;11(2):171-80.
16. Carchi T, Lapo B, Alvarado J, Espinoza-Montero PJ, Llorca J, Fernández L. A Nafion film cover to enhance the analytical performance of the CuO/Cu electrochemical sensor for determination of chemical oxygen demand. *Sensors*. 2019 Feb 6;19(3):669.
17. Huang X, Zhu Y, Yang W, Jiang A, Jin X, Zhang Y, Yan L, Zhang G, Liu Z. A self-supported CuO/Cu nanowire electrode as highly efficient sensor for COD measurement. *Molecules*. 2019 Aug 28;24(17):3132.
18. Directive H. Council Directive of 21 May 1991 concerning urban waste water treatment. Regulation (EC). 2003 Oct 31;50(284):1.
19. Choudhry NA, Kampouris DK, Kadara RO, Jenkinson N, Banks CE. Next generation screen printed electrochemical platforms: Non-enzymatic sensing of carbohydrates using copper (II) oxide screen printed electrodes. *Analytical Methods*. 2009;1(3):183-7.
20. Dhara K, Stanley J, Ramachandran T, Nair BG, Babu TG. Cupric oxide modified

- screen printed electrode for the nonenzymatic glucose sensing. *Journal of Nanoscience and Nanotechnology*. 2016 Aug 1;16(8):8772-8.
21. Dhara K, Thiagarajan R, Nair BG, Thekkedath GS. Highly sensitive and wide-range nonenzymatic disposable glucose sensor based on a screen printed carbon electrode modified with reduced graphene oxide and Pd-CuO nanoparticles. *Microchimica Acta*. 2015 Oct;182(13):2183-92.
 22. Huang TK, Lin KW, Tung SP, Cheng TM, Chang IC, Hsieh YZ, Lee CY, Chiu HT. Glucose sensing by electrochemically grown copper nanobelt electrode. *Journal of Electroanalytical Chemistry*. 2009 Nov 15;636(1-2):123-7.
 23. Leonardi SG, Marini S, Espro C, Bonavita A, Galvagno S, Neri G. In-situ grown flower-like nanostructured CuO on screen printed carbon electrodes for non-enzymatic amperometric sensing of glucose. *Microchimica Acta*. 2017 Jul;184(7):2375-85.
 24. Espro C, Marini S, Giusi D, Ampelli C, Neri G. Non-enzymatic screen printed sensor based on Cu₂O nanocubes for glucose determination in bio-fermentation processes. *Journal of Electroanalytical Chemistry*. 2020 Sep 15;873:114354.
 25. Liu XW, Pan P, Zhang ZM, Guo F, Yang ZC, Wei J, Wei Z. Ordered self-assembly of screen-printed flower-like CuO and CuO/MWCNTs modified graphite electrodes and applications in non-enzymatic glucose sensor. *Journal of Electroanalytical Chemistry*. 2016 Feb 15;763:37-44.
 26. Droog JM, Alderliesten PT, Bootsma GA. Initial stages of anodic oxidation of silver in sodium hydroxide solution studied by potential sweep voltammetry and ellipsometry. *Journal of Electroanalytical Chemistry and Interfacial Electrochemistry*. 1979 May 25;99(2):173-86.
 27. Bayesov A, Tuleshova E, Tukibayeva A, Aibolova G, Baineys F. Electrochemical behavior of silver electrode in sulphuric acidic solution during anodic polarization. *Oriental journal of Chemistry*. 2015;31(4):1867.
 28. Stonehart P, Portante FP. Potentiodynamic examination of surface processes and kinetics for the Ag₂O/AgO/OH⁻ system. *Electrochimica Acta*. 1968 Aug 1;13(8):1805-14.
 29. Patella B, Aiello G, Drago G, Torino C, Vilasi A, O'Riordan A, Inguanta R.

Electrochemical detection of chloride ions using Ag-based electrodes obtained from compact disc. *Analytica Chimica Acta*. 2022 Jan 15;1190:339215.

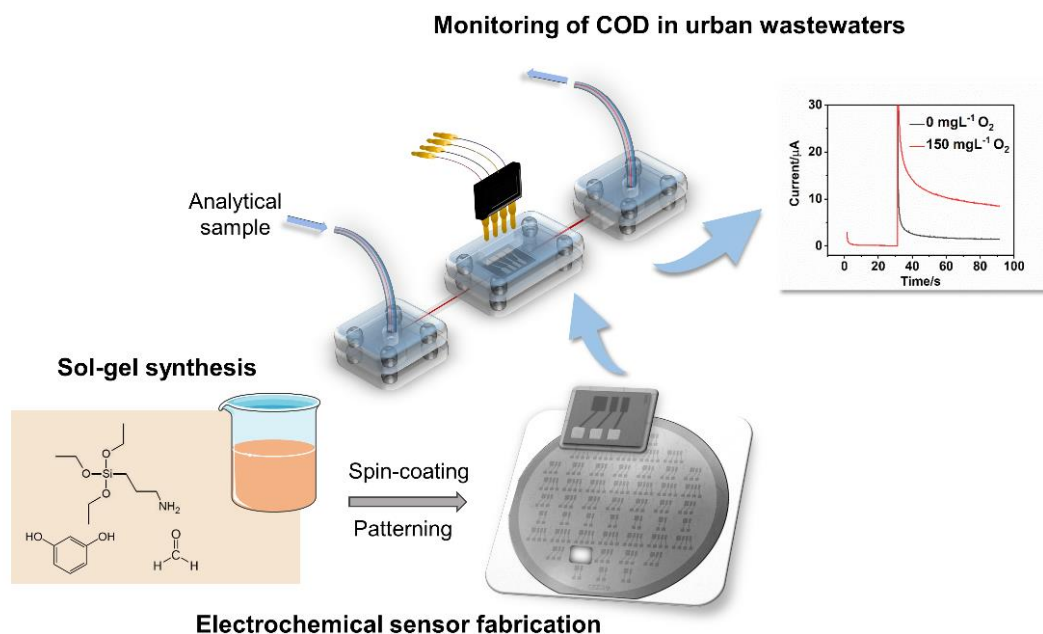
30. Pargar F, Kolev H, Koleva DA, van Breugel K. Microstructure, surface chemistry and electrochemical response of Ag| AgCl sensors in alkaline media. *Journal of Materials Science*. 2018 May;53(10):7527-50.
31. Chen T, Liu Z, Lu W, Zhou X, Ma H. Fabrication of free-standing nanoporous silver by selectively dissolving gold from gold–silver alloys via a novel converse dealloying method. *Electrochemistry communications*. 2011 Oct 1;13(10):1086-9.
32. Liu B, Hu X, Deng Y, Yang S, Sun C. Selective determination of trichloroacetic acid using silver nanoparticle coated multi-walled carbon nanotubes. *Electrochemistry communications*. 2010 Oct 1;12(10):1395-7.
33. Currie LA. Nomenclature in evaluation of analytical methods including detection and quantification capabilities (IUPAC Recommendations 1995). *Pure and applied chemistry*. 1995 Jan 1;67(10):1699-723.
34. Bashami RM, Soomro MT, Khan AN, Aazam ES, Ismail IM, El-Shahawi MS. A highly conductive thin film composite based on silver nanoparticles and malic acid for selective electrochemical sensing of trichloroacetic acid. *Analytica Chimica Acta*. 2018 Dec 7;1036:33-48.
35. Qian D, Li W, Chen F, Huang Y, Bao N, Gu H, Yu C. Voltammetric sensor for trichloroacetic acid using a glassy carbon electrode modified with Au@ Ag nanorods and hemoglobin. *Microchimica Acta*. 2017 Jul;184(7):1977-85.
36. Tu W, Lei J, Ju H. Functionalization of carbon nanotubes with water -insoluble porphyrin in ionic liquid: direct electrochemistry and highly sensitive amperometric biosensing for trichloroacetic acid. *Chemistry – A European Journal*. 2009 Jan 5;15(3):779-84.
37. Liu B, Deng Y, Hu X, Gao Z, Sun C. Electrochemical sensing of trichloroacetic acid based on silver nanoparticles doped chitosan hydrogel film prepared with controllable electrodeposition. *Electrochimica acta*. 2012 Aug 1;76:410-5.
38. Kurd M, Salimi A, Hallaj R. Highly sensitive amperometric sensor for micromolar detection of trichloroacetic acid based on multiwalled carbon nanotubes and Fe (II)–

phtalocyanine modified glassy carbon electrode. *Materials Science and Engineering: C*. 2013 Apr 1;33(3):1720-6.

39. Dai H, Xu H, Wu X, Lin Y, Wei M, Chen G. Electrochemical behavior of thionine at titanate nanotubes-based modified electrode: A sensing platform for the detection of trichloroacetic acid. *Talanta*. 2010 Jun 15;81(4-5):1461-6.
40. Nikolelis DP, Pantoulis S. A minisensor for the rapid screening of sucralose based on surface-stabilized bilayer lipid membranes. *Biosensors and Bioelectronics*. 2000 Nov 1;15(9-10):439-44.
41. Hammerich O, Speiser B, editors. *Organic electrochemistry*. Boca Raton, FL: CRC press; 2016.
42. Water S, World Health Organization. Guidelines for drinking-water quality [electronic resource]: incorporating first addendum. Vol. 1, Recommendations.
43. Recast EP. Directive 2010/31/EU of the European Parliament and of the Council of 19 May 2010 on the energy performance of buildings (recast). *Official Journal of the European Union*. 2010 Jun;18(06):2010.
44. Acrylamide OC. National Primary Drinking Water Regulations. *Kidney*. 2009;2(4-D):0-7.
45. Jin YL, EXL CC, Chen SJ, Xing DR, Chen XP, Wang ZH, Wei JR, Yang Y, Zhang HT, Ai YN, Zhuang L. GB 5749-2006 Standards for Drinking Water Quality.
46. Niu P, Fernández-Sánchez C, Gich M, Ayora C, Roig A. Electroanalytical assessment of heavy metals in waters with bismuth nanoparticle-porous carbon paste electrodes. *Electrochimica Acta*. 2015 May 20;165:155-61.
47. Niu P, Asturias-Arribas L, Jordà X, Goñi AR, Roig A, Gich M, Fernández-Sánchez C. Carbon-Silica Composites to Produce Highly Robust Thin-Film Electrochemical Microdevices. *Advanced Materials Technologies*. 2017 Dec;2(12):1700163.

Chapter 6

Fabrication and characterization of metal nanoparticle-modified carbon/silica thin-film electrochemical devices



Summary

This chapter describes the manufacturing of robust carbon thin-film electrodes on silicon substrates at the wafer level by combining sol-gel synthesis and photolithographic techniques. The fabricated electrode chips are integrated into a simple fluidic device and customized for the rapid chronoamperometric sensing of COD by modifying their surface with Cu NPs produced by a controlled potentiostatic process.

6.1 Introduction

As described in the previous chapters, Chemical oxygen demand (COD) is one of the important reference parameters for determining the water organic load.¹ As an indicator of contamination, COD is useful to assess the efficiency of the treatment process, and ensure compliance with the directives that regulate wastewater treatment.

There exists a high demand for better online monitoring of COD given that existing laboratory-based methods are too slow to provide timely results and do not provide a level of early warning of emerging water pollution in real-time.² On-line measurements are usually conducted via a bypass from the main water source (Figure 6.1). This approach shows several advantages such as the possibility of continuous monitoring, at a great reduction of the cost-per-analysis considering that sample has not to be collected, stabilized and transported to the laboratory.³

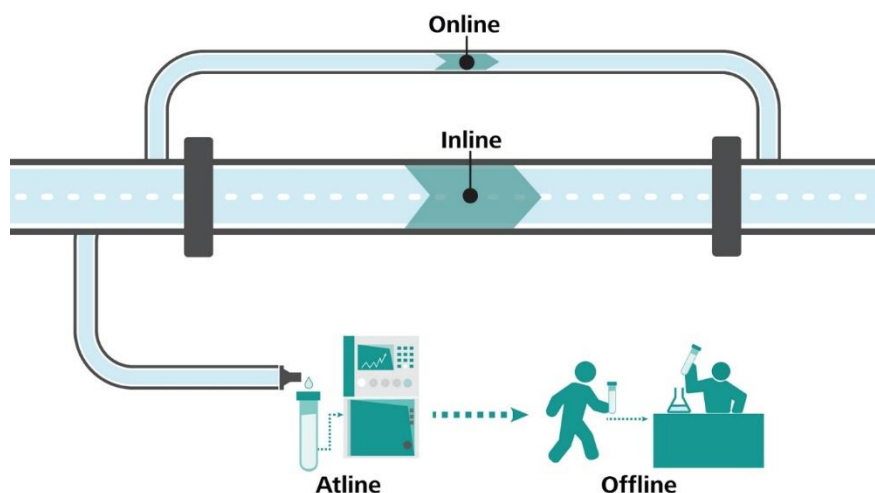


Figure 6.1. Diagram showing differences between offline, atline, online and inline analysis.
(<https://metrohm.blog/on-in-at-offline/>)

Miniaturized electrochemical sensors being amenable to integration in a fluidic system are highly appealing devices for the online monitoring of COD in waters. Miniaturized sensors fabricated by thin-film microfabrication technology are good candidates to be implemented in this scenario. Thin-films of different materials showing thicknesses from several nanometers to a few micrometers can be produced by different vapor and liquid deposition techniques. These can be patterned using conventional photolithography and etching processes to mass manufacture miniaturized structures with lateral resolutions between 1

and 100 μm .⁴ Thin-film electrochemical devices can be integrated into compact, affordable, user-friendly devices that required low-power electronics and enabled automatic online sampling and analysis.² Miniaturized engineered thin-film electrodes could be a good addition to the thick film (screen-printed) electrochemical devices presented in previous chapters. The screen-printed electrode production approach has mainly been developed to meet the demand for single-use detection. In addition, the screen printing technology shows a shortcoming in terms of device size reduction, since its maximum lateral resolution is around 80 μm .

Our group has previously reported on the production of robust carbon-silica thin films that could be patterned into miniaturized electrochemical transducers by combined lithographic / etching processes.⁵ The main challenges of this work were achieving high conductivity values to allow a good electrochemical performance of the devices and controlling the functional chemical groups that were produced on their surface during the fabrication process. Furthermore, the robust mass-production of devices at wafer-scale with high yields was not fully demonstrated.

During this chapter, we could overcome these limitations by taking a big leap towards the wafer-scale fabrication of robust carbon-silica thin-film electrodes showing excellent electrochemical performance compared to that of the glassy-carbon standard electrodes. The electrodes are integrated into a simple fluidic device and customized for the rapid chronoamperometric detection of COD by modifying their surface with Cu NPs produced by a controlled potentiostatic process. The resulting fluidic electrochemical sensor platform is promising for online monitoring applications. This is further assessed by analyzing three samples collected at different locations of a WWTP.

6.2 Fabrication and characterization of Cu NP-modified carbon/silica thin film electrode device

6.2.1 Preparation of C/SiO₂ films

The preparation of these films has been previously reported by our group,⁶ and applied in this work with some variations. Overall, the process consists in obtaining polymeric gel films by a sol-gel process followed by film pyrolysis in a reducing atmosphere. This involves three

main steps: (1) sol preparation, (2) spin-coating and formation of an organic thin film, (3) pyrolysis in a tubular furnace. In step 1, a certain amount of APTES was firstly added to 2 ml ethanol in a glass vial. Then, 0.4 g resorcinol was dissolved in the resulting solution followed by the addition of 0.54 ml formaldehyde. The mixture was continuously stirred at room temperature for a certain time to produce a sol with a certain viscosity. This is a key step since the sol viscosity, which can be controlled by the reaction time and the volume of added APTES, determines the agglomeration kinetics of the polymeric solution and thus the thickness and morphology of the deposited film.

To produce crack-free C/SiO₂ films of around 500 nm thickness, the viscosity was tuned by adjusting the reaction time at RT for different amounts of APTES. Sols with viscosities of 6-10 mPa·s resulted in high-quality crack-free films with thicknesses ranging from 400 to 800 nm.⁶ The experimental details of the preparation of C/SiO₂ films with different concentrations of APTES are shown in Table 6.1. In step 2, the sols were spin-coated to obtain the organic films (RF/SiO₂). The sols were initially spin-coated onto 1.5 cm x 1.5 cm SiO₂/Si substrates using a spinner (WS-650SZ-6NPP/LITE from Laurell Technologies) with a rotation speed of 4000 rpm for 45 s. A gel film was formed and aged in an oven at 60°C for approximately 4 h. After optimizing the preparation conditions, the sols were spin-coated onto 4-inch wafers. In step 3, the films were placed in a quartz tube to carry out the pyrolysis process under an Ar+H₂ (95%+5%) atmosphere to obtain the C/SiO₂ films. For the pyrolysis process, the furnace temperature was raised to 1000°C at a rate of 200°C·h⁻¹ with a gas flow of 100 cm³·min⁻¹ kept at this temperature for 2 h and then leave it to cool down until reaching RT.

The sheet resistance and the thickness of the films were measured using a four-point probe (MPI TS2000 SE from MPI Corporation) and a profilometer (Profilometer P16+ from KLA Tencor). The electrical conductivity, σ , was calculated from the following equation.^{7,8}

$$\sigma = \frac{1}{F \cdot R_s \cdot t} \text{ (S} \cdot \text{m}^{-1}\text{)}$$

, where F is a correction factor, R_s the sheet resistance and t the film thickness. The morphologies of the C/SiO₂ films with and without Cu NPs were characterized by SEM at 10 kV (Auriga from Carl Zeiss). Following our previous work⁶, a qualitative characterization of the interfacial adhesion of the C/SiO₂ films was done by adhering a piece of transparent tape (magic TM from 3M) to the films and then peeling it off and observing if the films were detached from the substrates.

Table 6.1. Sol compositions, reaction time, film thickness and results of the adhesion studies.

Sample	Ethanol (ml)	APTEs (ml)	Resorcinol (g)	Formaldehyde (ml)	Reaction Time (min)	C film thickness (nm)	Adhesion property	Conductivity (S/cm)
CS24-1	2	0.035	0.4	0.54	75	387±35	√√	84±6
	2	0.035	0.4	0.54	105	404±27	√√	
	2	0.035	0.4	0.54	120	520±10	√	
CS12-1	2	0.07	0.4	0.54	25	361±43	√√√	67±3
	2	0.07	0.4	0.54	32	427±16	√√√	
	2	0.07	0.4	0.54	48	430±8	√√√	
CS8-1	2	0.105	0.4	0.54	18	453±25	√√√	57±2
	2	0.105	0.4	0.54	25	501±16	√√√	
	2	0.105	0.4	0.54	29	590±62	√√√	
CS6-1	2	0.14	0.4	0.54	12	647±47	√√√	46±1.5
CS4-1	2	0.21	0.4	0.54	10	537	√√√	43±1.5

CS: carbon silica Reaction time: the time before spin-coating the sol. √ means good adhesion property and the more the number of √, the better the adhesion property.

Figures 6.2 A and 6.2 B show the representative photographic and optical microscope images of the RF/SiO₂ film spin-coated on Si/SiO₂ chips, together with the corresponding surface profile recorded with the profilometer. As previously reported,⁶ the film surface is not flat and presents a wave-like roughness morphology with an amplitude between 80 and 100 nm. Figures 6.2 C, 6.2 D, and 6.2 E display photographic, optical microscope and SEM images of the film after pyrolysis, namely C/SiO₂ film, together with the corresponding surface profile (Figure 6.2 F). This shows that the film kept the wave-like roughness with a lower amplitude between 30 nm and 40 nm, representing an almost 60% height reduction after the pyrolysis process.

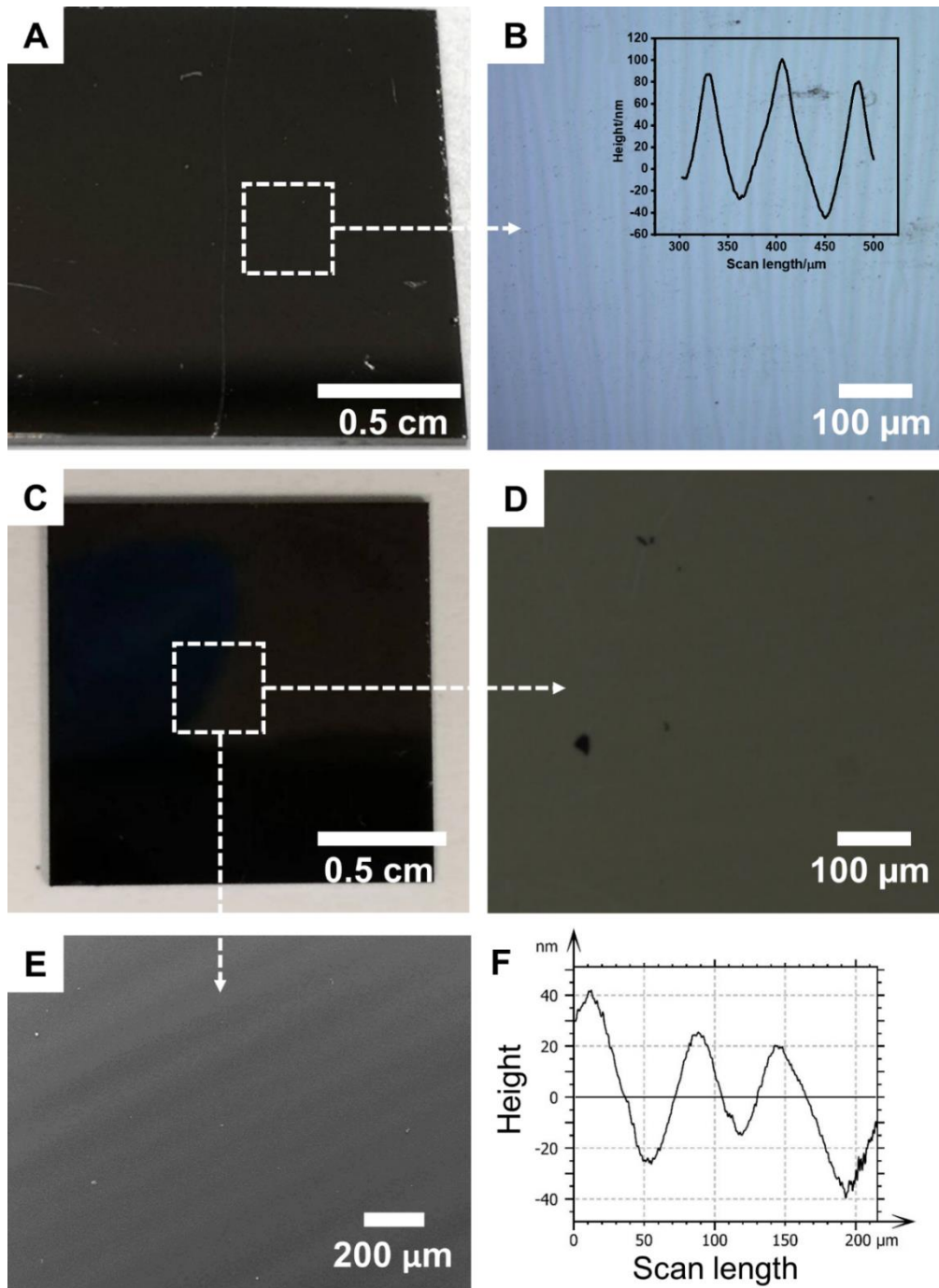


Figure 6.2. Picture (A and C), optical microscope (B and D) and SEM (E) images of the prepared RF/SiO₂ thin-film (A and B) and C/SiO₂ film (C, D and E). Panel F and the inset of panel B are the extracted surface profile scanned by the profilometer.

6.2.2 Optimization of the conductivity of the carbon/silica thin films

The main component of the analytical platform for measuring COD is the thin-film electrochemical sensor made of a C/SiO₂ material prepared by sol-gel chemistry. In order to produce a robust, sensitive, and reproducible electrochemical sensor platform, we firstly optimized the material synthesis conditions focusing on the carbon to silica relative content and pyrolysis temperature, looking at maximizing the electrode conductivity while keeping the mechanical stability. The ratio of C to SiO₂ is a key feature to achieving a strong adherence of the thin film to the Si/SiO₂ chip surface, but this ratio directly influences the film conductivity.^{5,6} The presence of SiO₂ hinders the transfer of electric charges through the carbon and reduces the overall conductivity of the C/SiO₂ film. We previously reported that a sol-gel prepared with resorcinol to APTES ratio of 4:1, pyrolyzed at 1000 °C produced C/SiO₂ thin-films showing a moderate conductivity and an acceptable electrochemical performance when compared with a glassy carbon standard electrode.

In this work, we focused on further reducing the proportion of SiO₂ in the C/SiO₂ film without compromising the film stability. For that, the amount of APTES (SiO₂ precursor) in the film was optimized while keeping the pyrolysis temperature to a set value of 1000°C. The different tested conditions together with the results of the peeling test carried out with all the produced films are summarized in Table 6.1. The results indicated that the films with thicknesses between 400 nm and 600 nm showed a strong interfacial adhesion when the molar ratio of resorcinol to APTES was 12:1 or lower. Higher ratios made the films easily peel off the chip surface. As expected, the conductivity of the C/SiO₂ film increased when the resorcinol to APTES ratio decreased (Figure 6.3 A and Table 6.1). 24:1 and 12:1 ratios produced films showing conductivity values of $84 \pm 6 \text{ S} \cdot \text{cm}^{-1}$ and $67 \pm 3 \text{ S} \cdot \text{cm}^{-1}$, respectively. These were over two- and three-fold higher than the highest ones previously reported by our group, being around $25 \text{ S} \cdot \text{cm}^{-1}$.^{5,6} In order to ensure the integrity and long-term mechanical stability of the films, the 12:1 ratio was eventually selected for manufacturing the thin-film electrodes. From this study, we anticipated that the electrochemical performance of the sensor devices could be dramatically improved, as shown below.

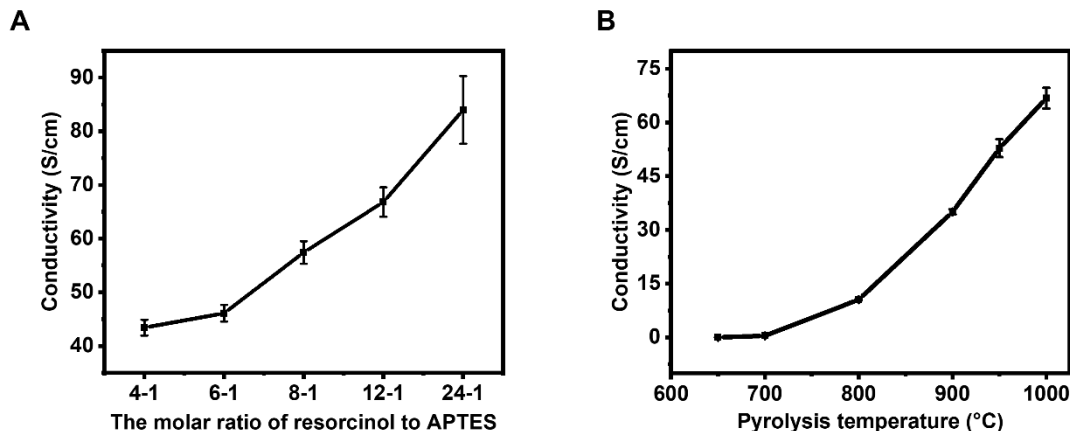


Figure 6.3. Electrical conductivity of the C/SiO₂ films prepared with gel having different molar ratios of resorcinol to APTES, obtained by varying the APTES amount (A), and the electrical conductivity of the C/SiO₂ films prepared with the 12:1 resorcinol to APTES ratio and pyrolyzed at different temperatures (B). The C/SiO₂ film was spin-coated on a 1.5x1.5 cm² SiO₂/Si substrate. The standard deviation of three measurements for different C/SiO₂ films was calculated and drawn as an error bar.

Next, the effect of the pyrolysis temperature on the film conductivity was studied in the range of 650 - 1350 °C. Figure 6.3 B shows that the conductivity increased with the pyrolysis temperature up to 1000 °C. At higher temperatures, the film's overall structure was degraded. SEM images of the resulting films in Figure 6.4 showing some flocculent or fibrous structures were generated on the substrate. This might be attributed to the formation of Si or SiC structures but it was not further investigated.^{9,10} Thus, 1000°C was selected for the purpose of producing stable C/SiO₂ conductive thin films and the manufacturing of electrochemical sensors.

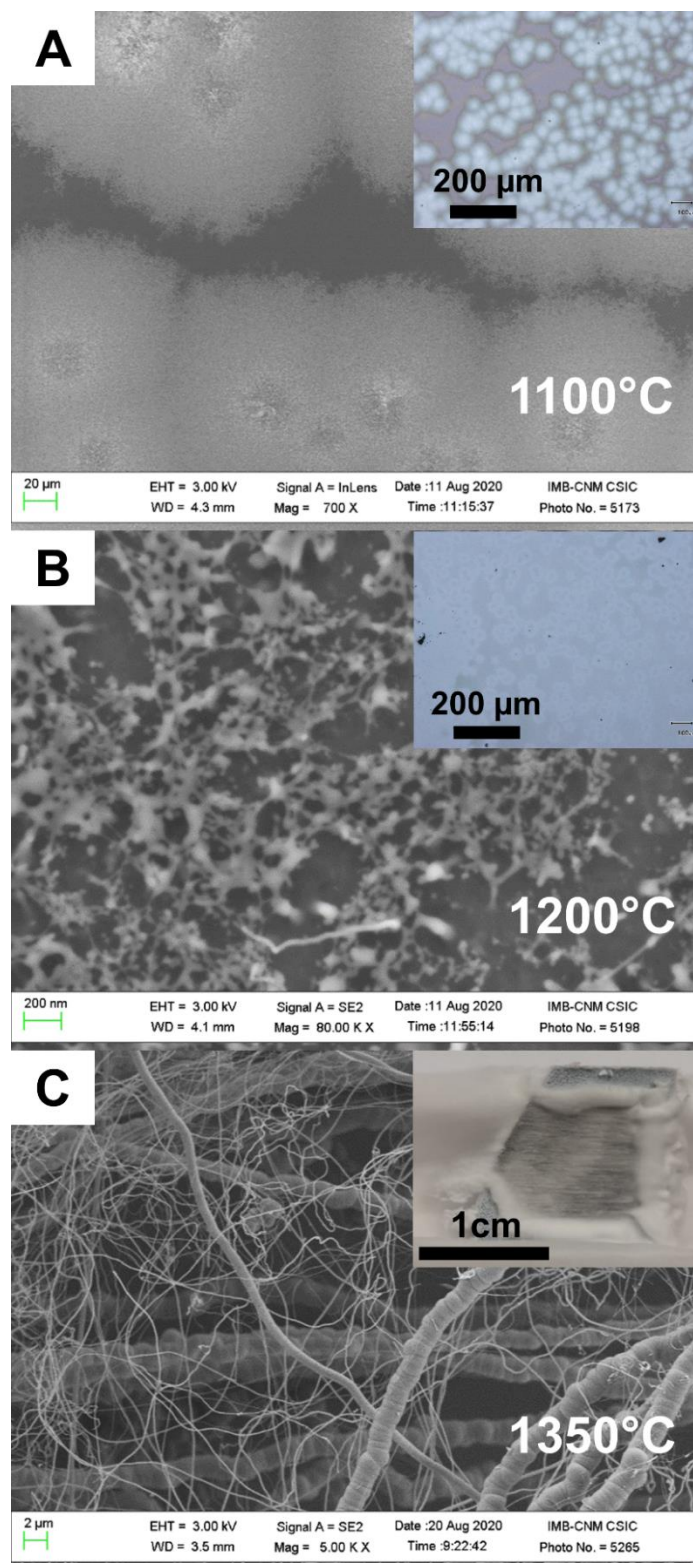


Figure 6.4. SEM images of C/SiO₂ film at different pyrolysis temperatures. (A) 1100°C, (B) 1200°C and (C) 1350°C. Inset in (A and B) are the optical microscope images and the inset in (C) shows the optical photo of the films.

6.2.3 Fabrication of carbon/silica thin-film electrodes at the wafer level by a photolithographic and etching process

Following these studies, the RF/SiO₂ films were prepared on 4-inch SiO₂/Si wafers. Thin films were patterned into miniaturized devices by combining conventional photolithography and RIE processes.⁵

The photolithography process was carried out in a cleanroom environment and consisted of the spin coating of a 4-μm thick HiPR 6512 positive photoresist layer onto the RF/SiO₂ film followed by a baking step at 90 °C for 60 s. The photoresist was then exposed to UV light through a photomask (Karl Suss MA6 mask aligner) showing the desired electrode patterns and then post-baked at 120°C for 120 s. Following the development of the photoresist to release the exposed patterns, the substrate was placed in a reactive ion etcher (Alcatel AMS-110 DE RIE) to etch the areas of the RF/SiO₂ film not covered by the photoresist using an SF₆ + O₂ plasma (P: 6 Pa; RF ICP: 600 W; RF chuck: 30W; O₂ mass flow: 150 sccm and O₂/SF₆ ratio: 9:1). The etching time was 7 min for a 1.5-μm thick RF/SiO₂ layer. Next, the remaining photoresist layer was stripped off in an acetone bath and the electrode patterns were released. Then, a pyrolysis step was carried out under the experimental conditions described in the previous section.

As shown in Figure 6.5 A, 51 RF/SiO₂ electrode chips containing two- (working electrode (WE) and counter electrode (CE) / reference electrode (RE)), three- (WE, CE and RE) and four (2 WEs, CE and RE) bar-like electrode cell arrangements were batch produced and eventually diced into chips of 11 mm x 9 mm lateral dimensions. The patterns presented extremely well-defined structures, revealing the excellent performance of this fabrication approach. Figure 6.5 B shows the images of the patterned C/SiO₂ electrodes, after dicing and pyrolysis at 1000°C. The C/SiO₂ pattern structure was kept during the pyrolysis step but the thickness was reduced to about 40% of the original RF/SiO₂ film. Conductivity values of the patterned electrodes were calculated to be 70±3 S·cm⁻¹, which is similar to the value of the non-patterned film (Table 6.1), showing that the photolithography process did not affect the material conductivity. Figure 6.5 C shows three fabricated C/SiO₂ electrochemical devices with a silver thick-film deposited on the electrode contact pads by screen printing.

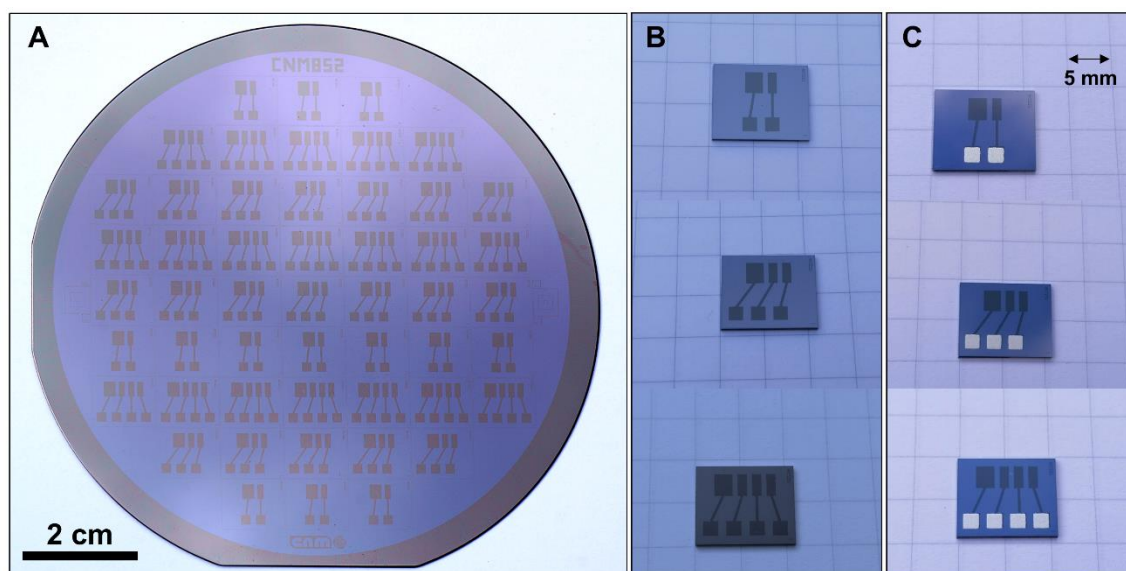


Figure 6.5. Thin-film electrode patterns prepared by photolithography and RIE processes on RF/SiO₂ thin films. (A) photograph of a 4-inch SiO₂/Si wafer containing 51 RF/SiO₂ electrodes; (B) photographs of three representative C/SiO₂ electrochemical devices; (C) photographs of three representative C/SiO₂ electrochemical devices after screen printing a silver layer on the electrode contact pads.

Figures 6.6 A and 6.6 B show images of the assembled PMMA cell for carrying out the sensor characterization in batch. The electrode chip inserted in the cell device is visualized as well as the integrated spring-loaded connectors contacting the silver pads. These pads were robust and resistant to possible scratches produced by the connectors. They also minimize the connector to pad contact resistance, ensuring stable and reproducible signals during the electrochemical measurements. Figures 6.6 C, 6.6 D and Figure 6.7 include detailed images of the C/SiO₂ electrode chip. The larger electrode (2x2.5 mm²) on the left was used as the counter electrode (CE), while the middle and right ones (1x2.5 mm²) were used as the working electrode (WE) and pseudo-reference (p-RE) electrodes, respectively. The distance between adjacent electrodes was 0.6 mm and the contact pads were located 2.9 mm apart from the electrode areas.

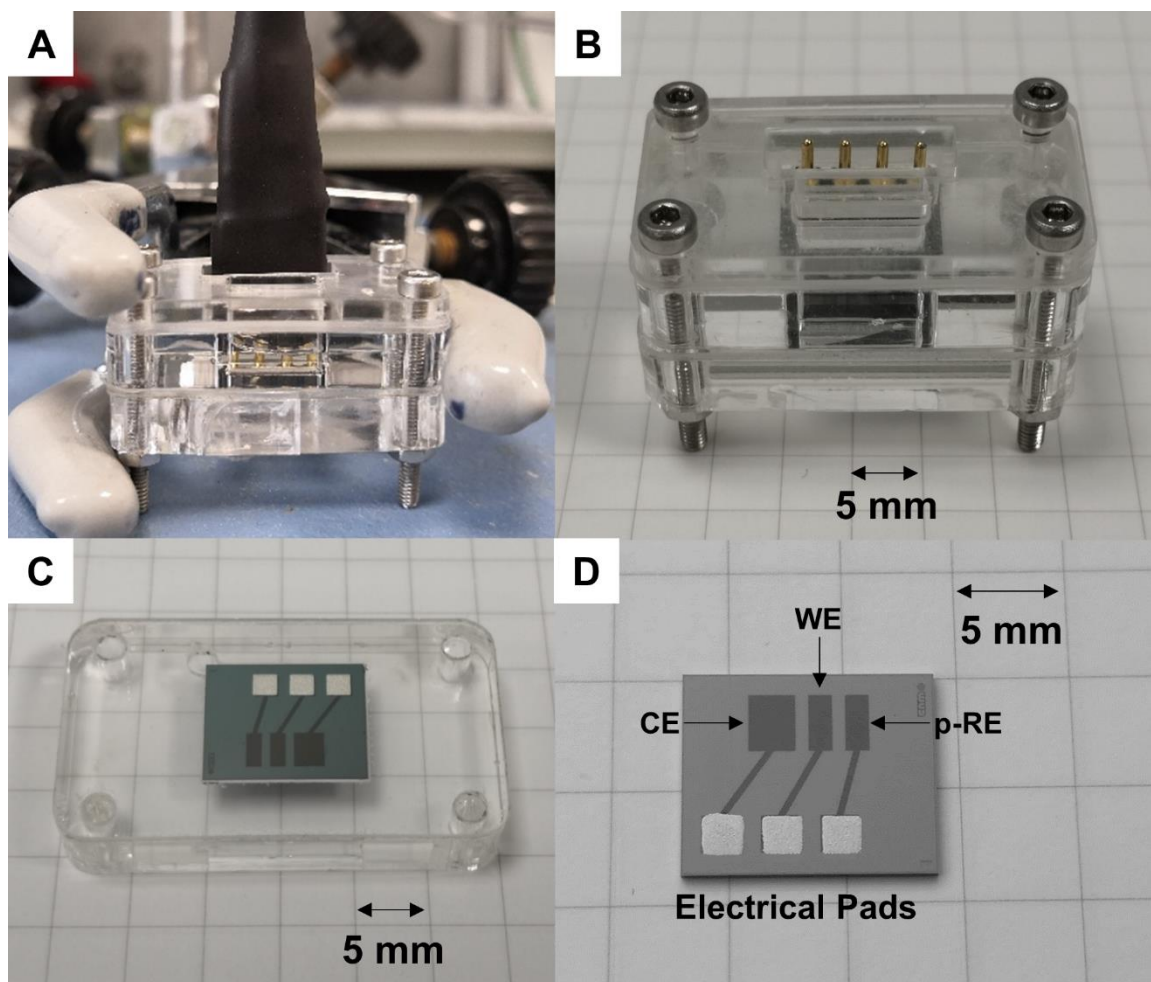


Figure 6.6. Photographs of the assembled cell for the electrode chip and COD sensor characterization (A-C) and the detail of the C/SiO₂ electrochemical device (D).

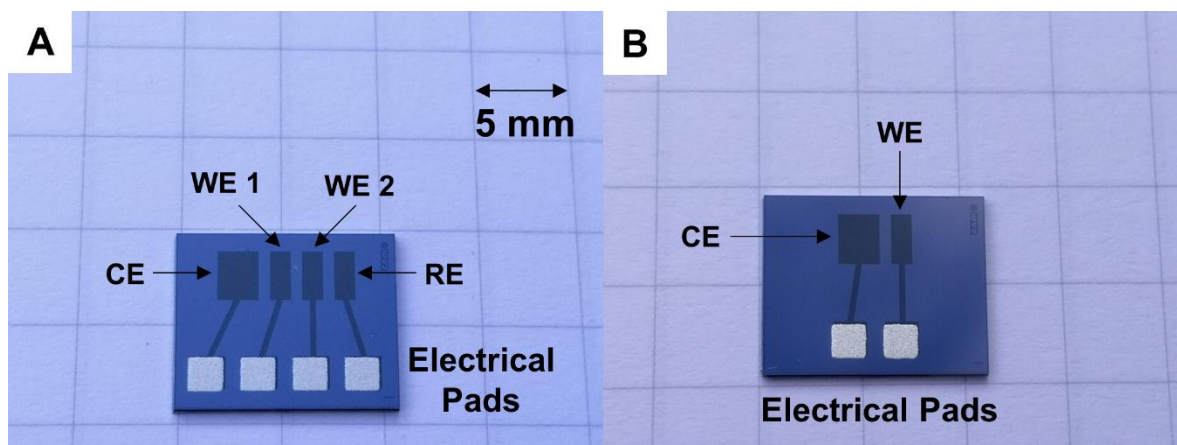


Figure 6.7. Detailed pictures of the C/SiO₂ chips. CE: counter electrode, WE: working electrode, RE: reference electrode.

6.2.4 Electrochemical characterization of the carbon/silica thin film electrodes

The performance of the C/SiO₂ electrodes was assessed by cyclic voltammetry in solutions containing different representative redox probes showing inner- or outer-sphere redox mechanisms and compared with the performance of a commercial glassy carbon electrode and our previously fabricated electrodes.⁵ This assessment took into consideration the effect of the surface composition and structure of the carbon electrodes on the electron transfer kinetics of the individual redox probe reactions. The surface chemistry, such as the density of surface oxides, the presence of other functional groups or impurities, as well as the surface electronic density of states (DOS), together with the formal potential of the redox probes, have a significant effect on the electron transfer (ET) kinetics at various carbon electrodes.⁵

The electrode response to the ferrocene outer-sphere redox probe is not sensitive to the presence of surface molecular defects and its electrochemical behavior only depends on the DOS of the carbon material. By contrast, the electrode response to the ferricyanide inner-sphere redox probe is strongly dependent on the presence of molecular defects that could act as electrocatalytic points to improve the ET kinetics at the electrode surface.^{5,11} Figure 6.8 A and Figure 6.9 A show the voltammetric responses of the C/SiO₂ electrode chip to ferricyanide and ferrocene-methanol redox species, respectively.

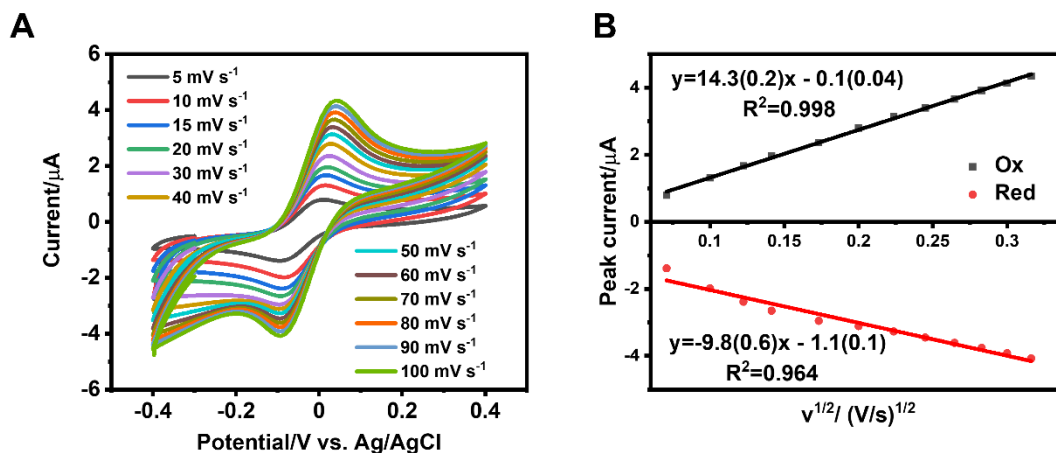


Figure 6.8. Cyclic voltammograms recorded in a 0.1 M KNO₃ solution containing 1 mM ferricyanide redox species at different scan rates (A), and the corresponding linear plots of the recorded anodic and cathodic peak current vs. the square root of scan rate (B).

Both inner-sphere and outer-sphere redox probes show quasi-reversible voltammetric signals at all scan rates.¹² The anodic to cathodic peak potential separations (ΔE_p) of ferricyanide and ferrocene-methanol are in the range of 85-122 mV and 70-90 mV at all scan rates, respectively. All of them are in accordance with the expected values for one electron electrochemical reactions. The peak currents for both anodic and cathodic signals recorded at scan rates ranging from 5 to 100 $\text{mV}\cdot\text{s}^{-1}$ show a linear dependence with the square root of the scan rate, indicating that diffusion-controlled redox processes took place (Figure 6.8 B and Figure 6.9 B).

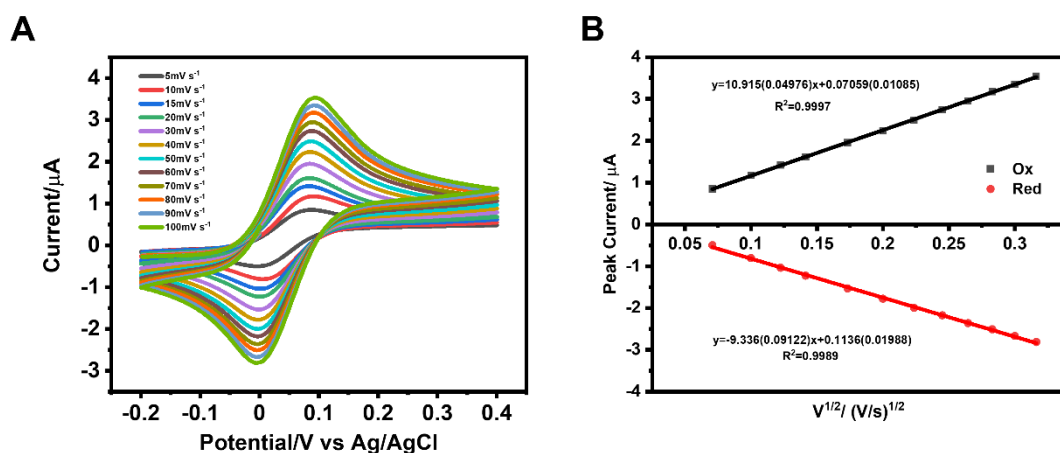


Figure 6.9. Cyclic voltammograms recorded in 0.1 M KNO₃ solution containing 1 mM ferrocene-methanol redox species at different scan rates (A), and the corresponding linear plots of the recorded anodic and cathodic peak current vs. the square root of the scan rate (B).

To more accurately compare the performance of our sensor to that of our previous devices and the standard glassy carbon electrode (GCE), we estimated apparent heterogeneous electron transfer rate constants (without correction of double-layer effects; k_{app}^0) by recording cyclic voltammetric signals at different scan rates and following the Nicholson method.⁵ The details are summarized in Table 6.2. Our sensor shows a higher k_{app}^0 value than the values estimated for electrodes A, B and C previously developed by us⁵ indicating that its performance has been significantly improved. In addition, the k_{app}^0 of our sensor is of the same order of magnitude as those of the commercial GCE. Our sensor marginally outperformed the GCE for the ferrocene-methanol oxidation process (outer-sphere redox reaction), whereas the opposite happens for the ferricyanide oxidation process (inner-sphere redox reaction). This valued evidence of a similar electrochemical performance of our sensor compared to that of the GC standard electrode in terms of electron transfer kinetics.

Table 6.2. Apparent heterogeneous electron transfer rate constants (k^0_{app}) obtained from the cyclic voltammetric measurements carried out with the fabricated electrode chips in 0.1 M KNO_3 solutions containing 1 mM Ferrocene-methanol or 1 mM Ferricyanide, at scan rates from 5 to 100 $\text{mV}\cdot\text{s}^{-1}$ ($n = 12$). The k^0_{app} values of GCE, electrodes A, B and C as cited in our previous work⁵ were used for comparison purposes.

Redox Species	$K^0_{app} (*10^{-4}\text{cm}\cdot\text{s}^{-1})$				
	Glassy carbon electrode	Electrode A	Electrode B	Electrode C	Our electrode
Ferrocene-methanol	55±9	26±2	18±2	15±2	74±8
Ferricyanide	54±9	~	~	~	33±4

6.2.5 Electrodeposition of Cu NPs on the surface of carbon/silica electrodes

The C/SiO₂ electrode chips were further applied to the development of an electrochemical sensor for COD by electrodepositing Cu NPs on the WE surface. The experimental conditions for the precise control of the Cu NPs deposition were optimized. Firstly, three different CuSO₄ concentrations (0.4, 1 and 4 mM) were studied and the Cu NPs electrodeposition was performed setting the accumulated charge to 325 μC . Keeping the latter value constant ensured that the amount of electrodeposited copper was the same, regardless of the CuSO₄ concentration.¹³ Thereby, the time required to reach this value decreased when the CuSO₄ concentration increased, being around 145 s, 72 s and 12 s, respectively.

In order to test the performance of the electrodeposited Cu NPs on the surface of the electrode, an analytical study was carried out that consisted of recording cyclic voltammograms in a 0.5 NaOH containing different concentrations of the glucose target analyte.^{14–17} Figure 6.10 shows the measurements carried out with the nanoparticles produced using a 4 mM CuSO₄ solution, as an example to visualize the analytical study. First, the cyclic voltammetric signals were recorded with Cu NPs-modified C/SiO₂ thin-film sensor in the absence (black curve) and presence of glucose (red curve) (Figure 6.10 A). A wide peak appears in the potential range of 0.4-0.6 V (vs. C pseudo-RE), which could be ascribed to the oxidation of glucose by the electrocatalytic effect of the Cu NPs. From these CVs, an overpotential of +0.7 V (vs. C pseudo-RE) was set for carrying out

chronoamperometric measurements in solutions containing increasing glucose concentrations (Figure 6.10 B).

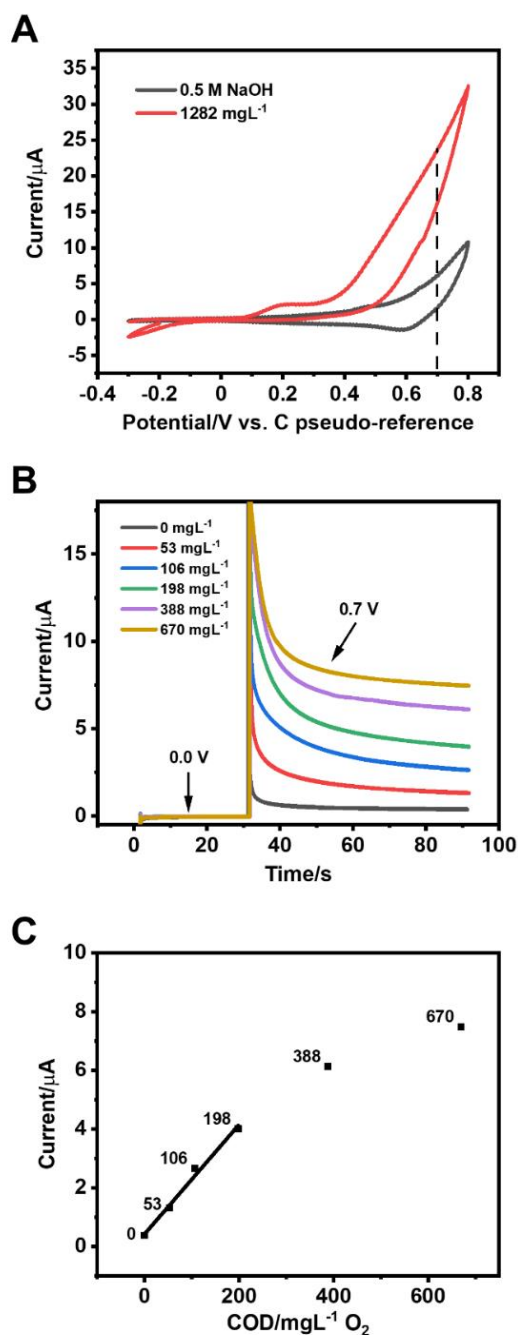


Figure 6.10. Cyclic voltammograms recorded before and after addition of glucose with Cu NPs-modified C/SiO₂ electrode in a 0.5 M NaOH solution at a scan rate of 100 mV s⁻¹ (A); Chronoamperometric responses of the Cu NPs-modified C/SiO₂ electrode recorded in solutions ranging from 0 to 670 mg L⁻¹ O₂ (equivalent to 0 to 629 mg L⁻¹ of glucose) (B); Calibration curve of the Cu NPs-modified C/SiO₂ electrode in the range between 0 and 670 mg L⁻¹ O₂ (C). The Cu NPs were prepared by the electrodeposition protocol described in the main text, in a 4 mM CuSO₄ solution at the accumulated charge of 325 μ C.

Taking the current recorded at 90 s, a calibration plot was produced that showed the linear dependence of the current with the glucose concentration (Figure 6.10 C). Similarly, the analysis results measured with the C/SiO₂ thin-film sensors produced by electrodepositing Cu NPs in 0.4 mM and 1 mM CuSO₄ solutions were obtained (Table 6.3). By comparing the sensitivity and linear range analytical parameters, the sensor manufactured using a 1 mM CuSO₄ solution was selected for further studies.

Table 6.3. Adjusted parameters and the electrochemical performance of the prepared sensor.

Group	Accumulated Charge (μC)	CuSO ₄ Concentration (mM)	Sensitivity*10 ³ ($\mu\text{A mg}^{-1}\text{L O}_2$)	Linear Range ($\text{mgL}^{-1}\text{O}_2$)
1	325	0.4	7.1 ± 0.4	53 - 198
		1	10.7 ± 0.3	53 - 670
		4	17.7 ± 0.6	53- 198
2	260	1	5.3 ± 0.5	53 - 198
	325		10.7 ± 0.3	53 - 670
	650		13.4 ± 0.2	53 - 388
	975		8.6 ± 0.7	53 - 198

Once the CuSO₄ concentration was fixed to 1 mM, the effect on the sensor response of the accumulated charge (260, 325, 650 or 975 μC) was studied. Similarly, after the electrodeposition of Cu NPs on the C/SiO₂ electrode, the electrocatalytic measurements for glucose were carried out and consequently, the calibration curves were constructed. When the accumulated charge reaches 325 μC , the sensor shows the best electrochemical performance (Table 6.3). This could be related to the distribution and aggregation of the generated Cu NPs on the surface of the working electrode.

Figure 6.11 shows the secondary electron SEM images of the electrogenerated nanoparticles for CuSO₄ concentrations of 1 mM at different accumulated charges. They revealed the presence of small bright particles on the dark film. The small particles can be attributed to the presence of Cu particles, while the darker film corresponds to the C/SiO₂ film electrode. The density of nanoparticles increases as the accumulated charge increases from 260 μC to 325 μC (Figure 6.11 A and 6.11 B). When the accumulated charge is 260 μC , the generated Cu NPs are sparsely distributed on the C film, indicating that the amount of Cu NPs formed may be insufficient to catalyze the glucose oxidation in a wide range of

concentrations and provide a linear calibration curve. By contrast, when the accumulated charge exceeded 650 μC , big sub-micron Cu particles were produced that might be the result of aggregation phenomena of CuNPs (Figure 6.11 C and 6.11 D). Furthermore, the larger the accumulated charge, the bigger the Cu particles produced. Of all the tested conditions, it appears that the Cu NPs produced when the accumulated charge was 325 μC , was uniformly distributed on the surface of the WE (Figure 6.11 B). Thus, 325 μC was used as the accumulated charge in the subsequent experiments to prepare the Cu NPs-modified C/SiO₂ electrodes, as shown in Figure 6.12.

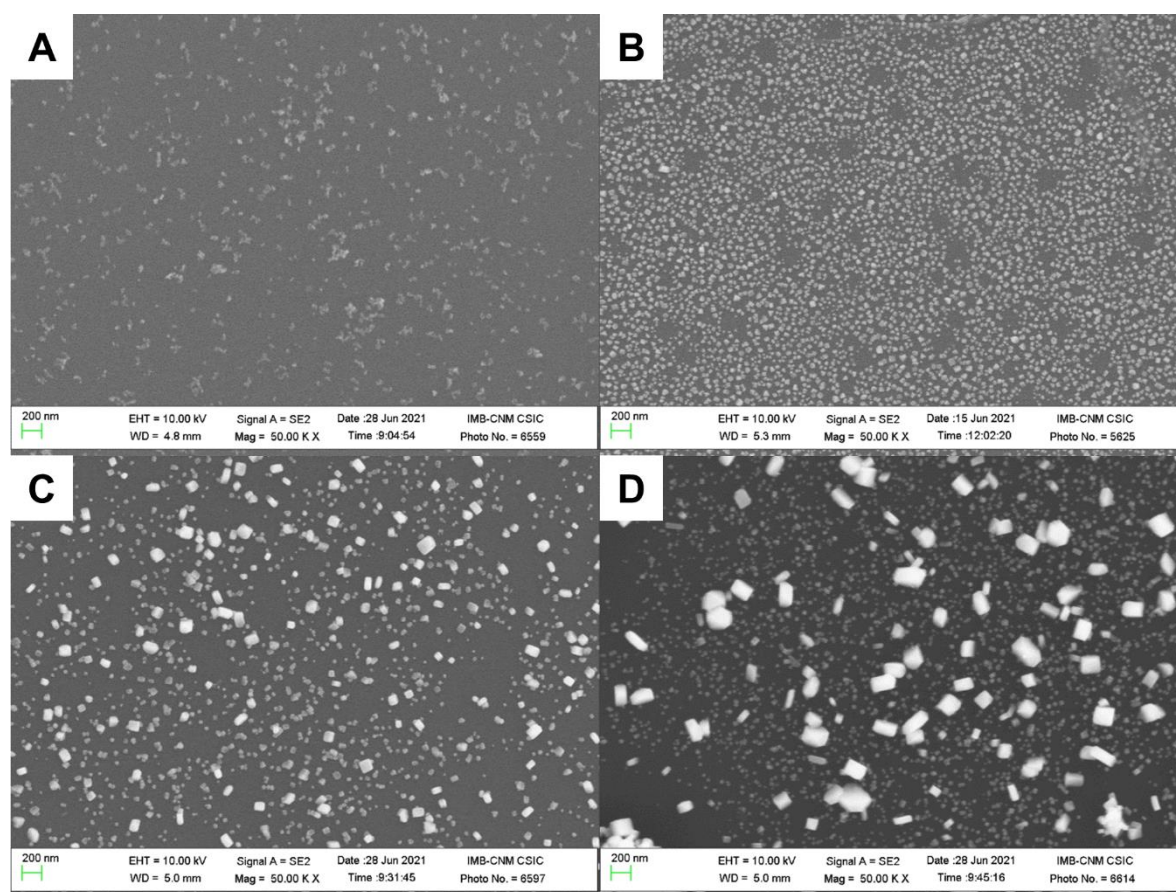


Figure 6.11. Secondary electron SEM images of the electrogenerated nanoparticles on the working electrodes at different accumulated charge values, (A) 260 μC , (B) 325 μC , (C) 650 μC , (D) 975 μC .

Figure 6.12 shows the SEM secondary electron images of the electrogenerated nanoparticles under optimized conditions, revealing the presence of small bright particles distributed on the C/SiO₂ thin-film working electrode surface, which could be attributed to the presence of Cu particles, showing sizes in the range of 35-50 nm. The particle size

distributions were obtained from a detailed study of different SEM images (Figure 6.13) using image J software.¹⁵ In addition, the reference and counter electrodes were also examined by SEM to show that no Cu NPs were deposited on either of them.

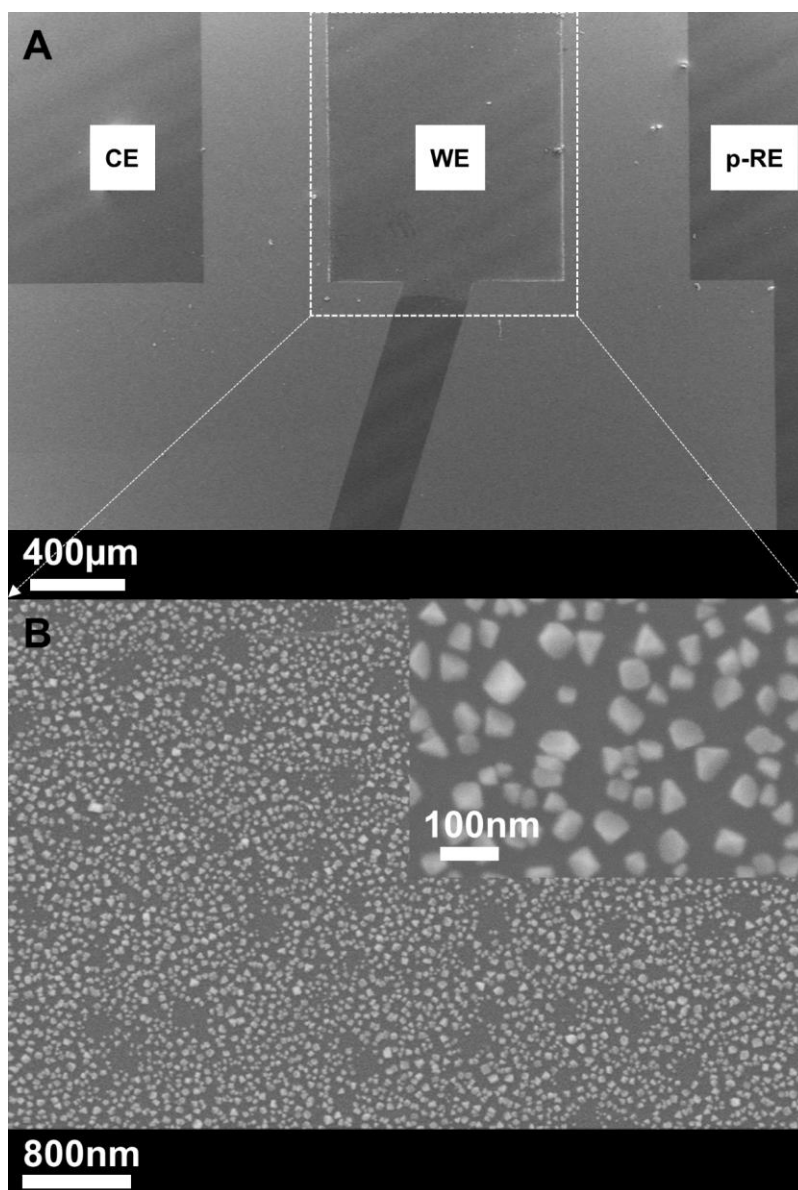


Figure 6.12. Secondary electron SEM images of a representative electrochemical device (A) and the SEM images of Cu NPs electrogenerated on the surface of the working electrode of C/SiO₂ chip.

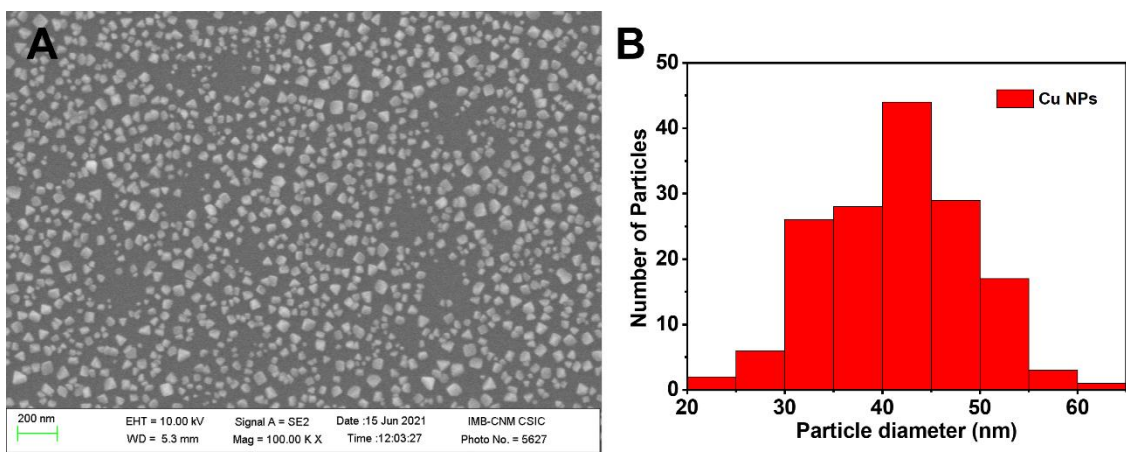


Figure 6.13. Secondary electron SEM images of Cu NPs (A) and particle size distribution histogram (B) of Cu NPs generated in a 1 mM CuSO_4 solution at the accumulated charge of 325 μC . The particle size distribution histogram was obtained from the detailed analysis of more than 150 particles viewed on SEM images.

6.2.6 Evaluation of the sensor performance for COD analysis

The analytical response of the Cu NP-modified C/SiO₂ electrode was first evaluated in batch with the assembled cell shown in Figure 6.6. The Cu NPs-modified C/SiO₂ thin-film electrode performances were assessed using glucose as the standard COD analyte.^{14–17}

Taking into account the well-known fact that carbon materials have good electrocatalytic performance under certain experimental conditions,^{18,19} we investigated the possible influence of the C/SiO₂ thin-film electrode on the electrocatalytic oxidation of glucose (Figure 6.14 A). For this, we tested the response of the bare C/SiO₂ thin-film electrode by CV in 0.5 M NaOH solutions with and without glucose. The recorded signals are nearly overlapped, indicating the negligible contribution of the C/SiO₂ film to the electrocatalytic oxidation of glucose.

Figure 6.14 B shows the voltammetric signals recorded with the Cu NPs-modified C/SiO₂ thin-film sensor in the absence (black curve) and presence of glucose (red curve). A wide peak appears in the range of 0.4–0.6 V (vs. C pseudo-RE), which can be ascribed to the electrocatalytic oxidation of glucose by the Cu NPs. Thus, an overpotential of +0.7 V was set for performing chronoamperometric measurements in solutions containing increasing glucose concentrations (Figure 6.14 C). The current recorded at 90 s time shows a linear dependence with the glucose concentration and was used to construct the calibration curve (Figure 6.14 D). The corresponding analytical parameters are summarized in Table 6.4. The

Cu NPs-modified C/SiO₂ thin-film sensor shows a linear range from 53 to 670 mg L⁻¹O₂ and a limit of detection of 28 mg·L⁻¹ O₂. As mentioned in previous chapters, the EU directive has set a COD threshold value in effluents at the exit of WWTPs of 125 mg·L⁻¹O₂ or, alternatively, this value should not exceed 25% of the COD at the WWTP influent.¹⁴ Therefore, the analytical response in the standard analyte of glucose indicates that the Cu NPs-modified C/SiO₂ sensor appears to be a good candidate for the measurement of COD in urban wastewaters.

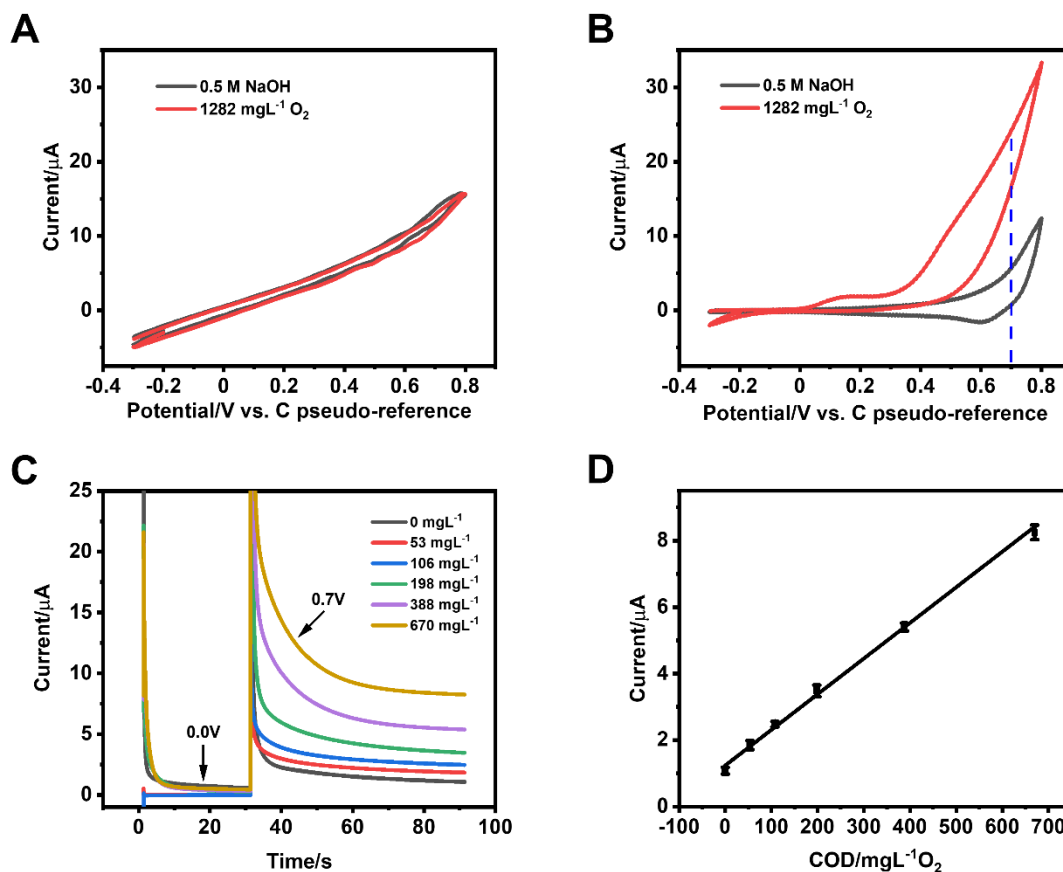


Figure 6.14. Cyclic voltammograms recorded before and after the addition of glucose with the C/SiO₂ electrode (A) and Cu NPs-modified C/SiO₂ electrode (B) in a 0.5 M NaOH solution at a scan rate of 100 mV·s⁻¹; Chronoamperometric responses of the Cu NPs-modified C/SiO₂ electrode recorded in solutions ranging from 0 to 670 mg·L⁻¹ O₂ (equivalent to 0 to 629 mg·L⁻¹ of glucose) (C); Calibration curve of the Cu NPs-modified C/SiO₂ electrode in the range between 0 and 670 mg·L⁻¹ O₂ (D). Each point represents the mean value of three measurements performed consecutively and the error bars are the corresponding standard deviation. The Cu NPs were prepared by electrodeposition method in 1 mM CuSO₄ solution at an accumulated charge of 325 μC.

Table 6.4. Analytical parameters of COD analysis obtained from the calibration curves of Cu NPs-modified C/SiO₂ electrode in the cell device and modular fluidic system.

device	sensor	slope*10 ³ ($\mu\text{A}\cdot\text{mg}^{-1}\cdot\text{L}\cdot\text{O}_2$)	intercept (μA)	R ² (n=3)	LOD ($\text{mg}\cdot\text{L}^{-1}\cdot\text{O}_2$)	Linear range ($\text{mg}\cdot\text{L}^{-1}\cdot\text{O}_2$)
Cell device	Cu NPs- modified C/SiO ₂ electrode	10.7±0.3	1.24±0.07	0.997	28	53 - 670
modular fluidic system		5.3±0.1	2.0±0.003	0.998	32.2	53 - 670

LOD is calculated using the 3 σ IUPAC criterion.

The sensor working stability was also studied. Figure 6.15 shows the variation of the sensor response during several consecutive assays using three different Cu NPs-modified C/SiO₂ electrodes. The sensor retained over 90% of its initial response after around 6 assays, indicating that the sensor could be re-used at least 6 times. After 6 measurements, the sensor response decreases rapidly. SEM images of a sensor used for more than 6 assays revealed that the Cu NPs were either consumed or aggregated (Figure 6.16). By carrying out a single measurement every 4 h, the same sensor could be applied for 1 day without requiring new electrodeposition of Cu NPs. After that, the C/SiO₂ surface could be easily regenerated and reused by electrodepositing fresh CuNPs, as explained below.

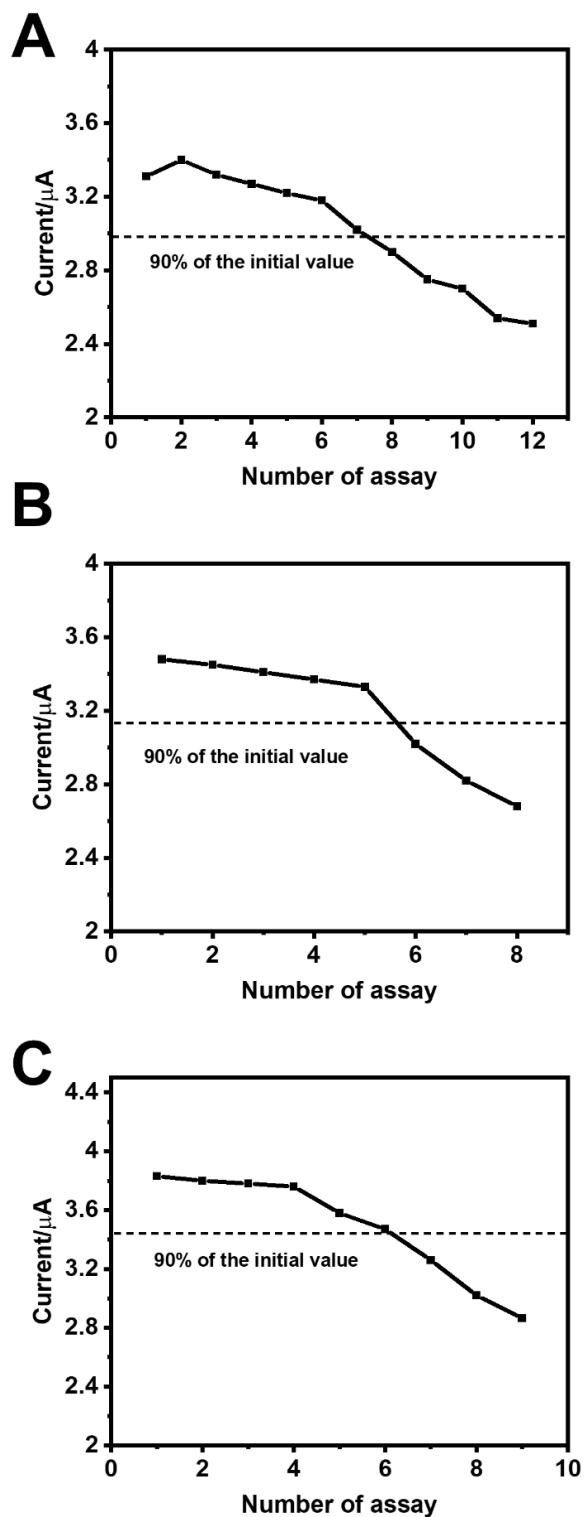


Figure 6.15. Variation of the sensor response after several consecutive assays using three different Cu NPs-modified C/SiO₂ sensors. Chronoamperometric measurements were carried out in 0.5 M NaOH solutions containing 198 mg L⁻¹ O₂, and the current values at 90 s were used as the analytical signal.

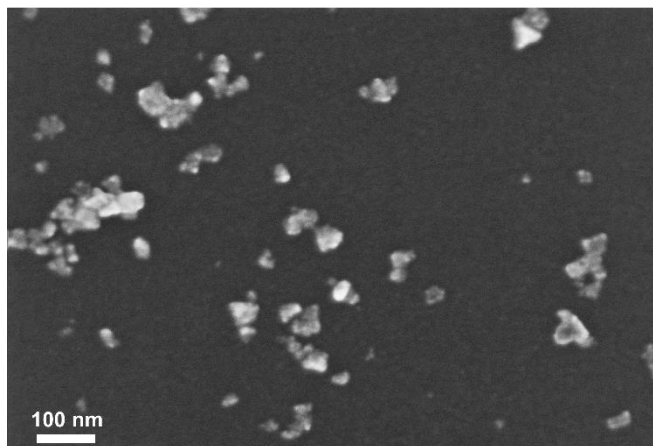


Figure 6.16. Secondary electron SEM images of the surface of one Cu NPs C/SiO₂ sensor after being used for six measurements.

The remaining Cu could be easily removed from the C/SiO₂ surface by performing an electrochemical cleaning process by applying an overpotential of 1 V (vs. C p-RE) in a 1 mM H₂SO₄ solution for 3 min. As shown in Figures 6.17 A and 6.17 C, after this process, the cyclic voltammogram recorded in 0.5 M NaOH appears to be quite similar to the one recorded with a new C/SiO₂ electrode, indicating that the remaining Cu was thoroughly removed. These cleaning and regenerating steps could be easily implemented in order to use the same C/SiO₂ for a large number of measurements.

It was demonstrated that the C/SiO₂ electrode could be reused more than 30 times during a period of 100 days, observing no evidence of physical degradation or a decrease in the electrode electrochemical performance. The thin-film electrodes could be stored in a sealed opaque bag to prevent the silver film pad from oxidation. Under these conditions, electrodes stored for over a year did not show any deterioration.

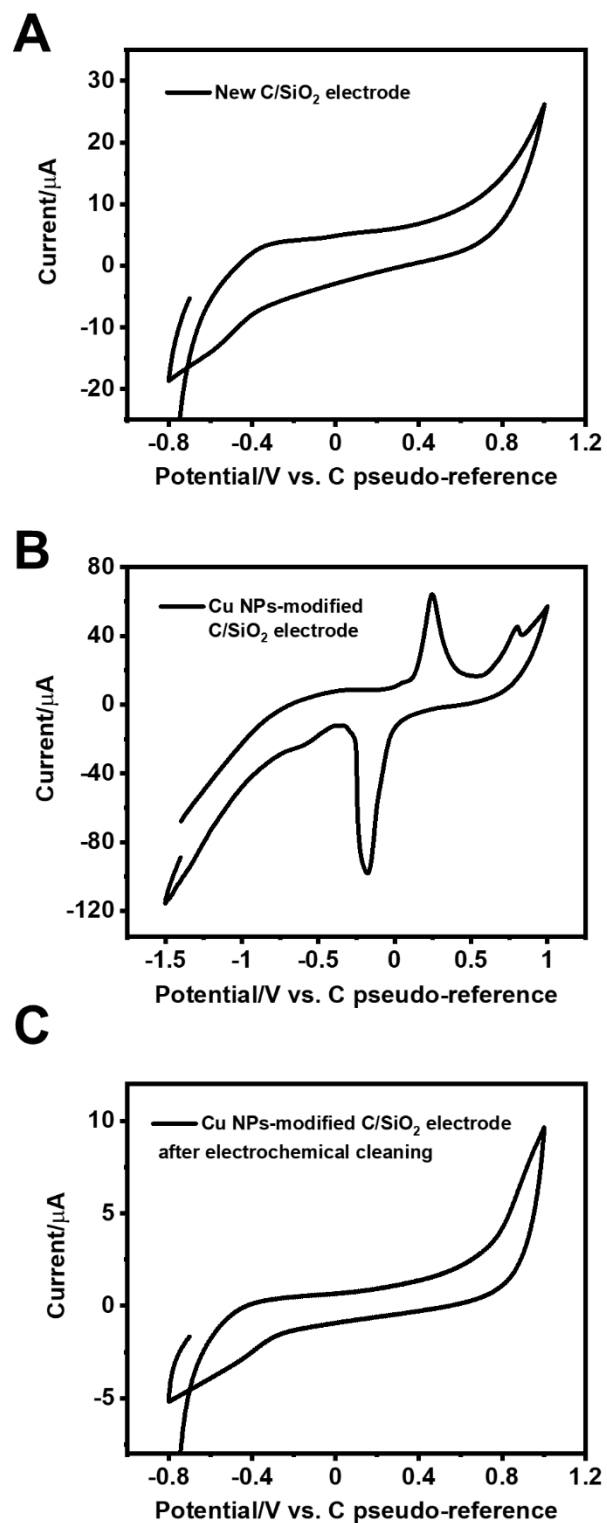


Figure 6.17. Cyclic voltammograms recorded in a 0.5 M NaOH solution at a scan rate of 100 mV s⁻¹ with a bare C/SiO₂ electrode (A), a freshly prepared Cu NP-modified C/SiO₂ electrode (B) and a Cu NPs-modified C/SiO₂ electrode after electrochemical cleaning.

6.2.7 Implementation of the Cu NP-modified C/SiO₂ sensor in a modular fluidic system

The potential deployed application of the presented electrochemical sensor for automatic monitoring of COD was assessed with the modular fluidic sensor platform (Figure 6.18). Figure 6.18 depicts the main components of the fluidic device. Inlet and outlet, flow cell and fluidic channel modules as well as the fluidic channel were defined (Figure 6.18 A). All these modules could be easily interconnected as shown in Figure 6.18 B and 6.18 C and described below. Flow conditions in the system were applied and controlled using a multichannel pressure & vacuum fluidic flow controller (OB1 MK3+, Elveflow). Inlet and outlet modules are connected to flasks by external tubing and used as reagents and waste containers, respectively. Valves were included to set up the sequential injection of the different reagents in the flow system. (Figure 6.18 D).

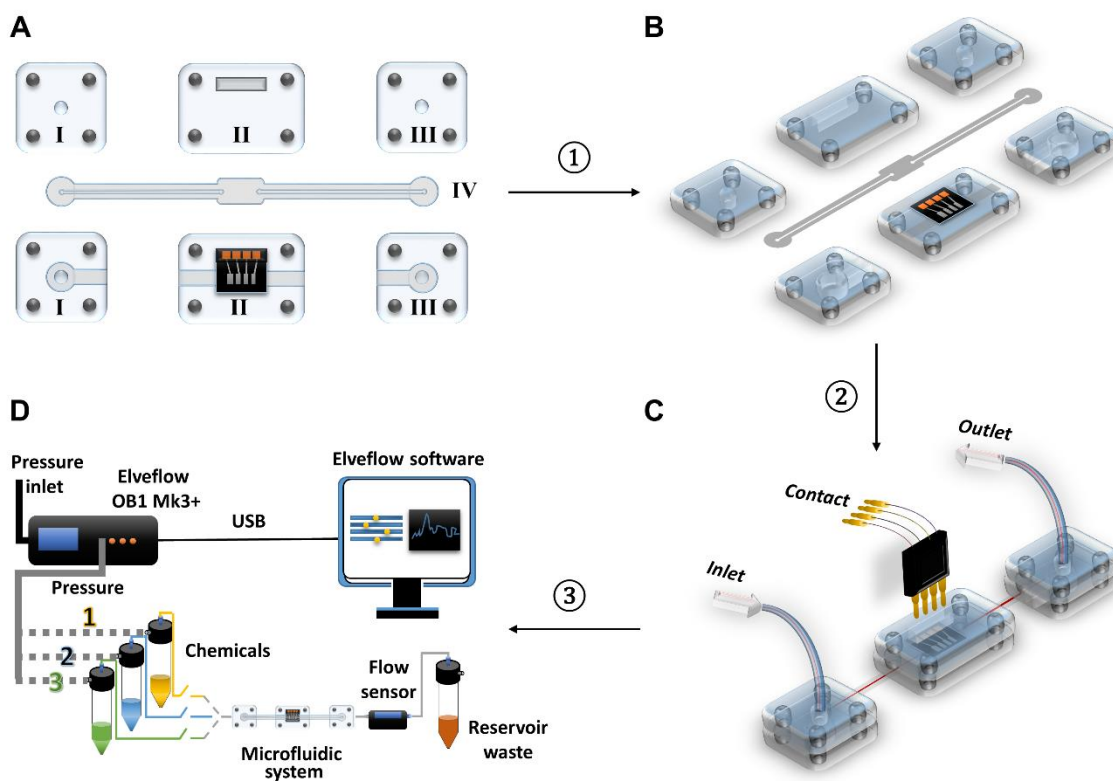


Figure 6.18. Scheme of the fluidic device. (A) different modules of the fluidic system: (I) inlet module, (II) electrode chip flow cell module, (III) outlet module, (IV) fluidic channel; (B) assembly of modular fluidic system device; (C) assembled modular fluidic device; (D) the whole modular fluidic system set-up.

175- μ m thick PSA was used to define the fluidic channel module by laser cutting. This had a length and width of 60 mm and 0.5 mm, respectively. It was sandwiched between two translucent 175- μ m thick polycarbonate sheets, each one including one inlet and one outlet having a 5 mm outer diameter and 1 mm inner diameter (Figure 6.18 A). Two 600- μ m thick cylindrical poly(dimethylsiloxane) (PDMS) gaskets with a 1-mm inner diameter were chemically bonded at the outer inlet and outlet,²⁰ in order to seal the channel once connected with the other modules and thus avoid fluid leakage. Likewise, a rectangular frame-shaped 9mm x 5mm PDMS gasket was also bonded around the area of the inner inlet and outlet in order to define a flow cell. The flow cell dimensions were 8 mm (length) x 3 mm (width) x 0.6 mm (height), with a total volume of 14.4 μ L.

Inlet and outlet modules comprised two symmetrical poly(methyl methacrylate) (PMMA) parts (10 mm x 15 mm x 30 mm), each one having four embedded neodymium disk magnets (2 mm diameter and 2 mm long, N48, Supermagnete, Gottmadingen, Germany). Magnets enabled the easy opening and closing of both modules and also to clamp of the ends of the fluidic channel module (Figure 6.18 B and 6.18 C). One orifice was opened on the top parts that served to insert 0.5-mm inner-diameter external Teflon tubes, which were bonded to the PMMA using an epoxy adhesive. The electrochemical flow cell was based on a similar PMMA clamping structure where the electrode chip was integrated and aligned with the fluidic channel module that defined the actual volume of the cell (Figure 6.18 C). The whole fluidic device is depicted in Figure 6.18 D and included a single fluidic inlet and outlet so that all the solutions are required for Cu NPs deposition and COD sensor performance (cleaning, calibration, sample preconditioning and COD measurement) were sequentially pumped.

Figures 6.19 and 6.20 A show the set-up used in the lab and a picture of the actual device for carrying out the electrochemical measurements. The planar configuration of the fluidic modules as well as the transparency of the materials enable fast inspection of the fluid flow and any other undesirable phenomena that may occur such as bubble formation or fluid leakage. This approach also enables simple disassembly and assembly of the fluidic modules, as well as the replacement of the sensor chips in just a few seconds. This reduces the time required to set up or repair the system and facilitates device manipulation by non-trained personnel.

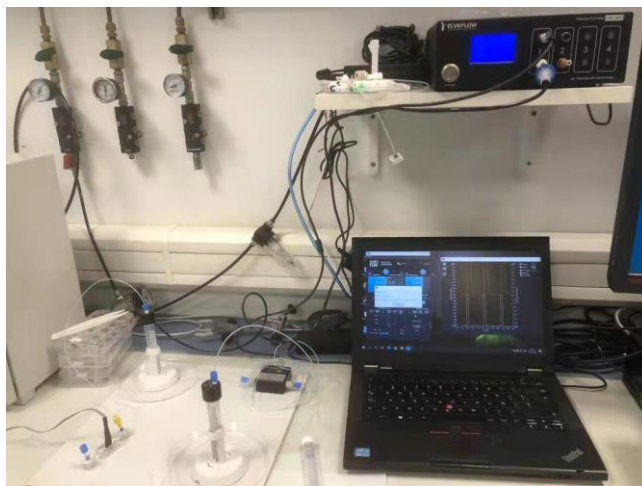


Figure 6.19. Photograph of the set-up to carry out the measurements with the modular fluidic system.

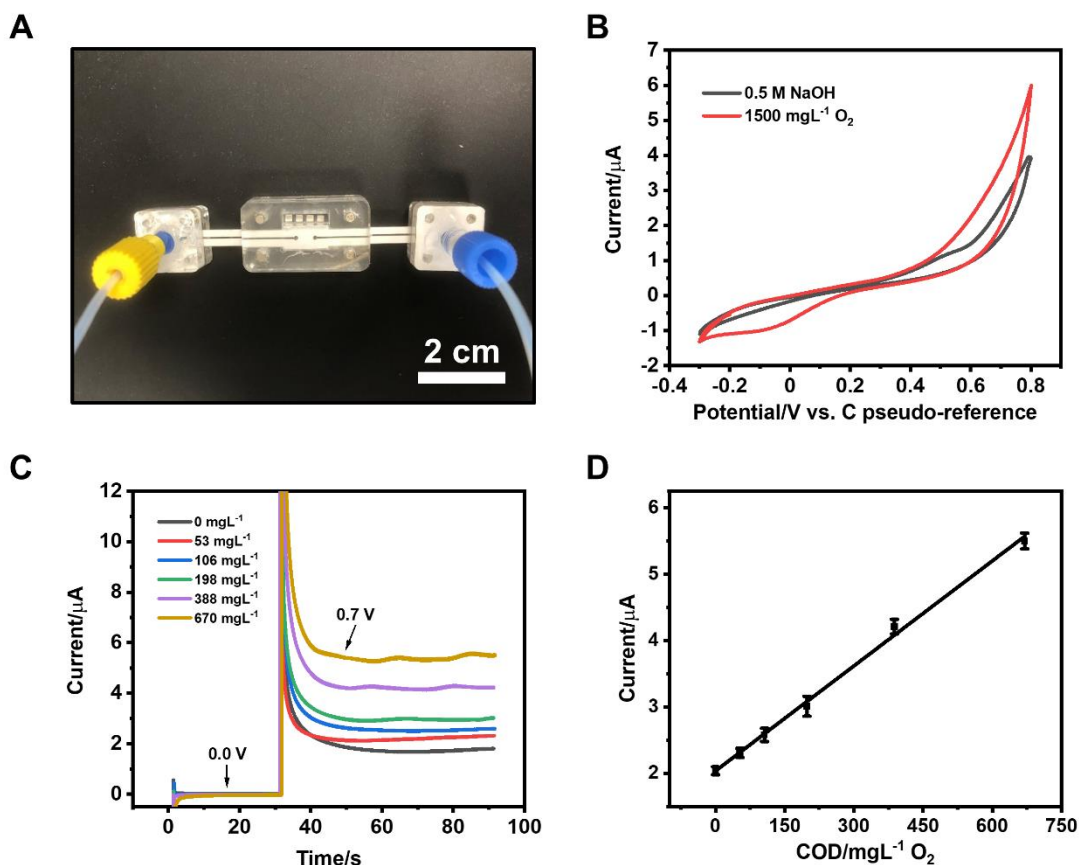


Figure 6.20. Fluidic system for the COD analysis (A); Cyclic voltammograms recorded before and after addition of glucose (1500 mg·L⁻¹) with the Cu NPs-modified C/SiO₂ electrode in a 0.5 M NaOH solution at a scan rate of 100 mV·s⁻¹ (B); Chronoamperometric responses of the Cu NPs-modified C/SiO₂ electrode recorded in solutions ranging from 0 to 670 mg·L⁻¹ O₂ (C); Calibration curve of the Cu NPs-modified C/SiO₂ electrode in the range between 0 and 670 mg·L⁻¹ O₂ (D). Each point represents the mean value of three measurements performed consecutively and the error bars are the corresponding standard deviation..

The sensor analytical performance in the fluidic platform was assessed following the same analytical experiments described above for the sensor performance in batch. The overall process included the initial formation of Cu NPs by pumping a 0.1 M H₂SO₄ solution containing 1 mM CuSO₄ at a rate of 20 $\mu\text{L}\cdot\text{min}^{-1}$ for 20 s. Then, the Cu NPs were electrodeposited over the WE surface by applying a potential of -1 V (vs. C p-RE) under continuous flow conditions until reaching 325 μC of accumulated charge.

Figure 6.21 shows the chronoamperometric signals recorded during the electrodeposition of Cu NPs outside and inside the fluidic system. The desired charge density was achieved faster than when working in batch, indicating faster electrodeposition kinetics under the convection conditions produced by the liquid flow. After the Cu NPs electrodeposition process, the system was cleaned by injecting deionized (DI) water at a rate of 65 $\mu\text{L}\cdot\text{s}^{-1}$ for 60 s. Following that, 0.5 M NaOH solution was pumped at a rate of 20 $\mu\text{L}\cdot\text{s}^{-1}$ for 20 s to ensure that the solution inside the system was fully renewed. Afterward, the voltammetric response was recorded in the 0.5 M NaOH background electrolyte solution. Similarly, the 0.5 M NaOH solution containing 1500 $\text{mg}\cdot\text{L}^{-1}$ of O₂ was also pumped into the fluidic system, and electrochemical measurements were performed in the flow condition.

The voltammetric response signals are shown in Figure 6.20 B. An anodic current increase due to the addition of glucose can be observed in the potential window between +0.5 and +0.7 V. Therefore, an overpotential of +0.7 V was selected for performing the chronoamperometric measurements. Chronoamperometric measurements were conducted under continuous flow conditions and are presented in Figure 6.20 C. The current at 90 s time was used as the analytical signal to plot the calibration curve (Figure 6.20 D). The estimated analytical parameters, also summarized in Table 6.4 show that even though the sensitivity of the sensor was reduced in the flow system, the linear range and limit of detection were similar. This evidences the potential application of the sensor approach for automatic COD measurements.

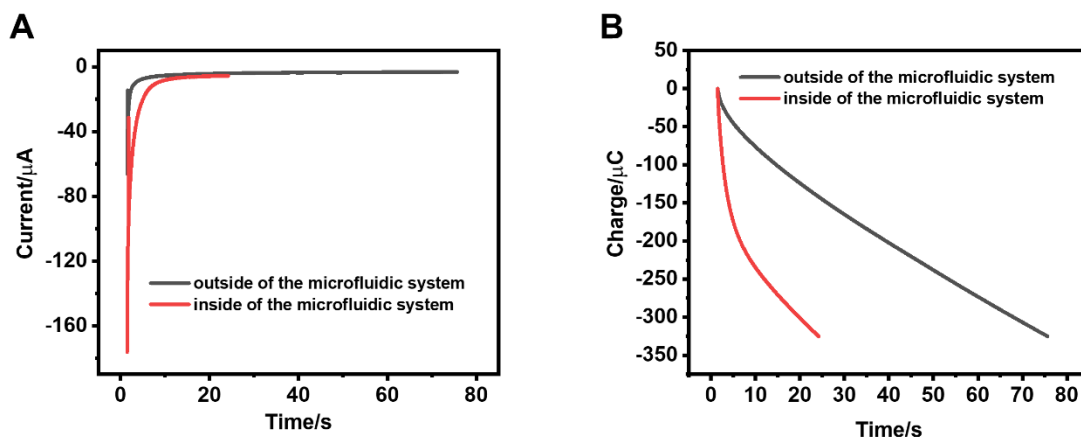


Figure 6.21. Chronoamperograms recorded during the electrodeposition of the Cu NPs over the C/SiO₂ WE surface outside (black color) and inside (red color) of the modular fluidic system.

The reusability of the sensor was also studied (Figure 6.22). After 6 measurements, the recorded current values decreased by less than 10%, in a similar way as with the sensor working in batch. Likewise, the C/SiO₂ electrodes could effectively be regenerated by removal of the remaining Cu by applying a potential of 1 V (vs. C p-RE) for 3 min under flow conditions.

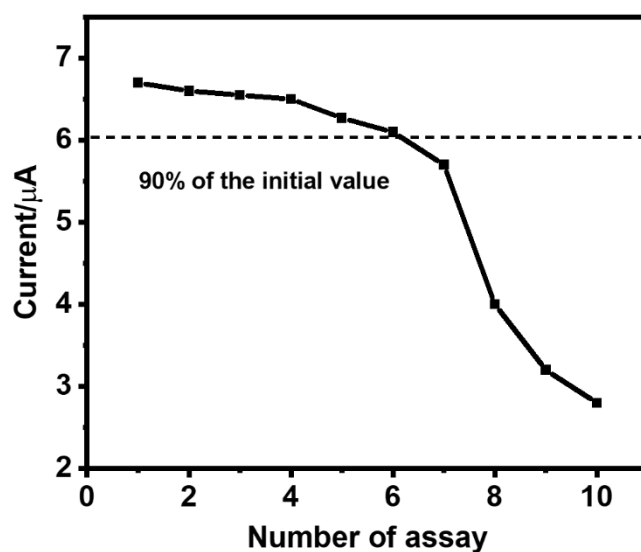


Figure 6.22. Variation of the sensor response recorded during several consecutive assays carried out in the modular fluidic system.

6.2.8 Analysis of urban wastewater samples

In order to provide an initial evaluation of the sensor potential application for the analysis of urban wastewater, we analyzed real samples collected at three different locations of a wastewater treatment plant: pretreatment effluent, clarifier effluent and the effluent. The values measured with the sensors were compared with those obtained from the analysis by an accredited laboratory using the standard dichromate method and the results are shown in Figure 6.23 and Table 6.5. It can be seen that the values recorded with the sensor both in the cell device (batch conditions) and the modular fluidic platform are in good agreement, within the error limits, with those of the standard dichromate method. The results demonstrate the potential of the sensor approach for carrying out deployed measurements of COD.

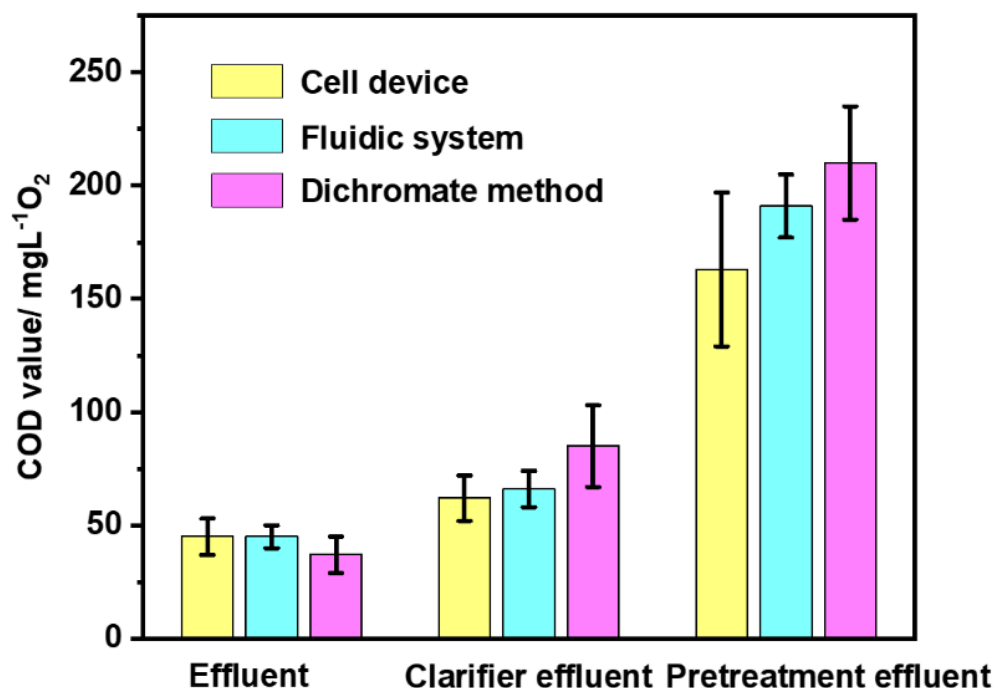


Figure 6.23. Graph of COD measurement of real water samples using Cu NPs-modified C/SiO₂ sensor and standard dichromate method. The standard deviation of three measurements was performed consecutively and drawn as an error bar.

Table 6.5. COD measurement of real water samples using Cu NPs-modified C/SiO₂ sensor and standard dichromate method.

Samples	1_Effluent	2_ Clarifier Effluent	3_ Pretreatment Effluent
Cu NPs-modified C/SiO ₂ sensor in cell device (mg·L ⁻¹ ·O ₂)	45±8	62±10	163±34
Cu NPs-modified C/SiO ₂ sensor in the modular fluidic system (mg·L ⁻¹ ·O ₂)	45±5	66±8	191±14
Dichromate method (mg·L ⁻¹ ·O ₂)	37±8	85±18	210±25

The standard deviation of three measurements was performed consecutively and written as an error bar.

6.3 Conclusions

A compact analytical platform that integrates a Cu-NP based C/SiO₂ thin-film electrochemical sensor for measuring COD was developed. C/SiO₂ thin-film electrodes were fabricated from an optimized formulation of a sol-gel composite material using standard microfabrication and screen-printing techniques at the wafer level. Electrochemical cells of different configurations were produced and showed excellent electrochemical performance compared with the glassy carbon standard electrodes and similar thin-film carbon electrodes previously reported. These electrochemical cells could be easily implemented in a device for batch electrochemical measurements or integrated into a compact fluidic system for carrying out automatic measurements. The resulting analytical platforms were applied to the development of a robust electrochemical sensor for measuring COD. In this regard, CuNPs were electrodeposited on the C/SiO₂ electrode surface under optimized conditions to engineer a Cu NPs-modified C/SiO₂ thin-film electrochemical sensor that was thoroughly assessed using standard solutions. Three real samples collected from a UWWTP were analyzed with the sensor platforms and COD values were in good agreement with those obtained by the standard dichromate method. These results demonstrate the potential of

the Cu NPs-modified C/SiO₂ thin-film electrochemical sensor for the analysis of COD and the feasibility of a system for the on-line and real-time estimation of the “organic loading” of urban wastewater. This technology could effectively contribute to the efficient management of water treatment in the near future.

As a wrapping up on the development of electrochemical sensors for COD, Table 7.1 summarizes the analytical parameters obtained from the calibration curves obtained for the sensors studied in this thesis. The results indicate the LOD of the different sensors for analysis of glucose is quite similar. On the contrary, their sensitivities vary a lot. Table 7.2 shows the COD detection of real water samples using our sensors and the standard dichromate method. Within the error limits, the responses of all our sensor are in good agreement with the COD values provided by the standard method. This demonstrates the potential of the presented sensor approaches to quantitatively detect the soluble COD in real water samples. If we consider the COD value from the standard dichromate method as the “true” value, the relative errors obtained from the three kinds of electrodes obey this order: CPE < SPE < Cu NPs-modified C/SiO₂ electrode. While the CPE performs better, it cannot be commercialized but is only used to evaluate electrode materials.

Table 7.1. Analytical parameters obtained from the calibration curves of our produced sensors for COD analysis. Glucose was adopted as the standard analyte.

Sensor	Slope*10 ³ ($\mu\text{A mg}^{-1}\text{L}^{-1}$ O_2)	Intercept (μA)	R ² (n=3)	LOD* ($\text{mgL}^{-1}\text{O}_2$)	Linear Range ($\text{mgL}^{-1}\text{O}_2$)
CPE _{Cu/C_1}	27.1 ± 0.4	3.3 ± 0.4	0.998	25.4	53 - 1500
SPE_Cu/C	10.4±0.3	13.4±0.1	0.995	23.6	53 - 1419
SPE_Cu/C_paper	5.9±0.2	5.8±0.2	0.996	24.4	53 - 394
SPE_Cu/C_paper _{NaOH}	1.6±0.1	1.2±0.1	0.997	26.0	53 - 394
Cu NPs-modified C/SiO ₂ electrode in cell device	10.7±0.3	1.24±0.07	0.997	28	53 - 670
Cu NPs-modified C/SiO ₂ electrode in fluidic system	5.3±0.1	2.0±0.003	0.998	32.2	53 - 670

*LOD is calculated using the 3 σ IUPAC criterion.

7.2. COD detection of real water samples using our produced sensors and standard dichromate method.

Electrodes	1_Effluent (mgL⁻¹O₂)	2_ Clarifier Effluent (mgL⁻¹O₂)	3_ Pretreatment Effluent (mgL⁻¹O₂)
CPE _{Cu/C_1}	39.5±9.8 (+6.2%)	93.2±9.4 (+9.8%)	216.3±12.4 (+3%)
SPE_Cu/C	38.9±4.6 (+4.6%)	98.8±2.7 (+16.3%)	220.0±10.8 (+4.8%)
SPE_Cu/C_paper	41.2±4.2 (+10.7%)	99.2±4.8 (+16.8%)	222.4±13.6 (+5.9%)
SPE_Cu/C_paper _{NaOH}	42.1±6.2 (+13.1%)	100.3±2.1 (+18.1%)	228.5±18.4 (+8.8%)
Cu NPs-modified C/SiO ₂ sensor in cell device	45±8 (21%)	62±10 (27%)	163±34 (22%)
Cu NPs-modified C/SiO ₂ sensor in the modular fluidic system (mg·L ⁻¹ ·O ₂)	45±5 (21%)	66±8 (22%)	191±14 (9%)
Dichromate method	37.2±7.8	84.9±17.8	210.0±25.0

References

1. Hao N, Dai Z, Xiong M, Han X, Zuo Y, Qian J, Wang K. Rapid potentiometric detection of chemical oxygen demand using a portable self-powered sensor chip. *Analytical Chemistry*. 2021 Jun 8;93(24):8393-8.
2. Storey MV, Van der Gaag B, Burns BP. Advances in on-line drinking water quality monitoring and early warning systems. *Water research*. 2011 Jan 1;45(2):741-7.
3. Online, Inline, Offline, At-line: How Miniaturised Mass Spectrometry Solves Problems in All Analytical Processes | Microsaic Systems. <https://www.microsaic.com/news/online-inline-offline-at-line-how-miniaturised-mass-spectrometry-solves-problems-in-all-analytical-processes/>.
4. Printed Electronics a Technology of the Past and Future | Altium. <https://resources.altium.com/p/printed-electronics-technology-past-and-future>.
5. Niu P, Asturias-Arribas L, Jordà X, Goñi AR, Roig A, Gich M, Fernández-Sánchez C. Carbon-Silica Composites to Produce Highly Robust Thin-Film Electrochemical Microdevices. *Advanced Materials Technologies*. 2017 Dec;2(12):1700163.
6. Niu P, Asturias-Arribas L, Gich M, Fernández-Sánchez C, Roig A. Electrochemically active thin carbon films with enhanced adhesion to silicon substrates. *ACS Applied Materials & Interfaces*. 2016 Nov 16;8(45):31092-9.
7. Miccoli I, Edler F, Pfnür H, Tegenkamp C. The 100th anniversary of the four-point probe technique: the role of probe geometries in isotropic and anisotropic systems. *Journal of Physics: Condensed Matter*. 2015 May 18;27(22):223201.
8. Munajat NA, Nurfaizy AH, Husin MH, Fadzullah SH, Omar G, Salim MA. The effects of different carbonization temperatures on the properties of electrospun carbon nanofibre from polyacrylonitrile (PAN) precursor. *Journal of Advanced Research in Fluid Mechanics and Thermal Sciences*. 2018;49(2):85-91.
9. Abolpour B, Shamsoddini R. Mechanism of reaction of silica and carbon for producing silicon carbide. *Progress in Reaction Kinetics and Mechanism*. 2020

May;45:1468678319891416.

10. Shirai H, Saito M, Pan LS, Abe T. Flow and diffusion analysis on the kinetics of reduction of fused silica in hydrogen. *Journal of Solid State Chemistry*. 2001 Aug 1;160(1):247-50.
11. Chen P, Fryling MA, McCreery RL. Electron transfer kinetics at modified carbon electrode surfaces: the role of specific surface sites. *Analytical Chemistry*. 1995 Sep 1;67(18):3115-22.
12. Hammerich O, Speiser B, editors. *Organic electrochemistry*. Boca Raton, FL: CRC press; 2016.
13. Giménez-Gómez P, Baldi A, Ayora C, Fernández-Sánchez C. Automated determination of As (III) in waters with an electrochemical sensor integrated into a modular microfluidic system. *ACS sensors*. 2019 Oct 28;4(12):3156-65.
14. Gutiérrez-Capitán M, Baldi A, Gómez R, García V, Jiménez-Jorquera C, Fernández-Sánchez C. Electrochemical nanocomposite-derived sensor for the analysis of chemical oxygen demand in urban wastewaters. *Analytical chemistry*. 2015 Feb 17;87(4):2152-60.
15. Duan W, Torras M, Roig A, Fernández-Sánchez C, Gich M. Composites of porous carbon and copper-based nanoparticles for the electrochemical analysis of chemical oxygen demand. *Materials Today Chemistry*. 2022 Jun 1;24:100899.
16. Silva CR, Conceição CD, Bonifácio VG, Teixeira MF. Determination of the chemical oxygen demand (COD) using a copper electrode: a clean alternative method. *Journal of Solid State Electrochemistry*. 2009 May;13(5):665-9.
17. Carchi T, Lapo B, Alvarado J, Espinoza-Montero PJ, Llorca J, Fernández L. A Nafion film cover to enhance the analytical performance of the CuO/Cu electrochemical sensor for determination of chemical oxygen demand. *Sensors*. 2019 Feb 6;19(3):669.
18. Byers JC, Güell AG, Unwin PR. Nanoscale electrocatalysis: visualizing oxygen reduction at pristine, kinked, and oxidized sites on individual carbon nanotubes. *Journal of the American Chemical Society*. 2014 Aug 13;136(32):11252-5.
19. Cao Y, Yu H, Peng F, Wang H. Selective allylic oxidation of cyclohexene catalyzed by nitrogen-doped carbon nanotubes. *ACS Catalysis*. 2014 May 2;4(5):1617-25.

20. Gimenez-Gomez P, Fernandez-Sanchez C, Baldi A. Microfluidic Modules with Integrated Solid-State Sensors for Reconfigurable Miniaturized Analysis Systems. ACS Omega. 2019 Apr 3;4(4):6192-8.

Chapter 7

Conclusions and Further Work

7.1 General Conclusions

This thesis aimed at the development of novel electrochemical sensors for the sensitive analysis of some specific water pollutants and indicators of water quality: organic matter, organohalides and heavy metals. The main progress and conclusions of this thesis are summarized below:

1. Three functional materials were successfully prepared using different approaches. Composites of porous carbon modified with copper-based nanoparticles were synthesized by the sol-gel chemical process. Carbon materials doped with silver nanoparticles were prepared from bread waste using the impregnation method. Porous carbons with different structures and textures were synthesized from different wood by-products by the high-temperature pyrolysis process. All of the material preparation methods are compatible with upscaling for mass manufacturing and low-cost fabrication.
2. The three produced materials were used to develop conventional carbon paste electrodes applied to evaluate the material's electrochemical performances. The composites of the porous C matrix and copper-based nanoparticles show excellent electrochemical performance for the quick and reliable analysis of dissolved COD in urban wastewater samples. The Ag/C composite exhibits a big potential for the analysis of halides (Cl^- , Br^- and I^-) and organohalides (sucralose and trichloroacetic acid). The achieved results indicate that bread waste can be doped with specific functional nanoparticles to produce high-added-value materials for the manufacturing of electrochemical sensors, thus contributing to the circular bio-economy. The carbon materials derived from wood by-products show superior electrochemical performance. The correlations between the types of biomass, carbon and electrochemistry were unlocked and used to select the more suitable wood material for the electrochemical application. Of the three tested wood by-products, Chestnut presented the best performance, which was linked to a lower hemicellulose content.

3. The three kinds of functional materials were successfully applied to the fabrication of screen-printed electrodes. A new electrode design with an integrated paper disk component impregnated with chemical species was successfully tested with the Cu/C nanocomposite and Ag/C active materials. It allowed bypassing sample filtering and conditioning manual steps making possible a sample-to-result analysis of dissolved COD and halogenated compounds, respectively. The new design shows great potential for in-field application due to its simplicity, robustness, and user-friendliness. The screen-printed electrodes prepared by the carbon material derived from the wood by-product were successfully applied for the analysis of heavy metals by electrode surface modification with bismuth active species. This approach could also be a good candidate for the on-site analysis of heavy metals in the near future.
4. Thin-film carbon electrodes were fabricated at a wafer-scale by combining a sol-gel material synthesis process, standard microfabrication and screen-printing technologies and show superior electrochemical performance compared with the glassy carbon standard electrode. A simple modular fluidic device was fabricated integrating the manufactured thin-film electrode chips and enabling the electrodeposition of functional Cu nanoparticles to construct an electrochemical sensor for automatically monitoring dissolved COD. The miniaturized electrochemical sensor shows great potential for monitoring this parameter in surface waters entering and exiting urban wastewater treatment plants (UWWTP).

7.2. Ongoing and Further Work

1. Upscaling the production of Cu/C composite and the screen-printed Cu/C electrodes can be investigated which is the crucial step in translating the laboratory research into a feasible industrial-scale production process.
2. The approach followed in this work to prepare porous carbon materials doped with Ag NPs from the bread waste can be extended to other similar composites with different types of nanoparticles, for instance, Cu, Bi, Au, Fe, or Co, which can be relevant in other sensing applications.
3. In our thesis, we have unlocked the biomass-carbon-electrochemistry workflow process. Guided by this knowledge, it will be quite attractive to fractionate or remove the hemicellulose in the biomass sample to improve the electrochemical

performance of the resulting carbon, keeping in mind that the process should be clean and sustainable.

4. It will be interesting to investigate the possibility of finding a one-pot synthesis to obtain carbon/silica thin films that contained the desired functional metal nanoparticles and process the material into thin-film electrodes by the microfabrication processes set up in this thesis. This possibility has been explored for the case of Cu without success due to the issues related to the interaction of the metal nanoparticles with the gases required for the etching step during the microfabrication process.
5. It will also be interesting to explore the fabrication protocol for depositing metal clusters (Cu or Ag) on carbon-silica thin-film electrodes at a wafer scale using the cluster beam deposition technique. The cluster beam deposition can be used to produce high-resolution micro-structured patterns by simple interposition of a non-contact stencil mask between the source and substrate. The nanoparticles prepared by this method are expected to retain the inherent structural properties of the deposited clusters, which will be of very small size and insignificant aggregation, showing in turn larger surface-to-volume ratios. This could result in a significant enhancement of the sensitivity and better catalytic performance of the resulting electrochemical devices.

Conferences and Publications of this Ph.D. Thesis

Conferences Attended

1. 2nd International Conference on Aerogels for Biomedical and Environmental Applications 2022, Athens, Greece (**Oral Presentation**)
Title: Tailoring xerogel of carbon and copper nanoparticle for the fabrication of screen-printed sensor for at-location analysis of dissolved chemical oxygen demand
Wenchao Duan, F. Javier del Campo, Martí Gich, César Fernández-Sánchez
1st Prize for the Best Oral Presentation
2. Athens Conference on Advances in Chemistry (acac2022), 2022, Athens, Greece (**Oral Presentation**)
Title: Upcycling bread waste into Ag-doped carbon functional material for fabricating screen-printed electrodes applied for the analysis of halogenated compounds
Wenchao Duan, Martí Gich, César Fernández-Sánchez
3. 18th International Conference on Electroanalysis ESEAC 2022, Vilnius, Lithuania (**Oral Presentation**)
Title: Miniaturized electrochemical sensors for in-field monitoring of chemical oxygen demand
Wenchao Duan, Murat Gunes, Antoni Baldi, F. Javier del Campo, Martí Gich, César Fernández-Sánchez
4. Elecnano 9 Electrochemistry for Nano & Nano for Electrochemistry, 2020 Paris, France (**Flash Presentation**)
Title: Screen-printed and thin film Cu-carbon nanocomposite electrochemical sensors for chemical oxygen demand analysis in water
Wenchao Duan, F. Javier del Campo, Miquel Torras, Anna Roig, Martí Gich, César Fernández-Sánchez
5. International Conference on Aerogels for Biomedical and Environmental Applications, 2020, Santiago de Compostela, Spain (**Oral Presentation and Poster**)

Title: Screen-printed electrodes made of Cu-doped carbon xerogel applied to the analysis of chemical oxygen demand in water

Wenchao Duan, Miquel Torras, F. Javier del Campo, Anna Roig, Martí Gich, César Fernández-Sánchez

1st Prize for the **Best Oral Presentation** and **1st Prize** for the Best Collaborative **Poster** Contribution

List of Publications

Research papers

1. **Wenchao Duan**, M. Torras, A. Roig, César Fernández-Sánchez, and Martí Gich. Composites of porous carbon and copper-based nanoparticles for the electrochemical analysis of chemical oxygen demand. **Materials Today Chemistry**, 2022, 24: 100899. <https://doi.org/10.1016/j.mtchem.2022.100899>
2. **Wenchao Duan**, Murat Gunes, Antonio Baldi, Martí Gich, and César Fernández-Sánchez. "Compact fluidic electrochemical sensor platform for on-line monitoring of chemical oxygen demand in urban wastewater." **Chemical Engineering Journal** (2022): 137837. <https://doi.org/10.1016/j.cej.2022.137837>
3. **Wenchao Duan**, F. Javier del Campo, Martí Gich, César Fernández-Sánchez, "In-field one-step measurement of dissolved chemical oxygen demand with an integrated screen-printed electrochemical sensor." **Sensors and Actuators B: Chemical**, 2022, 132304. <https://doi.org/10.1016/j.snb.2022.132304>
4. **Wenchao Duan**, César Fernández-Sánchez, Martí Gich. "Upcycling bread waste into a Ag-doped carbon material applied to the detection of halogenated compounds in waters." **ACS applied materials & interfaces**, under revision.
5. **Wenchao Duan**, Raquel Báez, Martí Gich, César Fernández-Sánchez. "Detection of chlorinated organic pollutants with an integrated screen-printed electrochemical sensor based on a silver nanoparticle carbon material derived from bread waste." In preparation.
6. **Wenchao Duan**, Amelia González, Martí Gich, César Fernández-Sánchez. "Unlocking the potential of wood by-products for screen-printed electrode electrochemical sensor for stripping analysis of Pb (II) and Cd (II) in water." In preparation.

Patent

Fernández-Sánchez C, **Wenchao Duan**, Gich. M. EU patent application: EP21383025.0. Priority date: 12th Nov. 2021

The Author

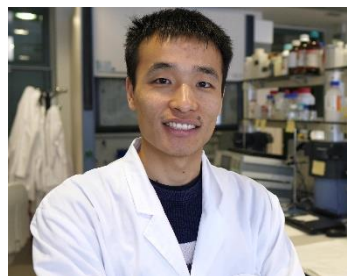
Personal information

Name: Wenchao Duan

Date of birth: 27/02/1992

Nationality: China

Email: duanwenchao227@gmail.com



Academic Records

10.2018-07.2022

Ph.D. in Materials Science

(Doctoral Student)

Thesis topic: Metal nanoparticle carbon nanocomposites to fabricate electrochemical devices for monitoring water pollutants

Group of Nanoparticles and Nanocomposite in ICMAB-CSIC and Group of Chemical Transducers in IMB-CNM-CSIC, Barcelona, Spain

Supervisors: Dr. César Fernández-Sánchez and Dr. Martí Gich

06.2015-06.2018

Master in Inorganic Chemistry

Thesis topic: Preparation of gold-based noble metal aerogels with controlled surface facets and study on their facet-dependent electrocatalytic performance

State Key Lab of Crystal Materials in Shandong University, Jinan, China

Supervisor: Prof. Haibing Xia

06.2011-06.2015

Bachelor in Chemistry

College of Chemistry and Materials Science, Hebei Normal University, Shijiazhuang, China

Technical Experience

1. **Sol-gel chemistry:** synthesizing resorcinol-formaldehyde polymeric film by a spin-coating process.
2. **Micro-fabrication techniques:** knowing the theoretical knowledge of photolithography and etching process to fabricate carbon microelectrodes devices.
3. **Screen-printing techniques:** mastering the fabrication of screen-printed electrodes.
4. **Electrochemistry:** mastering the electrochemical techniques of cyclic voltammetry, stripping voltammetry, chronoamperometric method.
5. **Clean room experience:** in my Ph.D., I always entered the clean room to carry out the experiments.
6. **Materials Characterization Techniques:** a) self-operating SEM, TEM, optical microscopy, profilometer and CO₂-laser engraving and cutting machine; b) being familiar to use the techniques of four-probe equipment, BET, TGA, XRD, rheometer, and Mastersizer for material characterization.
7. **Nanoparticles synthesis:** preparing Au NPs, Ag NPs, Au@Ag core-shell structures at different sizes.

Languages

	<u>Reading</u>	<u>Writing</u>	<u>Conversation</u>
Chinese	Excellent	Excellent	Excellent
English	Excellent	Excellent	Fluent

Other publications not related to this thesis

1. **Wenchao Duan**, Peina Zhang, Yujiao Xiahou, Yahui Song, Cuixia Bi, Jie Zhan, Wei Du, Lihui Huang, Helmuth Möhwald, and Haibing Xia. "Regulating surface facets of metallic aerogel electrocatalysts by size-dependent localized Ostwald ripening." **ACS applied materials & interfaces** 10, no. 27 (2018): 23081-23093.
2. **Wenchao Duan**, Hongkun Nie, Xiaoli Sun, Baitao Zhang, Guanbai He, Qi Yang, Haibing Xia, Ruihua Wang, Jie Zhan, and Jingliang He. "Passively Q-switched mid-infrared laser pulse generation with gold nanospheres as a saturable absorber." **Optics Letters** 43, no. 5 (2018): 1179-1182.
3. Wang, Cui, **Wenchao Duan**, Lixiang Xing, Yujiao Xiahou, Wei Du, and Haibing Xia. "Fabrication of Au aerogels with {110}-rich facets by size-dependent surface reconstruction for enzyme-free glucose detection." **Journal of Materials Chemistry B** 7, no. 47 (2019): 7588-7598.
4. Nie, Hongkun, **Wenchao Duan**, Junting Liu, Haibing Xia, Kejian Yang, Fengqiu Wang, Baitao Zhang, and Jingliang He. "Two-dimensional Au & Ag hybrid plasmonic nanoparticle network: broadband nonlinear optical response and applications for pulsed laser generation." **Nanophotonics** 9, no. 8 (2020): 2537-2548.
5. Wang, Cui, Chenshuo Wu, Lixiang Xing, **Wenchao Duan**, Xiang Zhang, Yi Cao, and Haibing Xia. "Facet-Dependent Long-Term Stability of Gold Aerogels toward Ethylene Glycol Oxidation Reaction." **ACS applied materials & interfaces** 12, no. 35 (2020): 39033-39042.